Semiconductors, Vol. 39, No. 8, 2005, pp. 861–877. Translated from Fizika i Tekhnika Poluprovodnikov, Vol. 39, No. 8, 2005, pp. 897–913.

REVIEW

Power Bipolar Devices Based on Silicon Carbide

P. A. Ivanov*^, M. E. Levinshtein*, T. T. Mnatsakanov, J. W. Palmour***, and A. K. Agarwal*****

** Ioffe Physicotechnical Institute, Russian Academy of Sciences, St. Petersburg, 194021 Russia*

*** All-Russia Electrotechnical Institute, Moscow, 111250 Russia*

**** Cree Inc., Durham NC 27703, USA*

^ e-mail: Pavel.Ivanov@mail.ioffe.ru

Submitted December 1, 2004; accepted for publication December 29, 2004

Abstract—High-voltage 4*H*-SiC bipolar devices, including rectifier diodes, bipolar junction transistors, and thyristors are discussed. The results of experimental and theoretical studies of the steady-state and transient characteristics of these devices are presented. Specific features of device operation, related to the specific electronic properties of silicon carbide and SiC-based *p–n* structures, are analyzed. © *2005 Pleiades Publishing, Inc.*

1. INTRODUCTION

One of the main directions currently being pursued in modern semiconductor electronics is the development and application of new wide-bandgap semiconductor materials: silicon carbide SiC and Group III nitrides. Due to its unique properties, such as a wide band gap (3–3.3 eV for different polytypes); extremely high critical field of avalanche breakdown (2–5 MV cm^{-1}); and thermal conductivity (3–5 W cm^{-1} K^{-1}), which exceeds that of copper at room temperature, SiC is considered a highly promising material for high-temperature, radiation-resistant, high-power, and high-speed electronics. In spite of technological problems related to the extremely high thermal stability, mechanical strength, and chemical inertness of SiC, in the early 1990s, a real breakthrough was achieved in relation to the technology required. This breakthrough has led stable progress in this area until the present time. Undoubtedly, one of the main achievements has been the development of the CVD technique for SiC [1, 2]. CVD material is used in the fabrication of virtually all the classical semiconductor devices: Schottky diodes, junction diodes, junction field-effect transistors, MOSFETs, bipolar junction transistors, gate turn-off thyristors, and microwave devices such as MESFET and IMPAT diodes. All over the world, a large number of companies are entering the industry of SiC electronics. Now, the first commercial SiC devices, high-power Schottky diode switches and high-temperature MESFETs for microwaves, are available.

In the last five years, considerable progress has been made in the fabrication, at the laboratory level, of high-power injection devices based on SiC. The principal element of any bipolar semiconductor device is a *p–n* junction capable of modulating the blocking base region using injected nonequilibrium carriers. For a long period, there was no success in the fabrication of *p–n*-SiC structures with a high density of nonequilibrium carriers because of their short lifetime (on the order of 1 ns). For a time, it was even thought that a long lifetime for nonequilibrium carriers was in principle impossible due to the high (at the level of 10^{20} cm^{-3} and even higher) concentration of stoichiometric defects in the form of excess Si. However, these misgivings proved groundless, and the problem of extending the lifetime of these structures was successfully resolved by means of CVD epitaxy. By the late 1990s, high-power 4*H*-SiC diodes, thyristors, and bipolar transistors had been produced that could block a voltage of several kilovolts and withstand a forward-current density of up to 10^4–10^5 A/cm^2. These high-voltage bipolar SiC devices demonstrated significant advantages over their Si and GaAs counterparts; specifically, they exhibited lower forward voltage drop at high current densities, higher working temperatures, and faster speeds [3–6]. These advances lead to systematic investigation of the electronic processes occurring in high-voltage bipolar 4*H*-SiC devices. In this Review, we summarize results of these studies and discuss certain features of the operation of these devices related to the specific properties of silicon carbide: a wide band gap, high critical field of avalanche breakdown and saturated velocity of electrons, strong temperature dependence of nonequilibrium carrier lifetime, incomplete ionization of acceptor impurities at room temperature, large difference between the electron and hole mobilities, effective electron–hole scattering at high forward current densities, etc. The majority of studies under discussion are related to devices developed by Cree Inc. (USA), the world leader in SiC electronics. The technologies derived by Cree allow the production of high-quality multilayer mesa-epitaxial *p–n* structures. The concentration of donor (nitrogen) and acceptor (aluminum) impurities in the epitaxial layers can be varied in a wide

Table 1. Structural parameters of 6-kV, 10-kV, and 20-kV 4*H*-SiC p^+–n_0–n^+ diodes

	Donor concentration in the base, cm^{-3}	Base thickness, μm
6-kV	1×10^{15}	50
10-kV	3×10^{14}	150
20-kV	3×10^{14}	200

range, from 10^{13} to 10^{19} cm^{-3}, and the layer thickness, from 0.1 to 200 μm. For the most part, the 4*H*-polytype of SiC is used in the production of bipolar devices, since it demonstrates several advantages over other polytypes: high and nearly isotropic mobility of majority carriers and relatively low dopant activation energy. Furthermore, at present, the technology related to this polytype is better developed than for the other SiC polytypes.

2. DIODES

In this section, we present the results of investigation of the steady-state and dynamic characteristics of 4*H*-SiC p^+–n_0–n^+ rectifier diodes rated at reverse voltages of 6, 10, and 20 kV [7–13] (denoted below as 6-kV, 10-kV, and 20-kV diodes). The impurity concentration in heavily doped emitter regions is ~10^{19} cm^{-3}, the doping level and thickness of the *n*-type base are determined by the maximum reverse blocking voltage (see Table 1).

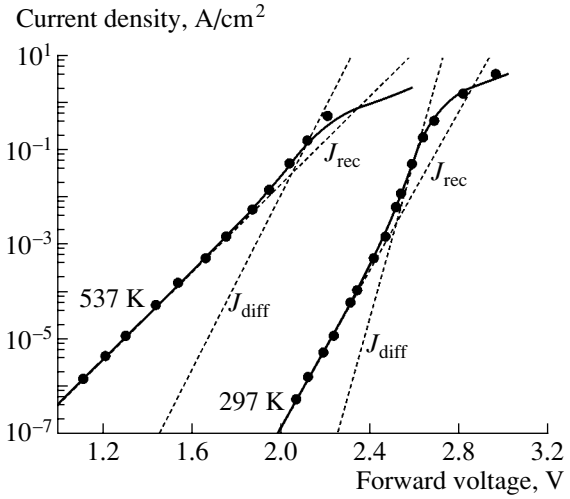

Fig. 1. Forward *I–V* characteristics of a 6-kV diode at a low current density. At T = 297 K, $j_{or} = 2.3 \times 10^{-24}$ A/cm^2, $j_{od} = 1.5 \times 10^{-45}$ A/cm^2, and $r_b = 7.4 \times 10^{-2}$ Ω cm^2. At T = 537 K, $j_{or} = 1 \times 10^{-11}$ A/cm^2, $j_{od} = 3 \times 10^{-21}$ A/cm^2, and $r_b = 1.7 \times 10^{-1}$ Ω cm^2.

2.1. Current–Voltage Characteristics at Low Current Density

At a low current density, the principal processes in the 4*H*-SiC diodes under study are generation and recombination of carriers in the space-charge region (SCR) of the *p–n* junction and diffusion transport of carriers across the base. Similar results were obtained in [14, 15]. "Excess" currents related to various structural inhomogeneities and to mechanisms of, e.g., field-assisted and field-assisted thermally activated tunneling, are virtually absent. Figure 1 shows an example of the forward current–voltage (*I–V*) characteristics of a 6-kV diode recorded at 297 and 537 K and forward current densities $j_f = 10^{-7}$–1 A/cm^2. In this range of current densities, the *I–V* characteristics are well approximated by the sum of the recombination (j_{rec}) and diffusion (j_{diff}) currents, with regard to the ohmic voltage drop across the diode base ($j_f r_b$, where r_b is the base resistivity):

$$\begin{aligned} j_f &= j_{rec} + j_{diff} \\ &= j_{or}\exp(qV_{pn}/2kT) + j_{od}\exp(qV_{pn}/kT), \\ V &= V_{pn} + j_f r_b. \end{aligned} \qquad (1)$$

At room temperature, the reverse current in the 4*H*-SiC diodes under study is so small that it is below the detection limit of our equipment. A considerable reverse current appears only at temperatures over 600 K. Figure 2 shows a reverse *I–V* characteristic of a 6-kV diode recorded at 685 K. It can be seen that $j_r \propto (V_{bi} + V)^{1/2}$, where V_{bi} is the contact potential of the *p–n* junction. Thus, the reverse current is due to thermal generation of carriers in the SCR of the *p–n* junction.

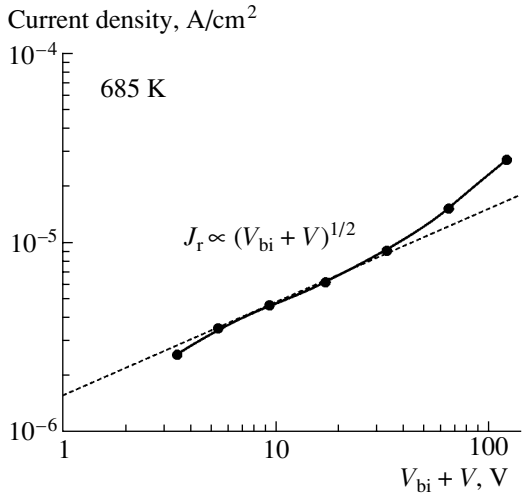

Fig. 2. Reverse *I–V* characteristic of a 6-kV diode at T = 685 K.

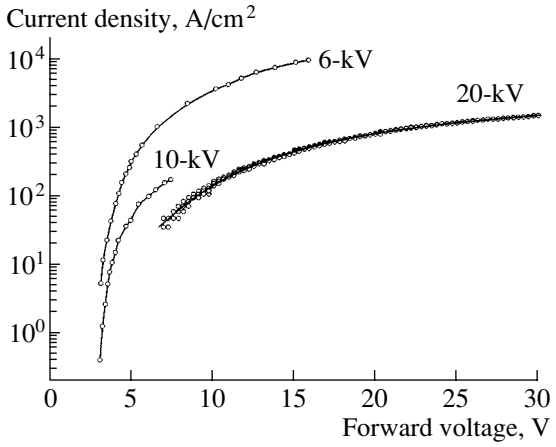

Fig. 3. Pulsed quasi-steady-state forward *I–V* characteristics of 6-kV, 10-kV, and 20-kV diodes. T = 293 K.

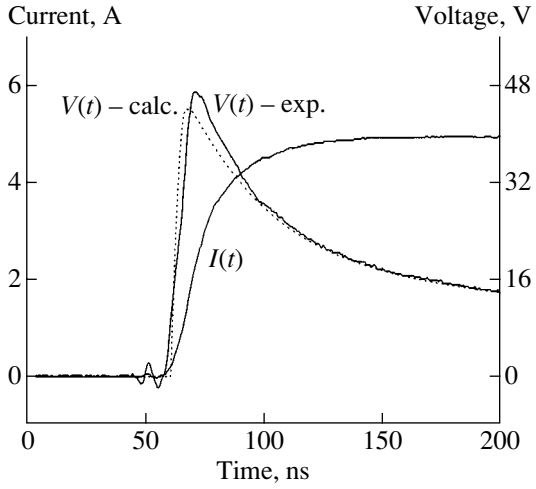

Fig. 4. Oscillograms of the current and voltage for the turn-on of a 6-kV diode. T = 293 K. The dotted line shows the results of calculations using the Issledovanie software.

2.2. Base Modulation at High Injection Levels

Figure 3 shows the pulsed quasi-steady-state *I–V* characteristics of 6-kV, 10-kV, and 20-kV diodes recorded at medium and high forward current densities. As can easily be seen, a rather deep base modulation resulting from injected carriers occurs in the 6-kV and 10-kV diodes. For example, at a forward current density of 180 A cm^{-2}, the differential resistivity of a 10-kV diode $r_d = dV/dj_f = 1.6 \times 10^{-2}$ Ω cm^{-2}, whereas the ohmic resistivity of an unmodulated base $r_b = W/q\mu_n n_0 = 0.39$ Ω cm^2 ($\mu_n = 800$ cm^2 V^{-1} s^{-1} and $n_0 = 3 \times 10^{14}$ cm^{-3}), i.e., 24 times the measured differential resistivity. For a 6-kV diode, the ohmic resistivity of an unmodulated base, $r_b = 6.5 \times 10^{-2}$ Ω cm^2, is 16 times $r_d = 4.1 \times 10^{-3}$ Ω cm^2. This situation is indicative of a rather high emitter injection coefficient and long lifetime of nonequilibrium carriers in the diode base.

In order to determine the lifetime of nonequilibrium carriers, the transient processes occurring in the diodes were studied: attainment of a steady-state forward voltage drop when subjected to a steplike forward current, post-injection voltage decay after a current break (Gossik, [16]), and recovery of the blocking properties of the diodes after switching from a forward to reverse bias (Lax, [17]).

2.3. Lifetime of Nonequilibrium Carriers: Diode Turn-on and Decay of Post-Injection Voltage

Figure 4 shows an oscillogram of the voltage across a 6-kV diode when subjected to a forward current that steeply increases from zero to 5 A. The diode demonstrates an "inductive" response to the current step, which indicates that a high density of nonequilibrium carriers is stored in the base. The $V(t)$ dependence exhibits an initial voltage spike, whose amplitude is determined by the resistivity of the base in an unmodulated state; furthermore, as nonequilibrium carriers are accumulated in the base, the voltage decreases to a steady-state value defined by the resistivity of the base in its modulated form. The characteristic time in which the steady state is attained (comparable with the nonequilibrium carrier lifetime [18]) is about 0.6 μs.

Figure 5 shows oscillograms of decay of the voltage across a 10-kV diode, recorded at temperatures of 293 and 514 K, after breaking the forward current. The oscillograms demonstrate three phases in the voltage decay: (i) a sharp drop in voltage, equal in magnitude to the steady-state voltage drop across the base under a forward current; (ii) a linear decrease in the post-injection voltage with time, which is related to recombination of excess carriers in the base; and (iii) a nonlinear voltage decrease after the disappearance of nonequilibrium carriers in the base, i.e., a discharge of the barrier capacitance of the *p–n* junction.

The linear portion of the rate of voltage decay ($\Delta V/\Delta t$) is inversely proportional to the lifetime τ of nonequilibrium carriers injected into the base [19]:

$$\frac{\Delta V}{\Delta t} = -\frac{2kT}{q}\frac{1}{\tau}. \qquad (2)$$

Here, kT is the thermal energy. Thus, at room temperature, the calculated value of τ is 0.6 μs for the 6-kV diodes and 1.55 μs for the 10-kV and 20-kV diodes. Assuming that the hole and electron mobilities in the base $\mu_p = 117$ and $\mu_n = 880$ cm^2 V^{-1} s^{-1}, respectively, we obtain the ambipolar diffusion coefficient $D_a = 2(kT/q)[\mu_n\mu_p/(\mu_n + \mu_p)] = 5.3$ cm^2 s^{-1}. The ambipolar diffusion length of nonequilibrium carriers in the base, $L_a = (D_a\tau)^{1/2}$, is 17.9 μm for the 6-kV diodes and 28.7 μm for the 10- and 20-kV diodes. These diffusion lengths can indeed provide sufficiently deep modulation of the bases in 6-kV and 10-kV diodes (the ratio of the base thickness to the diffusion length of nonequilibrium carriers is $W/L_a = 2.8$ and 5.2, respectively). Nevertheless,

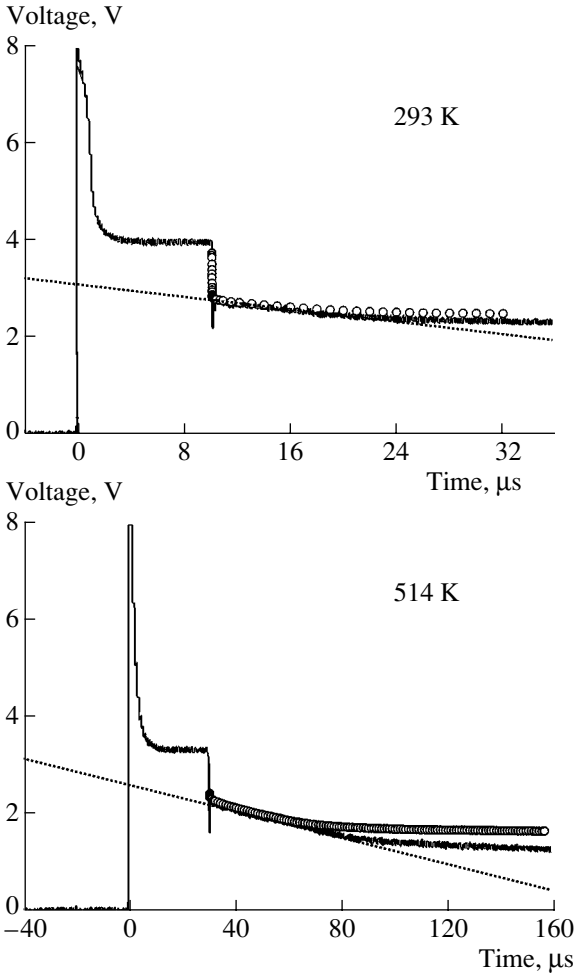

Fig. 5. Oscillograms of the post-injection voltage decay for a 10-kV diode after sharply breaking the current. The dotted line shows the results of calculations using the Issledovanie software.

these lengths are evidently insufficient for deep modulation of the 200-μm-thick base of a 20-kV diode (W/L_a = 7.0). It should be noted, however, that, as temperature increases, the lifetime of the nonequilibrium carriers in all the diodes increases several times (see Fig. 5), which leads to a decrease in the voltage drop, in spite of the carrier mobility decrease.

2.4. Lifetime of Nonequilibrium Carriers: Recovery of the Blocking Ability of Diodes after Switching from a Forward to Reverse Bias

As a rule, measurements using the Lax technique yield significantly shorter lifetimes of nonequilibrium carriers in 4*H*-SiC diodes than those obtained by applying Gossik's method [20–22]. Figure 6 shows oscillograms of 6-kV and 10-kV diodes after switching the current from the forward to the reverse direction. In the 6-kV diode, the Lax "plateau," the phase of constant reverse current, is virtually absent, while, in the

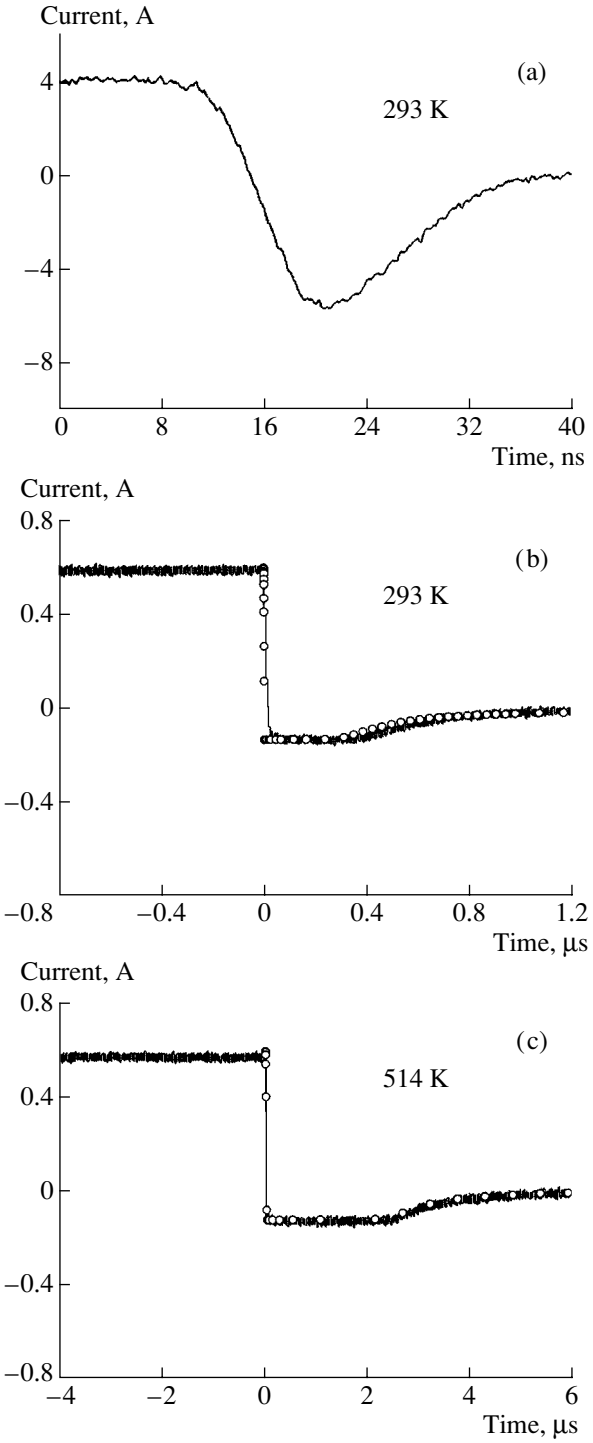

Fig. 6. Oscillograms of the current when (a) 6-kV and (b, c) 10-kV diodes are switched from the forward to reverse direction. The dotted lines show the results of calculations using the Issledovanie software.

10-kV diode, it is observed but its length is less than would be expected if we consider the lifetime of the nonequilibrium carriers (1.55 μs). The common and most probable reason for this "anomalous" behavior of

the diodes is that nonequilibrium carriers have a very short lifetime in a heavily doped p^+-emitter, i.e., a comparatively low emitter injection coefficient.

The observed difference in the behavior of the 6-kV and 10-kV diodes can be explained as follows. We assume that the lifetime in a thin layer of base, adjacent to the junction of a 6-kV diode, is as small as in the emitter. The formation of this layer may be caused by the fact that high-temperature epitaxial growth of a heavily doped *p*-layer raises the total amount of defects near the interface because of the lattice mismatch between the heavily doped and undoped layers, the related thermally induced stresses, the diffusion of Al impurity atoms, and self-diffusion. Due to presence of this "damaged" region in the part of the base that is adjacent to the *p–n* junction, the SCR starts to quickly recover after the diode has been switched from the forward to the reverse direction (the recovery time of the blocking properties is defined by the lifetime of nonequilibrium carriers in the damaged region); therefore, the phase of constant reverse current is virtually absent.

We believe that, in 10-kV diodes, the region exhibiting a short lifetime is somewhat remote from the *p–n* junction interface, presumably, due to a slightly extended doping profile in the emitter. In this case, the Lax plateau appears, but its duration depends on the distance between the *p–n* junction and the short-lifetime region.

The presence of a damaged layer in the base exerts no significant effect on the character of decay of the post-injection voltage in the diodes (in contrast to the Lax measuring mode). The fact is that, in high-voltage diodes, this layer is significantly thinner than the SCR width at a zero bias. Therefore, after the recovery of the SCR, the disrupted layer appears to be within the SCR. After breaking the forward current and recovery of the SCR, the emission of carriers from the quasi-neutral modulated base into the emitter is virtually zero. The rate of voltage decay is defined by the lifetime in the bulk of the base. These considerations define the advantages of the Gossik method, as compared to that of Lax, for determination of the nonequilibrium carrier lifetime in SiC diodes.

2.5. Simulation of the Steady-State and Transient Characteristics of Diodes

Numerical simulation of characteristics of bipolar 4*H*-Si devices was performed using the Issledovanie (Investigation) software [23], which was adapted for the purposes of studying 4*H*-SiC. This software is based on recent equations describing the carrier transport in semiconductors [24, 25], which correctly account for the whole set of nonlinear effects at high injection levels and under heavy doping: the Auger recombination, band-gap narrowing, dependence of kinetic coefficients and carrier lifetime on the doping level in heavily doped layers of the structure, etc. Using this software, we successfully simulated both the steady-state and the dynamic characteristics of 4*H*-SiC diodes and thyristors.

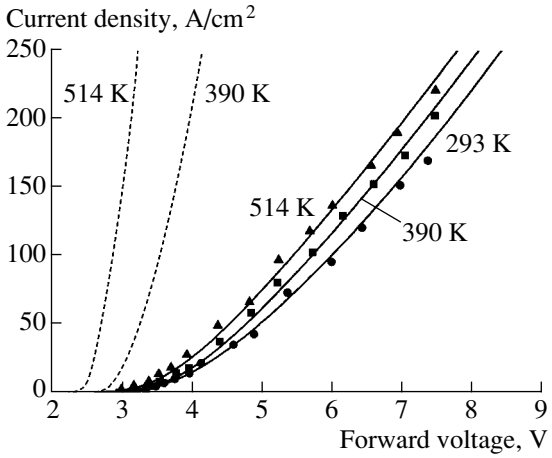

Fig. 7. Forward *I–V* characteristics of a 10-kV diode. The points show the experimental data; the dashed lines, calculation on the assumption of an "ideal" emitter; and the solid lines, calculation taking into account the damaged layer in the emitter.

Figure 7 shows the results of a computer simulation of the *I–V* characteristics of a 10-kV diode. In the first calculations, an "ideal" emitter was considered. In this case, it was assumed that the local lifetime of electrons at any point within the emitter is governed by the Auger and Shockley–Read recombinations (which were described by known relations from previous publications). As can be seen from Fig. 7, this simulation yields a much smaller forward voltage drop as compared to the experimental data. Such a result means that the real emitter injection coefficient is indeed smaller than that of the "ideal" emitter. Namely, the effective lifetime of electrons in the emitter is significantly shorter than the value that might be expected starting from the known values of the Auger recombination coefficient in 4*H*-SiC and the generally accepted Shockley–Read recombination model for heavily doped layers. The simulation showed that the *I–V* characteristics and Lax and Gossik's transient processes can be adequately described for a 10-kV diode under the assumption that the lifetime in the heavily doped region of the emitter is 0.43 ns at 297 K, 4.27 ns at 390 K, and 23.7 ns at 514 K, and the short-lifetime region lies at a distance of 0.5 μm from the metallurgical boundary of the *p–n* junction (see Figs. 5–7).

2.6. Specific Features of the Transient Characteristics of Diodes with a p-Type Base

As was first shown in [26, 27], the recovery of blocking properties in diodes with an *n*-type base is different from that in diodes with a *p*-type base: the former demonstrate rather "soft" recovery, whereas the latter may recover in a "sharp" mode. At the same forward

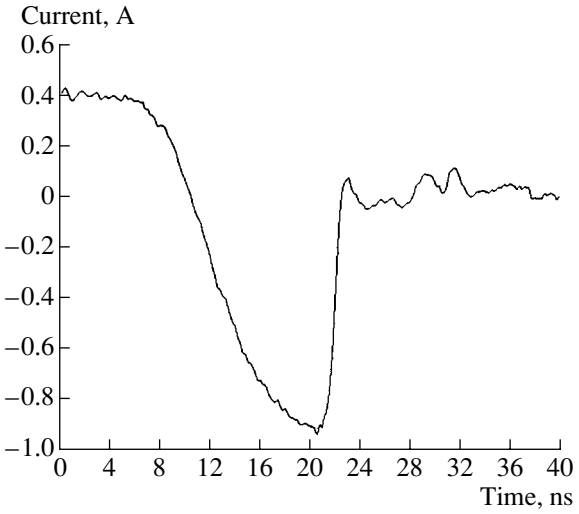

Fig. 8. Oscillogram of the current when a 4*H*-SiC diode with a *p*-type base is switched from the forward to reverse direction.

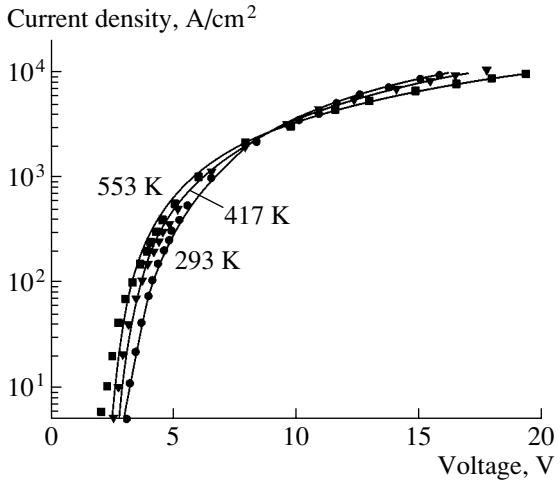

Fig. 9. Forward *I–V* characteristics of 6-kV diodes. The points show the experimental data and the solid lines, calculation taking into account electron–hole scattering.

currents and reverse biases, the maximum reverse current in *p*-type base diodes is significantly larger, and this current terminates very sharply; specifically, within less than one nanosecond (cf. Figs. 6 and 8).

The recovery processes in 4*H*-SiC diodes with *n*- and *p*-type bases were analyzed in [28] by numerical simulation of the dynamics of nonequilibrium electron–hole plasma using the Issledovanie software. The calculated time of current breaking in the *p*-base diodes was 0.5 ± 0.05 ns (in agreement with the experimental data), whereas, in the diodes with an *n*-type base, it was 3 ns. It was shown that the principal factor responsible for the different types of recovery behavior is the large ratio between the electron and hole mobilities in 4*H*-SiC ($b = \mu_n/\mu_p$).

It is known that a reverse field withdraws plasma from the near-anode region much faster than from the near-cathode one (these rates differ by a factor of b^2 before and b after the recovery of the emitter junctions [29]). In SiC, where $b = 7.5$, this process is even more pronounced than in Si ($b = 3$), and it dominates in all types of diodes, independently of the asymmetry of the emitter efficiency and the related initial inhomogeneity of the plasma distribution in a high-resistivity base. In a diode with a *p*-type base, a plasma-free region appears at the anode, expands quickly, and reaches the cathode before the cathode emitter junction recovers. Consequently, virtually all the nonequilibrium carriers are extracted from the base by the reverse current by the beginning of SCR recovery. In this case, the boundary of the recovering SCR moves in the absence of nonequilibrium carriers, i.e., with a saturation velocity.

2.7. I–V Characteristics at a High Forward Current Density: the Effect of Electron–Hole Scattering

Figure 9 shows the *I–V* characteristics of a 6-kV diode recorded at temperatures of 293–553 K and current densities up to $j = 10^4$ A cm^{-2}. As can be seen, at sufficiently high current densities, the temperature dependence of the *I–V* characteristics is inverted. The inversion point lies between current densities of 2000–3000 A cm^{-2}, which is at least an order of magnitude higher than the inversion current density for similar silicon structures. In order to explain this result, it is necessary to analyze the contributions of various nonlinear effects defining the run of the *I–V* characteristics at high current densities. The effects in question are related to heavy doping of the emitters: the narrowing of the band gap, decrease in the mobility of majority carriers, and bimolecular and Auger recombination. In addition, electron–hole scattering (EHS) must be taken into account. It should be noted that the effects related to EHS are also very important in such well-studied materials as Ge [30], Si [31, 32], and GaAs [33, 34], since they strongly reduce the carrier mobility in bipolar devices at high current densities.

To determine the parameters of EHS in 4*H*-SiC, we previously proposed a method based on analysis of the *I–V* characteristics of diode structures at high current densities [35]. The EHS-related component of the voltage drop across the base V_{eh} is usually written as

$$V_{eh} = \frac{j}{q}\int_0^{W_n}\frac{dx}{p\mu_{np}} = \frac{jW_n}{qGp_0}, \qquad (3)$$

where $\mu_{np} = Gp_0/p$ is the mobility due to EHS. Analysis of the experimental *I–V* characteristics of diodes at a high current density and computer simulation using the Issledovanie software showed that, at $T = 293$ K, the

constant Gp_0, which defines the mobility μ_{np}, equals 5.8×10^{19} V^{-1} cm^{-1} s^{-1} and the quantity qGp_0, which defines the contribution of EHS to *I–V* characteristics, is equal to 9.3 Ω^{-1} cm^{-1}. It is noteworthy that, as compared to other materials, the obtained values of the EHS parameters for SiC are smaller than those for Si by a factor of 2 [36], for Ge by 4 [30], and for GaAs by 60 [37]. This circumstance means that the effect of EHS is the corresponding number of times stronger in SiC than in Si, Ge or GaAs.

3. BIPOLAR JUNCTION TRANSISTORS

High-voltage mesa-epitaxial 4*H*-SiC bipolar junction transistors (BJTs) are currently produced in the form of *n–p–n* structures. In the transistors produced by Cree (1.8 kV, 10 A), a 20-μm-thick n_0-collector layer is doped with nitrogen to a concentration of 2.5×10^{15} cm^{-3} [38]. The base *p*-type layer, of 1 μm in thickness, is doped with Al to a concentration of about 2.5×10^{17} cm^{-3}. The emitter n^+-type layer, which is 0.75 μm thick, is doped with nitrogen at a concentration of 10^{19} cm^{-3}. The area of a discrete transistor is 1×1.4 mm^2. The emitter and base electrodes are formed as an interdigitated structure with an overlayer configuration. The width of the emitter fingers is 12 μm and their total length is 6 cm (the area of the emitter is 7.2×10^{-3} cm^2). In this section, we present the results of studies of the gain characteristics [39, 40] and on–off switching properties [41, 42] of these transistors.

3.1. Current Gain

One of the most important parameters of BJTs is the base current gain in the common-emitter circuit. In modern high-voltage 4*H*-SiC *n–p–n* BJTs, this gain reaches several tens at room temperature [43]. Figure 10 shows the dependence of a 1.8-kV transistor gain on the collector current $B(I_C)$ measured at fixed collector voltage of 100 V. As can be seen, under the effect of a small current, *B* increases as the collector current increases, reaches its maximum ($B_{max} = 20$) at $I_C = 6$ A, and then decreases rather sharply as the current further increases.

The BJT gain is affected by multiple processes [44]: carrier recombination in the bulk of the transistor base, recombination in the SCR of the emitter junction, surface recombination, "parasitic" injection of carriers from the base into the emitter (this process is enhanced as the emitter current density increases, which lowers the emitter efficiency), and base "broadening" at high current densities (this process starts to play a significant role when the average density of the carriers injected into the base becomes equal to the dopant concentration in the collector region).

The gain of relatively low-voltage SiC transistors was analyzed in [45]. However, among all the factors that can limit the gain, only carrier recombination in the bulk of the base and the emitter efficiency was considered in detail. We have performed a deeper analysis that took into account the carrier recombination in the SCR of the emitter junction, surface recombination, and recombination in the emitter bulk. We also took into account the effect of current crowding at the emitter edge, which must play an important role in *p*-base SiC transistors because of the comparatively high resistivity of the *p*-type material. To aid in the analysis, we proposed the following differential equation for the current density in the base:

$$j_B'' + \frac{\rho_B}{kT} j_B j_B' + \frac{\beta'}{\beta} j_\beta' = 0. \quad (4)$$

This equation differs from the known Hauser equation [46] in relation to the presence of the third term. This term accounts for the fact that, under the conditions of current crowding, the local gain β, which is dependent

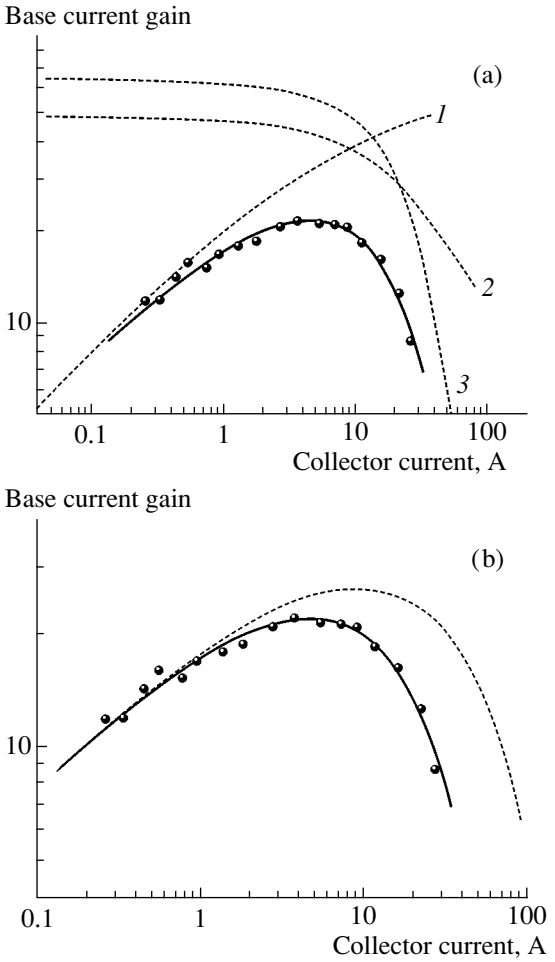

Fig. 10. Dependences of the common-emitter current gain of a 1.8-kV 4*H*-SiC transistor on the collector current. T = 293 K. The points represent the experimental data (V_{CB} = 100 V) and the solid lines, the calculated data. (a) The dashed lines show the contributions of individual recombination mechanisms (*1*) in the SCR, (*2*) at the surface, and (*3*) in the emitter. (b) The dashed line shows the calculated data for a hypothetical case $p_B = N_A$.

Table 2. Parameters of the BJT structure (used in the calculations)

Fixed parameters	Value
Electron mobility in the base, μ_{nB}, $cm^2\ V^{-1}\ s^{-1}$	700
Mobility of holes in the base, μ_{pB}, $cm^2\ V^{-1}\ s^{-1}$	150
Mobility of holes in the emitter, μ_{pE}, $cm^2\ V^{-1}\ s^{-1}$	50
Concentration of holes in the base, p_B, cm^{-3}	4×10^{16}
Adjustable parameters	**Value**
Ambipolar diffusion length in the base, L_a, μm	5.7
Preexponential factor of the recombination current in the SCR, j_{or}, A cm^{-2}	1.61×10^{-24}
Diffusion length of holes in the emitter, L_p, μm	0.2
Surface recombination rate, s, cm s^{-1}	4000

on the emitter current density, decreases in a direction going from the emitter edge toward its center:

$$\beta^{-1} \approx \beta_{rB}^{-1} + \beta_{rE}^{-1} + \beta_{rSCR}^{-1},$$
$$\beta_{rB}^{-1} = \beta_0^{-1} \approx \frac{w_B^2}{2L_a^2}, \quad \beta_{rE}^{-1} \approx \frac{D_{pE} j_E w_B^2}{q D_a^2 N_E L_{pE}}, \qquad (5)$$
$$\beta_{rSCR}^{-1} = \frac{j_{or}}{\sqrt{j_E j_{od}}}.$$

Here β_{rB} is the gain limited by recombination in the bulk of the base, β_{rE} is the gain limited by the decrease in the emitter injection coefficient at high injection levels, N_E is the donor concentration in the emitter layer, D_{pE} is the hole diffusion coefficient in the emitter, L_{pE} is the hole diffusion length in the emitter, w_B is the base thickness, D_a is the coefficient of ambipolar carrier diffusion in the base, and β_{rSCR} is the gain limited by carrier recombination in the SCR of the emitter junction.

The surface recombination current, which is dependent on the current density at the emitter edge, was calculated from the relation

$$I_{sr} = \frac{j_E(0) s w_B^2 Z_E}{2D_a}, \qquad (6)$$

where s is the surface recombination rate and Z_E is the width of an emitter finger. The Runge–Kutta method was applied to numerically integrate Eq. (4), and Eqs. (5) were solved using the dichotomy method at each integration step. One of the boundary conditions is quite obvious: the density of the base current is zero at the middle of an emitter finger ($j_B(L_E/2) = 0$). By varying the magnitude of j_B' (serving as the second boundary condition), we can obtain a number of values of $j_B'(x_i)$ and $j_E(x_i)$. Then, the total base and emitter currents can be calculated:

$$I_B = -Z_E w_B \sum_i j_B'(x_i) h + I_{sr},$$
$$I_E = Z_E \sum_i j_E(x_i) h. \qquad (7)$$

Here, h is the integration step over the coordinate. Finally, the current gain is calculated as $B = I_E/I_B$ for each value of the collector current $I_C \approx I_E$. The parameters used in the calculation are listed in Table 2.

The carrier mobilities μ_{nB}, μ_{pE}, and μ_{pB} from [47] were used. The value of p_B was calculated from the neutrality equation

$$p_B = N_v \exp\left(\frac{\Delta E_F}{kT}\right) = \frac{N_A}{1 + 2\exp\left(\frac{\Delta E_A - \Delta E_F}{kT}\right)}, \qquad (8)$$

where ΔE_F is the Fermi level position in the neutral bulk with respect to the valence band, N_v is the effective density of states in the valence band, and ΔE_A is the acceptor ionization energy. For $N_A = 2.5 \times 10^{17}$ cm^{-3}, $N_v = 2.5 \times 10^{19}$ cm^{-3}, $\Delta E_A = 0.19$ eV, the calculated value of p_B was 4×10^{16} cm^{-3} at 300 K. All the other parameters were chosen so as to obtain the best fit to the experimental $B(I_C)$ dependence. As can be seen from Fig. 10a, which shows the calculated data, the experimental results are well approximated in terms of the proposed model in the entire range of collector current under consideration. The maximum experimentally obtained transistor gain appeared to be nearly three times less than the "internal" gain, which is limited only by recombination in the bulk of the base: $B_{in} \approx 2L_a^2/W_B^2 = 65$. Three curves in Fig. 10a demonstrate individual contributions to the $B(I_C)$ dependence: those showing recombination in the SCR, surface recombination, and recombination in the emitter region. As can be seen, at a high current density, the principal contribution to the decrease in B at high currents is made by the decrease in the emitter injection coefficient, which is significantly enhanced by the effect of emitter current crowding. The role of crowding is illustrated by Fig. 10b, where the result calculated for the hypothetical limit of complete ionization of acceptors in the base, $p_B = N_A$, is shown.

3.2. Dynamic Characteristics

The turn-on time of a 1.8-kV transistor (about 130 ns for turn-on in the active mode in the common-emitter circuit) is defined by the recharging of its collector capacitance, which can be found by taking into account the Miller effect. When the transistor saturation mode is turned on, the characteristic time taken for the

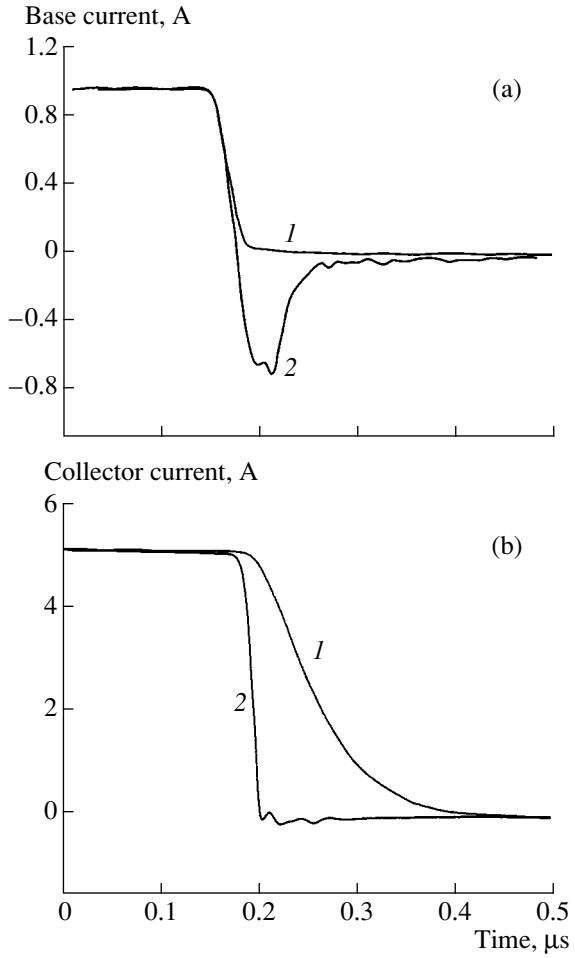

Fig. 11. Oscillograms of the (a) base and (b) collector current under the condition of turn-off of a 4*H*-SiC BJT (*1*) in the conventional mode and (*2*) by reversal of the base voltage.

collector current to rise slightly increases due to the increase in both the initial (because of the decrease in the collector voltage) and the final (because the collector junction is under a forward bias after turn-on) collector capacitance.

As a rule, the slowest process limiting the operation frequency of bipolar devices is the turnoff. This problem is especially important for high-power switching BJTs because, as the degree of BJT saturation in the on-state increases, the turn-on time decreases whereas the turn-off time, in contrast, increases. The turn-off time of the transistors under study significantly decreased if a reverse current pulse was applied to the base–emitter junction (Fig. 11). Prior to turnoff, the transistor was in a deeply saturated state: the saturation parameter was $N = (\beta I_b - I_{Csat})/I_{Csat} = 3$. Curves *1* in Fig. 11 illustrate a conventional turn-off process stimulated by breaking the base current (in our experiment, the time taken for the base current to decay, set by the external control circuit, was 35 ns). The total turn-off time, which includes the delay and decay of the collector current, was about

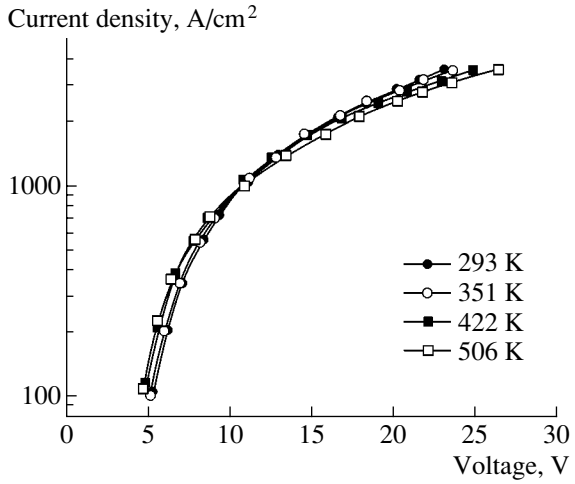

Fig. 12. *I–V* characteristics of a 2.6-kV thyristor in the on-state.

250 ns; at $N = 3$, the turn-on time of the transistor in the common-emitter circuit was about 50 ns, i.e., five times less than the turn-off time. However, if the sign of the gate voltage was reversed (as is done in Lax diode tests), the transistor turn-off time decreased to 25 ns (see Fig. 11, curves *2*). In this case, a 0.7-A reverse current pulse passed through the gate junction, which is similar to the current pulse at the switching of the diode from a forward to reverse bias: the minority carriers (electrons) are extracted from the transistor base by the reverse current of the emitter junction. It is interesting that the collector current completely terminates at a time when a considerable amount of nonequilibrium carriers still remain in the base. The reverse current of the emitter junction flows for 120 ns after the breaking of the collector current.

4. GATE TURN-OFF (GTO) THYRISTORS

The studied 2.6-kV thyristors have a *p*-type blocking base. The impurity (acceptor) concentration in this blocking base is 7×10^{14} cm^{-3}, and the base layer thickness is 50 μm. The emitter layers are doped to ~1×10^{19} cm^{-3}. The electron density in their thin *n*-type base is about 10^{18} cm^{-3}. The anode and gate electrodes are formed in an interdigitated structure. The total area of the anode is 3.7×10^{-3} cm^{-2}. As well as 2.6-kV thyristors, relatively low-voltage (400–700 V) thyristors were studied; these devices have the simplest configuration, involving a side gate electrode.

The *I–V* characteristics of the studied 2.6-kV thyristors when they are in the on-state are similar to the forward *I–V* characteristics of 6-kV diodes (cf Figs. 9 and 12). This circumstance implies that the lifetime of nonequilibrium carriers in the blocking base of the thyristors must be close to that in the diode base. In this review, we do not discuss the thyristor *I–V* characteris-

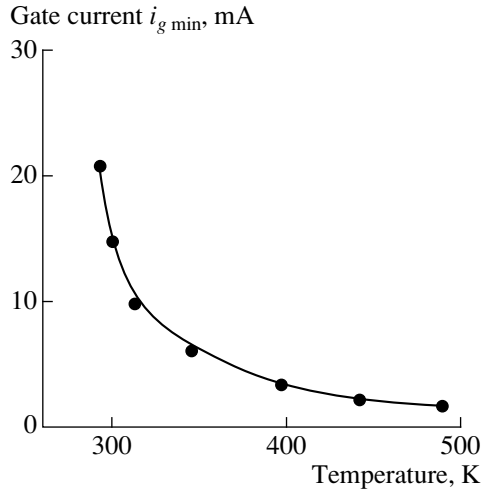

Fig. 13. Temperature dependence of the minimum gate current necessary for turn-on of a 2.6-kV thyristor.

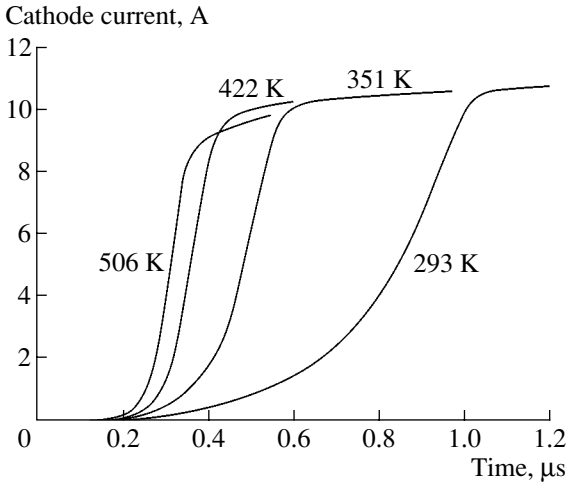

Fig. 14. The rise in the cathode current for gate-controlled turn-on of a 2.6-kV thyristor.

tics in detail; instead, we focus on their turn-on and turn-off characteristics [48–54].

4.1. Gate-Controlled Turn-on

Figure 13 shows the temperature dependence of the minimum gate current $I_{G\min}$ necessary to turn on a 2.6-kV thyristor. As can be seen, this current steadily decreases when heated from 300 to 500 K. The duration of the thyristor current rise τ_r also decreases steadily as the temperature increases (see Fig. 14, which shows the time dependences of the current for the thyristor turn-on). The observed temperature dependence of τ_r (a similar one was observed in [55]) seems "anomalous" as compared to Si and GaAs thyristors. In Si and GaAs thyristors, τ_r increases at higher temperatures, due to the decrease in carrier mobility, diffusion coefficient, and saturated velocity of the carriers (it is necessary to note that, in SiC, these quantities also decrease under the effect of heating).

The faster turn-on of 4*H*-SiC thyristors at elevated temperatures can be qualitatively accounted for by an additional ionization of the acceptors (due to their higher ionization energy, only 1–2% of the Al atoms in the emitter are ionized at room temperature), increase in the injection coefficient of the emitter junction, and increase in the gain of the *p–n–p* transistor section. A detailed analysis of this effect with the use of the charging method [56–58] leads to the following relation for the characteristic time taken for the current to increase:

$$\tau_r = \frac{1}{2}\frac{\sqrt{[(1-\gamma_1\alpha_{T1})\tau_2 + (1-\gamma_2\alpha_{T2})\tau_1]^2 + 4(\gamma_1\alpha_{T1} + \gamma_2\alpha_{T2} - 1)\tau_1\tau_2}}{\gamma_1\alpha_{T1} + \gamma_2\alpha_{T2} - 1} + \frac{(1-\gamma_1\alpha_{T1})\tau_2 + (1-\gamma_2\alpha_{T2})\tau_1}{\gamma_1\alpha_{T1} + \gamma_2\alpha_{T2} - 1}. \quad (9)$$

Here, γ_i, α_{Ti}, and τ_i ($i = 1, 2$) are the injection coefficient of the emitter junction, transport coefficient, and the time taken for diffusion transit of carriers across the base in the corresponding transistor section, respectively. The difference from the well-known relation describing the characteristic time taken for the current to rise in Si thyristors [59] is that, in our case, the injection coefficients of the emitter junctions are assumed to differ from unity (for Si thyristors, $\gamma_i = 1$). As can clearly be seen from Eq. (9), in the limit of small injection coefficients of the emitter junctions, when $(\alpha_1 + \alpha_2) = (\gamma_1\alpha_{T1} + \gamma_2\alpha_{T2}) = 1 + \delta$ ($\delta \ll 1$), the characteristic time taken for the current to rise τ_r decreases as the injection coefficient increases:

$$\tau_r = \frac{(1-\gamma_1\alpha_{T1})\tau_2 + (1-\gamma_2\alpha_{T2})\tau_1}{\gamma_1\alpha_{T1} + \gamma_2\alpha_{T2} - 1}. \quad (10)$$

A computer analysis using the Issledovanie software confirms the assumption that a high energy of acceptor ionization in 4*H*-SiC is the principal factor causing the faster turn-on of 4*H*-SiC thyristors at elevated temperatures.

The decrease in the minimum gate current observed when heating is applied is related mainly to an increase

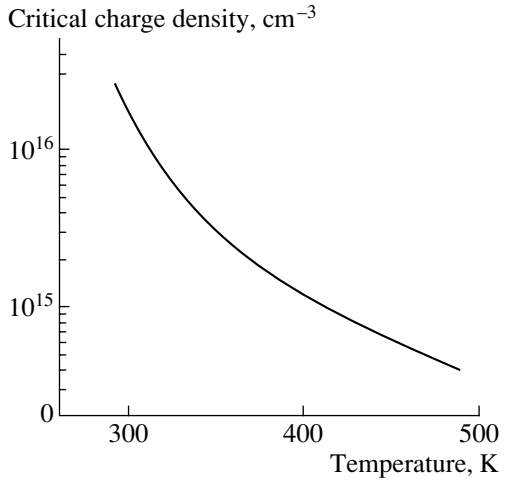

Fig. 15. Temperature dependence of the critical carrier density for gate-controlled turn-on of a 2.6-kV thyristor.

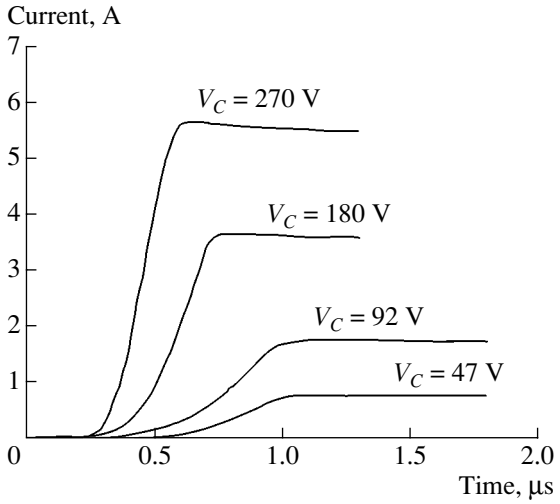

Fig. 16. Current increase during the turn-on of a 2.6-kV thyristor at different cathode voltages V_C and the maximum gate current.

in the lifetime of nonequilibrium carriers, with a corresponding decrease in the critical charge Q_{cr} of the thyristor turn-on. For a gate-controlled turn-on, the critical carrier density n_{cr} in a "thin" base of thickness W_n can be estimated as [60]

$$n_{cr} \approx \frac{Q_{cr}}{qW_n} \approx \frac{j_{g\min}\tau_r}{qW_n}. \quad (11)$$

Figure 15 shows the temperature dependence of the critical carrier density calculated from (11) using the experimental data (see Figs. 13 and 14). At room temperature, $n_{cr} \approx 2.7 \times 10^{16}$ cm^{-3}. As will be shown below, this value is close to n_{cr} observed when thyristor turn-on is effected by pulses of light. As the device is heated to 500 K, n_{cr} decreases to 4.3×10^{14} cm^{-3}, i.e., by nearly two orders of magnitude.

Regarding the homogeneity of the turn-on process in the thyristors under study, it can be estimated from the homogeneity of the recombination emission produced by the turned-on section of the device. It was found that, in the 2.6-kV thyristors under study, this emission was homogeneously distributed over the entire area, even at the minimum current, which is close to the hold-on current ($I_C \approx I_h$). In the 400-V thyristors, only about 1/8 of the total area of the device was in the on state at $I_C \approx I_h$ [61].

The homogeneity of recombination emission in the steady state does not guarantee that the turn-on is homogeneous during the process of current increase. A general idea of the homogeneity present in the turn-on process can be obtained from studies of the time dependences of the current through a thyristor and voltage drop across it at different gate currents [62]. At a high gate current, the critical charge necessary for turn-on is introduced along the entire emitter–base boundary line with a significant safety margin, and the turn-on is homogeneous. At the minimum gate current possible for turn-on, the critical density of carriers is reached at the "weakest" point. If the critical density at the other points of structure is significantly higher, the turn-on occurs only in a narrow current filament around the weak point. The current density in this filament is many times higher than the density exhibited under homogeneous turn-on. Accordingly, the electric field in the turn-on channel is proportionally higher. The rate of current increase in this situation is considerably higher (at the same current and voltage).

Figure 16 shows the time dependences of the current for when a 2.6-kV thyristor is turned on at different cathode voltages V_C and the maximum gate current I_G. As can be seen, the turn-on time decreases as V_C increases. Figure 17 shows the turn-on pattern at maxi-

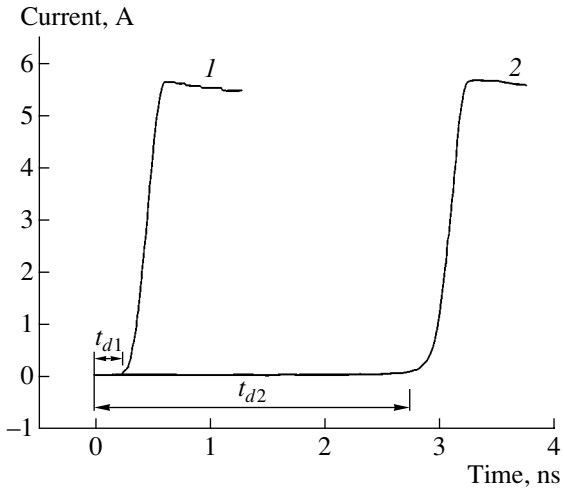

Fig. 17. Oscillograms of the current during the turn-on of a 2.6-kV thyristor at (*1*) I_G = 0.02 A and (*2*) I_G = 0.16 A. V_C = 270 V and T = 293 K.

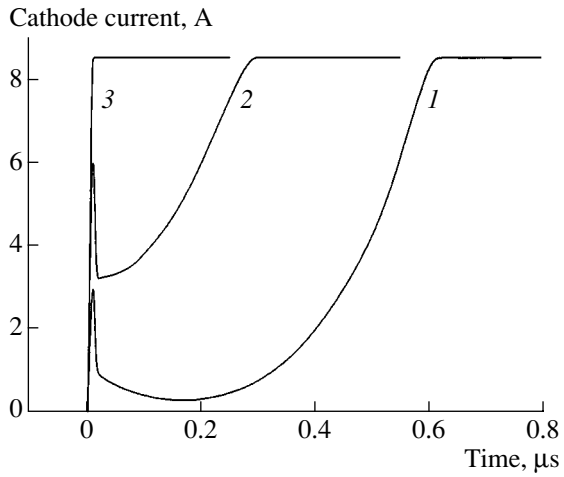

Fig. 18. Time diagrams of the turn-on of a 2.6-kV 4*H*-SiC thyristor under illumination by light pulses with different intensities. $I_1 < I_2 < I_3$.

mum (curve *1*) and minimum (curve *2*) I_G and fixed $V_C = 270$ V. As can be seen, the period of turn-on delay differs by more than a factor of 10 (in Si thyristors, this time increases as the gate current decreases [63]). However, at the turn-on front, the time dependences of the current are nearly identical, which implies homogeneity of the turn-on of the thyristors studied over virtually over the entire area.

It is necessary to note that the conditions for homogeneous turn-on are satisfied more easily in SiC thyristors than in Si thyristors. The reason is that the duration of phases of fast current increase (τ_f), diffusion redistribution of nonequilibrium carriers in the thyristor bases (τ_d), and spreading of the on-state (τ_{sp}) can be of the same order of magnitude (fractions of a microsecond), whereas, for Si thyristors, the relation $\tau_f < \tau_d \ll \tau_{sp}$ is typical (in high-power Si thyristors, τ_{sp} can be as long as several tens or hundreds of microseconds, due to their relatively large lateral size).

4.2. Turn-on using UV Laser Pulses

The possibility of ultrafast homogeneous turn-on of Si thyristors using light pulses of a sufficiently high power was demonstrated in [64, 65]. It was shown that, for a fast turn-on, the density of nonequilibrium carriers photogenerated in the structure has to be comparable with their density in the steady on-state at the given current.

Figure 18 shows time diagrams of the turn-on of a 2.6-kV 4*H*-SiC thyristor under illumination by pulses from a UV nitrogen laser LG-21 (with a wavelength of 337 nm and pulse width of 7 ns) at different intensities. The "threshold" energy necessary for turn-on was about 40 nJ. In these conditions, the process was similar to gate-controlled turn-on: the total turn-on time was about 1 μs. However, when the thyristor was illuminated by unattenuated light pulses with an energy of about 0.8 μJ, the turn-on time decreased to 10 ns, which was close to the duration of the laser pulse itself.

From the point of view of the dynamics of nonequilibrium carrier accumulation in the thyristor structure, the obtained data can be explained as follows. Taking into account that the lifetime of nonequilibrium carriers in the blocking base is several tenths of a microsecond (see below), a laser pulse of 7-ns width can be regarded as a δ-type impact. The light pulse excites a high photocurrent, which is proportional to the rate of photogeneration of carriers. It is noteworthy that the external current in this situation is maintained by the carrier emission from the emitters. The time dependence of current after the termination of the light pulse depends on the charge of the nonequilibrium carriers formed in bases during the illumination. If this charge is less than the "critical" value, recombination of nonequilibrium carriers dominates, and the thyristor is not turned on. If the charge produced under illumination slightly exceeds the critical value, it is further accumulated due to positive feedback in the thyristor, and the thyristor turns on spontaneously. In this case, the turn-on process is controlled by the diffusion of nonequilibrium carriers, similarly to the case of gate-controlled turn-on. If the light absorption coefficient is known, the critical density of nonequilibrium carries can easily be estimated. For the 4*H*-SiC thyristors under study, it is about 2×10^{16} cm^{-3}, which is close to critical density of nonequilibrium carriers in high-power Si and GaAs thyristors.

For a pulse energy of 0.8 μJ, the possible photocurrent can be estimated as ~30 A. At the same time, in our case, the external current was limited to 9 A by the forward bias and external load. This means that the blocking junction is saturated during the light pulse; i.e., it is "flooded" by nonequilibrium carriers, and the thyristor is similar to a *p–i–n* diode with inhomogeneously distributed electron–hole plasma. In this case, the transition to the final on-state after the termination of the laser pulse is maintained by the fast drift mechanism. Moreover, it is important that the transition to the steady state occurs at an invariable thyristor current; only the voltage drop across the thyristor changes slightly during this process. Therefore, the turn-on time of the thyristor, defined as the time taken for the current to increase, is determined by the duration of the laser pulse.

4.3. Critical Charge of SiC-Thyristor Turn-on

The concept of a critical charge for thyristor turn-on is very convenient when analyzing various steady-state and dynamic processes in thyristor structures. In particular, the critical charge determines the maximum permissible d*V*/d*t* ramp [60], the minimum gate current necessary for thyristor turn-on [66], the propagation velocity of the on-state [67], and the hold-on current and parameters of the current filaments [68].

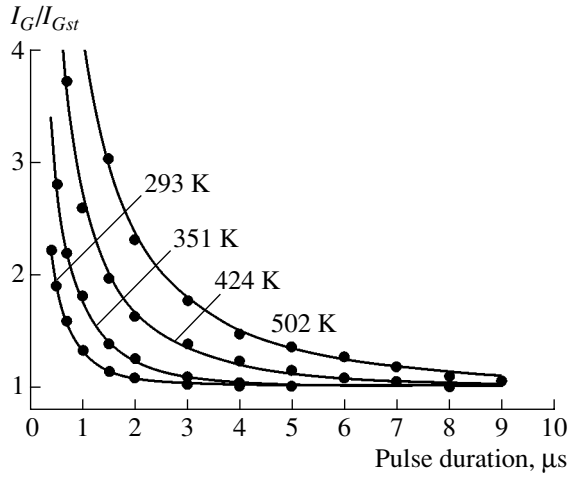

Fig. 19. The dependence of the relative magnitude of the gate turn-off pulse current I_G/I_{Gst} on the pulse width.

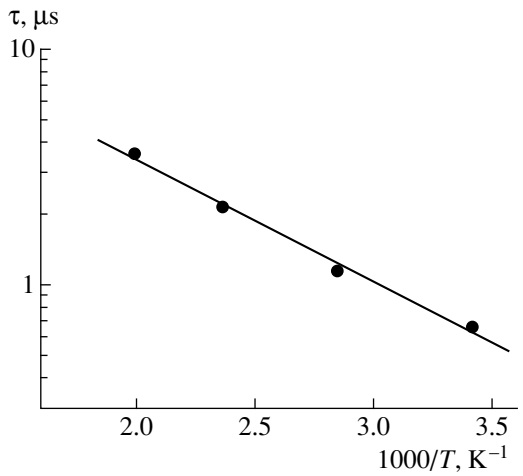

Fig. 20. Temperature dependence of the characteristic time τ*.

As was stated above, in the 2.6-kV 4*H*-SiC thyristors under study, the critical turn-on charge is close to that in Si and GaAs thyristors. Following from Uvarov's classical theory of critical charge [60], in the studied 4*H*-SiC thyristors, this charge must be 2–3 orders of magnitude smaller, since these devices have no technological shunting of the emitter. This circumstance implies that the physical mechanism of formation of the critical charge in 4*H*-SiC thyristors differs somehow from that in Si and GaAs thyristors.

This new mechanism was discovered in [69] by modeling. It is well known that the *S*-shaped *I–V* characteristic of a thyristor is formed due to positive feedback, which arises under the condition

$$\gamma_1\alpha_{T1} + \gamma_2\alpha_{T2} = 1 - \frac{j_{co}}{j}. \quad (12)$$

Here, j_{co} is the reverse current of the collector junction, and γ_i and α_{Ti} (i = 1, 2) are the injection coefficient of the emitter junction and the transport coefficient for the corresponding transistor section. Uvarov's theory assumes that γ_2, α_{T1}, and α_{T2} are constants, and only the injection coefficient γ_1 of the emitter junction, which usually has technological shunting, depends on the density of current flowing through the structure. The turn-on of Si thyristors usually occurs at low injection levels in the blocking base; therefore, the transport factors α_{T1} and α_{T2} may be considered constant. The dependence of γ_1 on j is very sharp near the turn-on point, so the dependence $\gamma_2(j)$ can be disregarded. Under these conditions, the critical turn-on charge of a thyristor is calculated from the relation [70]

$$Q_{cr} = \tau_r j_{Ro}, \quad (13)$$

where j_{Ro} is the density of the leakage current in the shunted emitter junction. In contrast to Si thyristors, the studied 2.6-kV 4*H*-SiC devices are turned on at a gate current corresponding to transition from a low to medium injection level in the blocking base of the structure. For this situation, a different relation from (13) was obtained in [69]:

$$Q_{cr} = \tau_r\gamma_1(j_{Ro} + j_{Reff}). \quad (14)$$

This relation differs from (13), first, by the presence of the injection coefficient γ_1 and, second, by some "additional leakage" in the emitter (j_{Reff}). This "shunting" reflects the contribution of a new mechanism, related to transition to a medium injection level in the blocking base, to the formation of the critical charge.

4.4. Thyristor Turn-off Using a Reverse Gate Current Pulse

In this section, we present the results of studies of thyristor turn-off using a reverse gate current pulse at temperatures of 293–500 K.

At the given cathode current and fixed temperature, the turn-off gain equal to the ratio between the turned-off cathode current and turning-off gate current, $K = I_C/I_G$, depended on the duration of the reverse current pulse Δt_G: as the pulse width increased, the gain increased and then leveled off at some "quasi-steady-state" value Δt_{Gst}. Figure 19 shows the dependence of the relative magnitude of the gate-turnoff pulse current I_G/I_{Gst} on Δt_{Gst} for different temperatures. At each temperature, the turned-off cathode current was set at nearly two times the thyristor hold-on current, which decreased as temperature increased. As can be seen from Fig. 19, the value of Δt_{Gst}, which corresponds to the quasi-steady-state turn-off mode, increased as the temperature increased. At T = 293 K, it was about 2.5 μs; after being heated to 500 K, it was over 10 μs. Evidently, the rise in Δt_{Gst} at elevated temperatures is related to an increase in the lifetime of nonequilibrium carriers in the blocking base of the thyristor. A semiem-

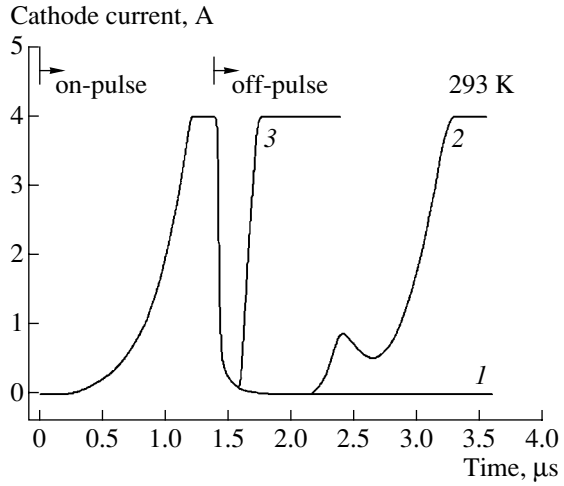

Fig. 21. Oscillograms of the cathode current during turn-on by gate shorting in (*1*) a quasi-steady-state and (*2, 3*) pulsed modes. The shorting pulse width Δt_{off} : (*1*) 20, (*2*) 0.2, and (*3*) 0.8 μs.

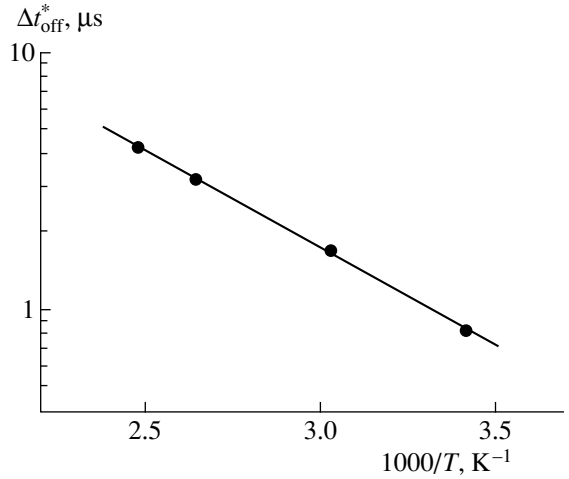

Fig. 22. Temperature dependence of Δt^*.

pirical relation for the I_G/I_{Gst} dependence on Δt_G was suggested in [71]:

$$I_G/I_{Gst} = \frac{1}{1 - \exp\left(-\frac{\Delta t_G}{\tau^*}\right)}. \quad (15)$$

Here, the parameter τ^* is the estimated carrier lifetime in the blocking base. The solid lines in Fig. 19 show the results of fitting the experimental data with the use of Eq. (13). As can be seen, the dependence of I_G/I_{Gst} on Δt_G is very well approximated by Eq. (13) at each temperature. Figure 20 shows the temperature dependence of the parameter τ^*. The lifetime of the carriers in the blocking p_0 base increases exponentially from about 0.6 μs at room temperature to 3.6 μs at 500 K. Both the lifetimes of the nonequilibrium carriers in the blocking p_0 base of high-voltage 4*H*-SiC thyristors and the temperature dependences of these lifetimes appeared to be close to those measured in the 6-kV diodes with an n_0 base. In both types of devices, the room-temperature lifetime is several tenths of a microsecond; as temperature increases, the lifetime increases exponentially with an activation energy of 0.11–0.13 eV, which leads to the conclusion that the lifetime of the nonequilibrium carriers in both *p*- and *n*-type 4*H*-SiC with a doping level of 10^{14}–10^{15} cm^{-3} is controlled by the same recombination centers.

4.5. Thyristor Turn-off by Pulsed Shorting of the Gate Junction

The maximum current that can be turned off by the reverse gate current is limited by leakage and breakdown of the low-voltage gate junction. At room temperature, the maximum turned-off current was about 3.3 A, which corresponds to a current density of about 1000 A cm^{-2}.

Another turn-off mode of 4*H*-SiC thyristors, pulsed ohmic shorting of the gate junction, was demonstrated in [72]. In our study, we used a Si MOSFET, whose channel resistance in the on-state was about 1 Ω, for this purpose. The maximum cathode current that could be turned off in this way in the quasi-steady-state mode decreased after heating. At room temperature it was not less than 10 A and decreased to 2.3 A at T = 496 K.

It was found that, to attain complete turn-off of a thyristor, the off pulse must be not shorter than a certain value Δt^*_{off}. In the opposite case, a thyristor spontaneously turned on after the termination of the pulse. An example of repeated turn-on at room temperature is presented in Fig. 21, which shows time dependences of the thyristor current in the quasi-steady-state (the shorting off-pulse width Δt_{off} = 20 μs (curve *1*)) and pulsed (Δt_{off} = 0.2 and 0.8 μs (curves *2* and *3*)) modes. It is understandable from general considerations that Δt^*_{off} is the time interval during which the charge of the carriers injected into the base decreases to a value close to the critical charge of thyristor turn-on. Figure 22 shows the temperature dependence of Δt^*_{off} plotted on the semilog scale. As can be seen, this time increases from 0.8 to 4.3 μs as the temperature increases from 293 to 404 K. The activation energy of Δt^*_{off} is close to the activation energy of the lifetime of nonequilibrium carriers. This circumstance indicates that the temperature dependence of the lifetime makes the major contribution to the temperature dependence of Δt^*_{off}.

5. CONCLUSION

Based on the results of studies of power bipolar SiC devices, we can reach several important conclusions.

At room temperature, the lifetime of nonequilibrium carriers in both *n*- and *p*-type 4*H*-SiC with a concentration of donor or acceptor impurities of 10^{14}–10^{15} cm^{-3} can be as long as 1 μs. Such lifetimes allow deep modulation of the bases of the rectifier diodes at a reverse voltage of up to 10 kV.

As the temperature increases, the lifetime of the nonequilibrium carriers increases exponentially and has an activation energy of 0.11–0.13 eV; at 550–600 K it can be as long as several microseconds. This strong temperature dependence of the lifetime leads to a number of consequences. For example, the critical charge of thyristor turn-on decreases from ~10^{16} to ~10^{14} cm^{-3}, i.e., by two orders of magnitude.

It is important to note that bipolar 4*H*-SiC devices can have thinner and more heavily doped blocking bases than Si and GaAs devices with the same blocking voltage, which makes it possible to have a shorter lifetime for nonequilibrium carriers in 4*H*-SiC devices at the same W/L_a ratio. Thus, SiC devices demonstrate a higher operation speed and lower forward loss at high current densities. In particular, at temperatures of about 500 K, 700-V thyristors have a characteristic turn-on time of about 1 ns [73] while, for 2.6-kV thyristors, this time is about 30 ns. Record-breaking switching frequencies have been obtained in 400-V 4*H*-SiC thyristors: 500 kHz for a switching current density of 14 kA cm^{-2} and 1 MHz for 2.7 kA cm^{-2} [74]. Therefore, power converters based on power SiC thyristors can provide a 5–10 times higher conversion frequency than their Si analogues.

Nevertheless, specific problems still remain with respect to 4*H*-SiC. For example, the electron–hole scattering in SiC is about 2, 4, and 60 times more effective than in Si, Ge, GaAs, respectively. At room temperature, heavily doped p^+-type emitters demonstrate a relatively low injection efficiency because of the short lifetime of the nonequilibrium carriers and relatively high ionization energy of the acceptor impurities in 4*H*-SiC. These factors lead to a higher forward voltage drop in diodes, an anomalous temperature dependence of the turn-on time in thyristors, and significant increase in the turn-on critical charge as compared to that estimated from Uvarov's classical theory. A possible way to solve the problem of the low injection efficiency of *p*-type emitters is the use of heteropolytype junctions and emitters fabricated from GaN, which has a wider band gap than SiC.

In bipolar junction transistors with *p*-type bases, the effect of current crowding at the emitter edge is strong at room temperature. At large collector currents, this enhances the surface recombination and recombination within the emitter and reduces the transistor gain by a factor of 3 as compared with that expected from the lifetime of nonequilibrium carriers in the base. In spite of this circumstance, a high output power in a high-frequency range is expected from 4*H*-SiC BJTs [75]. The same can be said of SHF *p*–*i*–*n* diodes when they are used as microwave switches [76].

There are still a number of other fundamental problems yet to be resolved. It is necessary to obtain, from electric measurements, information concerning the Auger recombination, which determines the injection coefficients of p^+–n_0 and n^+–p_0 junctions and their dependences on the current density (until now, only optical studies have been carried out). The pulsed breakdown of diodes and the impact of deep levels on this effect are waiting to be studied. The dependence of the drift velocity of holes on the electric field should also be investigated (at present, this dependence is known only for electrons). It is also necessary to study the degradation of *I*–*V* characteristics at high current densities (see, e.g. [77]), etc.

To conclude, it must be stated that, as well as obtaining results that have practical importance for technical applications, the study of 4*H*-SiC devices improved understanding of general problems in the physics of semiconductor devices. In fact, virtually all the theoretical models derived for describing the operation of Si devices had to be revised for 4*H*-SiC. The new information obtained in these studies should expand the application field of wide-bandgap semiconductor devices.

ACKNOWLEDGMENTS

The study at Cree Inc. was supported by the Office of Naval Research MURI program (contract No. N00014-95-1-1302, monitored by Dr. J. Zolper). The research at the Ioffe Physicotechnical Institute and the All-Russia Electrotechnical Institute was supported by the Russian Foundation for Basic Research (project nos. 05-02-16541 and 05-02-17768).

REFERENCES

1. O. Kordina, C. Hallin, R. C. Glass, *et al.*, Inst. Phys. Conf. Ser., No. 137, 41 (1994); H. Matsunami, Inst. Phys. Conf. Ser., No. 137, 45 (1994).
2. D. J. Larkin, P. G. Neudeck, J. A. Powell, and L. G. Matus, Inst. Phys. Conf. Ser., No. 137, 51 (1994).
3. O. Kordina, J. P. Bergman, A. Henry, *et al.*, Appl. Phys. Lett. **67**, 1561 (1995).
4. A. K. Agarwal, S. H. Ryu, R. Singh, *et al.*, Mater. Sci. Forum **338–342**, 1387 (2000).
5. C. F. Huang and J. A. Cooper, IEEE Electron Device Lett. **24**, 396 (2003).
6. M. E. Levinshtein, J. W. Palmour, S. L. Rumyantsev, and R. Singh, Semicond. Sci. Technol. **12**, 1498 (1997).
7. N. V. Dyakonova, P. A. Ivanov, V. A. Kozlov, *et al.*, IEEE Trans. Electron Devices **46**, 2188 (1999).
8. P. A. Ivanov, M. E. Levinshtein, J. W. Palmour, *et al.*, Semicond. Sci. Technol. **15**, 908 (2000).
9. P. A. Ivanov, M. E. Levinshtein, K. G. Irvine, *et al.*, Electron. Lett. **35**, 1382 (1999).
10. M. E. Levinshtein, T. T. Mnatsakanov, P. A. Ivanov, *et al.*, Electron. Lett. **36**, 1241 (2000).

11. M. E. Levinshtein, T. T. Mnatsakanov, P. A. Ivanov, *et al.*, IEEE Trans. Electron Devices **48**, 1703 (2001).
12. M. E. Levinshtein, T. T. Mnatsakanov, P. A. Ivanov, *et al.*, Electron. Lett. **39**, 689 (2003).
13. M. E. Levinshtein, T. T. Mnatsakanov, P. A. Ivanov, *et al.*, Solid-State Electron. **48**, 807 (2004).
14. N. I. Kuznetsov, E. V. Astrova, E. V. Kalinina, *et al.*, in *Proceedings of 3rd International HiTEC* (Albuquerque, NM, 1996), p. P77.
15. T. Kimoto, N. Miyamoto, and H. Matsunami, IEEE Trans. Electron Devices **46**, 471 (1999).
16. B. R. Gossik, J. Appl. Phys. **27**, 905 (1956).
17. B. Lax and T. Neustadter, J. Appl. Phys. **25**, 1148 (1954).
18. Yu. R. Nosov, *Switching in Semiconductor Diodes* (Nauka, Moscow, 1968; Plenum, New York, 1969).
19. H. Schlangenotto and W. Gerlach, Solid-State Electron. **15**, 393 (1972).
20. P. G. Neudeck and C. Fazi, Mater. Sci. Forum **264–268**, 1037 (1998).
21. T. Kimoto, N. Miyamoto, and H. Matsunami, IEEE Trans. Electron Devices **46**, 471 (1999).
22. Y. Sugawara, K. Asano, R. Singh, and J. W. Palmour, Mater. Sci. Forum **338–342**, 1371 (2000).
23. T. T. Mnatsakanov, I. L. Rostovtsev, and N. I. Philatov, Solid-State Electron. **30**, 579 (1987).
24. T. T. Mnatsakanov, I. L. Rostovtsev, and N. I. Filatov, Fiz. Tekh. Poluprovodn. (Leningrad) **18**, 1293 (1984) [Sov. Phys. Semicond. **18**, 807 (1984)].
25. T. T. Mnatsakanov, Phys. Status Solidi B **143**, 225 (1987).
26. I. V. Grekhov, P. A. Ivanov, A. O. Konstantinov, and T. P. Samsonova, Pis'ma Zh. Tekh. Fiz. **28** (13), 24 (2002) [Tech. Phys. Lett. **28**, 544 (2002)].
27. I. V. Grekhov, P. A. Ivanov, D. V. Khristyuk, *et al.*, Solid-State Electron. **47**, 1769 (2003).
28. I. V. Grekhov, A. S. Kyuregyan, T. T. Mnatsakanov, and S. N. Yurkov, Fiz. Tekh. Poluprovodn. (St. Petersburg) **37**, 1148 (2003) [Semiconductors **37**, 1123 (2003)].
29. H. Benda and E. Shpenke, Proc. IEEE **55**, 1331 (1967).
30. L. V. Davies, Nature **194**, 762 (1962).
31. F. Dannhauser, Solid-State Electron. **15**, 1371 (1972).
32. J. R. Krausse, Solid-State Electron. **15**, 1377 (1972).
33. R. A. Hopfel, J. Shah, P. A. Wolff, and A. C. Gossard, Phys. Rev. Lett. **56**, 2736 (1986).
34. R. A. Hopfel, J. Shah, P. A. Wolff, and A. C. Gossard, Appl. Phys. Lett. **49**, 572 (1986).
35. T. T. Mnatsakanov, M. E. Levinshtein, P. A. Ivanov, *et al.*, J. Appl. Phys. **93**, 1095 (2003).
36. V. A. Kuz'min, T. T. Mnatsakanov, and V. B. Shuman, Pis'ma Zh. Tekh. Fiz. **6**, 689 (1980) [Sov. Tech. Phys. Lett. **6**, 299 (1980)].
37. B. N. Gresserov and T. T. Mnatsakanov, Fiz. Tekh. Poluprovodn. (Leningrad) **24**, 1668 (1990) [Sov. Phys. Semicond. **24**, 1042 (1990)].
38. S. H. Ryu, A. K. Agarwal, R. Singh, and J. W. Palmour, IEEE Electron Device Lett. **22**, 124 (2001).
39. P. A. Ivanov, M. E. Levinshtein, S. L. Rumyantsev, *et al.*, Solid-State Electron. **46**, 567 (2002).
40. P. A. Ivanov, M. E. Levinshtein, A. K. Agarwal, *et al.*, in *Abstracts of 10th International Conference on Silicon Carbide and Related Materials (ISCSRM-2003)* (Lyon, France, 2003), p. 64.
41. P. A. Ivanov, M. E. Levinshtein, A. K. Agarwal, and J. W. Palmour, Semicond. Sci. Technol. **16**, 521 (2001).
42. P. A. Ivanov, M. E. Levinshtein, A. K. Agarwal, *et al.*, Solid-State Electron. **48**, 491 (2004).
43. Y. Tang, J. B. Fedison, and T. P. Chow, IEEE Electron Device Lett. **22**, 119 (2001).
44. A. Blicher, *Field-Effect and Bipolar Power Transistor Physics* (Academic, New York, 1981; Énergoatomizdat, Leningrad, 1986).
45. Y. Wang, W. Xie, J. A. Cooper, *et al.*, Inst. Phys. Conf. Ser., No. 142, 809 (1995).
46. R. Hauser, IEEE Trans. Electron Devices **11**, 238 (1964).
47. *Properties Advanced Semiconductor Materials: CaN, AlN, InN, BN, SiC, SiGe*, Ed. by M. E. Levinshtein, S. L. Rumyantsev, and M. S. Shur (Wiley, New York, 2001).
48. P. A. Ivanov, M. E. Levinshtein, S. L. Rumyantsev, *et al.*, Solid-State Electron. **44**, 2155 (2000).
49. A. K. Agarwal, P. A. Ivanov, M. E. Levinshtein, *et al.*, Semicond. Sci. Technol. **16**, 260 (2001).
50. M. E. Levinshtein, T. T. Mnatsakanov, P. A. Ivanov, *et al.*, Solid-State Electron. **45**, 453 (2001).
51. M. E. Levinshtein, T. T. Mnatsakanov, P. A. Ivanov, *et al.*, Solid-State Electron. **46**, 529 (2002).
52. M. E. Levinshtein, T. T. Mnatsakanov, S. N. Yurkov, *et al.*, Solid-State Electron. **46**, 1955 (2002).
53. M. E. Levinshtein, P. A. Ivanov, A. K. Agarwal, and J. W. Palmour, Electron. Lett. **38**, 592 (2002).
54. M. E. Levinshtein, P. A. Ivanov, T. T. Mnatsakanov, *et al.*, Solid-State Electron. **47**, 699 (2003).
55. L. Cao, B. Li, and J. H. Zhao, Solid-State Electron. **44**, 347 (2000).
56. F. E. Gentry, F. W. Gutzwiller, N. Holohyak, and E. E. Zastrow, *Semiconductor Controlled Rectifiers* (Prentice-Hall, Englewood Clifs, N.J., 1964).
57. R. L. Davies and J. Petruzella, Proc. IEEE **55**, 1318 (1967).
58. A. Blicher, *Thyristor Physics* (Springer, New York, 1976).
59. G. D. Bergman, Solid-State Electron. **8**, 757 (1965).
60. A. I. Uvarov, in *Physics of p–n-Junctions and Semiconductor Devices*, Ed. by S. M. Ryvkin and Yu. V. Shmartsev (Consultants Bureau, New York, 1971), p. 216.
61. M. E. Levinshtein, J. W. Palmour, S. L. Rumyantsev, and R. Singh, IEEE Trans. Electron. Devices **45**, 307 (1998).
62. S. V. Vaĭnshteĭn, Yu. V. Zhilyaev, and M. E. Levinshteĭn, Pis'ma Zh. Tekh. Fiz. **9**, 546 (1983) [Sov. Tech. Phys. Lett. **9**, 236 (1983)].
63. Yu. A. Evseev and P. G. Dermenzhi, *Power Semiconductor Devices* (Énergoizdat, Moscow, 1981) [in Russian].
64. I. V. Grekhov, M. E. Levinshteĭn, and V. G. Sergeev, Fiz. Tekh. Poluprovodn. (Leningrad) **8**, 672 (1974) [Sov. Phys. Semicond. **8**, 431 (1974)].
65. I. V. Grekhov, M. E. Levinshteĭn, and V. G. Sergeev, Fiz. Tekh. Poluprovodn. (Leningrad) **10**, 345 (1976) [Sov. Phys. Semicond. **10**, 206 (1976)].

66. M. I. D'yakonov and M. E. Levinshteĭn, Fiz. Tekh. Poluprovodn. (Leningrad) **12**, 1674 (1978) [Sov. Phys. Semicond. **12**, 992 (1978)].
67. M. I. D'yakonov and M. E. Levinshteĭn, Fiz. Tekh. Poluprovodn. (Leningrad) **12**, 729 (1978) [Sov. Phys. Semicond. **12**, 426 (1978)].
68. M. I. D'yakonov and M. E. Levinshteĭn, Fiz. Tekh. Poluprovodn. (Leningrad) **14**, 478 (1980) [Sov. Phys. Semicond. **14**, 283 (1980)].
69. T. T. Mnatsakanov, S. N. Yurkov, M. E. Levinshtein, *et al.*, Solid-State Electron. **47**, 1581 (2003).
70. A. I. Uvarov, in *Physics of p–n-Junctions and Semiconductor Devices*, Ed. by S. M. Ryvkin and Yu. V. Shmartsev (Consultants Bureau, New York, 1971), p. 170.
71. I. L. Kaganov, *Industrial Electronics* (Vysshaya Shkola, Moscow, 1968) [in Russian].
72. A. K. Agarwal, S. Seshadri, M. McMillan, *et al.*, Solid-State Electron. **44**, 303 (2000).
73. N. V. Dyakonova, M. E. Levinshtein, J. W. Palmour, *et al.*, Semicond. Sci. Technol. **13**, 241 (1998).
74. M. E. Levinshtein, J. W. Palmour, S. L. Rumyantsev, and R. Singh, Semicond. Sci. Technol. **14**, 207 (1999).
75. A. Agarwall, C. Capell, B. Phan, *et al.*, Mater. Sci. Forum **433–436**, 785 (2003).
76. A. V. Bludov, N. S. Boltovets, K. V. Vasilevskiĭ, *et al.*, Pis'ma Zh. Tekh. Fiz. **30**, 82 (2004) [Tech. Phys. Lett. **30**, 123 (2004)].
77. H. Lendenmann, J. P. Bergman, F. Dahlquist, and H. Hallin, Mater. Sci. Forum **433–436**, 901 (2003).

Translated by D. Mashovets

Semiconductors, Vol. 39, No. 8, 2005, pp. 878–880. Translated from Fizika i Tekhnika Poluprovodnikov, Vol. 39, No. 8, 2005, pp. 914–916.

CONFERENCE. A REVIEW

IV International Conference on Amorphous and Microcrystalline Semiconductors

(July 5–7, 2004)

E. I. Terukov^ (Chairperson of the Organizing Committee of the Conference)

Ioffe Physicotechnical Institute, Russian Academy of Sciences, Politekhnicheskaya ul. 26, St. Petersburg, 194021 Russia

^ e-mail: eug.terukov@pop.ioffe.rssi.ru

The IV International Conference on Amorphous and Microcrystalline Semiconductors was held in St. Petersburg on July 5–7, 2004. This conference was organized by the Ioffe Physicotechnical Institute of the Russian Academy of Sciences and the Center for Scientists (at Lesnoe, near St. Petersburg) at St. Petersburg State Polytechnical University. The chairperson of the organizing committee was E.I. Terukov; the members of the organizing committee were K.D. Tséndin, Yu.A. Nikolaev, and I.N. Trapeznikova.

There were 198 papers presented at the conference. The participants included scientists from France, Bulgaria, Canada, Great Britain, India, Mexico, Japan, Latvia, and a number of scientists from the Commonwealth of Independent States (Ukraine, Belarus, Kazakhstan, Moldova, Azerbaijan, and Uzbekistan).

The traditional "Kolomiets lecture," entitled "Laser-Induced Structural Changes in Te-based Chalcogenides: Physics and Applications," was delivered by A.V. Kolobov (Center for Applied Near-Field Optics, National Institute of Advanced Industrial Science and Technology, Tsukuba, Japan). In this lecture, extremely interesting and detailed data on the processes of writing information onto carriers composed of vitreous chalcogenide semiconductors were reported. During the plenary session, the lectures were delivered by leading scientists in the field of unordered semiconductors and included reviews of the latest achievements in the physics of the vitreous chalcogenide, amorphous, and organic semiconductors. The lecture delivered by N.V. Bodyagin (Ryazan State Academy of Radio Engineering) dealt with the development of alternative approaches to controlling the growth parameters of amorphous semiconductors taking into account the internal dynamic processes in the material. The lecture by A.S. Komolov (the Fock Research Institute of Physics at St. Petersburg State University) was concerned with analysis of the photovoltaic properties of films of copper phthalocyanine and certain organic semiconductors. The lecture by K.D. Tséndin (Ioffe Physicotechnical Institute, Russian Academy of Sciences, St. Petersburg) focused on the superconductivity effect and the role of defects in chalcogenide vitreous semiconductors. The lecture by É.N. Voronkov (Moscow Power Engineering Institute) was dealt with simulation of the breakdown dynamics in vitreous semiconductors. The lecture by Jean-Paul Kleider (L.G.E.P.–SUPERLEC, CNRS, France) was concerned with study of the energy-band states in amorphous or microcrystalline silicon and its alloys using a modulated photocurrent. Finally, the lecture by P.P. Seregin (St. Petersburg State Polytechnical University) was concerned with study of the order–disorder transition in the electronic subsystem of a semiconductor.

The scope of the conference encompassed the following seven topics, which were considered in special sessions:

(1) amorphous hydrogenated silicon and its alloys;

(2) amorphous and diamond-like carbon and other wide-gap semiconductors;

(3) microcrystalline and nanocrystalline semiconductors;

(4) organic semiconductors;

(5) chalcogenide and vitreous semiconductors;

(6) technical applications;

(7) accompanying materials.

In the papers devoted to amorphous silicon (*a*-Si), a great deal of attention was given to various technologies for fabricating amorphous films and to the interrelation between methods of fabricating the films and characteristics of the impurity- and defect-related states that affect physical properties such as electrical conductivity, luminescence, and optical absorption. Special attention was given to the papers delivered by A.G. Kazanskiĭ (Moscow State University), A.I. Kosarev (Institute Nacional for Astrophysics, Optics, and Electronics; Puebla; Mexico), M.V. Stepikhova (Institute of the Physics of Microstructures, Russian Academy of Sciences, Nizhni Novgorod), V.Yu. Timoshenko (Moscow State University), and A.V. Medvedev (Ioffe Physicotechnical Institute, Russian Academy of Sciences, St. Petersburg).

The paper delivered by A.G. Kazanskiĭ focused on theoretical and experimental studies of photoconductivity in microcrystalline silicon (μ*c*-Si). The results of

1063-7826/05/3908-0878$26.00

experimental studies on the photoconductivity in μ*c*-Si:H films were considered. The magnitude of the photoconductivity was studied in relation to the material's structure (the ratio between the crystalline and amorphous phases), the photon energy of the excitation radiation, temperature, the level of doping with donor and acceptor impurities, and the defect concentration. The experimental data were analyzed taking into account the existing models for recombination of nonequilibrium charge carriers in μ*c*-Si:H and the multiphase structure of the material. It was shown that it is possible to use the formalism developed for *a*-Si:H to interpret data on the photoconductivity in μ*c*-Si:H.

The paper delivered by S.M. Manakov (Al'-Farabi Kazakhstan National University, Almaty) was of great interest. This paper was concerned with the search for unconventional and ecologically harmless sources of gaseous silicon hydrides that can be used in semiconductor electronics for obtaining doped layers of crystalline and amorphous silicon.

Studies related to the development of a material for electroluminescent and laser structures that emit at a wavelength of 1.54 μm retained their importance. Among the papers devoted to this field, a great deal of attention was given to the paper delivered by A.V. Medvedev, concerned with the tenfold increase in the intensity of erbium-related spontaneous emission with energy close to the edge of the optical band gap in a one-dimensional periodic structure based on amorphous silicon, grown by plasma-assisted chemical deposition, and doped with erbium during growth.

The paper delivered by M.V. Stepikhova was also of much interest. This paper was concerned with studies of the luminescent properties of low-dimensional silicon structures. It was shown that the most intense luminescence, whose intensity exceeds the intensity characteristic of crystalline silicon by a factor of 2, is observed for structures with the lowest degree of crystallinity and nanocrystal sizes of 1–3 nm.

Similar problems were solved in the paper delivered by B.Yu. Timoshenko, which was concerned with studying the effect of inhomogeneity in the dielectric constant of a solid-state matrix on the width of the spectrum of erbium-related photoluminescence for structures with *nc*-Si/SiO_2. The established, and extremely efficient, enhancement of erbium-related photoluminescence (PL) and the possibility of controlling the PL characteristics by varying the sizes of the nanocrystals provides fresh opportunities for the use of erbium-doped *nc*-Si/SiO_2 structures in silicon-based optoelectronics.

The participants of the conference gave a lot of attention to problems related to the technology involved in obtaining microcrystalline and nanocrystalline semiconductors and alloys and to the study of their properties. The interest in these materials is caused, on the one hand, by their high optical stability and, on the other hand, by new dimensional effects. In the corresponding session, keen interest was manifested in the paper delivered by M.D. Efremov (Institute of Semiconductor Physics, Siberian Division, Russian Academy of Sciences, Novosibirsk). This paper dealt with the Coulomb blockade in the case of single-electron charging of a silicon quantum dot in the structure of single-electron states using, as an example, silicon oxide films with incorporated silicon nanocrystals. This composite material is now considered to be promising in relation to the fabrication of single-electron transistors and memory elements in which a floating gate is replaced by nanocrystalline silicon inclusions. The size of the nanocrystals (several nanometers) and their high density make it possible to achieve terabit memory, which has generated a particular interest in this object. The above properties, in addition to the photoluminescence observed in these films, can be extremely important for the development of next-generation devices in single-electron and single-photon nanoelectronics.

In the papers concerned with amorphous carbon and other wide-gap semiconductors, methods for obtaining and studying these materials were considered; in addition, attention was given to theoretical simulation of the properties of the materials under consideration. The attention of the participants was particularly attracted to the paper delivered by A.L. Talis (All-Russia Research Institute of Synthesis of Mineral Raw Materials, Aleksandrov, Russia), which was concerned with new studies on the structure of diamond-like carbon and a local approach to adequate description of the symmetry of four-coordinated structures in a condensed state (from nanostructures to quasi-crystals and crystals). A number of papers were devoted to the search for promising new materials based on the carbon matrix for various applications. These papers included that delivered by B.P. Popov (St. Petersburg State Polytechnical University), which was concerned with studies of the electron spin resonance in copper–carbon systems with intercalated metals and metallic clusters; the paper delivered by É.A. Smorgonskaya (Ioffe Physicotechnical Institute, Russian Academy of Sciences, St. Petersburg), focused on modification of *a*-Si:H with metals (Co, Cu, Mo, Ni) with the aim of forming new solid-state structures possessing a high density of metallic nanoclusters; and the paper delivered by É.I. Tochitskiĭ (Plasmotekh Engineering Center of the Belarussian Academy of Sciences), which was concerned with the development of methods for fabricating nanosized high-strength thin-film materials with controllable electrical properties and a high adhesion to substrates formed from various materials at a low condensation surface temperature. Much interest was aroused by the paper delivered by V.I. Berezkin (Research Center of Ecological Safety, Russian Academy of Sciences, St. Petersburg), which was concerned with studying the mechanisms of adsorption of organic compounds at crystalline fullerenes, and by that delivered by V.V. Sobolev (Izhevsk State University, Russia), which was on the electronic structure of fullerites.

In the session devoted to organic semiconductors, most of the discussion was on polymeric semiconductors that can find application in solar power engineering and microelectronics. The participants of the conference displayed keen interest in the review paper delivered by V.V. Shamanin (Institute of Macromolecular Compounds, Russian Academy of Sciences, St. Petersburg), which dealt with the preparation and systematic physicochemical study of a new class of organic compounds, i.e., homoconjugated organometallic polymers that exhibit clearly pronounced semiconductor properties, namely, photoconductivity, photoluminescence, and relatively high charge-carrier mobility. These polymers are also of interest for the development of thin-film organic light-emitting diodes, field-effect transistors, and solar cells with new mechanisms of charge and electronic-excitation transport.

Among the papers on chalcogenide and vitreous semiconductors, the attention of the participants was attracted to the paper delivered by V.Yu. Kolosov (Ural State University of Economics, Yekaterinburg, Russia), devoted to rotational distortions during the growth of crystalline grains in a vitreous matrix; the paper delivered by A.A. Babaev (Institute of Physics, Dagestan Scientific Center, Russian Academy of Sciences, Makhachkala), which was on special features of the photoluminescence in chalcogenide vitreous semiconductors; a series of the studies carried out by the team headed by V.V. Sobolev (Izhevsk State University, Russia), which were concerned with electronic structure and calculations of the fundamental optical functions of selenides, sulfides, and chalcogenides consisting of various elements; and a series of studies on the electrical properties of chalcogenide vitreous semiconductors that were carried out at the Uzhgorod National University, Ukraine (the corresponding paper was delivered by I.V. Fekeshgazi).

Many papers dealing with the technical applications of amorphous, microcrystalline, and vitreous semiconductors were presented at the conference. I would like to mention the paper delivered by I.M. Kotina (St. Petersburg Institute of Nuclear Physics, Gatchina), which was concerned with the use of a heterocontact between amorphous silicon and crystalline silicon in nuclear-radiation detectors; the paper delivered by M.D. Efremov (Institute of Semiconductor Physics, Novosibirsk), which focused on simulation of the characteristics of thin-film field-effect transistors based on films of hydrogenated amorphous silicon; and a series of studies related to the effect of the electrical properties of *a*-Si:H films on the current–voltage characteristics of thin-film field-effect transistors (these studies were carried out by a team of researchers, headed by S.P. Vikhrov, from Ryazan State Radio-Engineering Academy). Studies on the holographic writing of information have been continued with good results by a team headed by Ya. Teteris (Institute of Physics, University of Latvia, Riga, Latvia); the corresponding paper was presented by I. Kuzmina.

The topical issues of the conference were discussed at seven poster sessions, where 158 papers were presented.

It was noted at the closing round-table discussion that the presented papers were of high scientific quality and corresponded to the current state of world science. This inference is confirmed by the participation of scientists from Russia and the Commonwealth of Independent States in international conferences possessing the same scope as this conference and, also, by the large number of studies carried out by the authors in cooperation with scientists from prominent world scientific centers. A number of studies conducted by the participants of the conference were innovative and of great importance; moreover, the results of these studies were often being reported for the first time. In particular, these studies were concerned with the development and implementation of new approaches to the writing of information on carriers made of chalcogenide vitreous semiconductors and the development of a new class of polyhomoconjugated organometallic compounds that exhibit clearly pronounced semiconductor properties and demonstrate potential (as was mentioned above) in relation to the development and fabrication of a number of microelectronic devices.

The number of scientific personnel working in the field under consideration corresponds to the current state of Russian Science; in particular, this circumstance manifests itself in the fact that a large number of the studies reported at the conference were supported by international agencies (INTAS, NATO, and CRDF). According to the data mentioned in the abstracts of the papers presented at the conference, 32 participants of the conference were supported in their studies by the Russian Foundation for Basic Research; 25, by the Ministry of Education; 4, by the Ministry of Industry and Science; 2, by the International Science & Technology Centre; 17, by grants received from various Russian programs for the support of scientists and scientific schools; and 8, by INTAS. Fifteen of the participants were involved in other foreign programs. However, it was noted by the participants of the conference that the funding of studies carried out in the majority of research institutes is inadequate, especially in the case of providing the institutes with modern equipment for technology and research.

The scientific level of all the presented papers was fairly high. The proceedings of the conference have been published. In addition, the Program Committee recommended publishing the most interesting papers in this issue of "Fizika i tekhnika poluprovodnikov" ("Semiconductors").

The conference was made possible thanks to the support of the Russian Foundation for Basic Research (project no. 04-02-26090-g) and the help of the Ioffe Physicotechnical Institute, Russian Academy of Sciences.

Translated by A. Spitsyn

Semiconductors, Vol. 39, No. 8, 2005, pp. 881–883. Translated from Fizika i Tekhnika Poluprovodnikov, Vol. 39, No. 8, 2005, pp. 917–919.

CONFERENCE. ATOMIC STRUCTURE AND NONELECTRONIC PROPERTIES OF SEMICONDUCTORS

Fast Exothermic Processes in Porous Silicon

S. K. Lazarouk^, A. V. Dolbik, P. V. Jaguiro, V. A. Labunov, and V. E. Borisenko

Belarussian State University of Informatics and Radioelectronics, Minsk, 220027 Belarus

^ e-mail: serg@nano.bsuir.edu.by

Submitted December 27, 2004; accepted for publication January 12, 2005

Abstract—It is found that rapid oxidation of porous Si (*por*-Si) layers in air may occur in the form of combustion or explosion. Combustion occurs in *por*-Si layers thinner than 60 μm and impregnated with potassium nitrate, while explosion is observed in thicker porous layers. It is suggested that explosion develops by a thermal mechanism resulting from an exponential increase in the reaction rate with temperature. *© 2005 Pleiades Publishing, Inc.*

1. INTRODUCTION

Porous Si, which is obtained by electrochemical anodization of single-crystal Si in HF solutions, is a unique nanostructured material. Indeed, the size of its pores can be varied from several nanometers to several micrometers by selecting an appropriate anodization mode [1, 2]. The unusual properties of this material result from its developed internal surface and the presence of nanoscale structures. One of these properties is the recently found catalytic sustention of oxidation reactions leading to combustion and even explosion of reagents located in the pores [3–5]. The rules governing these unusual phenomena remain unknown.

The purpose of this study is to examine the fast exothermic processes of combustion and explosion in *por*-Si, find the necessary conditions for these reactions, and analyze the possible mechanisms involved in their development.

2. EXPERIMENTAL

As experimental substrates, we used *p*-Si single-crystal wafers doped with boron to a concentration of 10^{16} cm^{-3}. The porous Si layers were obtained by electrochemical anodization of the Si substrates in 48% aqueous HF. Anodization was carried out at current densities ranging from 10 to 100 mA/cm^2. The anodization time was correlated with combustion, while the processes with a time response of less than 1 ms were classified as explosion.

3. RESULTS AND DISCUSSION

Thermally initiated combustion of *por*-Si was observed for porous layers thicker than 15 μm. This process is caused by rapid oxidation of the nanoscale Si structures inside a porous layer [6]. Figure 1 shows the kinetics of the rise and decay of light intensity during combustion of 40-μm porous layers (*1*) free of filler and (*2*) impregnated with KNO_3. Pure *por*-Si burned for longer than 10 s. When it was impregnated with KNO_3 (40–50% Si and 30–40% KNO_3), it burned only for several tenths of a second. Rapid combustion was accompanied by a bright red-white flash. The flash size increased over time to reach its maximum value and then decreased as the porous material burned. It is noteworthy that rapid combustion was accompanied by spatter of the reaction products. The samples were studied after combustion using an optical microscope. It was found that, in the case of slow combustion, a larger part of the porous layer remains on the Si substrate, while, after rapid combustion, the porous layer is virtually absent from the substrate. This observation is indicative of the destruction and spatter of a porous layer during the reaction. The presence of microparti-

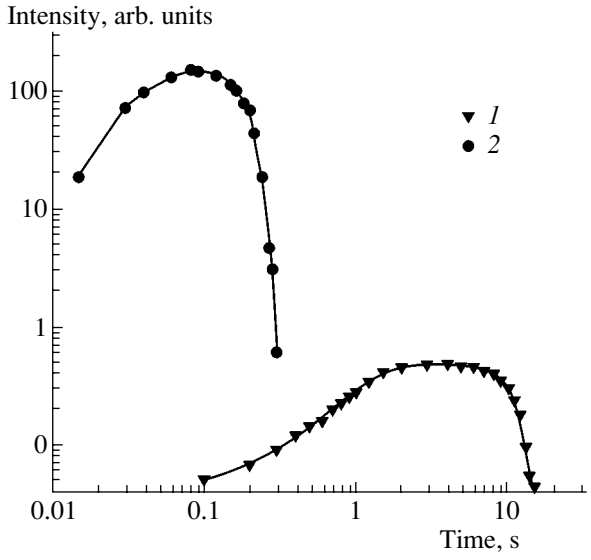

Fig. 1. Time dependence of the light intensity during combustion of (*1*) pure *por*-Si and (*2*) *por*-Si impregnated with KNO_3. The porous layer was 40 μm thick in both cases, and thermal initiation was applied.

1063-7826/05/3908-0881$26.00 © 2005 Pleiades Publishing, Inc.

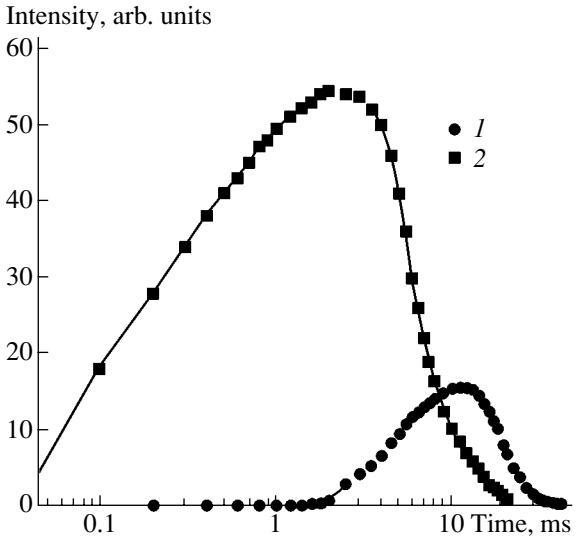

Fig. 2. Time dependence of the light intensity during rapid oxidation of *por*-Si layers impregnated with KNO_3. The thickness of the porous layer was (*1*) 50 and (*2*) 100 μm, and electrical initiation was applied.

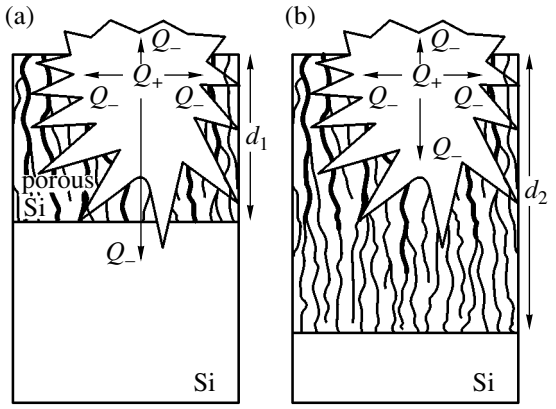

Fig. 3. Heat release and heat removal in *por*-Si during rapid oxidation: (a) combustion in thin porous layers with d_1 less than 60 μm and (b) explosion in thick porous layers with d_2 exceeding 60 μm.

cles of reaction products around the experimental samples after combustion confirms this conclusion. The filler KNO_3 plays the particular role of a solid oxidizer in the processes under study. During oxidation of dispersed materials, solid oxidizers are more efficient than gaseous ones because they limit the rate of transit of a gaseous agent through a porous nanostructure. This circumstance is precisely the cause of the distinction in the combustion rates of the impregnated and unimpregnated samples under consideration.

Study of the effect of the initiation methods on the combustion of the *por*-Si layers showed no significant distinction. The reactions under study were most intense for fresh samples. The combustion capability of the material was retained after storage at room temperature for 1–2 days. However, prolonged storage hindered combustion because of the passivation of the Si surface with a dense protective oxide.

As the thickness of a *por*-Si layer was increased from 50 to 60 μm or more, the behavior of the porous layers impregnated with KNO_3 changed. These changes are shown in Fig. 2. In addition to the increase in the flash size resulting from increasing the porous layer thickness, some new specific features of the reactions under study should be noted. For porous layers thicker than 50 μm, the reaction started with a certain delay with respect to the electric firing pulse, and the leading edge of the flash corresponded to the millisecond range. For the 60-μm porous layers, oxidation reactions developed without any delay with respect to the firing pulse, while the leading edge of the anodization flash was selected within 10–60 min to form porous layers from 5 to 100 μm thick.

The structure and thickness of the porous layers formed were studied by transmission electron microscopy. Porous layers in some of the experimental samples were impregnated in a 10% aqueous solution of KNO_3 and underwent subsequent rotary drying at room temperature. The porosity of the initial structures and the weight content of KNO_3 in the *por*-Si layers were determined gravimetrically by weighing the Si substrates.

Combustion and explosion in *por*-Si were initiated thermally, mechanically, or electrically. Thermal initiation was performed via the contact of experimental samples with an object heated to 900°C. Mechanical initiation was performed by scratching or pricking the *por*-Si surface with a metal needle. Electrical initiation was performed by passing a current pulse through the structure under study.

The kinetics of combustion and explosion was monitored by detecting optical emission from the *por*-Si regions in which these processes were initiated. For optical detection, we used a Si photodiode and subsequent signal processing in a digital oscilloscope. A video camera, recording the processes under study at a rate of 60 frames per second, was also used. Taking into account that the fundamental distinctions between combustion and explosion are the different development times of these processes and the presence of a shock wave [7], the processes for which the leading edge of the light pulse exceeded 1 ms corresponded to the microsecond range in our experiments. Similar specific features were also observed for the thicker porous layers.

It is well known that the fundamental distinctions between combustion and explosion are the value of the time response and the presence of a shock wave [7]. Thus, the combustion time response is in the millisecond and second ranges, while the time taken for explosion development is within nanosecond and microsecond ranges. On the basis of this fact, we may conclude

that, in the 60-μm and thicker porous layers, explosion occurs when a *por*-Si layer impregnated by KNO_3 is oxidized. This suggestion is confirmed by the difference in the acoustic accompaniment of the processes under study. For the *por*-Si layers thinner than 60 μm, the acoustic accompaniment is similar to a muted popping. In contrast, for the thicker layers, the sound becomes shriller and resembles a pistol shot, which indicates the formation of a shock wave. In addition, in the case of combustion, the flash color is red-white, while, during explosion, the flash can even be white-blue [3], which is indicative of the higher temperatures in the explosion zone.

Rapid oxidation can occur according to two main mechanisms [7, 8]. The first of these, the thermal mechanism, which imposes no special requirements on the chemical properties of reagents, is the most general. The essence of this mechanism lies in the fact that, when the amount of heat generated in a certain region exceeds the maximum amount that can be removed from this region, it is locally heated. This effect causes an increase in the exothermic reaction rate, which, generally, exponentially depends on temperature, and a further increase in heat generation. These factors cause an explosion in such systems. The heat generation in an explosion-like process can be described as

$$Q_+ = V_q A \exp(-E/RT).$$

Here, Q_+ is the released heat, V_q is the reaction heat, A is the preexponential factor, E is the activation energy of the reaction, R is the universal gas constant, and T is temperature.

Taking into account that the heat conductivity of bulk single-crystal Si is higher than that of *por*-Si by more than 2 orders of magnitude [1], the heat Q_- will mainly be removed towards the Si substrate. Therefore, the removed heat can be calculated by the formula

$$Q_- = (\lambda/d)(T - T_s)S.$$

Here, λ is the thermal conductivity, d is the thickness of the *por*-Si layer, S is the reaction area, T is the temperature in the reaction zone, and T_s is the environmental temperature.

The results of this study suggest that, in the case of rapid oxidation of *por*-Si layers thinner than 60 μm, the heat released (Q_+) and heat removed (Q_-) are balanced due to effective heat removal through the Si substrate, which leads to relatively slow combustion processes (Fig. 3a). As the thickness of the *por*-Si layer increases, the efficiency of heat removal via the substrate decreases sharply. Oxidation in such layers occurs when there is a significant misbalance between the heat released and the heat removed, which leads to local overheating and, as a consequence, to explosion of the porous layer (see Fig. 3b).

4. CONCLUSIONS

The conditions under which explosion and combustion of *por*-Si layers occurs have been determined. Impregnation of a porous layer with KNO_3 leads to considerable enhancement of combustion, which can acquire an explosive character under certain conditions. Similar behavior has also been observed for other dispersed materials such as coal dust or aluminum powder. However, only in the case of *por*-Si is it possible to obtain explosion in a film with a thickness of several tens of micrometers and a mass of explosive material smaller than one milligram. Therefore, we can state that an explosion at a microscale level (i.e., microexplosion) was obtained. Both of the processes under study (combustion and explosion of *por*-Si) can find practical application in the fabrication of certain devices. Specifically, combustion of *por*-Si can be used as an energy source for Si microactuators. Microexplosion can be used both in self-destructive Si chips and in the fabrication of Si integrated circuits to divide Si wafers into chips.

REFERENCES

1. L. T. Canham, *Properties of Porous Silicon* (INSPEC, London, 1997).
2. V. E. Borisenko and S. Ossicini, *What is What in the Nanoworld* (Wiley–VCH, Weinheim, 2004).
3. D. Kovalev, V. Y. Timoshenko, N. Kunzner, *et al.*, Phys. Rev. Lett. **87**, 68301 (2001).
4. F. V. Mikules, J. D. Kirtland, and M. J. Sailor, Adv. Mater. **14**, 38 (2002).
5. A. V. Dolbik, A. A. Kovalevskiĭ, S. K. Lazaruk, *et al.*, Izv. Belorus. Inzh. Akad., No. 1(15)/4, 41 (2003).
6. A. A. Kovalevskiĭ, A. V. Dolbik, S. K. Lazaruk, and V. A. Labunov, Izv. Belorus. Inzh. Akad., No. 2(18)/2, 47 (2004).
7. J. Warnatz, U. Maas, and R. W. Dibble, *Combustion: Physical and Chemical Fundamentals, Modeling and Simulation, Experiment, Pollutant Formation* (Springer, Berlin, 2001; Fizmatlit, Moscow, 2003).
8. R. Shale, in *High Speed Physics*, Ed. by von K. Vollrath and G. Thomer (Springer, Vienna, 1967; Mir, Moscow, 1971).

Translated by N. Korovin

Semiconductors, Vol. 39, No. 8, 2005, pp. 884–890. Translated from Fizika i Tekhnika Poluprovodnikov, Vol. 39, No. 8, 2005, pp. 920–926.

CONFERENCE.
ELECTRONIC AND OPTICAL PROPERTIES OF SEMICONDUCTORS

Interpretation of the Visible Photoluminescence of Inequisized Silicon Nanoparticles Suspended in Ethanol

V. E. Ogluzdin^

Prokhorov Institute of General Physics, Russian Academy of Sciences, ul. Vavilova 38, Moscow, 119991 Russia
^ e-mail: ogluzdin@kapella.gpi.ru

Submitted December 27, 2004; accepted for publication January 10, 2005

Abstract—Silicon nanoparticles obtained by laser-assisted dissociation of molecules of gaseous silane have been immersed in ethanol. If a cell filled with such a medium is exposed to radiation from an argon laser, the luminescent trace of the laser beam propagating through the cell is observed in the visible region of the spectrum. A model based on the Lorentz classical harmonic oscillator and a multiphoton scheme of interaction between laser radiation and a nearly resonant medium is used to derive a model of luminescence in a medium with suspended nanoparticles. The reported experimental data are discussed and compared with the predictions of the suggested model. © *2005 Pleiades Publishing, Inc.*

1. INTRODUCTION

One can consider two mechanisms when analyzing the decay of emission from fluorescent substances such as organic compounds, atomic media, or (recently) nanostructures. It is assumed that the situation is conventional if luminescent emission is related to one-photon absorption of incident radiation and involves an electron transition in the medium, and a delay in the emission of new photons is related to another electron transition. In this case, the decay of short-lived luminescent emission after the cessation of excitation is adequately described by an exponential time dependence and has already been considered in detail [1]. However, the assumption about one-photon excitation of a medium does not fully correspond to the pattern of interaction between the radiation and the medium. For example, the one-photon approach cannot account for the appearance of the occasionally observed anti-Stokes luminescence or the symmetry in the shape of the absorption and luminescence spectra [1]. In this context, it is reasonable to use another approach to the problem of luminescent emission. This alternative approach is based on a model of multiphoton-related increase in the transmittance of a medium [2].

The other mechanism that can cause the duration of luminescent emission from a medium to lengthen is suggested in this study and is based on the effect of a decrease in the speed of light. When considering this effect, we use effective values of the nonsaturated refractive index of a medium $n(\nu_i)$ for the luminescent emission photons (ν_i is one of the multitude of frequencies in the spectrum of luminescent emission). It should initially be noted that the value of the nonsaturated refractive index of a medium $n(\nu_i)$ can be unexpectedly large for some of the photons in the luminescent emission. If we manage to show that the above approach is of value, then the results of measurements of the duration of luminescent-emission decay can evidently be used to numerically estimate the refractive index of the medium under study. In this case, in order to conventionally determine the refractive index from the expression

$$n(\nu_i) = \frac{c}{V(\nu_i)} = \frac{ct}{s},$$

it is necessary to possess experimental data on the decay of luminescent emission t and the sizes s of the used cells or samples ($V(\nu_i)$ is the speed of light in the medium in relation to the frequency ν_i).

According to the law of conservation of energy, absorption of two photons with an excitation radiation of $2h\nu$ and creation of two new photons (a luminescence photon $h\nu_i$ and a photon absorbed in the medium $h\nu_{0j}$) occur in an elementary event of multiphoton-induced increase in the transmittance of the medium. This increase is typically observed in a situation where the excitation-radiation frequency ν and resonant eigenfrequency ν_{0j} of elementary oscillators in the medium (or, for example, the frequency of an interlevel transition ν_{0j} [3]) are not exactly in resonance. In this case, some of these nearly resonant dipoles (oscillators) can be found in an excited (inverse) state, which provides an exact increase in the transmittance of the medium. The return of these dipoles to the initial (unexcited) state can be accomplished either by a nonradiative transition due to the transfer of the stored energy to the medium in the form of heat or by a cascade steplike process (with the involvement of metastable states) of de-excitation emission, which is characteristic of phosphorescent crystals [1] (these crystals are not considered in this paper).

1063-7826/05/3908-0884$26.00 © 2005 Pleiades Publishing, Inc.

The aim of this study was to discuss and interpret the phenomenon of transient luminescence (fluorescence) characteristic of atomic, molecular, or nanosized structures; according to [4], this luminescence exhibits a finite duration that exceeds the period of optical oscillations. The model considered in this paper is primarily compared with the results of experimental studies of the luminescence of silicon nanoparticles suspended in ethanol; however, in the author's opinion, this model could also be applied to other media.

2. A MODEL OF MULTIPHONON-RELATED INCREASE IN THE TRASNITTANCE OF A MEDIUM. OBSERVATION OF LUMINESCENCE IN A MEDIUM CONSISTING OF AN ENSEMBLE OF CLASSICAL LORENTZ OSCILLATORS WITH DIFFERING FREQUENCIES. A RETARDATION OF THE PROPAGATION OF LUMINESCENT-EMISSION PHOTONS IN AN INHOMOGENEOUSELY BROADENED MEDIUM

The suggested model is based on the assumption that the medium under study can be considered as an ensemble of classical nanosized oscillators with different sizes and frequencies (in fact, these oscillators are optical electrons that are surrounded by a certain number of positive ions in a molecule or the medium's nanoparticles in a certain energy state). In spectroscopy, media in which the resonance frequencies of the medium particles do not coincide with each other and which are distributed within a wide spectral region are referred to as inhomogeneously broadened media.

As a rule, the frequency of the excitation radiation ν when observing luminescence is equal to or lower than the resonance eigenfrequency ν_{0j} of the oscillators (modes) in the medium. It should initially be noted (this will be shown below) that, otherwise, we would expect (if $\nu > h\nu_{0j}$), according to the model of multiphoton-related increase in the transmittance of a medium, the appearance of luminescent emission in the spectral region on the anti-Stokes side relative to the pump frequency.

This model was recently suggested in [2, 5] when discussing the luminescence of silicon nanoparticles suspended in ethanol [6, 7]. We now briefly consider the model of multiphonon-related increase in the transmittance of a medium. Taking into account the law of conservation of energy, we can represent the scheme of an elementary process of interaction between the radiation and luminescent medium and the process of generation of luminescence photons at the frequencies ν_i as

$$h\nu_i = 2h\nu - h\nu_{0j}, \quad (1)$$

where ν is the frequency of the excitation radiation, ν_i is the frequency of one of the components of the luminescent-emission spectrum detected as it exits the medium ($i = 1, 2, 3, ...$), and ν_{0j} is the eigenfrequency of the oscillators in the medium that are transferred to an excited state as a result of process (1) ($j = 1, 2, 3, ...$). The indices $0j$ characterize a set of resonance eigenfrequencies of the absorbing oscillators in the medium. The subscripts j correspond to a set of frequencies in the spectrum of the secondary radiation (luminescent emission) excited according to process (1).

It should be realized that the spectrum of eigenfrequencies of the oscillators in an inhomogeneously broadened medium ν_{0j} is, as a rule, broad and corresponds to spectral regions where one-photon absorption of optical radiation occurs (for example, according to results obtained using a spectrometer to measure the transmittance of optical radiation for this medium in an optical field with a low intensity).

We are now going to clarify the fate of the luminescent-emission photons with a frequency ν_i. As a rule, the peak in the luminescence spectrum is shifted with respect to the excitation-radiation frequency ν towards the Stokes region of the spectrum. The luminescent-emission spectrum is, as a rule [1], recorded when the direction of propagation of the luminescent emission does not coincide with that of the pump radiation; in addition, the medium under study should be located between the axis of the excitation-radiation beam and the window of the photodetector. A part of this medium at this axis is found to be in a condition of resonance (or almost resonance) saturation. However, as the distance from the axis of the excitation-radiation beam increases (for example, in the vicinity of the photodetector window), the conditions of radiation propagation can change, e.g., owing to a variation in the degree of saturation of the medium. According to expression (1), photons from the excitation radiation ν that propagates predominantly along the beam axis and luminescent-emission photons ν_i scattered within the solid angle 4π are present simultaneously in the medium. As a result of radiation reflection from the cell windows and walls, excitation-radiation photons and photons related to Raman scattering can be also found within the angle 4π [6, 7].

The rule of mirror symmetry for the spectra of luminescent emission and those of one-photon absorption in the medium [8] follows from relation (1); indeed, this relation can be rewritten as

$$\nu_{0j} - \nu = \nu - \nu_i.$$

The rule of the mirror symmetry amounts to the following statement: the difference between the frequency of the oscillators located within the medium and absorb radiation and the excitation-radiation frequency is equal to the difference between the excitation-radiation frequency and the frequency of luminescent emission (of one of its spectral components).

In addition, if the excitation-radiation frequency is higher than the eigenfrequency of the oscillators in the medium ($\nu > \nu_{0j}$), it follows from relation (1) that it is possible to observe luminescent emission whose fre-

quency is shifted to the anti-Stokes region with respect to the excitation-radiation frequency provided that the experimental conditions are optimized so that the absorption of this radiation by the medium is minimized. This optimization implies that the secondary luminescent-emission absorption by the medium is taken into account [1].

Before considering the issue of retardation of light and its relation to the luminescence phenomenon, we should recall a number of special features of the interaction between radiation and a medium that is composed of a set of harmonic noninteracting oscillators with different sizes and, consequently, different frequencies.

The suggested model is based on the following assumption. The major processes of scattering of optical emission from electrons in a separate molecule (or nanoparticle) suspended in a medium should be governed by laws that follow from the Lorentz model of a classical harmonic oscillator [9, 10].

An electron with a mass m is kept in equilibrium conditions at $x = 0$. When displaced, the electron is subjected to the restoring force Gx, where G is the elastic force per unit length of displacement. In the case under consideration, the quantity G should depend on the number of positive ions N in an individual molecule or nanoparticle; therefore, in general, $G_k = f(N)$, where N is the aforementioned number of ions in whose combined field the electrons oscillate ($N = 1, 2, 3, ...$) and the subscript k is related to the stereometry of the arrangement of these ions ($k = 1, 2, 3, ...$). The simplest equation of motion for the electron under consideration is written as [9, 10]

$$mx + G_k x = 0. \quad (2)$$

The well-known solution to this equation is a harmonic oscillation (mode) with the following resonance eigenfrequency:

$$\nu_{0j} = \frac{\sqrt{G_k/m}}{2\pi}. \quad (3)$$

Thus, we managed to determine the set of eigenfrequencies ν_{0j} characteristic of a medium of the type under consideration. In the case of a medium composed of identical atoms that each have a single electron, spectral characteristics are controlled by this specific electron, which features the frequency ν_{0j} (a single optical mode). In contrast, in the case of an ensemble of inequisized oscillators in a medium (molecules and nanoparticles), we have a broad spectrum, i.e., a superposition of resonance eigenfrequencies ν_{0j}. These frequencies represent modes that are shifted relative to each other but are independent of each other. Therefore, optical effects (including those of nonlinear optics) should be represented, as a rule, by broad spectral lines or bands, which reflect the contribution of a multitude of modes (resonance eigenfrequencies of the harmonic oscillators in the medium). These oscillators feature different elasticity G_k and different geometric orientation of their particles. According to formula (3), the resonance eigenfrequencies ν_{0j} should vary as the elasticity varies.

According to the Lorentz model of a classical harmonic oscillator, the refractive index of a medium $n(\nu) > 1$ if the excitation-radiation frequency ν is lower than the resonance eigenfrequency, $\nu < \nu_{0j}$, whereas $n(\nu) < 1$ if the excitation-radiation frequency is higher than the resonance frequency, $\nu > \nu_{0j}$ [9–11]. The fact that the refractive index differs from unity indicates there is a singularity for nearly resonant photons in the laser-radiation beam at the boundary of the medium [12]; i.e., only part of the incident radiation can penetrate beyond the surface that confines the medium with $n(\nu) \neq 1$ (in problems of linear classical optics). Primarily, this circumstance concerns photons whose frequency $\nu > \nu_{0j}$. In this case, destructive interference [10] should result in quenching of the emission. In the case of $\nu < \nu_{0j}$, the velocity of the emission propagation $V(\nu) = c/n(\nu)$ should slow down, since $n(\nu) > 1$. Data indicating that the refractive index in this region can be found much in excess of unity were provided, for example, in [11]. With regard to laser radiation, this difficulty is easily surmounted by a nonlinear-optical process that results in dynamic compensation of the dispersion. The problem of retardation of the luminescent (secondary) emission is related to the above circumstance and will be considered in Section 3.

3. A CONSEQUENCE FOLLOWING FROM THE MODEL. CONSIDERATION OF THE FACT THAT LUMINESCENT EMISSION HAS A LOW INTENSITY AND CANNOT DYNAMICALLY COMPENSATE THE DISPERSION OF INDIVIDUAL OSCILLATORS IN THE MEDIUM. FEASIBILITY OF OBSERVING RETARDATION OF THE OPTICAL LUMINESCENT EMISSION IF THE REQUIREMENTS OF THE MODEL ARE SATISFIED

We are not going to consider the case in which the frequency of the excitation (pump) radiation ν corresponds exactly to the resonance eigenfrequencies ν_{0j} of the optical electrons in the medium under study, as it has already been studied in detail [10, 11, 13] and is of interest in this study only due to the fact that the processes of one-photon absorption and emission compensate each other whereas the transmittance of the medium in the pump-radiation field increases, which brings about dynamic compensation of the dispersion in the spectral region that is located closest to the pump frequency. If there is a small difference between the frequency of the pump radiation and the resonance frequency of the medium ν_{0j}, dynamic compensation of the dispersion can be attained by six-photon parametric scattering [3, 14].

There remain two spectral regions that are of interest to us. The first region corresponds to the portion of the spectrum that is shifted to the anti-Stokes region in relation to the pump frequency and corresponds to specific oscillators in the medium. These oscillators, according to expression (1), absorb photons with the frequencies ν_{0j} in the course of the increase in transmittance, play the role of a heat exchanger, and transform the excess energy transferred to the medium into heat. There is also a second spectral region of interest corresponding to luminescent-emission frequencies ν_i where the absorption and the saturation processes are not as important. As a rule, this spectral region is located on the Stokes side in respect to the pump frequency (we denote the resonance eigenfrequencies in this spectral region as ν'_{0j}). The absorption and the saturation processes can be disregarded, since luminescent emission at the frequencies ν_i propagates within the solid angle 4π, which limits and reduces the optical-field strength.

We now clarify the fate of the luminescent-emission photons with frequencies of ν_i. It is established that, when a state of resonance interaction of the laser-radiation beams with a medium is almost attained, photons with identical frequencies can propagate through the same medium at different velocities, depending on the radiation intensity (or the degree of saturation of the medium). This circumstance has made it possible to experimentally show that there exist photons that travel faster than light and can give rise to Cherenkov radiation [14].

This study has the opposite aim: finding the conditions for propagation of ultraslow emission. We proceed by defining the absolute refractive index as $n(\nu_i) = c/V(\nu_i)$ [11]; in addition, we operate under the reasonable assumption that saturation effects can be disregarded if the strength of the luminescent-emission field E_i is low.

The following circumstance deserves attention. Two frequencies of oscillations of an optical electron in an atom (molecule or nanoparticle) are important [9–11]. According to [11], the resonance electron frequency is controlled by the frequency of the field of the excitation optical radiation. At the same time, it is very important that [9–11] the initial resonance frequency of the optical electrons in a medium is governed only by elasticity (by the force that affects the electrons and is divided by the displacement length; see relation (3)).

In this context, let us conditionally separate the oscillators into two types: active and passive oscillators. Active oscillators oscillate in phase with the frequency of the excitation-radiation field, and the dispersion curve of these oscillators can shift as the excitation-radiation frequency varies. The passive oscillators in the medium are rigidly related to a single frequency ν'_{0j} governed only by the interaction of the optical electrons with their environment (i.e., with the constituents of an atom, molecule, or nanoparticle that surround the optical electron). However, the initial presence of passive oscillators in the medium governs the initial value of the refractive index $n(\nu_i)$ of the luminescent emission at a frequency ν_i and the velocity of the propagation of this emission.

Table

Compound	Solvent	Lifetime of fluorescent state, ns	Refractive index (approximate estimate)
Anthracene	Hexane	5	~150
Benzene	Cyclohexane	23	~690
Naphthalene	Cyclohexane	110	~3300
Pyrene	Petrolatum	520	~15600

According to [11], in the case of gaseous media (and, also, substances with a higher density, i.e., liquids or solids), an inverse-proportionality relationship between the quantity $n(\nu_i) - 1$ and the frequency difference $\nu'_{0j} - \nu_i$ in the Sellmeier formula implies that the refractive index can be arbitrarily large if $\nu_i < \nu'_{0j}$ and $\nu_i \longrightarrow \nu'_{0j}$.

Therefore, taking into account the result reported in [11], we recognize that the value of the refractive index can increase without limit if the difference between the frequencies ν_i and ν'_{0j} becomes arbitrarily small.

In order to illustrate the model, we can use experimental data on the lifetime of the fluorescent state in standard media [15] to approximately estimate the value of the refractive index $n(\nu_i)$ (the accuracy of this estimation is limited by the accuracy of determining the distance traveled by the luminescent emission in the medium along the axis of the excitation-radiation beam towards the photodetector window (see table)).

It is large values of the refractive index that bring about the retardation of propagation of the luminescent emission in the medium. The value of the refractive index was estimated under the assumption that the distance traveled by the luminescent emission in the medium is equal to 1 cm. Unfortunately, Tibilov and Shakhverdov [15] did not report any data on this distance. Evidently, the value of the refractive index should be reduced by a factor of 10 for a cell with a length of 10 cm.

4. EXPERIMENTAL

After having discussed the suggested model and its consequences, such as the retardation of propagation of the luminescent emission in the medium, we now consider some provisional experimental data.

The method of laser-induced dissociation of monosilane SiH_4 in a gas stream makes it possible to obtain microdisperse silicon powders with ultrasmall Si

particles. The high chemical purity of silicon nanoparticles obtained in the course of condensation is characteristic of this method. Khokhlov *et al.* [16] used electron microscopy and X-ray diffraction to study the composition and sizes of Si particles as well as the variance in size in relation to the synthesis parameters. References to pioneering publications in this field can be also found in [16]. It was established that the powders obtained consist of crystalline and amorphous Si components. The size of a particle is determined, to a great extent, by the rate of flow of the SiH_4 gas stream across the focused beam of a CO_2 laser. It follows from the published data that the size of the particles can vary from 3 to 150 nm.

The unique characteristics of the obtained material stimulated studies on not only the morphology of the nanoparticles but also the physical properties of the powders. In this study, silane dissociation and the synthesis of nanosized powders were performed in a flow-through reactor using a silane stream surrounded by an argon flow. The schematic diagram of our experimental setup is similar to that used in [16]. The diameter of the silane stream at the exit from the gas-supplying nozzle was equal to 1 mm. The diameter of the nozzle that formed the enclosing argon flow was 3 mm. The gas was let in into the reactor under the conditions of continuous pumping down of the reactor using an evacuation system. In our experiments synthesizing the nanosized powder, the power was radiated by a CO_2 laser at a wavelength of 10.6 μm and was equal to 5–8 W. The laser radiation was focused so that the waist of the optical beam coincided with the silane stream. After the onset of the reaction, the irradiation could be accomplished under visual control. As a result of the silane dissociation brought about by the above procedure, a grayish-brown powder was found deposited on the reactor walls and in the vacuum trap. This powder consisted (according to the results of Raman scattering spectroscopy [6, 7]) of particles of crystalline and amorphous silicon that greatly varied in size. In the general case, mixing these powders with ethanol, acetone, and glycerol yields an almost unsettled turbid suspension. However, in a number of cases, the sedimentation process can be stimulated by consecutively diluting an alcoholic suspension; as a result, a sediment and a colloidal solution that has a light-yellow coloring, is transparent and stable, and scatters very little light are formed. In contrast to the initial suspension, the colloidal solution obtained exhibits a pronounced capability for photoluminescence (PL) when exposed to the radiation of the blue–green lines of an argon laser.

The studies were conducted using the Raman microscopy method. A DFS-24 automated spectrometer was employed in studies of the Raman and PL spectra. The spectra were excited using an emission line of an argon laser (488.0 nm and 100 mW). The laser radiation was focused to a spot with a diameter of 1 mm at the sample surface. A low-intensity band peaked at 600 nm was observed in the PL spectra of the initial powder. The PL intensity was appreciably higher for a colloidal solution of nanoparticles in ethanol; simultaneously, the peak of the giant luminescent emission shifted to the green region of the spectrum [6, 7].

4.1. Experimental Verification of the Suggested Model

In relation to our experiment, it is reasonable to first study the nature of the luminescent emission of the technical ethanol used (FSP 42-0053-1437-01) and investigate how this emission relates to rule of mirror symmetry (1).

A low-intensity luminescence signal with peaks in the range of 2.16–2.26 eV (575–548 nm) was detected in the Stokes (relative to the pump frequency) region of the spectrum if an argon laser (λ = 488.0 nm, ν = 20492 cm^{-1}) was used to excite the luminescence in commercial-grade ethanol without the addition of Si powder. If this weak signal at a frequency ν_i stems from process (1), then, according to the rule of mirror symmetry, we should look for a spectral feature in the region of a frequency ν_{0j} shifted to the anti-Stokes region.

An increase in the absorption of optical radiation in the wavelength range 424.0–439.0 nm (the ν_{0j} frequency) was found to represent the above feature. This circumstance was established using spectrophotometric measurements in a low optical field. It is in this spectral region that the transmittance T of a cell with ethanol begins to decrease as the wavelength becomes shorter. A decrease in the transmittance of low-intensity radiation by ethanol in the region of a frequency ν_{0j} is indicative of one-photon absorption of radiation and transfer of portions of the energy $h\nu_{0j}$ to dipoles in the medium.

At the same time, no significant absorption of radiation at the argon laser frequency ν = 20492 cm^{-1} (2.54 eV) was not observed according to the results of the spectrophotometric measurements in ethanol.

Thus, in our studies of the luminescence present in ethanol (with the amount of impurities specified in the certificate) using argon-laser radiation for pumping, the absorption of two pump photons $h\nu$ and generation of a single photon of luminescent emission at a frequency ν_i shifted to the anti-Stokes region of the spectrum occur in each elementary event (1). The medium's impurity dipoles whose eigenfrequency ν_{0j} is shifted to the anti-Stokes region of the spectrum are transferred to an excited state. The energy absorbed in this process is spent on the heating of the medium as a result of thermal relaxation of the excited dipoles. On the basis of this experiment, it is possible to tentatively conclude that process (1) is responsible for the ethanol luminescence.

4.2. Luminescence of a Medium Consisting of Ethanol and Si Nanoparticles

The spectrum of giant luminescence of the prepared colloidal solution of Si nanoparticles in ethanol was measured under the same conditions as described in Subsection 4.1. The luminescence spectrum of this medium occupies a range between ~1.85 eV (670 nm) and ~2.67 eV (464 nm) and has wings if an argon laser (488.0 nm) is used for excitation. Apparently, the position of the luminescence peak can change from measurement to measurement owing to either aging of the mixture or the method used for preparation of this mixture. The following position of the luminescent-emission peak was recorded: 2.25–2.28 eV (~543 nm).

According to the rule of mirror symmetry, it follows from relation (1) that the elementary dipoles absorbing excess energy and responsible for the luminescence in the vicinity of its peak (shifted to the Stokes region of the spectrum relative to the pump frequency) should have a wavelength at about 438.5–442.0 nm (i.e., should have a wavelength characteristic of the anti-Stokes (with respect to the pump frequency) region of the spectrum). A much wider spectral region corresponds to the dipoles that give rise to the broad luminescence spectrum. According to the rule of mirror symmetry and relation (1), the Stokes edge of the luminescence spectrum at 1.85 eV (670 nm) corresponds to dipoles with a frequency ν_{0j} and wavelength of about 383.2 nm, while the anti-Stokes edge at 2.67 eV (464 nm) corresponds to dipoles with a frequency ν_{0j} such that the wavelength is in the region of 514.2 nm.

The spectral range from 2.41 eV (514.2 nm) to 3.23 eV (383 nm) corresponds to the luminescence process; in this range, the elementary dipoles (i.e., the harmonic oscillators in the medium that absorb excess energy) are excited. This spectral region, corresponding to an ensemble of harmonic oscillators with a wide range of eigenfrequencies, was discussed in Section 2, devoted to consideration of the suggested model of the luminescence process as a whole. It is worth noting that the boundaries of this spectral region are controlled, to a large extent, by the sensitivity of the detecting system used and spectral characteristics of the photodetectors. According to the results of spectrophotometer-based study of the process of one-photon absorption in the above spectral range, 65% (at 383.2 nm) to 90% (at 514.2 nm) of incident radiation can pass through a cell containing the colloidal solution.

Thus, using the Lorentz model of a classical harmonic oscillator, a scheme of the multiphonon interaction of radiation with a medium close to a state of resonance, and the rule of mirror symmetry, we managed to explain the origin of luminescence in an artificially formed nanocomposite medium composed of silicon particles that had different sizes and were suspended in ethanol.

4.3. Tentative Conclusions Based on the Results

The model suggested in this study and the experimental data obtained do not contradict the main mechanisms and laws of the luminescence process [1, 17] and can be used to interpret fast luminescence [4].

Indeed, the broad emission band observed when luminescence is excited in a colloidal solution composed of ethanol and Si nanoparticles can be attributed to a classical size effect (this interpretation is confirmed by the fact that there is a large number of frequencies ν_{0j} corresponding to nanosized oscillators). This statement pertains to both the suspension of silicon inequisized nanoparticles in ethanol used in this study and porous silicon [18–20]. In our opinion, the method used to prepare the samples of porous silicon affects the pore sizes and, thus, the spread in the eigenfrequencies of the oscillators that are responsible for luminescence in this material.

If the excitation-radiation frequency ν is outside the region in which the absorption and luminescence spectra overlap ($\nu < \nu_{0j}$), then, according to the Stokes rule, only the luminescence-spectrum portion that is shifted to the Stokes (relative to the excitation frequency) region of the spectrum should be observed.

However, in the case under consideration, the excitation-radiation frequency ν is found to be within the region where the absorption and luminescence spectra overlap; i.e.,

$$\nu_{0j} > \nu > \nu_i, \quad \nu'_{0j}.$$

It is clear from relation (1) that one can observe luminescent emission at frequencies shifted to the anti-Stokes spectral region. This emission manifests itself as a wing of the luminescence line broadened on the side of the anti-Stokes spectral region with respect to the pump-radiation frequency. This observation does not contradict the Stokes rule: the luminescence spectrum and its peak should be always shifted to lower frequencies compared to the absorption spectrum [1, 17].

We can use the suggested model to interpret the rule of mirror symmetry. According to this rule, absorption and luminescence spectra exhibit mirror symmetry on the frequency scale [1, 17]. As can easily be verified, this rule follows from relation (1),

$$\nu_i = 2\nu - \nu_{0j} \text{ or } \frac{\nu_i + \nu_{0j}}{2} = \nu$$

and accounts for the essence of the size effect: the frequencies of natural oscillations of elementary dipoles ν_{0j} depend on the size of the nanoparticles, and a specific spectral component of the luminescent emission ν_i corresponds to each set of electric dipoles with a frequency ν_{0j}.

In our opinion, the nature of the anti-Stokes wing in the luminescence line and the shift of the luminescence spectrum to the green spectral region indicate that small particles (electric dipoles in the medium) with a

reduced elasticity G_i are excited. Apparently, the Stokes edge of the luminescence spectrum is set by the largest nanoparticles. For large nanoparticles with a higher elasticity G, the energy of an excited electron in a nanoparticle is ~3.23 eV. An increase in the size of the nanoparticles (for example, due to their coalescence) can bring about a further shift of the luminescence-spectrum wing to the Stokes region. In this context, it is worth noting that the presence of impurities in the form of light atoms of extraneous elements in silicon-containing samples should induce a shift of the luminescence spectrum to the anti-Stokes region whereas the presence of heavier impurity atoms should result in a shift to the Stokes region. As has previously been noted [18–20], molecular silicon compounds with oxygen, hydrogen, and nitrogen (as well as impurities) can affect the position of the peak in the luminescence spectrum.

The model suggested in this study and based on the use of a multiphoton process is consistent with the nonlinear dependence $I_{em} = f(I_{exc})$ reported by Savin *et al*. [18] as well as with the assumption [18] that multiphoton processes affect luminescence. Here, I_{em} is the luminescent-emission intensity and I_{exc} is the excitation-radiation intensity.

5. CONCLUSION

In this study, a model of the luminescence process based on the effect of a multiphoton-related increase in the transmittance of a medium is considered. A simple method for determining the unsaturated refractive index of a luminescent medium is suggested. This method is based on direct measurement of the luminescent-emission duration after cessation of the exposure to excitation radiation. The measurement takes into account the dimensions of the cell with the medium under study. It is suggested that a lag in the luminescent-emission signal is a consequence of retardation of the radiation propagation.

ACKNOWLEDGMENTS

I thank V.A. Karavanskiĭ, who suggested and implemented a method for preparing colloidal solutions and was the first to draw attention to the fact that these solutions can luminesce. I am also indebted to V.G. Plotnichenko and A.V. Chervyakov for their help with measuring the spectra and to V.S. Gorelik, S.B. Korovin, and V.I. Pustovoĭ for their participation in helpful discussions.

This study was supported by the Russian Foundation for Basic Research, project no. 03-02-17025.

REFERENCES

1. A. A. Babushkin, P. A. Bazhulin, F. A. Korolev, L. V. Levshin, V. K. Prokof'ev, and A. R. Striganov, *Methods of Spectral Analysis* (Mosk. Gos. Univ., Moscow, 1962) [in Russian].
2. V. E. Ogluzdin, Kratk. Soobshch. Fiz., No. 12, 3 (2003).
3. V. E. Ogluzdin, Zh. Éksp. Teor. Fiz. **79**, 361 (1980) [Sov. Phys. JETP **52**, 181 (1980)].
4. S. I. Vavilov, *Collected Works* (Akad. Nauk SSSR, Moscow, 1952), Vol. 2 [in Russian].
5. V. E. Ogluzdin, in *Proceedings of IV International Conference on Amorphous and Microcrystalline Semiconductors* (S.-Peterb. Gos. Pedagog. Univ., St. Petersburg, 2004), p. 131.
6. V. S. Gorelik, E. D. Obraztsova, V. E. Ogluzdin, *et al.*, in *Proceedings of V International Conference on Optics, Optoelectronics, and Technology* (Ul'yan. Gos. Univ., Ul'yanovsk, 2002), p. 27.
7. V. S. Gorelik, V. E. Ogluzdin, I. A. Razmatulaev, *et al.*, in *Proceedings of IV International Conference on Amorphous and Microcrystalline Semiconductors* (S.-Peterb. Gos. Pedagog. Univ., St. Petersburg, 2004), p. 132.
8. V. L. Levshin, *Photoluminescence of Liquids and Solids* (Nauka, Moscow, 1951) [in Russian].
9. C. F. Bohren and D. R. Huffman, *Absorption and Scattering of Light by Small Particles* (Wiley, New York, 1983; Mir, Moscow, 1986).
10. F. S. Crawford, Jr., *Waves* (McGraw-Hill, New York, 1968; Nauka, Moscow, 1974).
11. M. Born and E. Wolf, *Principles of Optics*, 3rd ed. (Pergamon, Oxford, 1966; Nauka, Moscow, 1970).
12. V. E. Ogluzdin, Kratk. Soobshch. Fiz., No. 9, 3 (2002).
13. P. G. Kryukov and V. S. Letokhov, Usp. Fiz. Nauk **99**, 169 (1969) [Sov. Phys. Usp. **12**, 641 (1969)].
14. V. E. Ogluzdin, Usp. Fiz. Nauk **174**, 895 (2004) [Phys. Usp. **47**, 829 (2004)].
15. S. S. Tibilov and P. A. Shakhverdov, in *Spectroscopy of Photoconversions in Molecules*, Ed. by I. A. Akimov *et al.* (Nauka, Leningrad, 1977), p. 92 [in Russian].
16. E. M. Khokhlov, D. V. Kolmykov, N. N. Kononov, *et al.*, Laser Phys. **8**, 1070 (1998).
17. L. V. Tarasov, *An Introduction to Quantum Optics* (Vysshaya Shkola, Moscow, 1987) [in Russian].
18. D. P. Savin, Ya. O. Roizin, D. A. Demchenko, *et al.*, Appl. Phys. Lett. **69**, 3048 (1996).
19. L. T. Canham, Appl. Phys. Lett. **57**, 1046 (1990).
20. P. M. Tomchuk, D. B. Dan'ko, and O. É. Kiyaev, Fiz. Tverd. Tela (St. Petersburg) **42**, 1964 (2000) [Phys. Solid State **42**, 2017 (2000)].

Translated by A. Spitsyn

Semiconductors, Vol. 39, No. 8, 2005, pp. 891–893. Translated from Fizika i Tekhnika Poluprovodnikov, Vol. 39, No. 8, 2005, pp. 927–930.

CONFERENCE.
ELECTRONIC AND OPTICAL PROPERTIES OF SEMICONDUCTORS

Photoluminescence of Erbium-Doped Aluminum Oxide Films with Embedded Silicon Nanoparticles

S. K. Lazarouk*^, A. V. Mudryi, A. V. Ivanyukovich**, A. A. Leshok*, D. N. Unuchek*, and V. A. Labunov***

** Belarussian State University of Informatics and Radioelectronics, Minsk, 220027 Belarus*
^ e-mail: serg@nano.bsuir.edu.by
*** Institute of Solid-State and Semiconductor Physics, National Academy of Sciences of Belarus, ul. Brovki 17, Minsk, 220072 Belarus*

Submitted December 27, 2004; accepted for publication January 10, 2005

Abstract—Erbium-doped aluminum oxide films with embedded Si nanoparticles have been obtained by magnetron sputtering of a composite (Al + Er_2O_3 + Si) target and subsequent electrochemical anodization at room temperature. The photoluminescence (PL) spectra of these films are measured in the temperature range 4.2–300 K. Efficient PL is observed at a wavelength of 1.54 μm without preliminary annealing of the samples, which indicates the possibility of activating Er^{3+} ions without any high-temperature treatment. The aluminum oxide films with embedded Si nanoparticles were observed to show stronger PL at a wavelength of 1.54 μm than similar films without Si nanoparticles. This effect can be explained by additional pumping of Er-based luminescence centers and energy transfer from the Si nanoparticles. *© 2005 Pleiades Publishing, Inc.*

Erbium-doped materials are of great interest because the luminescence peak of Er^{3+} ions coincides with the optical absorption minimum in standard Si waveguides [1]. Aluminum oxide is an useful host material for Er ions since the processes involved in its fabrication are well developed, inexpensive, and highly compatible with Si technology. In this study, we examined the luminescent properties of Er-containing Al_2O_3 films with embedded Si nanoparticles. The luminescence spectra of the films under study were compared with the results earlier reported in [2], where similar Al_2O_3 films without Si nanoparticles were examined.

The samples under study were obtained by deposition of Al films on Si (100) wafers using magnetron sputtering of a specially prepared Al target. The areas of the Er_2O_3 and Si inserts were about 1 and 4% of the total sputtering area, respectively. Deposition was carried out at an anodic bias of 400 V and a current of 0.7 A in argon at a pressure of 0.1 Pa. The film thickness was 0.7 μm. The as-deposited films were anodized in a 2% aqueous solution of H_2SO_4 at a current density of 20 mA/cm^2 for 10 min, washed with deionized water, and dried at room temperature. As a result, we obtained 1-μm porous Al_2O_3 films. The elemental composition of the films was determined by depth profiling using secondary-ion mass spectroscopy (SIMS) (Cameca IMS-4f) and Auger spectroscopy (PHI-660 Perkin-Elmer). The obtained samples were divided into three groups. The samples in the first and second groups were annealed in the temperature range 100–1200°C for 15 min in vacuum and in air, respectively. The samples in the third group were not annealed.

Photoluminescence (PL) of the samples in all three groups was measured at 300, 78, and 4.2 K. The samples were pumped by a Xe lamp. The other details of the PL measurements can be found in [3].

Auger depth profiling of the prepared anodic films showed a uniform distribution of Si atoms over the film thickness (Fig. 1). The Si content was 2 at %. We have previously shown [4] that, during anodization of an Al–Si alloy, most of the Si atoms remain unoxidized because of the different anodization rates of Al

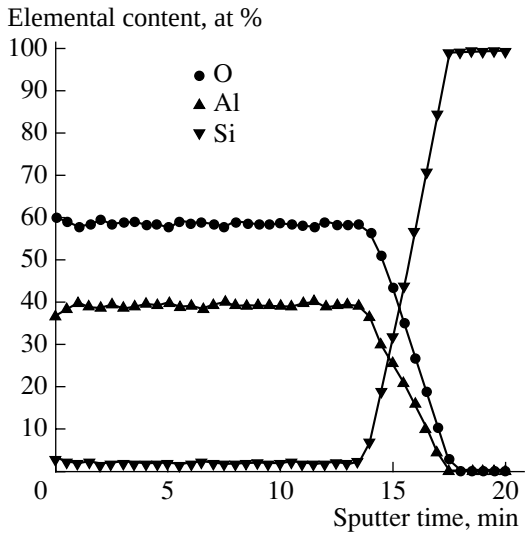

Fig. 1. Auger depth profiles of Al, Si, and O in an Al_2O_3 film with embedded Si nanoparticles.

1063-7826/05/3908-0891$26.00 © 2005 Pleiades Publishing, Inc.

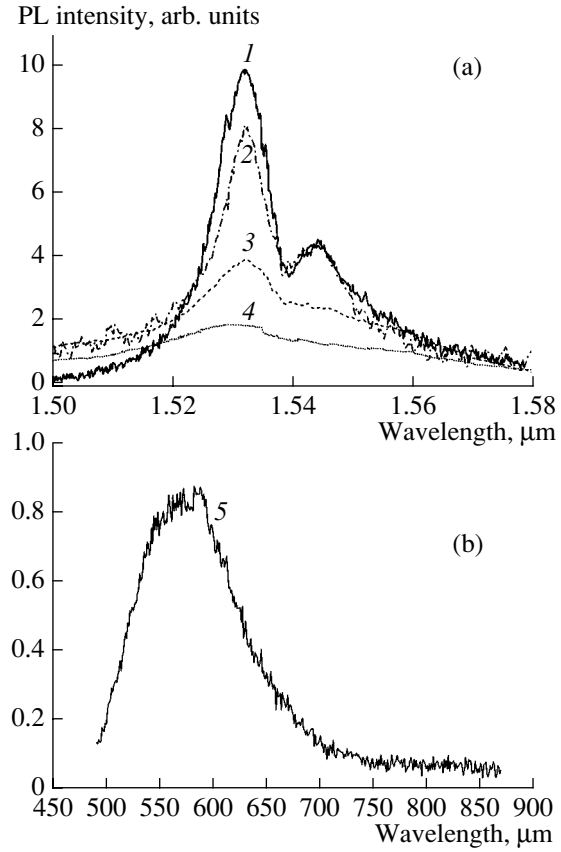

Fig. 2. (a) IR and (b) visible photoluminescence spectra of Er-doped Al_2O_3 films measured at (*1*) 4.2, (*2*) 78, and (*3*–*5*) 300 K. (*1*–*3*, *5*) Films with embedded Si nanoparticles and (*4*, data from [2]) without Si nanoparticles.

(1 nm/V) and Si (0.2 nm/V). It is this difference that is responsible for the formation of Si nanoparticles in the Al_2O_3 host. The distribution of Er atoms is not shown in Fig. 1 due to the limited resolution of the Auger analysis. Therefore, the Er content, 0.2 at %, was determined from the SIMS data.

Erbium-doped Al_2O_3 films with embedded Si nanoparticles show strong PL at a wavelength of 1.54 μm immediately after anodization. This fact means that high-temperature annealing is not necessary for optical activation of the Er atoms. The PL spectra of the films in the vicinity of 1.54 μm measured at 4.2, 78, and 300 K and the PL spectrum of a similar film without Si nanoparticles from [2] are shown in Fig. 2a. The shape and position of the peak are characteristic of internal 4*f* electron transitions in Er^{3+}, which were discussed in detail in [2]. The integrated intensity of the luminescence of the Er-doped Al_2O_3 films with embedded Si nanoparticles was found to be higher than that of the film without Si nanoparticles by a factor of 2–3. Figure 2b shows the PL spectrum of the Si nanoparticles in the Al_2O_3 host. The spectrum peaks in the yellow-orange range.

Anodic aluminum oxide consists of a polycrystalline γ-Al_2O_3 phase [5] with a highly nonideal lattice. This circumstance leads to the formation of impurity levels, which are related to the compositional inhomogeneity and structural defects of the material. An Al_2O_3 insulator host with defects in its anion sublattice contains so-called color centers (*F* centers). These centers consist of two oxygen vacancies that capture two electrons [6].

F centers are optically excited by UV photons. An excited *F* center relaxes into a steady state and emits a visible photon [7]. The PL measurements of the Er-doped anodic Al_2O_3 samples with embedded Si nanoparticles showed the presence of a wide strong luminescence band peaked at an energy corresponding to the transition of an *F* center from the first excited state to a steady state. The energy released during the relaxation of an *F* center is sufficient to transfer the inner 4*f* electron of the Er^{3+} ion to an excited state.

The spectra of silicon nanoparticles embedded into Al_2O_3 films contain a broad absorption band [8], which facilitates stronger optical absorption and generation of excitons in these films. The energy of the excitons depends on the nanocrystal size. The energy released during electron–hole recombination in a Si nanoparticle is sufficient to transfer an Er^{3+} ion to an excited state [9]. Excitons can recombine radiatively or, when an Er^{3+} ion is in immediate proximity to a nanocrystal, nonradiatively, thereby transferring the Er^{3+} ion to one of the possible excited states. The excess energy released during the Auger recombination is absorbed by free electrons and phonons [10]. In this process, the effective absorption cross section for Er^{3+} ions increases by several orders of magnitude as compared with the direct absorption of Er^{3+} ions in the insulator host. A schematic diagram of the excitation of an Er^{3+} ion is shown in Fig. 3.

Figure 4 shows PL intensity versus annealing temperature in the case of 15-min annealing in vacuum and in air. The PL intensity decreases in the temperature range 200–500°C, with subsequent recovery within 500–800°C.

It is well known that Er luminescence is observed at a wavelength of 1.54 μm when trivalent Er^{3+} ions possess an oxygen environment [1]. Therefore, the PL of materials implanted with Er and O ions can be observed only after high-temperature annealing, which leads to recrystallization of the amorphous layer and ordering of the Er atoms' oxygen environment [11]. We detected characteristic Er luminescence in the unannealed Er-doped Al_2O_3 films. This observation suggests that an oxygen environment is formed around the Er atoms during electrochemical anodization, as in the case of high-temperature processes.

A structural feature of the as-prepared Al_2O_3 films, in comparison with the annealed samples, is a higher content of OH groups [5]. It is these groups that are responsible for the optical activity of the Er atoms,

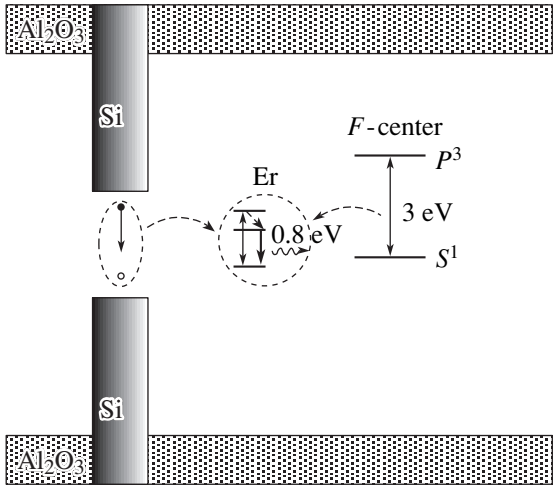

Fig. 3. Schematic diagram of the excitation of an Er^{3+} ion in an Al_2O_3 host with embedded Si nanoparticles.

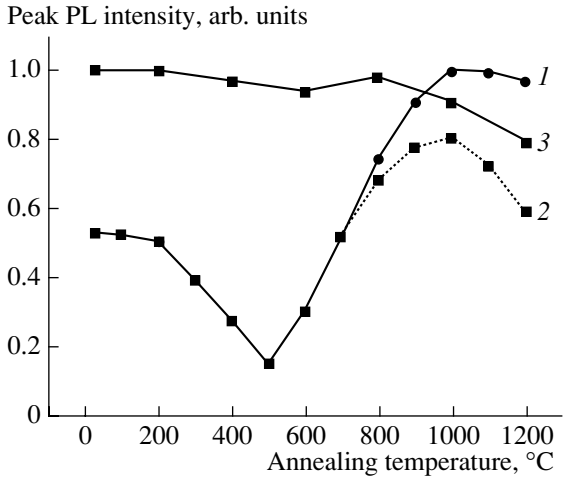

Fig. 4. Dependences of the room temperature PL intensity of the films under study on the annealing temperature: (*1*) peak at a wavelength of 1.54 μm, annealing in air; (*2*) peak at a wavelength of 1.54 μm, annealing in vacuum; and (*3*) peak at a wavelength of 580 nm, annealing in air.

which is confirmed by the observation of erbium PL at annealing temperatures as high as 200°C. Further annealing of Al_2O_3 in the temperature range 200–500°C changes the structure of this material. In this case, hydrogen diffuses from the Al_2O_3 films [5] and destroys the oxygen environment possessed by the Er atoms, which leads to a decrease in the PL intensity. At annealing temperatures of 500°C and higher, optically active Er–O clusters start to be formed and there is a corresponding recovery of the PL intensity.

The films annealed in air at temperatures above 800°C showed stronger PL than those annealed in vacuum due to the formation of a large number of optically active Er–O clusters. In this case, the decrease in the PL intensity in the samples annealed above 1000°C can be attributed to breaking of the Er–O bonds. Silicon nanoparticles demonstrate stable visible PL at annealing temperatures as high as 1000°C. However, at annealing temperatures above 1000°C, the PL intensity decreases, which can be attributed to the thermal oxidation of Si and decrease in the number of Si nanoparticles.

We showed that embedding of Si nanoparticles into Er-doped anodic aluminum oxide films enhances PL at a wavelength of 1.54 μm. Luminescence of optically active Er centers was observed in the as-prepared samples. The method developed can be used to fabricate waveguide amplifiers operating at 1.54 μm.

ACKNOWLEDGMENTS

This study was supported in part by INTAS, grant no. 03-51-6486.

REFERENCES

1. A. Polman, J. Appl. Phys. **82**, 1 (1997).
2. S. K. Lazarouk, A. V. Mudryi, and V. E. Borisenko, Appl. Phys. Lett. **73**, 2272 (1998).
3. V. D. Tkachev, A. V. Mudryi, and N. S. Minaev, Phys. Status Solidi A **81**, 313 (1984).
4. S. K. Lazarouk, A. A. Leshok, and V. E. Borisenko, Izv. Ross. Akad. Nauk, Ser. Fiz. **67** (2), 178 (2003).
5. L. Young, *Anodic Oxide Films* (Academic, New York, 1961; Énergiya, Moscow, 1967).
6. B. D. Evans, G. J. Pogatshnik, and Y. Chen, Nucl. Instrum. Methods Phys. Res. B **91**, 258 (1994).
7. V. S. Kortov, I. I. Mil'man, S. V. Nikiforov, and V. E. Pelenev, Fiz. Tverd. Tela (St. Petersburg) **45**, 1202 (2003) [Phys. Solid State **45**, 1260 (2003)].
8. P. D. J. Calcott, *Properties of Porous Silicon* (INSPEC, London, 1997), p. 204.
9. Y. H. Xie, E. A. Fitzgerald, and Y. J. Mii, J. Appl. Phys. **70**, 3223 (1991).
10. I. N. Yassievich, A. S. Moskalenko, O. B. Gusev, and M. S. Bresler, in *Proceedings of NATO Advanced Research Workshop on Towards the First Silicon Laser, Trento, Italy, 2002*, Ed. by L. Pavesi, S. Gaponenko, and L. Dal Negro (Kluwer Academic, Dordercht, 2003).
11. G. N. van den Hoven, E. Snoeks, A. Polman, *et al.*, Appl. Phys. Lett. **62**, 3065 (1993).

Translated by N. Korovin

Semiconductors, Vol. 39, No. 8, 2005, pp. 894–897. Translated from Fizika i Tekhnika Poluprovodnikov, Vol. 39, No. 8, 2005, pp. 931–934.

CONFERENCE.
ELECTRONIC AND OPTICAL PROPERTIES OF SEMICONDUCTORS

Nanostructuring of Crystalline Grains of Natural Diamond Using Ionizing Radiation

N. A. Poklonski*^, T. M. Lapchuk*, N. I. Gorbachuk*, V. A. Nikolaenko, and I. V. Bachuchin****

** Belarussian State University, pr. F. Skoriny 4, Minsk, 220050 Belarus*
^ e-mail: poklonski@bsu.by
*** Russian Research Center Kurchatov Institute, ul. Akademika Kurchatova 1, Moscow, 123182 Russia*
Submitted December 27, 2004; accepted for publication January 12, 2005

Abstract—Crystalline grains of type IIa natural diamond (the average grain mass is ~1 mg) are studied after their irradiation with neutrons in a nuclear reactor at a neutron fluence of ~10^{21} cm^{-2}. The irradiation is found to bring about a decrease in the macroscopic density of the grains by 40%. A quadrature signal of electron spin resonance (ESR) with a *g* factor equal to 2.00006 and a paramagnetic-relaxation time > 10^{-5} s is detected for the first time. Metastable uncompensated electron spins residing at the inner surface of the nanovoids may be the cause of the appearance of this signal. A similar signal is also observed for C_{60} fullerite powder. The results of an ESR spectroscopy study of the irradiated diamonds are consistent with data obtained from Raman scattering spectroscopy (the appearance of an anomalously broad band peaked at 950 cm^{-1} instead of a narrow single line at 1332 cm^{-1} in the initial sample) and electron microscopy (the appearance of nanostructuring). It is established that nanostructuring of diamond under the effect of ionizing radiation brings about the appearance of dc electrical conductivity with an activation energy of 0.17 eV in the temperature range 30 to 300°C. © *2005 Pleiades Publishing, Inc.*

1. INTRODUCTION

Diamond is a promising material for electronics; however, the uses of diamond are limited by the lack of acceptable doping technologies applicable to it in relation to the formation of *n*-type layers (see, for example, [1, 2]). Therefore, it is important to search for methods for controlling the electrical properties of diamond without affecting its chemical composition. According to Malinovskiĭ [3], spatial nanostructuring (inhomogeneity on a nanometer scale) is characteristic of various amorphous materials; i.e., periodicity in the arrangement of atoms, which is inherent in crystals, is retained only within several coordination shells. Nanoinhomogeneities are not separate formations; rather, they represent fragments (building blocks) of amorphous materials and glasses. This circumstance makes it possible to consider ionizing radiation, which gives rise to disordering of crystals (and, under some conditions, to ordering [4]), as a method for producing new nanostructured materials and device structures based on diamond. The aim of this study was to gain insight into the properties of crystalline grains of diamond exposed to high fluences of ionizing radiation in a nuclear reactor.

2. RESULTS AND DISCUSSION

1. We studied single-crystal grains of type IIa natural diamond (the average grain mass was 1 mg). The samples were irradiated in the nuclear reactor at the Russian Research Center, Kurchatov Institute. The neutron fluence was measured using activation detectors made of ^{54}Fe [5]. The temperature during irradiation was measured using isochronous annealing of diamond or silicon carbide [6]. The temperature of the samples in the course of irradiation was maintained at about 100°C.

Expansion of the diamond samples was evaluated from the radiation-induced variation in its density $|\Delta\rho/\rho_0|$, where $\rho_0 = 3.55$ g/cm^3 is the density of unirradiated diamond and $\Delta\rho = \rho - \rho_0 < 0$ is the decrease in the density (expansion) as a result of irradiation. In order to measure $|\Delta\rho/\rho_0|$, we used the thermogradient tube method [7]; the error in determination of $|\Delta\rho/\rho_0|$ amounted to 1%. We studied the initial diamond grains and those irradiated with a neutron fluence of ~10^{21} cm^{-2} and found the radiation-induced expansion to be $|\Delta\rho/\rho_0| \approx 40\%$.

2. An electron microscopy (EM) image of the cleaved surface of the irradiated diamond was obtained using an LEO 1455 VP scanning electron microscope (the electron energy was 20 keV and the current through the sample was 20 pA) and is shown in Fig. 1. The EM image of the cleaved surface of the unirradiated diamond is shown in the inset (in the middle of the panel). The change in the morphology of the cleaved diamond surface (appearance of a flawed surface) is indicative of radiation-stimulated change in the diamond structure on a nanometer scale.

1063-7826/05/3908-0894$26.00 © 2005 Pleiades Publishing, Inc.

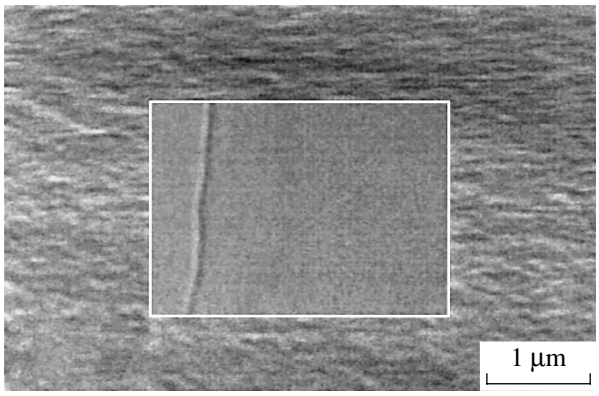

Fig. 1. Electron microscopy image of the cleaved surface of diamond irradiated in a nuclear reactor with a ~10^{21} cm^{-2} fluence of neutrons. The image of the cleaved surface of the initial (unirradiated) diamond is shown in the inset (in the center of the panel).

3. Measurements of the electron spin resonance (ESR) were carried out in an H_{102} resonator at a frequency of 9.3 GHz of microwave radiation with a power as high as 70 mW. The polarizing magnetic field was modulated with a frequency of 100 kHz. The ESR spectra of the samples were measured at room temperature. ESR signals were not observed for the initial (unirradiated) diamond grains. In the ESR spectrum of the irradiated samples (Fig. 2a), both an in-phase signal (the reference-voltage phase and ESR signal phase at the synchronous detector input coincide, $\varphi = 0°$) and a quadrature signal (the reference-voltage and the ESR-signal phase differ by $\varphi = 90°$) were observed. This observation is indicative (according to [8]) of the presence of paramagnetic centers that have comparatively long (>10^{-5} s) relaxation times. It is worth noting that signal *3* (Fig. 2a), which had a *g* factor of 2.00006 and width $\Delta B_3 = 0.06$ mT, was detected for the first time in the ESR spectrum of the irradiated diamond samples at $\varphi = 90°$.

Under the same conditions of measuring the ESR spectra, we studied high-purity (>99%) C_{60} fullerite powders extracted from carbon black using toluene. The carbon black was obtained by evaporating graphite in an electric arc [9]. According to Shpilevskiĭ [10], C_{60} fullerite powder obtained using this method consists of crystalline grains with sizes of ~1–5 μm. We detected two types of lines in the ESR spectra of the fullerite powders in air (Fig. 2b): line *1* was in phase ($\varphi = 0°$) with the field of high-frequency (100 kHz) modulation of the polarizing magnetic field and line *2* in quadrature ($\varphi = 90°$). The width of the line for the in-phase (*1*) signal was equal to $\Delta B_1 = 0.125$ mT with $g_1 = 2.00236$. Simultaneously with line *2*, we observed another signal (*3*) with a *g* factor $g_3 = 2.00002$ and linewidth $\Delta B_3 = 0.06$ mT (Fig. 2b). It is noteworthy that the ESR lines (with $g_1 = 2.0023$ and $g_3 = 2.000$) were related to fullerene C_{60} (see, for example, [11]).

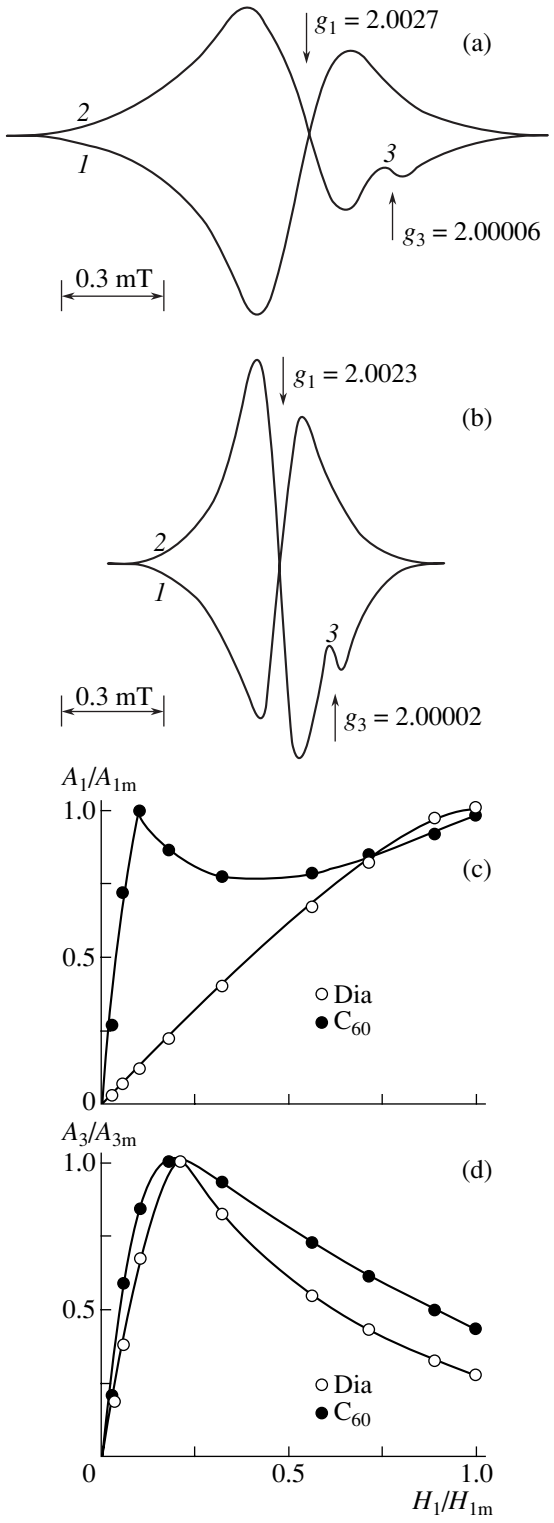

Fig. 2. (a) The ESR spectra of a sample ($|\Delta\rho/\rho_0| \approx 40\%$) of type II*a* natural diamond with a mass of 1 mg; (b) the ESR spectrum of a C_{60} fullerite powder with a mass of 2 mg for (*1*) $\varphi = 0°$ and (*2*, *3*) $\varphi = 90°$ (measurements at a temperature of $T \approx 300$ K and at $H_1/H_{1m} = 0.5$); and (*c*, *d*) dependences of amplitudes A_1 and A_3 (normalized to maximum values A_{1m} and A_{3m}) of signals *1* and *3* for the diamond (Dia) and C_{60} fullerite powder on the strength H_1 of the microwave-field magnetic component with measurements at (c) $\varphi = 0°$ and (d) $\varphi = 90°$. The value of H_{1m} corresponds to a microwave power of 70 mW.

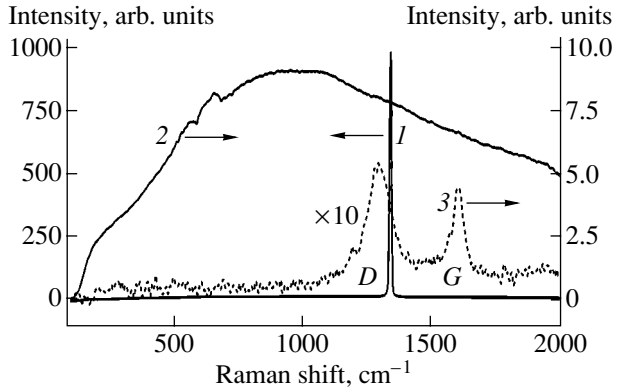

Fig. 3. The Raman spectra (measured at a temperature of 80 K) for (*1*) the initial diamond, (*2*) diamond after irradiation, and (*3*) schungite (the carbon content 98 wt %; the Raman signal intensity is increased by a factor of 10).

We studied the dependences of the ESR signal amplitudes on the microwave-radiation power for the irradiated diamond grains and for the fullerite C_{60} powder. We preliminarily established that the width, intensity, and *g* factor of the ESR signals were not affected by exposure of the samples to vacuum with a pressure as low as 10^{-2} Torr or by annealing for 30 min at 200°C in air. In Figs. 2c and 2d, we show the dependences of amplitudes A_1 and A_3 of signals *1* and *3* for the irradiated diamond (Fig. 2a) and C_{60} fullerite powder (Fig. 2b) on the strength H_1 of the microwave-field magnetic component in an H_{102} resonator. It can be seen that the characteristics of saturation of the paramagnetic centers responsible for the lines with *g* factors $g_3 = 2.00006$ (for a grain of natural diamond irradiated in a reactor) and $g_3 = 2.00002$ (for fullerite C_{60} powder) coincide only for the quadrature ESR signal (cf. Figs. 2c and 2d).

Thus, both in the irradiated diamond and C_{60} fullerite powder, we observe paramagnetic centers with relatively long (>10^{-5} s) relaxation times [12], nearly coinciding *g* factors and linewidths, and similar characteristics for the dependences of the signal *3* amplitudes on the strength H_1 of the magnetic component of the microwave field. A possible cause of the appearance of line *3*, related to paramagnetic centers with relatively long relaxation times (>10^{-5} s), both in the irradiated diamond and C_{60} fullerite powder may be uncompensated electron spins that reside at the inner surface of nananovoids [13] in the irradiated diamond and inside the carbon cage in separate C_{60} molecules (or in voids in the fullerite powder grains).

The hypothesis that there are uncompensated electron spins at the surface of nanovoids in irradiated diamond grains is confirmed by the fact that only the paramagnetic centers responsible for line *3* in Fig. 2a are metastable. After the resonance was repeatedly (about 30 times) attained, line *3* was no longer observed in the ESR spectra of either the irradiated diamond or the C_{60} fullerite powder. This circumstance could be caused by a rearrangement of the spin system that forms line *3*, which results from relaxation (stimulated by ESR measurements) of the elastic-stress fields [14] in the irradiated diamond. Poklonskiĭ *et al*. [15] reported an increase (by several hundred times) in the rate of this rearrangement of the spin system when ESR was measured in porous structures.

4. Raman scattering in the diamond grains was excited by a Nd:YAG laser (the wavelength was λ = 1064 nm and the radiation power was varied from 30 to 500 mW). The Raman spectra were detected in the backscattering geometry at 80 K.

In Fig. 3, we show the Raman spectra of the (*1*) initial and (*2*) irradiated diamond samples and, also, for comparison, (*3*) the spectra of a natural nanostructured material (schungite). As follows from Fig. 3, the change in the diamond structure as a result of irradiation manifests itself in the appearance of an anomalously broad band with a peak at 950 cm^{-1} and the disappearance of a narrow separate line at 1332 cm^{-1} in the Raman spectrum. The presence of the *D* and *G* bands in the Raman spectra is characteristic of carbon-containing nanostructured materials with clusters of graphene layers and sp^2-hybridized bonds (see, for example, [16–18]). These materials include schungite (Fig. 3, spectrum *3*) and ultradisperse diamond samples. It is worth noting that traces of natural C_{60} fullerenes have been found in schungite [19]. The *G* and *D* bands in the Raman spectra of nanoporous carbon and in the spectra of amorphous hydrogenated carbon are typically not separated; a single broad band has a peak in the range of 1300–1600 cm^{-1}. As far as we know, the peaks of the broad Raman bands for the above materials are not located in the vicinity of 950 cm^{-1}. However, a number of bands [11, 20] have been observed in the range 300 to 1000 cm^{-1} in the Raman spectra of fullerites and carbon nanotubes. Therefore, the shift of the peak in spectrum *2* to the vicinity of 950 cm^{-1} is probably caused by the presence of nanostructures (or nanovoids) with distorted graphene planes in the bulk of the irradiated diamond. Novgorodova [21] showed that defects with distorted graphene planes could be formed.

5. The dc electrical conductivity was measured using the conventional method. Electrical contacts to the diamond grains were formed by depositing a silver paste. The diamond grains became conducting only after irradiation in the reactor. The electrical-conductivity activation energy for diamond (with expansion $|\Delta\rho/\rho_0| \approx 40\%$) was equal to 0.17 eV in the temperature range 30–300°C. Apparently, this thermal activation energy is caused by manifestation of hopping transport of electrons via intrinsic radiation defects [22] as a result of pinning of the Fermi level at these defects [23].

3. CONCLUSIONS

Irradiation of grains of type IIa natural diamond in a nuclear reactor with a neutron fluence of ~10^{21} cm^{-2} brings about not only a decrease in the density by 40% but also a change in the morphology of the cleaved surface (appearance of inhomogeneities on a nanometer scale). Radiation-induced rearrangement of the diamond-grain structure is accompanied by (i) the appearance of a quadrature ESR signal (g_3 = 2.00006) that can be attributed to metastable paramagnetic centers with paramagnetic relaxation times > 10^{-5} s; (ii) the appearance of an anomalously broad band peaked at 950 cm^{-1} in the Raman spectrum and the disappearance of a single narrow line at 1332 cm^{-1}; and (iii) the transition of the diamond grains to a conducting state with an activation energy of 0.17 eV for dc electrical conductivity in the temperature range 30 to 300°C.

REFERENCES

1. S. K. Iton, Yu. E. Evstefeeva, Dzh. K. Éngus, *et al.*, Élektrokhimiya **39**, 170 (2003).
2. V. S. Vavilov, Usp. Fiz. Nauk **167** (1), 17 (1997) [Phys. Usp. **40**, 15 (1997)].
3. V. K. Malinovskiĭ, Fiz. Tverd. Tela (St. Petersburg) **41** (5), 805 (1999) [Phys. Solid State **41**, 725 (1999)].
4. I. P. Chernov, A. A. Mamontov, P. A. Cherdantsev, and B. V. Chakhlov, Izv. Vyssh. Uchebn. Zaved., Fiz. **37** (12), 58 (1994).
5. S. M. Zaritsky, P. A. Platonov, Yu. A. Nikolaev, *et al.*, in *Reactor Dosimetry: Radiation Metrology and Assessment* (American Society for Testing and Materials, West Conshohocken, PA, 2001), ASTM STP 1398, p. 53.
6. V. A. Nikolaenko and V. I. Karpukhin, *Temperature Measurements with the Help of Irradiated Materials* (Énergoatomizdat, Moscow, 1986) [in Russian].
7. M. Ya. Kats, *New Methods for Studying Minerals in a Gravitation Field* (Nauka, Moscow, 1966) [in Russian].
8. J. R. Harbridge, G. A. Rinard, R. W. Quine, *et al.*, J. Magn. Reson. **156** (1), 41 (2002).
9. V. D. Shimanovich, A. I. Zolotovskiĭ, I. P. Smyaglikov, and S. M. Pankovets, Zh. Prikl. Spektrosk. **68** (3), 393 (2001).
10. É. M. Shpilevskiĭ, in *Diamond Films and Films of Related Materials* (NNTs Khark. Fiz.-Tekh. Inst., Kharkov, 2003), p. 242 [in Russian].
11. C. A. Reed and R. D. Bolskar, Chem. Rev. **100** (3), 1075 (2000).
12. N. A. Poklonskiĭ, T. M. Lapchuk, and N. M. Lapchuk, in *Proceedings of IV International Conference on Amorphous and Microcrystalline Semiconductors, St. Petersburg, 2004* (Fiz.–Tekh. Inst. Ross. Akad. Nauk, St. Petersburg, 2004), p. 91.
13. É. L. Nagaev, Zh. Éksp. Teor. Fiz. **100**, 961 (1991) [Sov. Phys. JETP **73**, 530 (1991)].
14. R. B. Morgunov, Usp. Fiz. Nauk **174** (2), 131 (2004) [Phys. Usp. **47**, 125 (2004)].
15. N. A. Poklonskiĭ, I. V. Pototskiĭ, and N. I. Gorbachuk, in *Proceedings of IV International Conference on Amorphous and Microcrystalline Semiconductors, St. Petersburg, 2004* (Fiz.–Tekh. Inst. Ross. Akad. Nauk, St. Petersburg, 2004), p. 151.
16. S. V. Kholodkevich, V. I. Berezkin, and V. Yu. Davydov, Fiz. Tverd. Tela (St. Petersburg) **41** (8), 1412 (1999) [Phys. Solid State **41**, 1291 (1999)].
17. A. M. Danishevskiĭ, É. A. Smorgonskaya, S. K. Gordeev, and A. V. Grechinskaya, Fiz. Tverd. Tela (St. Petersburg) **43** (1), 132 (2001) [Phys. Solid State **43**, 137 (2001)].
18. A. E. Aleksenskiĭ, M. V. Baĭdakova, A. Ya. Vul', *et al.*, Fiz. Tverd. Tela (St. Petersburg) **39** (6), 1125 (1997) [Phys. Solid State **39**, 1007 (1997)].
19. V. A. Reznikov and Yu. S. Polekhovskiĭ, Pis'ma Zh. Tekh. Fiz. **26** (15), 94 (2000) [Tech. Phys. Lett. **26**, 689 (2000)].
20. P. J. Horoyski, M. L. W. Thewalt, and T. R. Anthony, Phys. Rev. B **54** (2), 920 (1996).
21. M. I. Novgorodova, Dokl. Akad. Nauk **367** (2), 241 (1999).
22. R. Coates and E. W. J. Mitchell, Adv. Phys. **24** (5), 593 (1975).
23. V. N. Brudnyi, S. N. Grinyaev, and V. E. Stepanov, Physica B (Amsterdam) **212** (4), 429 (1995).

Translated by A. Spitsyn

Semiconductors, Vol. 39, No. 8, 2005, pp. 898–903. Translated from Fizika i Tekhnika Poluprovodnikov, Vol. 39, No. 8, 2005, pp. 935–939.

CONFERENCE.
ELECTRONIC AND OPTICAL PROPERTIES OF SEMICONDUCTORS

Permittivity Spectra and Characteristic Energy Losses of Electrons in ZnO at 100 K

V. Val. Sobolev*^, V. V. Sobolev*, and E. I. Terukov**

** Udmurt State University, Krasnoarmeĭskaya ul. 71, Izhevsk, 426034 Russia*

^ e-mail: sobolev@uni.udm.ru

*** Ioffe Physicotechnical Institute, Russian Academy of Sciences, Politekhnicheskaya ul. 26, St. Petersburg, 194021 Russia*

Submitted December 27, 2004; accepted for publication January 12, 2005

Abstract—For the first time, full sets of fundamental optical functions have been obtained for zinc oxide in the range 0–30 eV at 100 K for **E** ⊥ **c** and **E** || **c** polarizations. Spectra of the transverse and longitudinal components of transitions and their basic parameters (peak energies E_i, half-widths H_i of transition bands, band areas S_i, and oscillator strengths f_i) have also been determined for the first time. The calculations are performed using synchrotron experimental reflectance spectra. The main features of spectra of the optical functions and components of transitions are established. These features are compared to the results of known theoretical calculations of the bands and spectra of optical functions. © *2005 Pleiades Publishing, Inc.*

1. INTRODUCTION

Zinc oxide exhibits unique piezo- and pyroeffects, high fusion temperature and heat conductivity, and high direct-transition energy ($E_{gd} \approx 3.3$ eV) [1]. It crystallizes in a wurtzite structure (C_{6V}^4, $z = 2$), with a polar axis c parallel to the [0001] direction. The Zn3*d* valence bands are located close to the uppermost valence bands. This circumstance leads to an appreciable hybridization of the O2*p* and Zn3*d* states and to a more complex structure of bands than is known for other II–VI compounds [1–3].

The purpose of this study was to obtain and theoretically analyze new information on the spectra of optical functions and the structure of elementary transitions in ZnO crystals in a wide energy range of fundamental absorption.

2. CALCULATION METHODS

In order to carry out this task, we first obtained the spectra of full sets of fundamental optical functions: the absorption coefficient (μ), indices of refraction (n) and absorption (k), imaginary (ε_2) and real (ε_1) parts of the permittivity (ε), functions for the characteristic volume ($-\mathrm{Im}\varepsilon^{-1}$) and surface ($-\mathrm{Im}(1 + \varepsilon)^{-1}$) energy losses of electrons, etc. [4]. They were calculated using integral Kramers–Kronig relations and analytical formulas based on experimental reflectance spectra $R(E)$.

The calculated permittivity spectra (ε_1 and ε_2) and energy losses ($-\mathrm{Im}\varepsilon^{-1}$ of electrons and $\mathrm{Re}\varepsilon^{-1}$) were then decomposed into elementary transverse and longitudinal components using integral Argand diagrams, for which we determined the following basic parameters: peak energies E_i, band half-widths H_i, band areas S_i proportional to the transition probabilities, and oscillator strengths f_i.

The methods used to calculate the set of optical functions and the decomposition of the integral spectra of optical functions into components have previously been described in detail and frequently applied [4–7].

For ZnO, the polarization reflectance spectra $R(E)$ are known for the orientations of the wave electric vector **E** ⊥ **c** and **E** || **c** at 100 K in the energy range E = 0–25 eV [8]. From these spectra, we calculated the spectra of the complete set of optical functions for the polarizations **E** ⊥ **c** and **E** || **c**. For brevity, we show only the spectra of ε_1, ε_2, μ, $-\mathrm{Im}\varepsilon^{-1}$, and $-\mathrm{Im}(1 + \varepsilon)^{-1}$ in the figure.

The experimental spectra $R(E)$ contain narrow peaks at 3.24 eV (**E** ⊥ **c**) and 3.35 eV (**E** || **c**), broad peaks of almost nonpolarized radiation at 8.7 eV (**E** ⊥ **c**) and 8.8 eV (**E** || **c**), and a peak of strongly polarized radiation at 11.15 eV (**E** || **c**), which is observed in the **E** ⊥ **c** polarization as a step. Furthermore, in the range 12–18 eV, there is a very broad band that has its most intense almost nonpolarized peak at 15.2 eV, a peak at 12.65 eV (**E** ⊥ **c**), and steps at ~13.7 and 16.8 eV (**E** ⊥ **c**); in addition, a weak broad peak is observed at ~21.0 eV (**E** || **c**).

3. CALCULATION OF THE SETS OF OPTICAL FUNCTIONS AND DISCUSSION

In the calculated (experimental–calculated) spectra of the remaining optical functions, analogues of peaks and steps are also observed in $R(E)$ but with different distributions of the relative intensity and with various shifts in energy. The $R(E)$ peaks in the $\varepsilon_2(E)$ spectrum located at the longest wavelengths shifted to higher

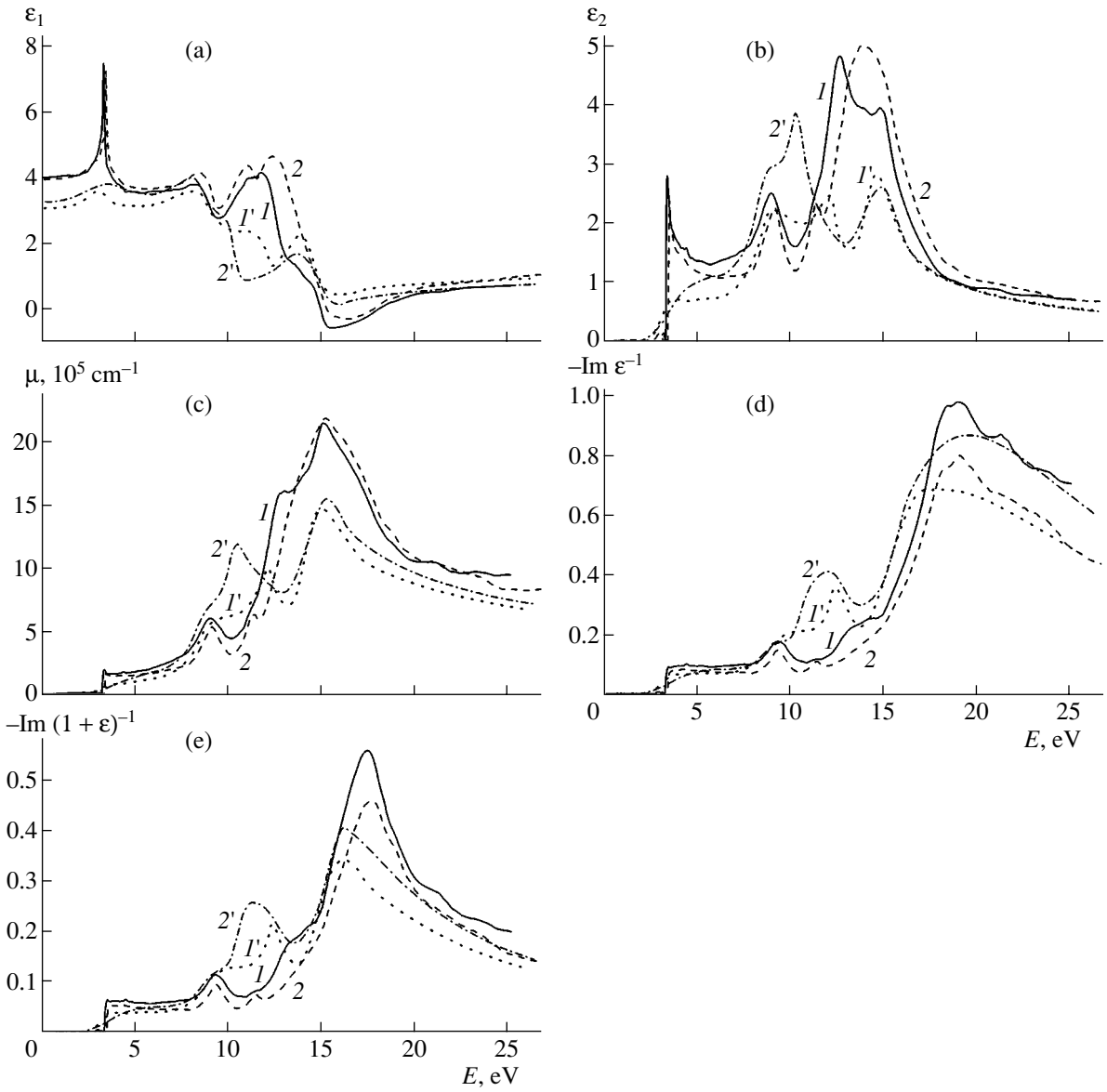

Fig. 1. Spectra of (a) ε_1, (b) ε_2, (c) μ, (d) $-\mathrm{Im}\varepsilon^{-1}$, and (e) $-\mathrm{Im}(1+\varepsilon)^{-1}$ calculated for ZnO crystals on the basis of (*1*, *2*) experimental [8] and (*1'*, *2'*) theoretical [11] $R(E)$ spectra (*1*, *1'*) for $\mathbf{E} \perp \mathbf{c}$ and (*2*, *2'*) for $\mathbf{E} \parallel \mathbf{c}$.

energies by ~0.04 ($\mathbf{E} \perp \mathbf{c}$) and 0.05 eV ($\mathbf{E} \parallel \mathbf{c}$). The $R(E)$ peaks at ~8.7 eV shifted by ~0.07 ($\mathbf{E} \perp \mathbf{c}$) and 0.2 eV ($\mathbf{E} \parallel \mathbf{c}$), the step at ~11.10 eV ($\mathbf{E} \perp \mathbf{c}$) in the $\varepsilon_2(E)$ spectrum was barely observable, and the energy of the $R(E)$ peak at ~11.15 eV ($\mathbf{E} \parallel \mathbf{c}$) increased only by ~0.05 eV. The peak at 12.65 eV ($\mathbf{E} \perp \mathbf{c}$) shifted to lower energies by ~0.1 eV, the peaks at ~13.7 eV shifted by ~0.1 eV, and the peak energy at ~15.2 eV decreased by ~0.5 eV. Almost all the absorption peaks shifted to higher energies by ~(0.1–0.5) eV.

In the $\varepsilon_1(E)$ spectra, the $R(E)$ peaks at the longest wavelengths were observed at ~3.3 eV almost without any shift, while the energies of all the other peaks increased by ~(0.5–1) eV.

All the peaks in the spectra of characteristic energy losses of electrons shifted, with respect to the $\varepsilon_2(E)$ peaks, to higher energies by ~0.1 eV (for 3.3 eV) and by 0.2–0.5 eV (in the range 9–15 eV). None of the high-energy peaks observed in the loss spectra at ~18.3, 19.0, 21.3, and 23.4 eV were observed in the permittivity spectra. This circumstance is due to certain characteristic features of the ε_2 and $-\mathrm{Im}\varepsilon^{-1}$ spectra: the $\varepsilon_2(E)$ intensity in the range of $E > 15$ eV decreases drastically; in contrast, the $-\mathrm{Im}\varepsilon^{-1}$ function is most intense in this energy range.

According to the generally accepted models, all the peaks and steps of the fundamental optical functions of ZnO crystals result from direct band-to-band transitions or metastable excitons. The peaks at the longest

wavelengths are related to free excitons. A high spectral resolution enables us to observe the triplet structure of these peaks, which can be attributed to the triplet structure of the upper valence band [1–3].

The ZnO bands were theoretically considered in [9–14]. The results of these studies, which concerned the structure of the bands, are generally in agreement but significantly differ in relation to the width of the upper valence band, the Zn3*d*-band position, the E_{gd} value, and the band dispersion. Therefore, it is natural that there is a dramatic difference in the data on the intensity and energy of the transition bands.

In certain studies, a semiquantitative explanation of the nature of the $R(E)$ or $\varepsilon_2(E)$ peaks was suggested, according to which the entire energy range should be divided into 5–6 regions. The long-wavelength spectral peaks at ~3.3 eV are caused by free excitons. The other peaks (at ~8.8, 11.0, 12.5, 13.8, 14.7, and 16.0–22.0 eV) are associated with transitions in the directions U ($U_1 \longrightarrow U_1$ and U_4 at ~9 eV), in the Brillouin-zone volume (12–13 eV), from the Zn3*d* bands to the second group of conduction bands (14–15.5 eV), and from bonding valence *p* bands to the antibonding conduction *p* bands (17–21 eV) [9]; with the transitions $M_2 \longrightarrow M_1$, $H_3 \longrightarrow H_3$ (9.2 eV), $\Gamma_5 \longrightarrow \Gamma_6$ (11.9 eV), $M_3 \longrightarrow M_4$, and $\Gamma_5 \longrightarrow \Gamma_5$ (13.0–13.7 eV) [10]; and with transitions near the points M (~8.0, 15.5 eV) and in the directions U (10.5 eV) and M–Γ (12 eV) [11].

The polarization reflectance spectra of ZnO in the range 0–18 eV were calculated theoretically in [10, 11]. The data presented in [10] dramatically differ from the experimental spectra [8], while the results of the other calculation [11] are very close to the experimental data [8]. Therefore, on the basis of the theoretical $R(E)$ spectra from [11], we calculated the polarization spectra of all the remaining optical functions, some of which are shown in Fig. 1.

The peak at the longest wavelength in the experimental reflectance curves for $\mathbf{E} \perp \mathbf{c}$ and $\mathbf{E} \parallel \mathbf{c}$ and the spectra of the other functions calculated (experimental–calculated) from them are caused by free excitons. Therefore, this peak should be absent in the theoretical spectra of optical functions obtained using the bands.

It follows from direct comparison of the ε_2 spectra that the theoretical calculations reproduce the experimental–calculated curves well only for the peaks at 8.8 and 14.7 eV. However, the most intense peak, at 3 eV, for $\mathbf{E} \perp \mathbf{c}$ is not observed in them, and the theoretical peak at ~10 eV takes the minimum position in the experimental–calculated spectra. Similar features are also observed in the spectra of the other optical functions.

The noted considerable distinctions between the theoretical and experimental–calculated spectra of the optical functions of ZnO crystals in a wide energy range of fundamental absorption are caused mainly by errors in the theoretical calculations of the bands in [11].

4. RESULTS OF DECOMPOSITION OF THE ε_2 AND $-\mathrm{Im}\varepsilon^{-1}$ SPECTRA INTO TRANSVERSE AND LONGITUDINAL COMPONENTS

The fundamental problem of determining a complete set of the most intense bands and their basic parameters is known in all fields of spectroscopy (optical, nuclear, etc.) [4, 15]. In the general case, when there is a spectral curve for only one arbitrary function, this problem is considered as mathematically incorrect (i.e., it has many solutions). In optical spectroscopy, the methods used to reproduce the spectrum of the integral reflectance curve $R(E)$ or the imaginary part $\varepsilon_2(E)$ of the permittivity with sets of N Lorentz oscillators with a very large number ($3N$) of adjustable parameters are widely employed. Sometimes, the spectrum of the real part $\varepsilon_1(E)$ of the permittivity is known in addition to $\varepsilon_2(E)$. In this case, combined use of the $\varepsilon_2(E)$ and $\varepsilon_1(E)$ spectra enables us to apply the method of integral Argand diagrams and to unambiguously decompose (not reproduce!), without adjustable parameters, the $\varepsilon_2(E)$ spectrum into transverse components and to determine their parameters [4, 15]. The longitudinal components of transitions manifest themselves in the $-\mathrm{Im}\varepsilon^{-1}$ and $\mathrm{Re}\varepsilon^{-1}$ spectra of characteristic losses [16]. The method for determining their parameters is similar to that used in the case of transverse components of transition bands.

The main results of the decomposition of $\varepsilon_2(E)$ and $\mathrm{Im}\varepsilon^{-1}$ into components are listed in Tables 1 and 2. In total, we found 24 components in the range 2–30 eV. The most intense and broad components (16') of volume characteristic losses are caused by the excitation of plasmons. The energy of the band peak is independent of the polarization, but the intensity is more than ~1.33 times higher for $\mathbf{E} \perp \mathbf{c}$ than for $\mathbf{E} \parallel \mathbf{c}$. Naturally, plasmons do not manifest themselves in the $\varepsilon_2(E)$ spectra.

15 different components are primarily observed in the remaining 23 components in the polarization spectra of ε_2 and $\mathrm{Im}\varepsilon^{-1}$. Only for one polarization did we find 12 components: 1, 3′, 4, 6, and 19 (ε_2, $\mathbf{E} \perp \mathbf{c}$); 4, 6, 9, 19, and 17′ ($\mathrm{Im}\varepsilon^{-1}$, $\mathbf{E} \perp \mathbf{c}$); 2, 3, 5, 7, 8, 15′, and 20 (ε_2, $\mathbf{E} \parallel \mathbf{c}$); and 3, 5, 7, 8, 15′, and 20 ($\mathrm{Im}\varepsilon^{-1}$, $\mathbf{E} \parallel \mathbf{c}$). The other seven components are strongly polarized: $S_i(\mathbf{E} \perp \mathbf{c})/S_i(\mathbf{E} \parallel \mathbf{c}) = 3.0$ (9), 3.1 (11), 1.7 (15), 0.4 (10), 0.26 (12), 0.54 (16), and 0.30 (18). From this analysis, it follows that almost all the components of the transitions are strongly polarized. The relations between the component-band areas (we denote their ratio as $S_\perp/S_\parallel$) are as follows: the areas under the bands of the transverse components can exceed those of the longitudinal analogues by ~7–34 times (1, 3–13) for both polarizations, can be ~2–10 times smaller (17, 18), or are almost identical $S_\perp \approx S_\parallel$ (15, 16, 20). This observation indicates that the probability of excitation of the transverse components essentially exceeds that of their longitudinal analogues in a wide range of transition energies.

Table 1. Peak energies E_i, half-widths H_i, and band amplitudes I_i of the transverse (ε_2) and longitudinal ($-\mathrm{Im}\varepsilon^{-1}$) components of the transitions in ZnO crystals

No.	E_i				H_i				I_i			
	E ⊥ c		**E ∥ c**		**E ⊥ c**		**E ∥ c**		**E ⊥ c**		**E ∥ c**	
	ε_2	$-\mathrm{Im}\varepsilon^{-1}$	ε_2	$-\mathrm{Im}\varepsilon^{-1}$	ε_2	$-\mathrm{Im}\varepsilon^{-1}$	ε_2	$-\mathrm{Im}\varepsilon^{-1}$	ε_2	$-\mathrm{Im}\varepsilon^{-1}$	ε_2	$-\mathrm{Im}\varepsilon^{-1}$
1	3.28	3.57	–	–	0.25	0.45	–	–	1.44	0.08	–	–
2	–	–	3.40	–	–	–	0.20	–	–	–	1.30	–
3'	3.58				0.72		–	–	0.86	–	–	–
3			3.70	3.70			0.80	0.66	–	–	1.05	0.08
4	4.34	4.42	–		1.4	1.20	–	–	0.80	0.09	–	–
5	–	–	4.70	4.90	–	–	1.7	1.20	–	–	0.65	0.09
6	6.20	6.10	–	–	3.1	1.60	–	–	0.85	0.09	–	–
7	–	–	6.70	6.70	–	–	3.2	1.60	–	–	0.75	0.08
8	–	–	8.40	8.0	–	–	1.5	0.80	–	–	0.38	0.04
9	8.80	9.3	9.00	9.3	2.3	1.2	1.0	1.3	1.84	0.16	1.40	0.15
10	11.1	11.4	11.2	11.4	1.2	1.1	1.6	1.3	0.56	0.10	1.04	0.10
11	12.5	12.7	12.9	12.9	1.8	1.0	1.6	1.2	3.80	0.13	1.42	0.09
12	13.7	13.7	13.7	13.8	1.4	1.2	2.0	1.2	1.24	0.18	3.33	0.11
13	14.7	14.7	15.0	15.0	1.6	1.3	1.8	1.3	2.43	0.17	1.95	0.19
14	16.0	16.0	15.5	–	1.9	1.3	1.9	–	0.97	0.31	0.90	–
15'	–	–	16.4	16.3	–	–	1.2	1.3	–	–	0.84	0.27
15	17.2	17.3	17.5	17.5	2.0	1.4	1.0	1.4	0.39	0.50	0.47	0.31
16	18.7	18.4	18.7	18.3	1.7	1.3	1.7	1.7	0.28	0.47	0.52	0.33
16'	–	19.1	–	19.1	–	1.6	–	1.6	–	0.60	–	0.44
17'	–	20.1	–	19.7	–	1.1	–	1.6	–	0.40	–	0.20
17	20.7	21.5	20.9	20.9	2.9	1.8	3.2	1.6	0.51	0.66	0.60	0.43
18	22.9	23.4	23.4	23.7	2.0	2.9	2.9	2.8	0.17	0.57	0.37	0.45
19	25.1	25.1	–	–	4.9	2.0	–	–	0.50	0.45	–	–
20	–	–	26.8	26.8	–	–	4.2	3.6	–	–	0.55	0.39

Note: Energies are given in eV.

The established components produced by decomposition of the ε_2 and $\mathrm{Im}\varepsilon^{-1}$ spectra result from direct interband transitions or metastable excitons, except for the case of the long-wavelength components related to free excitons.

Theoretical calculations of the ZnO bands [9–14] yield results that dramatically differ with regard to the dispersion and mutual disposition of the bands. This fact complicates the choice of schematic diagram for the specific and unambiguous relation between the found components and the transitions between band pairs. It is generally accepted that the most intense transitions are expected between band pairs that are covariant in the largest area of the Brillouin zone [4]. We used this simplified model for estimating the energies of such transitions in the vicinity of the point Γ and at the points of intersection of the directions Δ, *U*, and *S* for

Table 2. Band areas S_i, oscillator strengths f_i, and ratios $S_i(\varepsilon_2)/S_i(-\mathrm{Im}\varepsilon^{-1})$ for $\mathbf{E} \perp \mathbf{c}$ ($S_\perp$) and $\mathbf{E} \parallel \mathbf{c}$ ($S_\parallel$) in ZnO crystals, and theoretical energies E_i of the transitions and their localization

No.	S_i				f_i		$S_\perp$	$S_\parallel$	E_i
	$\mathbf{E} \perp \mathbf{c}$		$\mathbf{E} \parallel \mathbf{c}$		$\mathbf{E} \perp \mathbf{c}$	$\mathbf{E} \parallel \mathbf{c}$			
	ε_2	$-\mathrm{Im}\varepsilon^{-1}$	ε_2	$-\mathrm{Im}\varepsilon^{-1}$					
1	0.36	0.05	–	–	1.59	–	7	–	–
2	–	–	0.26	–	–	2.56	–	–	–
3'	0.62	–	–	–	1.01	–	–	–	–
3	–	–	0.84	0.08	–	1.90	–	10	–
4	1.11	0.15	–	–	0.90	–	7	–	3.8(G)
5	–	–	1.11	0.15	–	1.01	–	8	5.0(G)
6	2.67	0.21	–	–	1.21	–	13	–	7.5 (Δ)
7	–	–	2.36	0.19	–	1.20	–	12	
8	–	–	0.57	0.05	–	0.21	–	12	9.5 (Δ, Σ)
9	4.22	0.29	1.39	0.29	1.05	0.20	14	5	10(*U*)
10	0.67	0.17	1.66	0.20	0.12	0.35	4	8	11.0(*S*)
11	6.85	0.20	2.20	0.16	0.84	0.32	34	13	12.6(*U*)
12	1.78	0.33	6.83	0.20	0.17	0.77	5	34	14.0(*S*)
13	3.80	0.33	3.51	0.38	0.31	0.30	13	9	14.6(*U*)
14	1.87	0.63	1.69	–	0.14	0.13	3	–	16.7(Δ)
15'	–	–	1.00	0.55	–	0.07	–	–	
15	0.77	1.05	0.45	0.66	0.06	0.03	0.7	0.7	17.8(*U*)
16	0.48	0.94	0.89	0.86	0.03	0.06	0.5	1	
16'	–	1.44	–	1.08	–	–	–	–	–
17'	–	0.68	–	0.49	–	–	–	–	20.3(*U*)
17	1.47	1.82	1.89	1.06	0.11	0.28	0.8	1.7	
18	0.34	2.50	1.08	1.91	0.03	0.08	0.1	0.5	22.0(*U*)
19	2.46	1.38	–	–	0.19	–	2	–	–
20	–	–	2.31	2.12	–	0.17	–	1.1	–

Note: Energies are given in eV.

the bands from [11] (the last column in Table 2). These results do not contradict our calculations of the energies of the components.

5. CONCLUSION

Thus, complete sets of polarized spectra of optical functions are obtained for the first time for a zinc-oxide hexagonal crystal in the range 0–30 eV. The parameters of the transverse and longitudinal components of the transitions are determined, and the main features of the spectra of the optical functions and the parameters of the transitions are established. These results enable us to consider, for the first time, the electronic structure and optical properties of ZnO crystals on the basis of deeper and more detailed information on integral reflectance spectra than that available until now and to

create new grounds for theoretical calculations of zinc-oxide properties.

ACKNOWLEDGMENTS

This study was supported by the Competitive Center of Fundamental Natural Sciences (St. Petersburg State University).

REFERENCES

1. *Proceedings of International Conference on II–VI Semiconducting Compounds, 1967*, Ed. by D. G. Thomas (Benjamin, New York, 1967).
2. V. V. Sobolev, *Bands and Excitons of II–VI Compounds* (Shtiintsa, Chisinau, 1980) [in Russian].
3. V. B. Lazarev, V. V. Sobolev, and I. S. Shaplygin, *Chemical and Physical Properties of Simple Oxides of Metals* (Nauka, Moscow, 1983) [in Russian].
4. V. V. Sobolev and V. V. Nemoshkalenko, *The Methods of Computational Physics in the Theory of Solid State. Electronic Structure of Semiconductors* (Naukova Dumka, Kiev, 1988) [in Russian].
5. V. V. Sobolev, S. V. Smirnov, and V. Val. Sobolev, Fiz. Tverd. Tela (St. Petersburg) **43**, 1980 (2001) [Phys. Solid State **43**, 2063 (2001)].
6. V. V. Sobolev, A. P. Timonov, and V. Val. Sobolev, Fiz. Tverd. Tela (St. Petersburg) **42**, 632 (2000) [Phys. Solid State **42**, 648 (2000)].
7. V. V. Sobolev, A. I. Kalugin, V. Val. Sobolev, and V. I. Kormilets, J. Wide Bandgap Mater. **8**, 87 (2001).
8. J. L. Freeouf, Phys. Rev. B **7**, 3810 (1973).
9. U. Rossler, Phys. Rev. **184**, 733 (1969).
10. S. Bloom and J. Ortenburger, Phys. Status Solidi **58**, 561 (1973).
11. J. R. Chelikowsky, Solid State Commun. **22**, 351 (1977).
12. Y. Mi, H. Odaka, and Sh. Iwata, Jpn. J. Appl. Phys. **38**, 3453 (1999).
13. J. E. Jaffe, R. Pandey, and A. B. Kunz, J. Phys. Chem. Solids **52**, 755 (1991).
14. D. Vogel, P. Kruger, and J. Pollmann, Phys. Rev. B **54**, 5495 (1996).
15. V. V. Sobolev, Zh. Prikl. Spektrosk. **63**, 143 (1996).
16. D. Pines, *Elementary Excitations in Solids* (Benjamin, New York, 1963; Mir, Moscow, 1965).

Translated by V. Bukhanov

Semiconductors, Vol. 39, No. 8, 2005, pp. 904–909. From Fizika i Tekhnika Poluprovodnikov, Vol. 39, No. 8, 2005, pp. 940–944.

CONFERENCE.
SEMICONDUCTOR STRUCTURES, INTERFACES, AND SURFACES

Characterization of an *a*-Si:H/*c*-Si Interface by Admittance Spectroscopy[1]

A. S. Gudovskikh[1, 2]^, J.-P. Kleider[1], and E. I. Terukov[3]

[1] *Laboratoire de Génie Électrique de Paris, UMR 8507, CNRS, Universités Paris VI et Paris XI, École Supérieure d'Électricité, F-91192 Gif-sur-Yvette Cedex, France*

^ *e-mail: goudovskikh@lgep.supelec.fr*

[2] *St. Petersburg State Electrotechnical University (LETI), St. Petersburg, 197376 Russia*

[3] *Ioffe Physicotechnical Institute, Russian Academy of Sciences, St. Petersburg, 194021 Russia*

Submitted December 27, 2004; accepted for publication January 12, 2005

Abstract—The capabilities of admittance spectroscopy for the investigation of *a*-Si:H/*c*-Si heterojunctions are presented. The simulation and experimental results, which compare very well, show that the admittance technique is sensitive to the parameters of both the *a*-Si:H layer and the *a*-Si:H/*c*-Si interface quality. In particular, the curves showing capacitance versus temperature have two steps, accompanied by two bumps in the temperature dependence of the conductance. The first step, occurring in the low temperature range (100–200 K), is related to the transport and response of gap states in the *a*-Si:H layer. The second step, occurring at higher temperatures (>200 K), is caused by a carrier exchange with interface states and appears when the interface defect density exceeds 5×10^{12} cm^{-2}. Then, the interface defects affect band bending, and, thus, the activation energy of de-trapping, which favors exchange with electrons from *a*-Si:H and holes from *c*-Si, respectively, for an increasing defect density. © *2005 Pleiades Publishing, Inc.*

1. INTRODUCTION

(Hydrogenated amorphous silicon)–(crystalline silicon) heterojunctions, *a*-Si:H/*c*-Si, are of great interest for practical applications and theoretical studies. One attractive practical usage of such heterostructures is high efficiency solar cells (up to 21%) fabricated entirely at low temperatures, thus reducing the cost [1]. The theoretical interest is due to the fact that *a*-Si:H/*c*-Si heterojunctions can be used as a modeling structure for amorphous–crystalline semiconductor heterojunctions, since *c*-Si is a well-known material and the properties of *a*-Si:H have also received sufficient study to be used as an amorphous modeling material. However, in both cases, the properties of the *a*-Si:H/*c*-Si interface are critical for photovoltaic application as well as for modeling. For photovoltaic applications, recombination at the interface states may significantly decrease solar cell efficiency, and uncertainty at the interface causes a lot of difficulties for modeling. Thus, efficient methods of interface characterization are needed to study the interface properties and to optimize the fabrication process.

It is known that the frequency and temperature dependence of junction admittance is very sensitive to exchanges with trap levels, and its variations with applied dc bias are strongly dependent on interface properties [2, 3]. Recently, admittance spectroscopy has been successfully applied to studying the interface properties of *a*-Si:H/*c*-Si heterostructures [4–6]. It was shown that, generally, in the experimental temperature dependence of the capacitance $C(T)$, two steps may be observed that are shifted to higher temperatures when the measurement frequency is increased. The first step, occurring in the low temperature range (100–200 K), was attributed to the activation of transport in the *a*-Si:H layer, and the second step, occurring at higher temperatures (>200 K), was ascribed to the response of the interface states. However, in order to assess admittance spectroscopy as a method of characterization of silicon heterostructures, it is important to gain more insight into these two capacitance steps by studying the influence of different heterojunction parameters. We have presented both the results of simulations of admittance spectra and the results of experimental measurements for different *a*-Si:H/*c*-Si heterojunctions. Comparison of the modeling results with the experimental data allows us to determine and verify the effect of the *a*-Si:H and *c*-Si parameters, as well as the defect density at the *a*-Si:H/*c*-Si interface, on admittance properties.

2. SIMULATION DETAILS AND EXPERIMENT

The modeling of the heterostructure admittance and its dependence on temperature, frequency, and bias was carried out using a numerical PC program, AFORS–HET, developed at the Hahn-Meitner-Institut (HMI) in Berlin [7]. We considered a single heterojunction between *n*-type *a*-Si:H and *p*-type *c*-Si that had two

[1] This article was submitted by the authors in English.

front and back ohmic contacts. The band diagram of the simulated structures is presented in Fig. 1. The material parameters used in calculations for the *c*-Si and *a*-Si:H layers are given in the table. The value of the conduction band offset, equal to 0.15 eV, and the distribution of the density of states (DOS) in *a*-Si:H were taken from UV-excited photoemission experiments [8]. In particular, the DOS in *a*-Si:H was assumed to consist of two exponential band tails with characteristic energies, kT_v and kT_c, of 0.106 and 0.068 eV for the valence and conduction bands, respectively, with a pre-exponential factor of 2×10^{21} cm^{-3} eV^{-1}, and two Gaussian deep defect distributions of a donor and acceptor type at 0.46 and 0.66 eV above the valence band maximum, respectively, with a pre-exponential factor of 1.8×10^{20} cm^{-3} eV^{-1}. The interface was described by introducing an additional interface layer with a thickness of 1 nm between *c*-Si and *a*-Si:H. The defect distribution in this interface layer was assumed to be constant within the band gap, with donor (acceptor)-like defects in the lower (upper) part of the band gap. In the following, N_{ss} (in cm^{-2}) denotes the interface defect density, which is determined as the product $d_{\text{int}}N_{\text{it}}$, where d_{int} is the thickness of the interface layer (1 nm) and N_{it} (in cm^{-3}) is the defect density in this layer, which is the integral over the band gap of the DOS, g_{it} (in cm^{-3} eV^{-1}).

Two series of numerical calculations of the admittance as a function of temperature and frequency were performed:

1. To study the admittance features in the low temperature range (100–200 K), we varied the *a*-Si:H layer thickness, $d_{a\text{-Si : H}}$; characteristic energy of the exponential conduction band tail in *a*-Si:H, kT_c; and *c*-Si doping density, N_a. N_{ss} was set at 10^{11} cm^{-2}.

2. To investigate the admittance behavior in the "high" temperature range (200–350 K) we varied the interface defect density, N_{ss}, and the capture cross section for electrons and holes in the interface states, σ_n and σ_p, respectively. The parameters of the *c*-Si and *a*-Si:H layers were kept constant.

The results of the simulations are supplied by experimental measurements obtained from various *a*-Si:H/*c*-Si heterostructures. Samples with different *a*-Si:H layer thicknesses and *c*-Si doping densities were provided by the Hahn-Meitner-Institut, Berlin, while another series of samples with various *c*-Si surface treatments was provided within the framework of the French national project SiNERGIES. The admittance measurements as a function of temperature and frequency, $C(T, \omega)$ and $G(T, \omega)$, were performed in a liquid nitrogen cryostat in the temperature range 93–333 K using an HP4284A impedance meter at frequencies in the range 20–1 MHz at a reverse bias of 0.1 V.

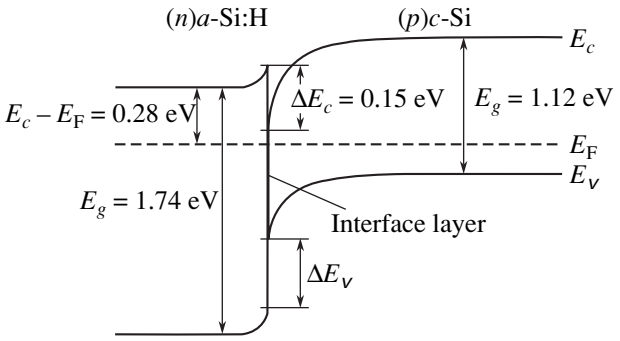

Fig. 1. Band diagram used in the simulation.

3. RESULTS

3.1. Low Temperature Region

The simulated $C(T, \omega)$ and $G(T, \omega)$ curves for heterojunctions with *a*-Si:H layer thicknesses of 10, 40, and 80 nm and a *c*-Si doping density of 10^{16} cm^{-3} are shown in Fig. 2a. The experimental curves for two structures with *a*-Si:H thicknesses $d_{a\text{-Si : H}} < 10$ nm and $d_{a\text{-Si : H}} = 40$ nm and the same *c*-Si doping density are shown in Fig. 2b. It can be seen that the simulated and measured results have similar tendencies and similar absolute values. The small monotonic increase in the capacitance as the temperature rises is due to the statistical shift of the Fermi level in both *c*-Si and *a*-Si:H, reducing the built-in potential and, thus, the width of the space-charge region as the temperature increases. The characteristic feature of the curves is the presence of a step in the capacitance in a temperature range of 100–200 K. This step is accompanied by a maximum in the conductance, and both the capacitance step and the conductance maximum are shifted to higher temperatures as the frequency increases [5]. This shift in the temperature versus frequency can be used to obtain the activation energy of the underlying process. For the simulated curves, the activation energy is equal to 0.28 eV, and, for the experimental curves, this parameter is approximately equal to 0.2 eV. The amplitude of the capacitance step increases as the *a*-Si:H layer thickness increases.

In order to study the influence of the *c*-Si substrate doping density N_a on the capacitance properties in this

Main parameters of the heterojunction layers used in calculations

Parameter	*c*-Si	Interface layer	*a*-Si : H
Band gap, eV	1.12	1.12	1.74
Doping density, cm^{-3}	10^{15}–2×10^{18}	10^{15}–2×10^{18}	10^{20}
Electron affinity, eV	4.05	4.05	3.9
Thickness, nm	300000	1	10–80

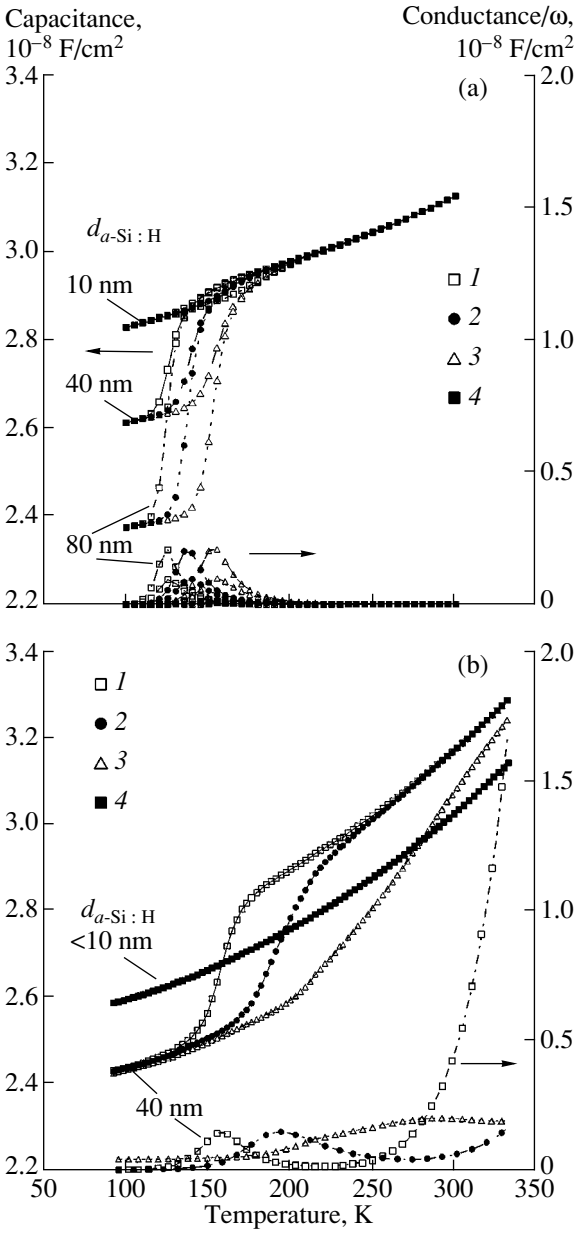

Fig. 2. (a) Calculated and (b) experimental $C(T)$ and $G(T)$ curves for different thickness of the *a*-Si:H layer ($d_{a\text{-Si : H}}$) measured at frequencies of (*1*) 100 Hz, (*2*) 1 kHz, and (*3*) 10 kHz, and at a reverse bias of 0.1V; (*4*) *c*-Si.

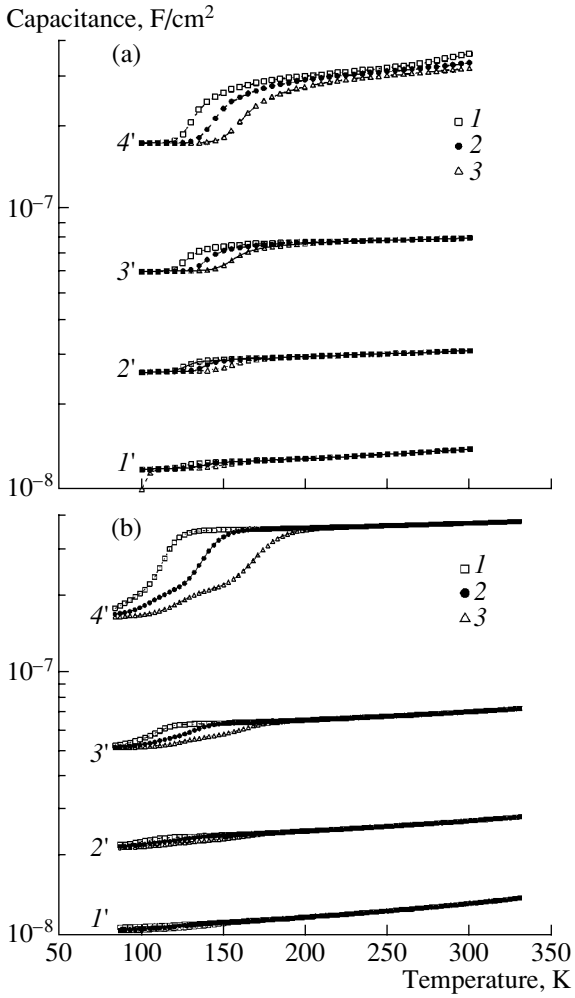

Fig. 3. (a) Calculated and (b) experimental $C(T)$ curves for different values of *c*-Si doping density N_a measured at frequencies of (*1*) 100 Hz, (*2*) 1 kHz, and (*3*) 10 kHz, and at a reverse bias of 0.1 V. N_a, cm^{-3}: (*1*') 1.8×10^{15}, (*2*') 10^{16}, (*3*') 1×10^{16}, and (*4*') 2×10^{18}.

temperature region, we simulated and measured $C(T, \omega)$ curves at different values of N_a: 1.8×10^{15}, 10^{16}, 7×10^{16} and 2×10^{18} cm^{-3}. The curves are shown in Fig. 3. Again, there is a very good correlation between the calculated and measured curves. The amplitude of the capacitance step increases as doping density is increased.

Finally, the effect of the DOS in *a*-Si:H was simulated by varying kT_c while keeping the same position, 0.28 eV below the conduction band minimum, of the Fermi level in *a*-Si:H. This simulation was carried out for $N_a = 2 \times 10^{18}$ cm^{-3} because the effect at this doping density is more pronounced. Three calculated curves for kT_c, equal to 0.068, 0.1, and 0.15 eV, are shown in Fig. 4. The amplitude of the step changes in different ways: the top limit of the step significantly rises as kT_c increases, while the bottom limit slightly decreases.

3.2. High Temperature Region

In the second series of simulations, the interface parameters were varied. The influence of the interface defect density N_{ss} on the behavior of the $C(T, \omega)$ curves is shown in Fig. 5a, where N_{ss} shifted from 10^{10} to 10^{14} cm^{-2} for N_a equal to 10^{15} cm^{-3}. When N_{ss} varied from 0 to 10^{10} cm^{-2}, no difference in the $C(T, \omega)$ and $G(T, \omega)$ curves was observed. When N_{ss} increased to 10^{12} cm^{-2}, a slight rise in the capacitance value was observed but without any visible deviation of the

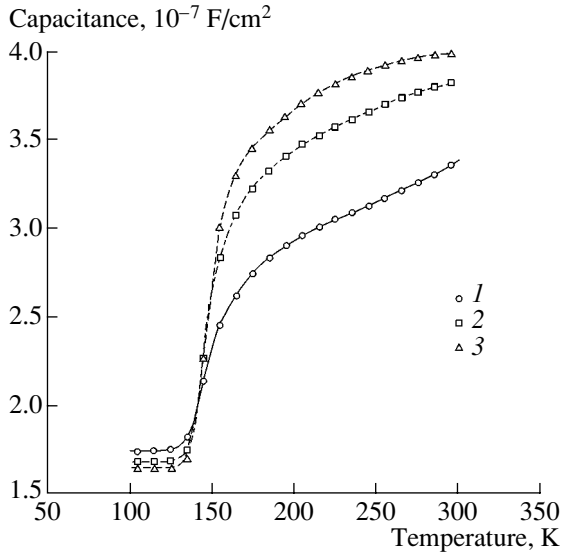

Fig. 4. Calculated $C(T)$ curves for different values of characteristic energy of the conduction band tail in *a*-Si:H (kT_c) at a frequency of 1 kHz and at a reverse bias of 0.1 V. kT_c, eV: (*1*) 0.68, (*2*) 0.1, and (*3*) 0.15.

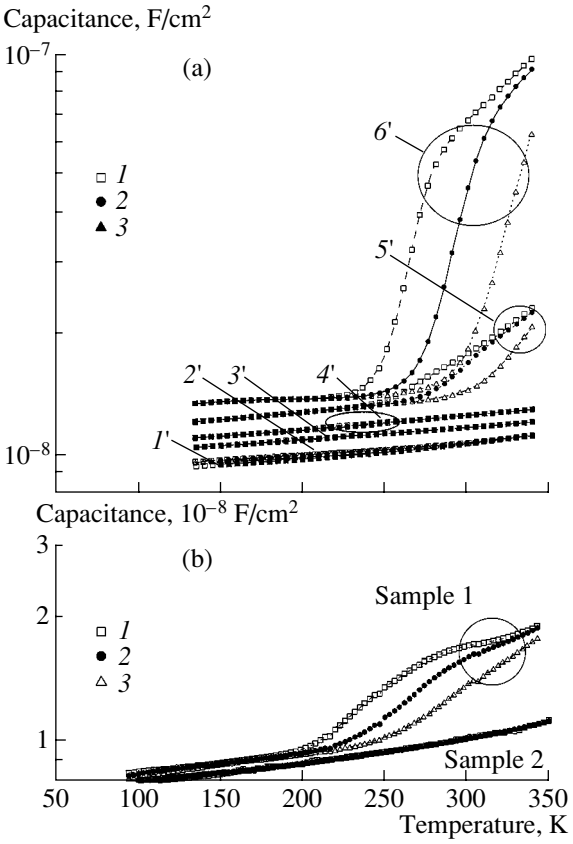

Fig. 5. $C(T)$ curves (a) calculated for the following values of interface defect density N_{ss}, cm^{-2}: (*1'*) 10^{10}–10^{11}, (*2'*) 10^{12}, (*3'*) 5×10^{12}, (*4'*) 10^{13}, (*5'*) 5×10^{13}, and (*6'*) 10^{14}; (b) measured for two samples with different interface treatments at frequencies of (*1*) 100 Hz, (*2*) 1 kHz, and (*3*) 10 kHz, and at a reverse bias of 0.1 V.

dependence on temperature and frequency. As N_{ss} reaches 5×10^{12} cm^{-2}, the capacitance value significantly increases and the character of the curves changes. The second capacitance step appears at higher temperatures (200–250 K) and is accompanied by a second conductance peak, which is not shown in the figure for reasons of clarity. An activation energy of 0.43 eV can be deduced from this step. At N_{ss} equal to 5×10^{13} cm^{-2}, the capacitance level further increases and the second step is shifted to higher temperatures (250–300 K), with a significantly larger amplitude and activation energy of 0.48 eV. Finally, when N_{ss} equals 10^{14} cm^{-2}, the absolute value of the capacitance further increases and the amplitude of the second step drastically rises, with a slight decrease of the activation energy to 0.47 eV. The position of this step is shifted to higher temperatures when the capture cross section for interface states, $\sigma = \sigma_n = \sigma_p$, decreases, as is shown in Fig. 6, where $C(T)$ curves calculated for three different values of σ are presented; N_{ss} is set at 5×10^{13} cm^{-2}. It should be noted that, from a practical point of view, the appearance of the second capacitance step is a well-defined feature for a rough estimation of the interface quality.

In Fig. 5b, we present experimental $C(T, \omega)$ curves for two structures that underwent different interface treatments. Sample 1, which has an efficiency of 9–10%, exhibits a step at high temperatures, while the second sample, with an efficiency of 12–14%, does not have any step in this temperature region. Thus, the low efficiency of sample 1 is caused by the poor interface quality, and an estimation of N_{ss} gives a value in the order of 5×10^{13} cm^{-2}. In contrast, N_{ss} for sample 2 is less than 10^{12} cm^{-2}.

Analysis of the sensitivity of the $C(T, \omega)$ curves to N_{ss} shows that the limit of the sensitivity, i.e., the minimum value of N_{ss} for the second capacitance step to appear does not depend significantly on the doping density of *c*-Si.

4. DISCUSSION

The presence of the step in the $C(T)$ curves at low temperatures is attributed to the onset of transport or the response of gap states at the Fermi level in the *a*-Si:H emitter [5]. At very low temperatures, below the step, the capacitance is given by $\varepsilon A/(d_{a\text{-Si : H}} + W_{c\text{-Si}})$, where ε is the dielectric permittivity, A is the diode area, $d_{a\text{-Si : H}}$ is the *a*-Si:H thickness, and $W_{c\text{-Si}}$ is the width of the depletion layer in *c*-Si. Above the onset, the capacitance changes to $\varepsilon A/(l_{\text{eff}} + W_{c\text{-Si}})$, as determined by the sum of the depletion region $W_{c\text{-Si}}$ in *c*-Si and the effective depletion length l_{eff} in *a*-Si:H. This effective depletion length is a kind of Debye length related to the density of gap states responsible for the change in capacitance. From the step in the capacitance, we can thus

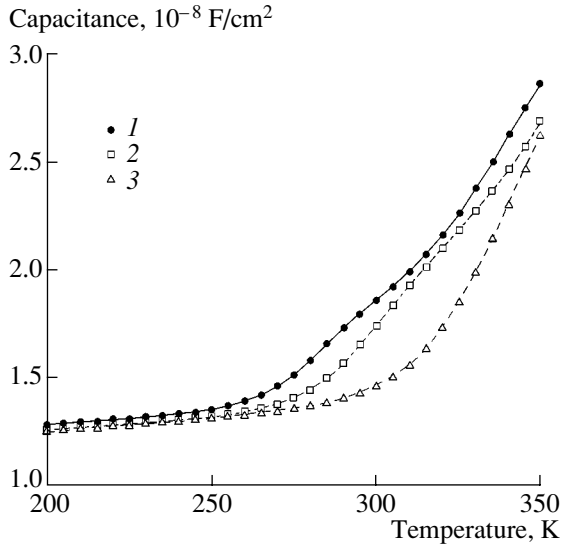

Fig. 6. Calculated $C(T)$ curves for different values of the capture cross section σ measured at a frequency of 1 kHz and reverse bias of 0.1 V. σ, cm^{-2}: (*1*) 10^{-13}, (*2*) 10^{-14}, and (*3*) 10^{-15}.

determine the difference between the entire *a*-Si:H layer thickness and the effective depletion length, $d_{a\text{-Si:H}} - l_{\text{eff}}$. Therefore, for the structure with an *a*-Si:H thickness of 40 nm shown in Fig. 2b, we obtain $d_{a\text{-Si:H}} - l_{\text{eff}} = 36$ nm. This value approximately corresponds to the total thickness of the *a*-Si:H layer. The activation energy of this process corresponds to the difference between the conduction band and Fermi level in *a*-Si:H ($E_c^{a\text{-Si:H}} - E_{\text{F}}^{a\text{-Si:H}}$).

Increasing the doping density of *c*-Si (N_a) leads to a decrease in $W_{c\text{-Si}}$, and, therefore, the capacitance becomes more sensitive to variation of effective thickness from $d_{a\text{-Si:H}} + W_{c\text{-Si}}$ to $l_{\text{eff}} + W_{c\text{-Si}}$; furthermore, the absolute value of the capacitance increases. For high values of $N_a \approx 10^{18}$ cm^{-3}, which are comparable with the *a*-Si:H effective doping density, the depletion length l_{eff} in *a*-Si:H is no longer negligible when compared with $W_{c\text{-Si}}$. Thus, the capacitance is more sensitive to the DOS in *a*-Si:H. This circumstance is illustrated by the simulations in Fig. 3, where the increase of the conduction tail characteristic energy, which corresponds to an increase in the DOS, leads to a decrease in l_{eff} that results in an increase in the capacitance value above the step. In contrast, the decrease in the capacitance below the step as kT_c increases is caused by an increase in $W_{c\text{-Si}}$, which, in turn, is due to the more pronounced band bending in *c*-Si when the DOS in *a*-Si:H is increased.

The second step, at high temperatures, is caused by trapping and emission of charge carriers at the interface states. Before analysis of the simulation results, we should recall that the calculation was performed under the assumption of a constant distribution of interface defect density and with the capture cross sections for those interface states equal for electron and holes ($\sigma = \sigma_n = \sigma_p$).

Firstly, increasing N_{ss} to 10^{12} cm^{-2} leads to a slight decrease in the band bending in *c*-Si and, therefore, the depletion region width $W_{c\text{-Si}}$. Thus, in the $C(T, \omega)$ curves, one can observe a slight increase in the capacitance level but with no step, since the contribution of the interface states to the capacitance is negligible. When N_{ss} is in the range 5×10^{12}–10^{13} cm^{-2} the step at higher temperatures occurs due to the exchange of electrons between interface states near the Fermi level and the conduction band of *a*-Si:H. The activation energy of this process corresponds to the difference between the conduction band in *a*-Si:H and the quasi Fermi level for electrons $E_{\text{F}n}$ at the interface $(E_c^{a\text{-Si:H}} - E_{\text{F}n})_{\text{it}}$. The value of the activation energy increases as N_{ss} increases because of the rise in band bending in *a*-Si:H, and the step is shifted towards higher temperatures. Further increasing N_{ss} ($N_{ss} \geq 5 \times 10^{13}$ cm^{-2}) leads to a case where $(E_c^{a\text{-Si:H}} - E_{\text{F}n})_{\text{it}}$ is greater than the difference between the quasi Fermi level for the holes $E_{\text{F}p}$ and the valence band in *c*-Si at the interface $(E_{\text{F}p} - E_v^{c\text{-Si}})_{\text{it}}$. In this case, the exchange of holes between the interface states and valence band in *c*-Si prevails. The amplitude of the step becomes larger, and the activation energy corresponds to $(E_{\text{F}p} - E_v^{c\text{-Si}})_{\text{it}}$. Increasing N_{ss} to 10^{14} cm^{-2} leads to a slight decrease in the activation energy and, therefore, to a shift of the step to lower temperatures.

5. CONCLUSIONS

The low-temperature step in the $C(T)$ curves (and the corresponding bump in the $G(T)$ curves) is related to the transport and response of gap states in the *a*-Si:H layer. From the activation energy of this step, one can determine the position of the Fermi level in *a*-Si:H, and, from the absolute values of the capacitance below and above the step, the difference $d_{a\text{-Si:H}} - l_{\text{eff}}$ can be obtained. If one knows the thickness of the *a*-Si:H layer $d_{a\text{-Si:H}}$, the effective depletion length l_{eff} in *a*-Si:H can be found, which is related to the band bending in *a*-Si:H.

The high-temperature step in the $C(T)$ curves is caused by a carrier exchange with interface states and appears when N_{ss} exceeds 5×10^{12} cm^{-2}. This step can be used for a rapid estimation of the interface quality. We have shown that, when N_{ss} is increased above 5×10^{12} cm^{-2}, first, an exchange of electrons with *a*-Si:H takes place, which leads to only a limited step in the capacitance as a function of temperature; then, for higher values of N_{ss}, an exchange of holes with *c*-Si prevails and the step in the $C(T)$ curves is much more pronounced.

ACKNOWLEDGMENTS

Part of this work was carried out within the framework of the French national project SiNERGIES. The authors are grateful to Prof W. Fuhs and Dr. M. Schmidt at HMI, Berlin, for the supplied samples. Thanks also to Dr. R. Stangl for providing and explaining the AFORS–HET software.

REFERENCES

1. M. Taguchi, K. Kawamoto, S. Tsuge, *et al.*, Prog. Photovoltaics **8**, 503 (2000).
2. D. V. Lang, J. D. Cohen, and J. P. Harbinson, Phys. Rev. B **25**, 5285 (1982).
3. D. L. Losee, J. Appl. Phys. **46**, 2204 (1975).
4. T. Unold, M. Rösch, and G. H. Bauer, J. Non-Cryst. Solids **266–269**, 1033 (2000).
5. A. S. Gudovskikh, J. P. Kleider, A. Froitzheim, *et al.*, Thin Solid Films **451–452**, 345 (2004).
6. A. S. Gudovskikh, J. P. Kleider, R. Stangl, *et al.*, in *Proceedings of 19th European Photovoltaic Solar Energy Conference* (Paris, 2004), p. 697.
7. R. Stangl, A. Froitzheim, M. Kriegel, *et al.*, in *Proceedings of 19th European Photovoltaic Solar Energy Conference* (Paris, 2004), p. 1497.
8. M. Schmidt, A. Schöpke, L. Korte, *et al.*, J. Non-Cryst. Solids **338–340**, 211 (2004).

Semiconductors, Vol. 39, No. 8, 2005, pp. 910–916. Translated from Fizika i Tekhnika Poluprovodnikov, Vol. 39, No. 8, 2005, pp. 945–952.

CONFERENCE.
LOW-DIMENSIONAL SYSTEMS

Coulomb Blockade of the Conductivity of SiO_x Films Due to One-Electron Charging of a Silicon Quantum Dot in a Chain of Electronic States

M. D. Efremov^, G. N. Kamaev, V. A. Volodin, S. A. Arzhannikova, G. A. Kachurin, S. G. Cherkova, A. V. Kretinin, V. V. Malyutina-Bronskaya, and D. V. Marin

Institute of Semiconductor Physics, Siberian Division, Russian Academy of Sciences, Novosibirsk, 630090 Russia

^ e-mail: efremov@isp.nsc.ru

Submitted December 27, 2004; accepted for publication January 12, 2005

Abstract—The electrical characteristics of metal–oxide–semiconductor (MOS) structures with silicon nanoparticles embedded in silicon oxide have been studied. The nanocrystals are formed by decomposition of an oversaturated solid solution of implanted silicon during thermal annealing at a temperature of ~1000°C. At liquid-nitrogen temperature, a stepped current–voltage characteristic is observed in a MOS structure consisting of Si nanocrystals in a SiO_2 film. The stepped current–voltage characteristic is, for the first time, quantitatively described using a model in which charge transport occurs via a chain of local states containing a silicon nanocrystal. The presence of steps is found to be associated with one-electron charging of the silicon nanocrystal and Coulomb blockade of the probability of a hop from the nearest local state to the conducting chain. The local states in silicon dioxide are assumed to be related to an excess of silicon atoms. The presence of such states is confirmed by measurements of the differential conductance and capacitance. For MOS structures implanted with silicon, the differential capacitance and conductance are found to be higher, compared to the reference structures, in the range of biases exceeding 0.2 V. In the same bias range, the conductance is observed to decrease under ultraviolet irradiation due to a change in the population of the states in the conductivity chains.

1. INTRODUCTION

Silicon dioxide films with silicon nanocrystals are now considered as a prospective material for the fabrication of single-electron transistors and memory cells, in which the floating gate is replaced by nanocrystalline silicon inclusions. Silicon nanocrystals in silicon oxide are “deep” quantum dots that luminesce at room temperature due to the effect of quantum confinement of charge carriers [1, 2]. Both the electrical and the optical properties of silicon nanocrystals are of great scientific interest [3]. To a large extent, these properties are determined by the spectrum of electronic states in the nanocrystals. Numerous studies have focused on theoretical description of the electron spectrum [4–7]. Direct quantum-mechanical methods of calculation are applied to small-sized silicon nanocrystals (less than 1 nm). For larger sized crystals, the application of these methods is limited by modern computation facilities; therefore, a method of calculation based on the effective-mass approximation is used. It should also be noted that direct quantum-mechanical methods imply the passivation of nanocrystals with hydrogen in the case of isolated silicon nanocrystals. However, the solution to the problem involving the use of the effective-mass method implies the presence of an interface with a wider gap material. This case corresponds to a silicon nanocrystal in a dielectric environment. Comparison of the results of these and other versions of the calculation is of interest and, in principle, makes it possible to find the phenomenological parameters of the effective-mass approximation, which can describe the structure of the electronic levels of silicon nanocrystals in various dielectric environments with sufficient accuracy.

A small nanocrystal size can ensure low capacitance for transitions in a two-barrier system, which is sufficient for observation of the “Coulomb blockade” effect. In some experiments, effects have been discovered that can be described on the basis of the features of charge transport through quantum states localized in silicon nanocrystals [8].

Due to the existence of high potential barriers at the silicon–silicon dioxide interface (3.2 eV and 4.34 eV for electrons and holes, respectively), the quantum confinement properties of silicon nanocrystals can be observed even at room temperature. However, if the barrier height increases, the probability of tunneling through a thin silicon oxide layer decreases exponentially. This circumstance complicates the formation of thin transparent walls for tunneling transitions. At the same time, observation of the Coulomb blockade of the conductance for practically accessible barrier thicknesses becomes, in principle, possible if the electron transport through a quantum dot is due to multiple elastic-tunneling events involving surface or localized

1063-7826/05/3908-0910$26.00 © 2005 Pleiades Publishing, Inc.

states. In this case, the charge transport mechanism via the states in silicon dioxide is of fundamental importance.

Here, we present the results of an experimental study of the electrical properties of silicon dioxide films containing nanocrystalline silicon inclusions.

2. EXPERIMENTAL

We conducted an experimental study of MOS (metal–oxide–semiconductor) structures with silicon nanocrystals buried in silicon oxide. Samples with different substrate conductivity types and varying insulator thicknesses were used. The silicon nanocrystals were introduced into the silicon dioxide layer using implantation of Si^+ ions with an energy of 25 keV at a dose of 3×10^{16} cm^{-2} (for an *n*-type substrate with an oxide thickness of 75 nm) and with an energy 150 keV at a dose of 7×10^{17} cm^{-2} (for a *p*-type substrate with an oxide thickness of 300 nm). Postimplantation annealing of the structures was performed at 1000°C for two hours in an N_2 atmosphere. Earlier, it was shown that such annealing of structures implanted with silicon results in the formation of nanocrystalline inclusions with an average size of ~5 nm and in the appearance of a photoluminescence line with a wavelength of about 750 nm [9]. The MOS structures were formed by thermal evaporation of aluminum in vacuum through a mask on a cold substrate. On the back side of the structures, an ohmic contact was formed by depositing a eutectic In–Ga mixture. The reference MOS structures were also fabricated on the part of the sample surface covered by a metal mask during implantation, and the rest of the fabrication process was the same as for the structures under study.

For the obtained MOS structures, we measured the differential capacitance and conductance as functions the applied voltage in the frequency range 1–145 kHz and the static current–voltage characteristics. Differential characteristics were measured by applying ac and dc voltage; the ac voltage was equal to 20 mV and the dc voltage continuously varied from –10 to +10 V. The ac signal from the load resistance was measured in a synchronous detection mode. The values of the differential capacitance and conductance were recorded simultaneously using two synchronous detectors with a phase shift of 90°.

We also studied the capacitance–voltage characteristics and the voltage dependence of the conductance of the MOS structures containing nanocrystals in the oxide layer after exposure to ultraviolet radiation. The samples were irradiated for 1 h in the absence of bias voltage at the electrodes and during the measurement of the characteristics. A high-pressure DDS-30 deuterium lamp with a continuous spectrum in the wavelength range of 200–400 nm was used as the radiation source. In order to study the effect of ultraviolet radiation, we also performed measurements for structures without nanocrystals in their oxide layer.

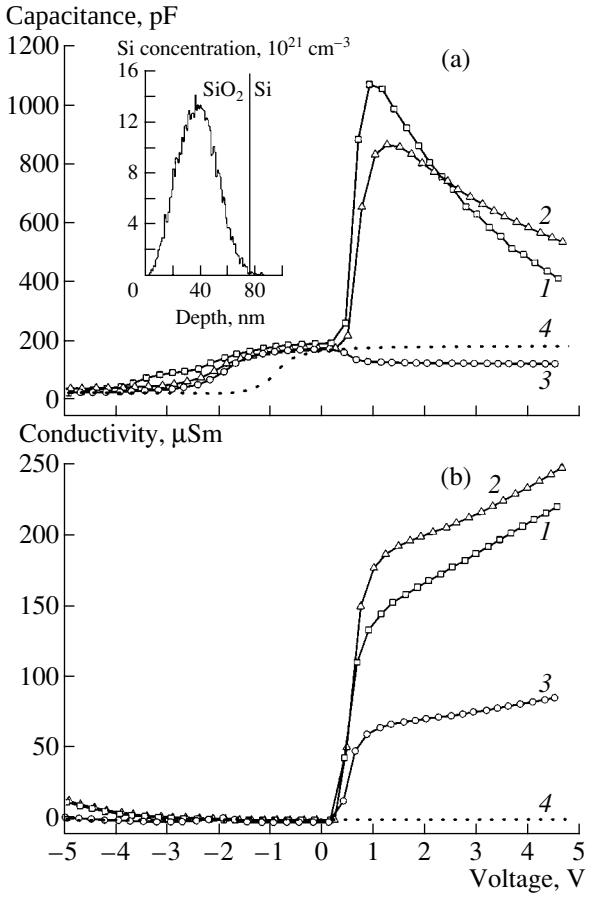

Fig. 1. Differential (a) capacitance and (b) conductance of a MOS structure (*1–3*) containing silicon nanocrystals in its insulator layer and (*4*) without nanocrystals. Measurement frequency: (*1*) 1.12, (*2*) 10, and (*3*, *4*) 145 kHz. The inset shows the spatial distribution of Si in a SiO_2 film with a thickness of 75 nm after implantation of Si^+ ions with an energy of 25 keV at a dose of 5×10^{16} cm^{-2}.

3. EXPERIMENTAL RESULTS AND DISCUSSION

3.1. Differential Current–Voltage and Capacitance–Voltage Characteristics

The capacitance–voltage (*C–V*) characteristics of the reference MOS structures had a rather conventional shape corresponding to the usual high-frequency *C–V* characteristics of MOS structures, with a capacitance saturation of ~185 pF (at a positive bias), which corresponds to the capacitance of an insulator of specified thickness (see Fig. 1a, curve *4*).

The differential capacitance and conductance characteristics appeared to be different for the MOS structures without and with silicon nanocrystals in silicon oxide (see Fig. 1). Compared to the reference sample, the flat-band voltage was shifted by –1 to 1.5 V to the region of negative bias, indicating the presence of an additional positive charge in the oxide with an excess silicon concentration. Furthermore, at frequencies of 1.12 and 10 kHz, a sharp increase in capacitance and, at

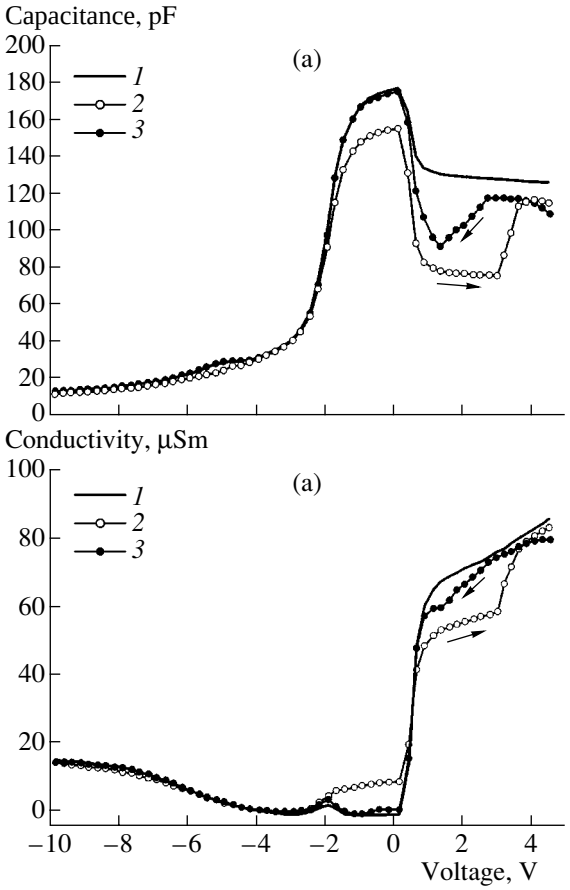

Fig. 2. Differential (a) capacitance and (b) conductance of a MOS structure containing silicon nanocrystals in its insulator layer at frequency 145 kHz. The measurements where carried out (*1*) in the dark and (*2*, *3*) under ultraviolet illumination.

a frequency of 145 kHz, some decrease in capacitance at voltages exceeding 0.2 V were observed. It should be noted that the experimental differential conductance of the MOS structures also increased substantially under positive biases exceeding 0.2 V. In addition, the differential conductance at the frequency 145 kHz was much smaller than at lower frequencies (see Fig. 1b). For the reference sample, no appreciable increase in differential conductance with bias was observed. The region of voltages where differences in the capacitance and conductance were observed is the same, and, therefore, at these voltages, the recharging of electronic states in silicon oxide, which makes a substantial contribution to both the measured quantities, occurs. These electronic states are probably related to the presence of excess silicon in the oxide. They may be also associated with silicon clusters appearing in the oxide after irradiation and thermal annealing. The increase in the measurement frequency to 145 kHz reduces the observed effect, as there is not enough time for some of the states to be recharged. Since, at a given applied voltage, the space-charge region in the semiconductor is in the accumulation mode and the capacitance of the MOS structure is entirely determined by the capacitance of the insulator, all the changes in the total capacitance of the structure are due to recharging of the states in the insulator. Thus, the silicon implantation and formation of silicon nanocrystals in the silicon oxide during subsequent annealing result in the appearance of electronic states in the oxide, which, after recharging, change the differential capacitance and conductance of the MOS structures.

We may assume that, at room temperature, the main mechanism of charge transport in the oxide is hopping. In silicon oxide, the probability of charge carrier hops from one state to another depends on their charge state. This state can be changed by ultraviolet radiation, which was accomplished experimentally. Figure 2 shows the differential capacitance and conductivity of a MOS structure under ultraviolet radiation. The measurements were performed at a frequency of 145 kHz. In the region of voltages exceeding 0.2 V, the capacitance and conductance of the MOS structures with silicon nanocrystals in their oxide layer decrease. Furthermore, a hysteresis of the characteristics is observed in this range of voltages. In the range of voltages from –2 to 0 V, illumination increases the differential conductance of the MOS structures. The effect of illumination on the differential conductance can be associated with two mechanisms. The first one is related to conventional photoconductivity and occurs when the conductance of a sample grows with the intensity of incident light due to the appearance of additional charge carriers in the bands of delocalized states. The second mechanism, which is more complicated, can decrease the conductance of a sample, since the charge carriers generated by light occupy the empty states in the conducting chains entirely responsible for the conductance of the structure. The filling of empty states can result in blocking of the conducting chain, thus decreasing the total conductance of the oxide layer. In our case, both these mechanisms are, apparently, effective in the voltage ranges –2 V to 0 V and above 0.2 V, respectively. The presence of a hysteresis is naturally explained, since the charge state in the conducting chains also depends on the applied bias and the charge states of the conducting chains may be different depending on whether the scanning bias is increased or decreased.

The shape of the *C*–*V* characteristics did not change under ultraviolet irradiation of the structures without nanocrystals; however, these characteristics were shifted to the region of negative bias, indicating accumulation of a positive built-in charge inside the insulator. Charging of the insulator by ultraviolet irradiation can be attributed to the fact that there are two types of traps in the band gap of SiO_2. The first type of traps are shallow electron traps and the second type are deep hole traps. Under ultraviolet irradiation, electron–hole pairs are formed inside SiO_2, photoexcited electrons are captured by the electron traps, and holes are captured by the hole traps. Since the electron traps are shallow and the mobility of the electrons captured by these traps

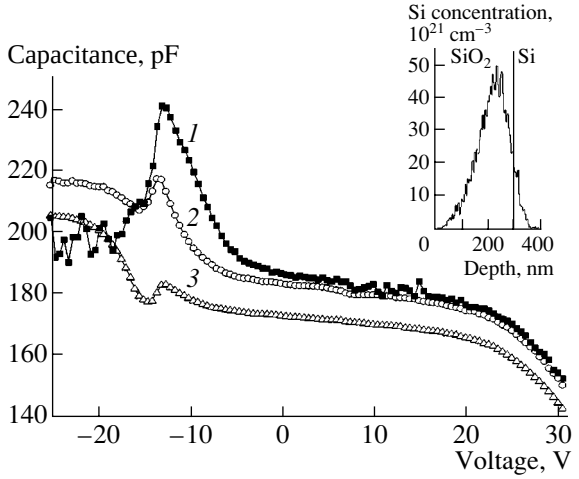

Fig. 3. Capacitance–voltage characteristics of a MOS structure containing silicon nanocrystals in its insulator layer. Measurement frequency: (*1*) 1, (*2*) 10, and (*3*) 145 kHz. The inset shows the spatial distribution of Si in an SiO_2 film with a thickness of 300 nm after implantation of Si^+ ions with an energy of 150 keV at a dose of 7×10^{17} cm^{-2}.

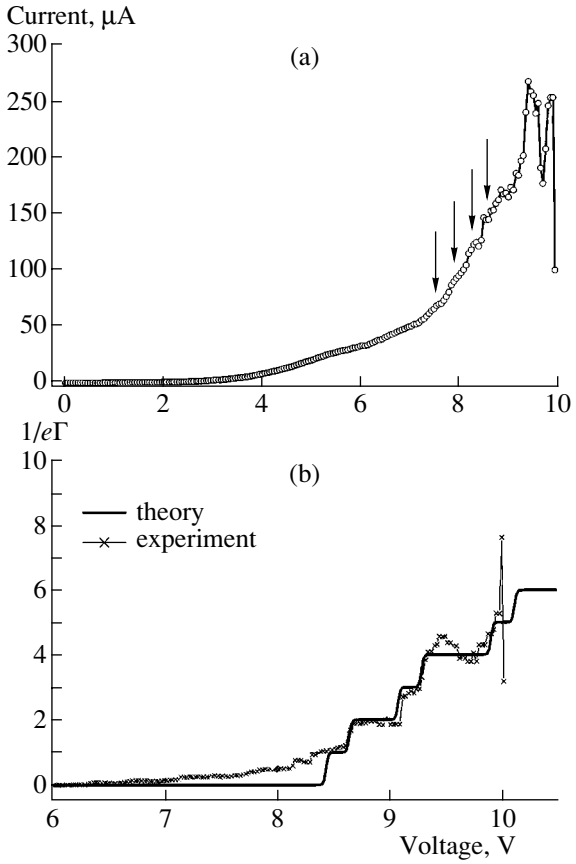

Fig. 4. Current–voltage characteristics of a MOS structure containing silicon nanocrystals in its silicon dioxide layer. (a) Experiment at $T = 300$ K; (b) experiment at $T = 77$ K and calculation for a two-barrier structure.

is higher, electrons rapidly flow to the metal or to the conduction band of the semiconductor. The hole traps are deep states that provide a long lifetime for the captured holes. As a result, holes stay on the traps and the insulator acquires a positive charge, changing the flat-band voltage and shifting the *C–V* characteristic to the region of negative voltages. In order to remove this positive charge, it was necessary to anneal the insulator at temperatures as high as 350°C for 15–20 min.

Figure 3 shows the results of the measurement of the *C–V* characteristics for a MOS structure containing silicon nanocrystals in its oxide. In this case, the thickness of the oxide was equal to 300 nm and the substrate had *p*-type conductivity. Analysis of the *C–V* characteristics revealed the presence of a peak at a bias of ~(–12) V, corresponding to recharging of the local electronic states in the insulator. The amplitude of the peak decreased as the measurement frequency was increased, since there is no time for some of the states to be recharged at high frequencies. The observation of a relatively narrow peak in the *C–V* characteristic corresponds to a narrow energy distribution of local states in the oxide.

3.2. Static Current–Voltage Characteristics

We measured the static current–voltage (*I–V*) characteristics of the MOS structures with silicon nanocrystals in their oxide layer at room temperature. For most of the experimental samples, *I–V* characteristics of a diode type were observed. The excess silicon introduced by implantation creates electronic states in the bulk of the insulator, and the insulator becomes conducting. Since the current easily flows across the insulator from the semiconductor to the metal contact, we may assume that such a structure has a *I–V* characteristic similar to that of Schottky diodes. An *I–V* characteristic asymmetric with respect to the sign of the voltage was experimentally observed.

However, for approximately 10% of the studied structures, no sharp increase in the current was observed when a bias was applied. In these cases, the forward *I–V* characteristic was flatter. In Fig. 4a, a typical *I–V* characteristic of such a structure is shown. In the region of voltages from 7 to 9 V, a poorly pronounced structure, reproduced for a given sample, is seen. For bias voltages exceeding 9 V, instability of the current in the sample was observed. Apparently, for structures of this type, the current increase is not fast and monotonic, in contrast to that observed for most of the structures at 0.7 V. Furthermore, the voltage dependence of the current above approximately 7 V contains sharp kinks and small plateaus, which are marked by arrows on the plot. Numerous authors [10–13] relate the appearance of such kinks and plateaus in the *I–V* characteristics to resonant tunneling via localized states in the insulator layer. The reproducibility of poorly pronounced features in the dc *I–V* characteristics makes it

possible to assume that these features may be due to the charging of states in the silicon nanocrystals. If the temperature was lowered to 77 K, the reproducible features assumed the stepped shape shown in Fig. 4b. Step-shaped dc *I–V* characteristics were observed in the region of voltages from 8.5 to 9.5 V. For voltages of ~9.5 V at room temperature, instability of the measured current was observed. Such current fluctuations have also been observed in many studies of the resonant current over quantum confinement levels or impurity levels in the insulator [11, 14].

It should be noted that the steps in the *I–V* characteristic (Fig. 4b) are not equidistant and the current plateaus are of different extent. For a qualitative explanation of the stepped shape of the *I–V* curve, a model was used in which the current through the oxide layer of a MOS structure flowed along the chains of electronic states. The chains may contain states corresponding to the quantum confinement energy levels of an electron localized in a silicon nanocrystal. The model also takes into account single-electron charging of the nanocrystal by the current flowing through it.

The main benefit of the model consists in the following. We assumed that the conductance of the oxide is determined by the hopping mechanism of charge transport. Charge carriers hop via the states in the oxide, which form a system of chains and make a substantial contribution to the total oxide conductance. The presence of a silicon nanocrystal in a chain increases this contribution, since the localization radius of the electron wave function for a nanocrystal is much greater than the corresponding radius for a local center. A local center in the chain of states from which the electron hops to the silicon nanocrystal plays the role of the emitter, and the center accepting an electron hopping from the nanocrystal plays the role of the collector. We may expect that, as the temperature decreases, the contribution of the chains of states without silicon nanocrystals to the conductance decreases more rapidly because of greater localization of the wave functions of the states. At low temperatures, the contribution of the conductance of one or several chains can become dominant.

A nanocrystal, being a multiple-charge center, can block the conductance of such a chain when charged by several electrons or holes. In experiments, this circumstance can manifest itself as a stepped *I–V* characteristic against a background of the current determined by the other conducting chains. Thus, the Coulomb blockade is observed only for chains for which the probability of electron transition from the emitter in the nanocrystal is much higher than the probability of tunneling from the nanocrystal to the collector. The other chains make a contribution that smoothly depends on voltage and does not contain the features discussed above.

In order to estimate the consistency of the model, we performed a theoretical analysis of the *I–V* characteristics of a MOS structure using the approach described in [15].

3.3. Simulation of dc I–V Characteristics for MOS Structures with Silicon Nanocrystals

In [15], an expression for the tunneling current through the states in a quantum well in a two-barrier structure was obtained. A silicon substrate with *n*-type conductivity played the role of one electrode and the other electrode was an aluminum contact. The quantum well was formed by a silicon nanocrystal in the SiO_2 layer. The expression for the tunneling current describing a stepped *I–V* characteristic is given by [15]

$$I = e\Gamma_c \times \left[n + \frac{[p(n) - q(n)]}{p(n) - q(n) + [q(n) + 1]\exp\left[-e\eta\dfrac{(V_b - V_{\varepsilon_n})}{kT}\right]} \right].$$

In this expression, Γ_c is the probability of tunneling from the nanocrystal to the collector, n is the number of electrons in the quantum well, p is the degeneracy of an unoccupied level, q is number of electrons at an unoccupied level, η is the part of the voltage that drops between the emitter and the quantum well, V_b is the voltage applied to the structure, V_{ε_n} is the threshold voltage necessary for transition of an electron from the emitter to the quantum level with energy ε_n, T is temperature, k is the Boltzmann constant, and e is the elementary charge.

The threshold voltage is determined both by the energy spectrum of the nanocrystal $\varepsilon_l(n)$ and by the characteristic electrostatic one-electron charging energy δ of a nanocrystal with the capacitance C,

$$V_{\varepsilon_n} = V_t + \frac{\varepsilon_l(n) + \delta n}{e\eta},$$

$$\delta = \frac{e^2}{C};$$

here, V_t is the threshold voltage required for the transition of an electron to the ground state of the silicon nanocrystal. The probability Γ_e of the electron finding itself in the Ge nanocrystal is determined by electron hopping along the conducting chain and by the position of the nanocrystal in the chain.

The energy spectrum of a silicon nanocrystal located in a wider gap SiO_2 matrix was calculated using the solution to a spherically symmetric Schrödinger equation in the effective-mass approximation. The following parameters were used in the calculations: the hole effective mass $m_h = 0.19m_0$; the electron effective mass $m_e = 0.26m_0$; the barrier heights were 4.34 eV and 3.2 eV for holes and electrons, respectively [16]. The change in the masses at the heterointerface was taken into account and the effective mass of charge carriers in SiO_2 was assumed to be $m_b = m_0$.

The Schrödinger equation was solved for a spherically symmetric case [17]:

$$\Delta\Psi + \frac{2m}{\hbar^2}[E - U(r)]\Psi = 0.$$

The electron wave function in a spherically symmetric case can be presented as the product of the radial wave function and the spherical function in each of the regions where the mass is constant:

$$\Psi(r, \theta, \phi) = \Phi(r)Y(\theta, \phi).$$

In our case, the potential is spherically symmetric, and, for all such potentials, the angular dependence of wave function is universal and is determined by the spherical functions. For the radial part of the wave function, we have the equation

$$\frac{1}{r^2}\frac{\partial}{\partial r}\left(r^2\frac{\partial}{\partial r}\Phi(r)\right) - \frac{L(L+1)}{r^2}\Phi(r) + \frac{2m}{\hbar^2}[E - U(r)]\Phi(r) = 0.$$

After the change of variables $\Phi(r) = \chi(r)/r$, the equation assumes the form

$$\frac{\partial^2\chi(r)}{\partial r^2} + \left[\frac{2m}{\hbar^2}[E - U(r)] - \frac{L(L+1)}{r^2}\right]\chi(r) = 0.$$

For the orbital moment L equal to zero, we can use the solution to the problem relating to a one-dimensional potential well:

$$\frac{d^2\chi(r)}{dr^2} + \left[\frac{2m}{\hbar^2}[E - U(r)]\right]\chi(r) = 0.$$

Here, $\chi(r)/r$ determines the radial part of the wave function. The condition $\chi(r = 0) = 0$ must be satisfied if the wave function is to be finite at the origin. This condition can be satisfied if the wall of the potential at $r = 0$ is assumed to be infinitely high. The role of the well width is played by the nanocrystal radius R and the potential has the following form:

$$U(r) = \begin{cases} \infty & \text{for } r = 0, \\ 0 & \text{for } 0 < r < R, \\ U_0 & \text{for } r \geq R. \end{cases}$$

Calculation of the energy states for the silicon nanocrystals made it possible to find the *I–V* characteristic that is shown in Fig. 4b, where it is compared to the experimental results. The calculated *I–V* characteristic is in good agreement with the experimental data. Therefore, we may assume that the observed features in the *I–V* curves are related to the Coulomb blockade, where single-electron charging of the nanocrystal built into a conducting chain blocks the hop of the next electron into the nanocrystal due to the increased electrostatic potential. This effect can be observed provided that the following relation is satisfied:

$$\frac{e^2}{2C} \gg kT.$$

This relation implies that the electrostatic charging energy for the nanocrystal must be substantially higher than the thermal energy. Estimations show that, for a nanocrystal 2–5 nm in size, with regard to the dependence of the permittivity on the nanocrystal size, the electrostatic energy is about 60–32 meV; i.e., it is an order of magnitude higher than kT at liquid- nitrogen temperature (6.63 meV). One further condition for the observation of the Coulomb blockade is that the probability of an electron entering the nanocrystal located in the main conducting chain must be higher than the probability of it leaving the nanocrystal. In our case, this condition was satisfied by statistical selection of the experimental samples. The probability of one-step electron tunneling from the metal into the nanocrystal across the oxide layer is very low, and, in our case, the electron, presumably, reaches the nanocrystal by repeated tunneling hops via the states in SiO_x We believe that the presence of these states in SiO_x is caused by those excess silicon atoms that are introduced by ion implantation and are not concentrated in the nanocrystals.

The theoretical *I–V* characteristic has a stepped shape and contains two groups of steps separated by a wide plateau. The first stepped increase in the current arises when the emitter level coincides with the ground single-electron quantum confinement level E_0 in the nanocrystal. When the condition $\Gamma_e \gg \Gamma_c$ is satisfied, a single electron is accumulated in the potential well, thus increasing the energy of the system by e^2/C [15]. The following stepped increase in the current occurs when the emitter level coincides with the two-electron ground state possessing the energy $E_1 = E_0 + e^2/C$. After filling of the ground quantum confinement level, the number of electrons in the nanocrystal is equal to two and the energy of the entire system is increased by $2e^2/C$. Therefore, the next step in the *I–V* characteristic appears when the emitter level coincides with the next one-electron level, whose energy is now $E_1 + 2e^2/C$, and the number of electrons in the well after that becomes equal to three. Further filling of the levels occurs in a similar way. Thus, one-electron charging of the nanocrystal removes the degeneracy of the quantum-confinement levels. Such an approach disregards the interaction of electrons in the well. The levels E_0 and E_1 were calculated using the one-electron approximation. It is quite possible that, when a silicon nanocrystal is occupied by four or more electrons, this interaction becomes important, and this fact can explain the current instability observed at voltages exceeding 9.5 V.

It should be noted that both the theoretical and the experimental *I–V* characteristics in Fig. 4b are normalized by the quantity $e\Gamma_c$, where, from comparison with

the experimental data, the value of the probability Γ_c of tunneling to the collector was taken to be 7×10^9 s^{-1}. Then, the levels of the steps observed in the experiment become equal to the series of natural numbers 1, 2, 3, and 4. They correspond to the number of electrons in the nanocrystal for an applied bias and reflect the fact that the current in the Coulomb blockade mode is determined by the product of the number of electrons in the quantum dot and the probability of transition to the collector.

In the case of a silicon nanocrystal ~5 nm in diameter, the separation between quantum-confinement levels is greater than the characteristic electrostatic energy e^2/C, and, therefore, the narrow plateaus in the *I–V* characteristic correspond to the energy differences between one- and two-electron states and the wide plateaus correspond to the energy differences between the quantum-confinement levels. Thus, we may conclude that we have observed resonant tunneling through the ground and first excited quantum-confinement levels of the nanocrystal and a fine structure related to the splitting of confinement levels due to one-electron charging of the nanocrystal.

4. CONCLUSIONS

Thus, we observed a stepped *I–V* characteristic of a MOS structure with silicon nanocrystals in its oxide layer at liquid-nitrogen temperature. The stepped *I–V* characteristic was quantitatively described in the context of a model that implies the existence of charge transport along a chain of local states containing a silicon nanocrystal. The presence of the steps was attributed to one-electron charging of the silicon nanocrystal and to the Coulomb blockade of the probability of electron hopping from the nearest local state in the conducting chain. We assumed that the local states in silicon oxide correspond to small-sized clusters of excess silicon atoms, formed as a direct result of ion implantation of silicon. The presence of such states in silicon oxide is confirmed by the measurements of differential conductance and capacitance. For the MOS structures implanted with silicon, we observed an increase in differential capacitance and conductance with respect to the reference structures for bias voltages exceeding 0.2 V. In same region of voltages, the conductance of the structures decreases under ultraviolet irradiation, which changes the filling of the chains.

REFERENCES

1. T. Shimizu-Iwayama, K. Fujita, S. Nakao, *et al.*, J. Appl. Phys. **75**, 7779 (1994).
2. G. A. Kachurin, I. E. Tyschenko, V. Skorupa, *et al.*, Fiz. Tekh. Poluprovodn. (St. Petersburg) **31**, 730 (1997) [Semiconductors **31**, 626 (1997)].
3. Y. C. King, T. J. King, and C. Hu, in *International Electron Devices Meeting Technical Digest* (1998), p. 115.
4. C. Delerue, M. Lannoo, and G. Allan, Phys. Rev. Lett. **84**, 2457 (2000).
5. A. Zunger and L.-W. Wang, Appl. Surf. Sci. **102**, 350 (1996).
6. B. Delley and E. F. Steigmeier, Appl. Phys. Lett. **67**, 2370 (1995).
7. D. Babic, R. Tsu, and R. F. Greene, Phys. Rev. B **45**, 14150 (1992).
8. R. Tsu, Appl. Phys. A **71**, 391 (2000).
9. G. A. Kachurin, A. F. Leĭer, K. S. Zhuravlev, *et al.*, Fiz. Tekh. Poluprovodn. (St. Petersburg) **32**, 1371 (1998) [Semiconductors **32**, 1222 (1998)].
10. Q. Ye, R. Tsu, and E. H. Nicollian, Phys. Rev. B **44**, 1806 (1991).
11. R. Tsu, X.-L. Li, and E. H. Nicollian, Appl. Phys. Lett. **65**, 842 (1994).
12. R. Tsu, Appl. Phys. A **71**, 391 (2000).
13. Y. Inoue, A. Tanaka, M. Fujii, *et al.*, J. Appl. Phys. **86**, 3199 (1999).
14. I. I. Abramov and A. L. Danilyuk, Zh. Tekh. Fiz. **68** (12), 93 (1998) [Tech. Phys. **43**, 1485 (1998)].
15. D. V. Averin, A. N. Korotkov, and K. K. Likharev, Phys. Rev. B **44**, 6199 (1991).
16. V. A. Burdov, Fiz. Tekh. Poluprovodn. (St. Petersburg) **36**, 1233 (2002) [Semiconductors **36**, 1154 (2002)].
17. L. D. Landau and E. M. Lifshitz, *Course of Theoretical Physics*, Vol. 3: *Quantum Mechanics: Non-Relativistic Theory*, 3rd ed. (Nauka, Moscow, 1974; Pergamon, New York, 1977).

Translated by I. Zvyagin

Semiconductors, Vol. 39, No. 8, 2005, pp. 917–923. Translated from Fizika i Tekhnika Poluprovodnikov, Vol. 39, No. 8, 2005, pp. 953–960.

CONFERENCE.
AMORPHOUS, VITREOUS, AND POROUS SEMICONDUCTORS

Processes of Growth of Disordered Semiconductors in the Context of Self-Organiziation Theory

S. P. Vikhrov^, N. V. Bodyagin, T. G. Larina, and S. M. Mursalov

Ryazan State Radio Engineering Academy, Ryazan, 390024 Russia

^ e-mail: mel@rgrta.ryazan.ru

Submitted December 27, 2004; accepted for publication January 10, 2005

Abstract—The possibility of applying the concepts and methods of self-organization theory to the growth of disordered semiconductors is justified. A basic method for analyzing the dynamics of complex systems is described. The invariants of random dynamics are considered in the context of the processes involved in material growth. New principles for the construction of technological systems are stated. *© 2005 Pleiades Publishing, Inc.*

1. INTRODUCTION

The development of ever more complicated devices for micro- and nanoelectronics as well as the necessity of a substantial increase in the rate of film growth without deterioration of the films' device characteristics requires deeper insight into the laws of structure formation and the properties of disordered materials and their evolution. A number of problems related to material technology need to be solved, particularly, the irreproducibility of a structure and its properties, the thermodynamic metastability of a structure, and the imperfection of the algorithms of technology optimization.

These problems are interrelated and arise because the processes of solid-state formation are usually considered in the context of equilibrium thermodynamics. This approach does not correspond to complex internal dynamic processes occurring in matter during synthesis, which are essentially nothing else but complex behavior, i.e., self-organization [1–4]. The processes in these materials are characterized by the following basic attributes of self-organizing systems: thermodynamic openness, pronounced nonequilibrium, symmetry breaking, and a discontinuous change in physical characteristics. Therefore, a different approach to the processes of growth of disordered materials, which would make it possible to simulate the structure of amorphous semiconductors and control the technologies required for micro- and nanostructures, is necessary.

In our opinion, such an approach should be based on the concepts and methods of complex systems' theory (self-organization and nonlinear processes) and on related concepts of deterministic chaos that can be considered as the supercomplex ordered behavior of dynamic systems whose structure cannot be established by "classical" methods of the study of order (for example, by the Fourier method).

It should be noted that complex systems' theory itself is still being developed and its methods are far from perfect. However, even using only the philosophy and methodology of this theory makes it possible to critically reanalyze many widely accepted statements on solid state physics and to substantially advance our understanding and control of complex processes during the formation of a solid state structure.

2. METHODOLOGICAL APPROACH TO THE STUDY OF PROCESSES INVOLVED IN THE FORMATION OF DISORDERED SEMICONDUCTORS IN THE CONTEXT OF SELF-ORGANIZATION THEORY

The idea of self-organization has emerged as an alternative explanation to the appearance of ordered structures in disordered media. The appearance of coherence in an originally chaotic medium is considered as the main attribute of self-organization. A system is called self-organizing if it acquires some spatial, temporal, or functional structure without exposure to external factors, i.e., spontaneously [1]. A self-organized system acquires new collective properties not initially possessed by its elements. These properties are seen as correlations; i.e., reproducible mutual relations between distant parts of the system are created and maintained. In crystals, the correlations correspond to medium- and long-range order, structures described by systems of equations with fractal dimensionality, etc. In disordered materials, the correlations exist as a small (with respect to the number of atoms) set of modes, i.e., harmonics forming chaotic dynamics.

From the point of view of complex systems' theory, a self-organized system still has a small number of order parameters that determine its behavior. This circumstance underlies the main idea in experimental studies of these systems: it is not necessary to investigate the dynamics of the entire original infinite-dimensional phase space. Rather, it suffices to observe the

attractor of a system; in many cases, in the mathematical description, the dimensionality of the attractor appears to be rather low, e.g., 3, 5, or something similiar [5]. The attractor in the theory of nonlinear systems characterizes a system's state when determined by a small number of parameters and attained as the evolution time tends to infinity [6].

The main method applied to analysis of complex systems dynamics is the Tackens embedding method. In this method, the behavior of a system can be decoded from any dynamic or spatial characteristic; indeed, any signal from a system contains information about all the processes inside it, since all the parts of a dynamic system are interrelated and can be considered as a whole. Thus, it is possible to study the dynamics of a system by measuring any of the dynamic variables at one point at regular intervals. The obtained sequence of data is usually processed using the Grassberger–Procaccia algorithm. Thus the form and dimensionality of the attractor, number of degrees of freedom, Lyapunov exponents, and other dynamics parameters are determined. This method was originally developed for study of the behavior of systems whose state varied over time; later, it was adapted to studying spatially distributed systems, e.g., material surfaces [7, 8].

In order to prove the fact that the structure of noncrystalline materials represents "frozen" deterministic chaos [4, 8–10], i.e., cannot actually be represented as a random atomic network, the structure of the surface of amorphous hydrogenated silicon (*a*-Si:H) was studied using scanning tunneling microscopy and atomic-force microscopy (AFM) [11]. The surface structures of different materials were experimentally studied using the Tackens embedding method. It was assumed that the surface provided a "frozen" image of the dynamic pattern of the processes included in material growth from the gas phase, for example, *a*-Si:H (disregarding the relaxation processes), and, hence, the distribution of a substance over the surface contained information on the space–time growth dynamics. The height of the surface profile of a structure was chosen as the variable to be measured (with reference to some level taken as zero), since it uniquely describes the distribution of the substance on the growth surface and represents the processes of space–time evolution.

3. TOPOLOGICAL INVARIANTS OF THE CHAOTIC DYNAMICS OF MATERIAL GROWTH

It is convenient to introduce different categories for the behavior of the systems by using, as a label, the fractal dimensionality D of the corresponding attractor, which is determined according to the Grassberger–Procaccia algorithm [6, 12]. It allows us to distinguish between systems described by extremely complicated chaotic, but, at the same time, deterministic, behavior and systems exhibiting purely random behavior. Using the dimensionality of the attractor, we can estimate the number n of order parameters, such that all the other degrees of freedom of the system are adjusted to these parameters:

$$n > 2D + 1. \tag{1}$$

As was noted above, the trajectory in a p-dimensional phase space can be reconstructed starting from the one time (position)-dependent variable $X(t)$ and by choosing, as coordinates, the quantities $X(t)$, $X(t + T)$, $X(t + 2T)$, …, $X(t + (p - 1)T)$, where T is a properly defined delay time. Since the time t is discretized, we obtain a series of p-dimensional vectors (N) representing the phase diagram of a dynamic system. Thus, we set the reference point $\mathbf{X}_i$ for all the available data and can calculate the distances from this point to the remaining $N - 1$ points: $|\mathbf{X}_i - \mathbf{X}_j|$. We can now calculate the number of points in the phase space that are located at a distance from $\mathbf{X}_i$ not exceeding some given quantity r. By repeating this process for all the values of i, we can calculate the quantity $C(r)$, known as the correlation integral:

$$C(r) = \lim_{N \to \infty} [1/N^2] \sum_{i,\, j = 1}^{N} \Theta_{i \neq j} (r - |\mathbf{X}_i - \mathbf{X}_j|). \tag{2}$$

Here, $\Theta(x)$ is a unit-step function equal, by definition, to unity at positive x and zero at other values of x.

We fix some small number ξ and use it as a measure for probing the attractor structure. If the attractor is linear, then, obviously, the number of probing points, from which the distance to a given point does not exceed r, is proportional to r/ξ. If the attractor is a surface, then the number of such points is proportional to $(r/\xi)^2$. In a more general case, where the attractor represents a D-dimensional manifold, the number of points is proportional to $(r/\xi)^D$. Therefore, we can expect that, at relatively small r, the function $C(r)$ varies in the form

$$C(r) = r^D. \tag{3}$$

Thus, we can determine the correlation dimensionality from the slope of the dependence of $\ln C(r)$ on $\ln r$:

$$D = \lim_{r \to 0} \lim_{N \to \infty} [d \ln C(r, N)/d \ln r]. \tag{4}$$

The algorithm for calculating D can be summarized as follows.

(i) Starting from a given temporal (spatial) sequence, we construct correlation function (2) for successively increasing values of the dimensionality n of the phase space.

(ii) Using (4), we determine the slope D near the origin and its dependence on the increasing value of n.

(iii) If D, as a function of n, attains a plateau above some value n, then the system represented by this temporal (spatial) sequence must have an attractor. The quantity D determined by the instant of saturation should be considered as the dimensionality of the attractor. Finite nonintegral values of D signify that

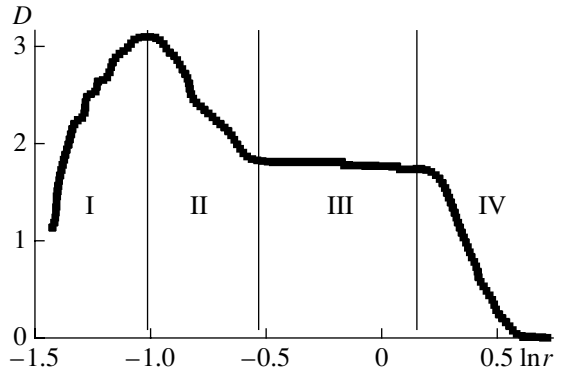

Fig. 1. A typical $D = f(\ln r)$ dependence.

dynamic chaos is observed in the system. The value of n after which saturation is attained determines the minimum number of variables necessary for simulating the behavior that corresponds to a given attractor. It should be noted that, for a random-noise sequence, the tendency towards saturation is not observed and the quantity D is not defined [6].

In most of the experimental and numerical studies of chaotic systems, the slope of the $C(r)$ curve in the log–log plot, i.e., $D = d[\ln C(r)]/d(\ln r)$, has been studied as a function of $\ln r$. A typical shape for this plot is shown in Fig. 1, where we can see that there are four regions.

Region I. In this region, the cell size is too small. Each cell contains only a few points and one cannot estimate the true probabilities p_i of, at some instant, a point on the phase trajectory being in cell i.

Region II. In this region, the sample is insufficient to represent the Cantor structure of the attractor. In addition, the experimental error or the accuracy attained when finding the points of the attractor are usually important.

Region III. The points of the curve in this interval characterize the fractal dimensionality of the attractor. To expand region III, we can increase the size of the sample, improve the experimental accuracy, or choose the best way of selecting the variables to be analyzed.

Region IV. The cell size tends to the attractor size and does not characterize its Cantor structure.

The characteristic attributes of the deterministic chaos in distributed systems are [11] as follows:

(I) The presence of a linear section on the dependence D on $\ln r$ and, therefore, the presence of a plateau in the dependence of $d[D(r, n)]/d(\ln r)$ on $\ln r$ in a certain interval of r;

(II) saturation of the quantity $\Delta D = D(n) - D(n - 1)$ at large n.

By measuring the height of the profile of the *a*-Si:H samples across the surface in discrete intervals, we obtained a three-dimensional image of square areas of the surface. The height of the profile was measured at $(12–15) \times 10^3$ points. As was shown in [11, 12], this number of points is sufficient for revealing the topology of the attractor.

The *a*-Si:H samples were prepared by low-frequency glow discharge from 100% SiH_4 at a discharge power of 50 mW cm^{-2}, pressure of 70 Pa, silane feed rate of 200 cm^3/s, and substrate temperatures of 100, 225, and 325°C [13]. Figures 2, 3, and 4 show AFM images of the surfaces of these samples (Fig. 2), the distribution function of the profile height h (ρ is the probability density) (Fig. 3), and the dependence of D and $dD/d\ln r$ on n and $\ln r$ (Fig. 4, curves *1* and *2*, respectively).

When studying the image of the surface visually, we can clearly see that its roughness decreases as the substrate temperature increases. The convexity regions increase and the rest of the surface becomes smoother. The distribution function changes accordingly: the variance decreases and the maximum is shifted to the region of lower values of the profile height.

The dependence of $D = f(n, \ln r)$ on the substrate temperature is complicated. In all cases, three different segments are observed in the ranges: from 0 to –0.6, from –0.6 to –1.4, and from –1.4 to –1.8. In these segments, there are regions with a linear slope that saturates at the embedding dimensionality of $n = 8$. Such behavior indicates that the required distribution has a deterministic chaotic character. As the substrate tem-

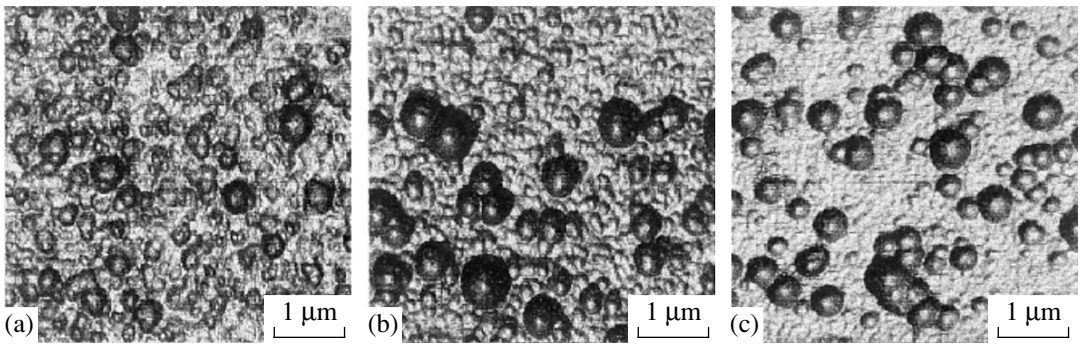

Fig. 2. Surfaces of *a*-Si:H samples grown at substrate temperatures of (a) 100, (b) 225, and (c) 325°C [11].

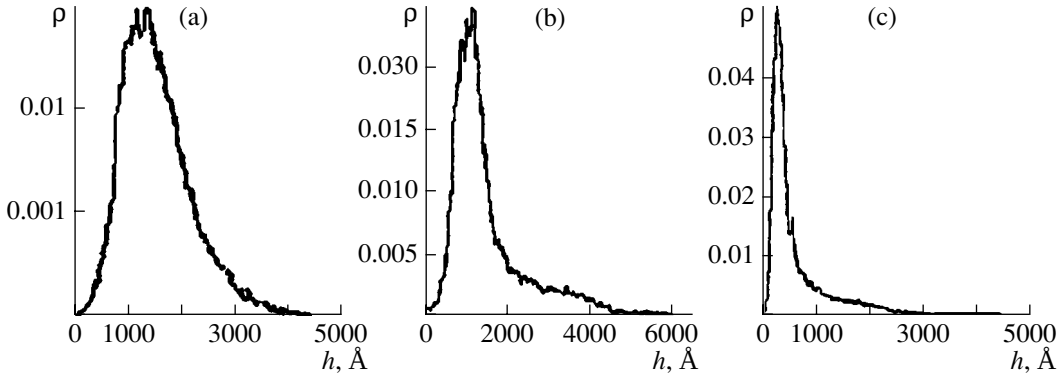

Fig. 3. Distribution functions of the height of the profile for *a*-Si:H samples grown at substrate temperatures of (a) 100, (b) 225, and (c) 325°C [11].

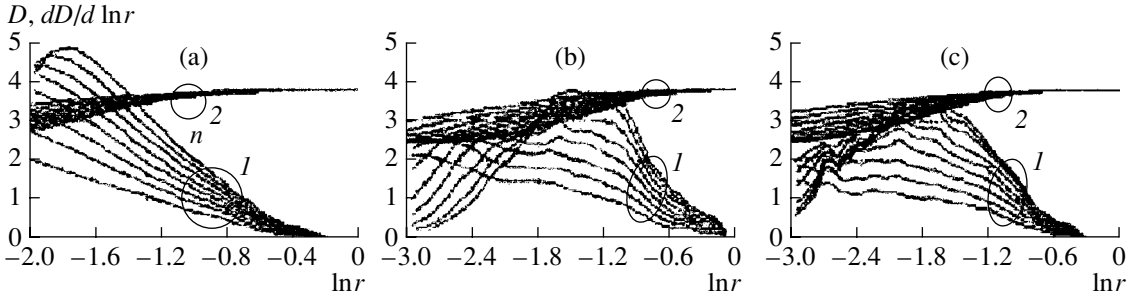

Fig. 4. Dependences of (*1*) *D* and (*2*) *dD*/*d*ln*r* on ln*r* for *a*-Si:H samples grown at substrate temperatures of (a) 100, (b) 225, and (c) 325°C [11].

perature increases, these segments become more pronounced. Apparently, their existence indicates that growth is determined by three different mechanisms.

By analyzing the results of the experimental studies, we can make the following conclusions. The landscape of the *a*-Si:H surface represents an image of a "frozen" instant of the growth processes, and the structure of the surface of the material can be described as "frozen" dynamic chaos [8, 14]. This chaos manifests itself as a very complicated irregular behavior that is superficially similar to the usual thermal chaos but, in fact, is fundamentally different from it. In the mode of dynamic chaos, the amplitude of deviation from the mean is comparable to the mean itself but the number of space–time scales is so large that the behavior of the system seems chaotic. For thermal chaos, all the characteristic scales are microscopic and fluctuations around the mean are extremely small.

Thus, fractal dimensionality allows us to define the dimensionality and the form of the growth dynamics. It is a convenient measure for the identification of systems. However, it is not as useful for practical applications (simulation and control). Physicists and technologists studying the processes involved in the growth of different materials and the control of these processes are very interested in other topological invariants reflecting the geometrical properties of the dynamics-characterizing vector field, namely, the Lyapunov exponents.

The Lyapunov exponents are the most informative dynamic invariants. We now consider their physical meaning and the calculation procedure in more detail. We choose two close points, $x'(0)$ and $x''(0)$, located on the attractor and find the time variation in the distance $d(t) = |x'(t) - x''(t)|$ between them. Here, $x'(t)$ and $x''(t)$ are solutions to an nth-order differential equation describing the space–time evolution of a system with the initial parameters $x'(0)$ and $x''(0)$. If the attractor is a singular point, then $d(t) = 0$. If the attractor is a limiting cycle, then $d(t)$ is a periodic function of time. For a strange attractor, we have $d(t) \propto \exp(\lambda_t t)$, $\lambda_t > 0$ (of course, as long as $x'(t)$ and $x''(t)$ are sufficiently close) [15].

The quantity λ_t is called the Lyapunov exponent:

$$\lambda_t(x'(0), \boldsymbol{\omega}) = \lim_{t \to \infty} \lim_{d(0) \to 0} \{(1/t)\ln d(t)/d(0)\}. \quad (5)$$

Here, ω is the vector from the point $x'(0)$ to the point $x''(0)$. We can say that the Lyapunov exponent, if it is positive, characterizes the average rate at which two infinitely close trajectories diverge (or converge if it is negative).

Lyapunov exponents determine the correlation time τ_c in a system. After this time, the correlation between

the characteristics of a process at close instants is weakened and multidimensional distribution functions factorize into the product of one-dimensional functions.

In [11], we suggested estimating λ_t on the basis of the following reasoning. Let two points, initially separated by an infinitesimal distance ε, appear, after a certain period of time, at a distance of $\sim\varepsilon\exp(\lambda_t t)$. The correlation time is exactly the time after which the infinitesimal difference in the initial conditions becomes comparable to the characteristic attractor size R. Using this reasoning, we can write the expression for τ_c as follows:

$$\tau_c = \frac{1}{\lambda_t}\lim_{\varepsilon\to 0}\ln(R/\varepsilon). \quad (6)$$

As regards the growth processes, the presence of positive temporal Lyapunov exponents means that, after a time proportional to the correlation time, the structure of the overlying layers does not copy the structure of the underlying layers. If we consider two different, but simultaneous, technological processes, after the time τ_c, the correlation between the structures of the growing materials vanishes. If we estimate τ_c using formula (6), then ε is determined by the error (fluctuations) Δp in the control parameters of the technological process or by fluctuations in the surrounding medium f:

$$\varepsilon = \Delta p + f. \quad (7)$$

By generalizing formulas (4)–(6), we can write the following expression for τ_c:

$$\tau_c = A/\lambda_t. \quad (8)$$

Here, A is a constant whose value depends on the choice of criterion for the degree of correlations.

By analogy with systems evolving over time, to obtain instant images of our space–time system, we can introduce the concept of spatial Lyapunov exponents λ_r, whose number is equal to the dimensionality of the space containing the spatial attractor.

The Lyapunov spatial and temporal exponents λ_r and λ_t characterize the stability of a space–time system from different sides. We can assume that λ_r characterizes the instability of spatial distribution or, in other words, its sensitivity to the difference in initial spatial positions. We consider a cross section of the surface of the material when formed under certain conditions. We fix a point with the coordinate x_0, where the height of the profile is h_1. We assume that another surface has been formed under the same conditions. Its difference from the first surface consists only in the difference of the height of the profile at the point x_0, and this difference is infinitesimal. Provided that even one of the spatial Lyapunov exponents is positive, the difference δ in the heights of the surface profile becomes comparable to the average height P of the profile at a distance l_c from the point x_0. At such distances, the profiles are completely different. By analogy with τ_c, we call the quantity l_c the correlation length,

$$l_c = (1/\lambda_r)\lim_{\delta\to 0}\ln(P/\delta). \quad (9)$$

By analogy with formulas (5)–(8), expression (9) can be written in the following form:

$$l_c = B/\lambda_r. \quad (10)$$

The presence of positive Lyapunov exponents for the system of equations describing the structure of the material signifies that this structure has no spatial translational symmetry, i.e., the structures of two regions of the material, located at a distance $l > l_c$ from each other, are not correlated. If $l_c \ll L$ (L is the size of the system), there is no long-range order in the system and we can assert that the structure of the material is noncrystalline. The structure and the properties of the regions of the material located at a distance from each other exceeding the correlation length do not coincide.

From the standpoint of thermodynamics, λ_r characterizes a nonequilibrium state of the system; i.e., it measures its deviation from the globally stable state of thermodynamic equilibrium. Thus, if the structure of the material corresponds to the equilibrium state, it means that the substance is distributed in space randomly or, ideally, periodically. For such a distribution, there are no positive Lyapunov exponents. The presence of exponents $\lambda_r > 0$ means that the distribution differs from equilibrium. Therefore, after growth, relaxation processes occur in the structure of the material that transform it to the equilibrium (crystalline) state. This state can exist for quite a long time, since the external conditions do not permit attainment of the equilibrium. It is technologically important that the Lyapunov exponents make it possible to determine the limits of predictable (controlled) growth of the structure on different space–time scales, i.e., to actually determine the limits of reproducibility of the material characteristics.

The fact that irreproducibility is determined by the instability of chaotic dynamics makes us rather skeptically assess the possibility of using the traditional method of increasing reproducibility by increasing the accuracy attained when specifying the control parameters. Therefore, other approaches to improving reproducibility, based on understanding the dynamic processes occurring in the material during solidification, are necessary. We believe that the principles of control applied to existing technologies should also be changed, since they aim to control the chaotic dynamics of the material by linear methods and these methods do not correspond to the material properties arising upon solidification. In relation to new technologies, it must be recognized that the control parameters should be consistent with the internal dynamic processes in the material. Below, we consider principles of the construction of technological systems based on this approach [16].

4. PRINCIPLES OF THE CONSTRUCTION OF TECHNOLOGICAL SYSTEMS

The compatibility principle reflects the requirement for consistency of the control parameters with the internal properties of the material upon solidification. The control system must understand and reproduce the language of the system we wish to control. In this way, the highest control efficiency is realized. The consistency between the external factors and the properties of the material is more important than the intensity and duration of the action of these factors. It should be borne in mind that it is impossible to attain 100% efficiency, since uncertainty about the behavior of a complex system is always present. This factor is a fundamental property. On the basis of experimental data, corresponding changes in the control parameters are determined so that two substantially different problems can be solved:

(i) stabilization of periodic orbits in the chaotic mode, i.e., the destruction of chaos;

(ii) stochastization of the system by connecting it to another chaotic system.

The choice of method is determined by the aims of the technology in question. For example, if the growth of a perfect crystalline structure or reproduction of some structural inhomogeneity is required, then it is necessary to pass quickly the stage of chaos and to stabilize the periodic dynamics of the system, for example, by applying the Grebogi–Otto–Yorke method, which is used for stabilizing the unstable orbits of a chaotic attractor. In contrast, to synthesize amorphous materials, a chaotic drive is useful. If the problem is to eliminate macroinhomogeneities, then it is necessary to destroy the nonlinear superposition of a limited number of modes. In all cases, the characteristics of the control factors should be formed on the basis of exact knowledge of the dynamics of the material upon solidification.

The hierarchy principle. Nature has a hierarchical structure. This hierarchical structure grants relative autonomy to the different levels of the system subordinated to the main controller, but, at the same time, it introduces a forced abandonment of control over all the changes that occur in the system. This structure implies that control should also be constructed according to the hierarchical principle. Therefore, when stating a control problem, it is necessary to divide the system into levels and choose a level to be responsible for the required properties.

For technologies related to noncrystalline materials, this procedure means that a certain level must be chosen for control purposes: nano-, micro-, structure–chemical inhomogeneities, etc. Then, the dynamics at this level should be studied and the corresponding control factors should be determined. In this case, the problem of incomplete control arises; i.e., the control is possible only at some levels responsible for certain properties.

The adequacy principle. The control systems should, apparently, have the same order of complexity as the systems to be controlled; i.e., the set of possible modes of behavior of the control system must not be less informative. Generally speaking, it is necessary to have a control device of such complexity that it can independently and continuously search for constraints and statistical correlations and optimize the states of certain parts of the controlled system.

It is quite probable that the dynamics of formation of a noncrystalline structure is so complicated that it cannot be investigated and simulated. In this case, a previously grown material, considered as a black box, can be used as a certain reference element for the technology. Using the corresponding excitations, we can transfer the eigenvibrations of this element to the structure that is formed. A general diagram of this method is as follows:

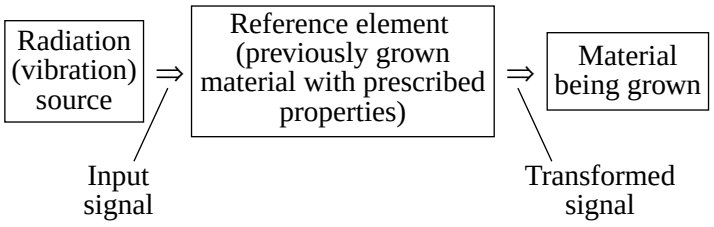

The principle of time synchronization. The time scales of the controls must coincide with those for the corresponding processes in the controlled system.

The locality principle. Self-organization is one of the processes during which the system can be controlled. It has restricted space–time scales and occurs in a local region of space. The processes involved in formation of an amorphous structure are localized in a quite definite region, namely, in the intermediate layer between the gas or liquid phase from which the solid state structure grows and the already grown structure. The controls must be localized in space–time, i.e., they must be finally oriented to the surface states.

The uncertainty principle. Generally, it should be borne in mind that efforts directed at increasing the control efficiency or reproducibility cannot change the probabilistic random character of the formation of the structures [15].

5. CONCLUSIONS

By applying complex systems theory (self-organization) to the description of disordered materials and the laws of their formation, we can not only simulate the synthesis of a disordered material from a new standpoint but, first and foremost, gain insight into the physical nature of some of the fundamental problems related to these materials. Thus, it becomes clear that the growth process corresponds to a self-organization mode that can be described by a limited number of degrees of freedom; moreover, the distribution of a substance on the surface, representing a picture of a frozen instant of the growth process, has a deterministic chaotic character. Thus, the presence of correlations, i.e., reproducible ratios between the atoms (molecules) in different parts of the system, is a deterministic factor during synthesis. The correlation scales allow us to estimate the reproducibility of the grown structure.

Our main conclusion is that a new approach to the process of formation of noncrystalline structures, self-organization, allows us to consider the principles of the technologies related to these materials in new terms and means that there are real prospects for a substantial increase in the efficiency of these technologies. The development of this line of research will, quite probably, not only result in improvement of the reproducibility of the material characteristics and make the process of technology optimization much faster but, first and foremost, will make it possible to intentionally synthesize materials with substantially new properties.

REFERENCES

1. A. A. Aĭvazov, N. V. Bodyagin, and S. P. Vikhrov, Izv. Vyssh. Uchebn. Zaved., Élektron., No. 1, 39 (1997).
2. N. V. Bodyagin, S. P. Vikhrov, and S. N. D'yakov, in *Physics of Semiconductors and Microelectronics* (RGRTA, Ryazan, 1995), p. 92 [in Russian].
3. S. P. Vikhrov, A. A. Aĭvazov, and N. V. Bodyagin, Vestn. RGRTA **1**, 77 (1996).
4. S. P. Vikhrov and N. V. Bodyagin, in *Physics of Semiconductors and Microelectronics* (RGRTA, Ryazan, 1995), p. 3 [in Russian].
5. H. D. I. Ababranel, R. Rown, J. J. Sidorovich, and L. S. Tsimiring, Rev. Mod. Phys. **65**, 1331 (1993).
6. G. Nicolis and I. Prigogine, *Exploring Complexity* (Freeman, New York, 1989; Mir, Moscow, 1990).
7. A. A. Aivazov, N. V. Bodyagin, S. P. Vikhrov, and S. V. Petrov, J. Non-Cryst. Solids **114**, 157 (1989).
8. N. V. Bodyagin, S. P. Vikhrov, and A. A. Aĭvazov, Izv. Vyssh. Uchebn. Zaved., Élektron., Nos. 3–4, 7 (1997).
9. N. V. Bodyagin, Izv. Vyssh. Uchebn. Zaved., Élektron., No. 2, 31 (1997).
10. A. A. Aivazov, N. V. Bodyagin, and S. P. Vikhrov, Mater. Res. Soc. Symp. Proc. **420**, 145 (1996).
11. N. V. Bodyagin, S. P. Vikhrov, T. G. Larina, S. M. Mursalov, and V. N. Timofeev, *Nature of Nonreproductivity of the Structure and Properties of Materials for Micro- and Nanoelectronics* (RGRTA, Ryazan, 2004) [in Russian].
12. T. S. Akhromeeva, S. P. Kurdyumov, G. G. Malinetskiĭ, and A. A. Samarskiĭ, *Nonstationary Structures and Diffusion Chaos* (Nauka, Moscow, 1992) [in Russian].
13. N. V. Bodyagin and S. P. Vikhrov, *Control of Growth Processes of Semiconductor Materials* (RGRTA, Ryazan, 1997) [in Russian].
14. N. V. Bodyagin and S. P. Vikhrov, Pis'ma Zh. Tekh. Fiz. **23** (19), 77 (1997) [Tech. Phys. Lett. **23**, 767 (1997)].
15. S. P. Vikhrov and N. V. Bodyagin, *New Approach to Development of Technological Systems by the Example of a-Si:H Layer Growth* (RGRTA, Ryazan, 1994) [in Russian].
16. N. V. Bodyagin, S. P. Vikhrov, S. M. Mursalov, and I. V. Tarasov, Mikroélektronika **31**, 307 (2002) [Microelectronics **31**, 260 (2002)].

Translated by I. Zvyagin

Semiconductors, Vol. 39, No. 8, 2005, pp. 924–927. Translated from Fizika i Tekhnika Poluprovodnikov, Vol. 39, No. 8, 2005, pp. 960–963.

CONFERENCE.
AMORPHOUS, VITREOUS, AND POROUS SEMICONDUCTORS

Photoinduced Relaxation of Metastable States in (*a*-Si:H):B

N. N. Ormont^, I. A. Kurova, and G. V. Prokof'ev

Faculty of Physics, Moscow State University, Vorob'evy gory, Moscow, 119992 Russia

^ e-mail: ormont@phys.msu.ru

Submitted December 27, 2004; accepted for publication January 12, 2005

Abstract—The kinetics of thermal relaxation of an ensemble of photoinduced metastable electrically active B atoms in (*a*-Si:H):B films is studied after partial relaxation of the ensemble in the dark and under illumination of various intensities and duration. The parameters of a stretched exponential function that describes the ensemble kinetics are determined. It is found that photoinduced relaxation of metastable states manifests itself under conditions in which its rate exceeds the rate of the states' photoinduced generation. It is shown that the variations in the relaxation-time distribution function of metastable states caused by thermal and photoinduced relaxation are similar. © *2005 Pleiades Publishing, Inc.*

Photoinduced relaxation of metastable dangling bonds in amorphous hydrogenated Si was originally predicted theoretically [1] and then experimentally observed in undoped *a*-Si:H films [2, 3]. We have previously observed photoinduced relaxation of metastable electrically active impurity atoms (MEAIs) in lightly B-doped *a*-Si:H films [4, 5]. The aim of this study was to examine the photoinduced relaxation of these atoms in lightly B-doped *a*-Si:H films in more detail, specifically, to examine the kinetics of variation in their relaxation-time distribution function under illumination.

We studied B-doped *a*-Si:H films obtained by deposition in RF glow discharge plasma. The films were doped from the gas phase. According to SIMS data, the total B concentration was $N_B = 3 \times 10^{17}$ cm^{-3}.

The experimental procedure and its justification were described in detail in [4, 5]. The procedure is based on determination and comparison of the parameters of the thermal relaxation kinetics of MEAI ensembles obtained by partial relaxation of an ensemble, which was preliminarily generated by intense illumination, in the dark and under illumination. A stretched exponential function with parameters characterizing the ensembles describes the kinetics of thermal relaxation of these ensembles:

$$N(t) = N(0)\exp(-(t/\tau_0)^{\beta}).$$

Here, $N(0)$ is the total initial MEAI concentration in an ensemble; τ_0 is the effective relaxation time of an ensemble, which is close to the value of τ at the peak of the distribution function $f(\tau)$ for MEAIs; and β^{-1} characterizes the half-width of the function $f(\tau)$. It was also shown that, for the (*a*-Si:H):B films studied, the kinetics of variation in the dark conductivity of a film $\sigma_d(t)$ at a given temperature reflects the kinetics of variation in the concentration of atoms in the ensemble at this temperature according to the relation

$$N(t) = A\log[\sigma_d(t)/\sigma_{d0}].$$

Here, σ_{d0} is the equilibrium dark conductivity at this temperature and A depends primarily on the temperature and constant density of states in the region of the shift of the Fermi level during the relaxation of the MEAIs.

In this study, we measured the kinetics of variation in the conductivity of an (*a*-Si:H):B film with different ensembles of photoinduced MEAIs at 410 K. It is noteworthy that the formation of photoinduced MEAIs increased the film conductivity, while their relaxation decreased the film conductivity. Figure 1 shows the experimental time dependences of $\log[\sigma_d(t)/\sigma_{d0}]$, which are described by stretched exponential functions with different parameters (curves *1–7*). These curves reflect the kinetics of relaxation of the MEAIs in the following ensembles.

Curve *1* corresponds to thermal relaxation of the initial MEAI-I ensemble, which was formed by preliminary irradiation of the film under study for 300 s with white light at an intensity of 80 mW cm^{-2} from a halogen lamp with an IR filter.

Curves *2*, *4*, and *6* correspond to thermal relaxation of the same ensemble after its partial thermal relaxation for 100, 300, and 1200 s, respectively.

Curves *3*, *5*, and *7* correspond to thermal relaxation of the same ensemble after its partial thermal relaxation under a low illumination intensity of 1.3 mW cm^{-2} for 100, 300, and 1200 s, respectively.

The parameters of curves *1–7*, which reflect the kinetics of thermal relaxation of the MEAI-I ensemble under different conditions, are given in Table 1.

The data listed in Table 1 show the following.

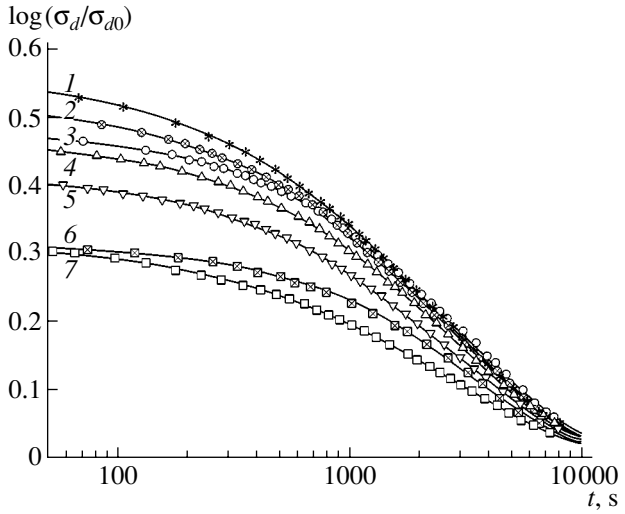

Fig. 1. Kinetics of variation in the dark conductivity of an (*a*-Si:H):B film after the formation of the MEAI-I ensemble in the film (curve *1*). The kinetics of variation in the dark conductivity of this film after the formation of the above ensemble in the film and its subsequent partial relaxation in the dark (curves *2–4*) and under low-intensity illumination at 1.3 mW cm^{-2} (curves *5–7*) for 100, 300, and 1200 s.

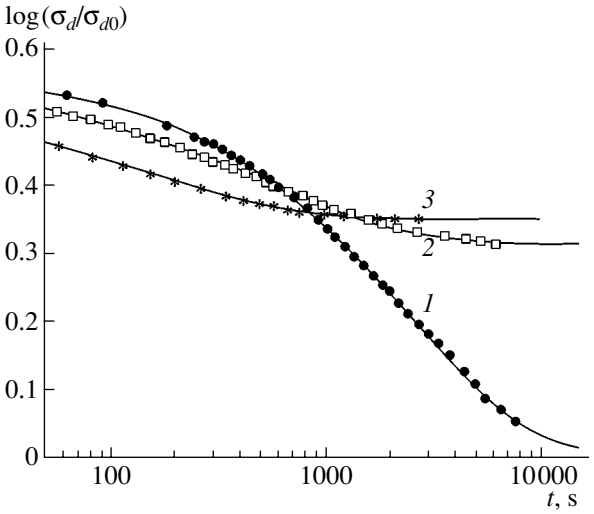

Fig. 2. Kinetics of variation in the dark conductivity of an (*a*-Si:H):B film after formation of the MEAI-I ensemble in the dark (curve *1*) and under illumination with intensities of 1.3 and 10 mW cm^{-2} (curves *2* and *3*).

(i) The MEAI concentration decreases and τ_0 and β increase as the time taken for partial thermal relaxation of the MEAI-I ensemble increases. This behavior indicates that thermal relaxation is mainly related to states with short relaxation times. Due to this circumstance, the effective relaxation time increases and the width of the distribution function $f(\tau)$ decreases.

(ii) All the parameters ($N(0)$, τ_0, and β) of thermal relaxation of the ensembles, which were obtained after partial relaxation of the MEAI-I ensemble in the dark and under illumination, are different. This fact indicates that photoinduced relaxation of the MEAIs takes place.

(iii) These distinctions depend on the time taken for preliminary partial relaxation of the MEAI-I ensemble. At short times, the parameter $N(0)$ decreases under illumination, while τ_0 and β increase similarly to, but to a greater extent than, the increase observed for relaxation in the dark. As the time taken for preliminary relaxation increases, illumination acts in a different way; specifically, the decrease in the parameter $N(0)$ is smaller, and τ_0 and β decrease rather than increase. This observation indicates that the distribution function $f(\tau)$ is broadened towards the short-time region. This effect of illumination is due to the fact that the photoinduced formation of the MEAIs becomes important for long periods of partial relaxation of the MEAI-I ensemble under illumination.

The above explanation is confirmed by the following experimental data. Figure 2 shows the kinetics of variation in the film conductivity during relaxation of the MEAI-I ensemble in the dark (curve *1*) and under illumination with a power density of 1.3 mW cm^{-2} (curve *2*) and 10 mW cm^{-2} (curve *3*). It can be seen that, for long times, the steady-state conductivity of the film (curves *2* and *3*) exceeds the equilibrium dark conductivity (curve *1*), indicating an increase in the MEAI content in the film due to their photoinduced formation under the effect of prolonged illumination.

Table 1. Parameters of thermal relaxation of various MEAI ensembles before and after partial relaxation of the MEAI-I ensemble in the dark and under illumination at an intensity of 1.3 mW cm^{-2}

MEAI ensembles	$N(0)$, arb. units		τ_0, s		β	
MEAI-I	0.57		2520		0.77	
MEAIs-I after partial relaxation	in the dark	under illumination	in the dark	under illumination	in the dark	under illumination
60 s	0.54	0.51	2680	2910	0.8	0.82
100 s	0.53	0.49	2800	3230	0.82	0.84
300 s	0.47	0.42	2950	2860	0.84	0.8
1200 s	0.32	0.34	3620	2690	0.89	0.73

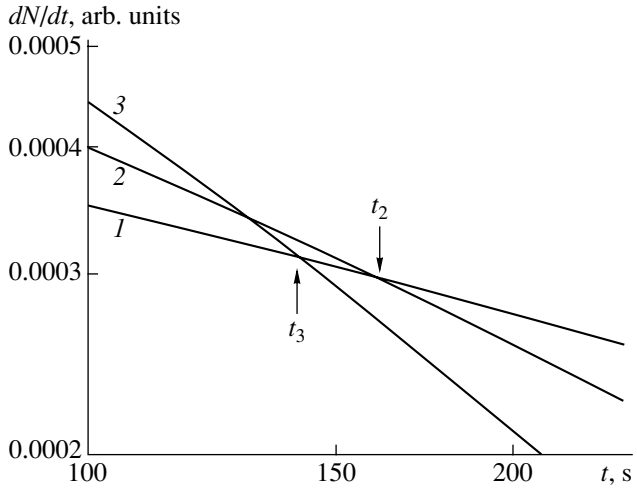

Fig. 3. Time dependences of the rates of variation in the MEAI content in an (*a*-Si:H):B film in the dark (curve *1*) and under illumination at intensities of 1.3 and 10 mW cm^{-2} (curves *2* and *3*).

By differentiating curves *1*, *2*, and *3* (Fig. 2) with respect to time, we obtain the time dependences of the rates of the MEAI concentration variation in the dark, $v_1(t)$, and under illumination, $v_2(t)$ and $v_3(t)$. Figure 3 shows the dependences $v_1(t)$, $v_2(t)$, and $v_3(t)$, which correspond to curves *1*, *2*, and *3*, respectively. It can be seen that, for short times, the relaxation rates of the MEAIs under illumination (v_2 and v_3) are higher than the rate of their thermal relaxation v_1. At the time instants t_2 and t_3, the rates v_2 and v_3 become equal to the rate v_1, while, for longer times, the rates v_2 nd v_3 become lower than v_1. The rates v_2 and v_3 are determined by four rates, namely, by those of thermal and photoinduced relaxation and generation of MEAIs, whereas the rate v_1 is determined by only two rates, namely, by those of thermal relaxation and generation of MEAIs. Therefore, at time the instants t_2 and t_3, the rates of photoinduced relaxation and photoinduced generation of the MEAIs become equal. Thus, if the time taken for preliminary partial relaxation of the MEAI-I ensemble under illumination is shorter than the time t_c at which the rates of photoinduced relaxation and generation of the MEAIs become equal, photoinduced formation of the MEAIs during partial relaxation under illumination is weak. In this case, photoinduced relaxation is dominant. If the time taken for partial relaxation is longer than t_c, photoinduced formation of the MEAIs becomes dominant. Figure 3 also shows that $t_3 < t_2$; i.e., as the intensity of illumination increases, the critical time t_c decreases.

Table 2. Parameters of thermal relaxation of different MEAI ensembles before and after partial relaxation of the MEAI-I ensemble in the dark and under illumination for 300 s at different light intensities

MEAI ensembles	$N(0)$, arb. units	τ_0, s	β
MEAI-I	0.57	2520	0.77
MEAI-I after partial relaxation:			
in the dark	0.47	2880	0.81
under illumination at 0.5 mW cm^{-2}	0.44	2920	0.82
under illumination at 1.3 mW cm^{-2}	0.42	2820	0.8
under illumination at 10 mW cm^{-2}	0.40	2680	0.77

Table 1 shows the obtained parameters, $N(0)$, τ_0, and β, of the complete thermal relaxation of the MEAI-I ensemble as well the parameters of the ensembles obtained after partial relaxation of this ensemble for various time intervals in the dark and under low-intensity illumination at 1.3 mW cm^{-2}. According to Fig. 3, at this illumination intensity, the time t_c is 160 s. The times taken for preliminary relaxation are shorter, specifically, 60 and 100 s. This condition ensures a low rate of photoinduced generation of the MEAIs during preliminary relaxation of the MEAI-I ensemble under illumination, and, consequently, the variation in the parameters $N(0)$, τ_0, and β is determined by the photoinduced relaxation of the MEAI-I ensemble, which has short relaxation times. The times taken for preliminary relaxation, which are equal to 300 and 1200 s, exceed t_c = 160 s. This circumstance causes a low rate of photoinduced relaxation of the MEAIs during preliminary relaxation of the MEAI-I ensemble; consequently, the variation in the parameters τ_0 and β is determined by the photoinduced formation of MEAIs with short relaxation times.

Table 2 shows the relaxation parameters of the MEAI-I ensemble after its partial relaxation for 300 s in the dark and at various illumination intensities in the range 0.5–10 mW cm^{-2}. It can be seen that the total initial concentration $N(0)$ of MEAIs in the ensembles decreases monotonically as the illumination intensity increases during preliminary partial relaxation of this ensemble. However, τ_0 and β vary nonmonotonically as the intensity increases. For a low illumination intensity (0.5 mW cm^{-2}), the values of τ_0 and β are greater than in the absence of illumination during preliminary relaxation of this ensemble. As the illumination intensity increases to 1.3 and 10 mW cm^{-2}, τ_0 and β decrease. This behavior is due to the fact that the time t_c, when the rates of photoinduced relaxation and photoinduced formation of the MEAIs become equal, decreases as the illumination intensity increases. Therefore, photoinduced relaxation of the MEAIs is dominant at low illumination intensities, since the time 300 s < t_c. For illumination intensities of 1.3 and 10 mW cm^{-2}, photoinduced formation of the MEAIs is dominant, since 300 s > t_c. Correspondingly, for low illumination intensities, τ_0 and β increase due to photoinduced relaxation of the MEAIs with short relaxation times τ. For higher intensities, τ_0 and β decrease due to photoinduced formation of the MEAIs with short relaxation times τ.

Thus, we have established that the photoinduced relaxation of photoinduced metastable electrically active B atoms in (*a*-Si:H):B films manifests itself during their relaxation under illumination, when the rate of photoinduced relaxation of metastable states substantially exceeds the rate of their photoinduced generation. The fulfillment of this condition depends on the initial concentration of photoinduced metastable states and on the illumination intensity and duration. Our studies also show that the variations in the distribution function $f(\tau)$ for the ensemble of photoinduced metastable states resulting from thermal and photoinduced relaxation are similar. This result indicates that the mechanisms of thermal and photoinduced relaxation are identical.

This study was supported by the program "Integration."

REFERENCES

1. D. Redfield, Appl. Phys. Lett. **52**, 492 (1988).
2. R. Meaudre and M. Meaudre, Phys. Rev. B **45**, 12134 (1992).
3. H. Gleskova, P. A. Morin, and S. Wagner, Appl. Phys. Lett. **62**, 2063 (1993).
4. I. A. Kurova, N. N. Ormont, and A. L. Gromadin, Fiz. Tekh. Poluprovodn. (St. Petersburg) **37**, 142 (2003) [Semiconductors **37**, 131 (2003)].
5. I. A. Kurova, N. N. Ormont, and A. L. Gromadin, Fiz. Tekh. Poluprovodn. (St. Petersburg) **37**, 753 (2003) [Semiconductors **37**, 727 (2003)].

Translated by N. Korovin

Semiconductors, Vol. 39, No. 8, 2005, pp. 928–933. Translated from Fizika i Tekhnika Poluprovodnikov, Vol. 39, No. 8, 2005, pp. 964–969.

CONFERENCE.
AMORPHOUS, VITREOUS, AND POROUS SEMICONDUCTORS

The Mechanisms of Current Transport and Properties of *a*-SiC:H/*c*-Si Heterostructures

A. A. Sherchenkov^, B. G. Budagyan, and A. V. Mazurov

Moscow State Institute of Electronic Engineering (Technical University), Zelenograd, Moscow oblast, 103498 Russia
^e-mail: budaguan@ms.miee.ru

Submitted December 27, 2004; accepted for publication January 12, 2005

Abstract—The properties of *a*-SiC:H/*c*-Si heterostructures formed at various alloy carbon contents are studied. A dominant mechanism of carrier transport in the heterostructures is established. Equivalent electric circuits, which make it possible to describe the current–voltage characteristics of heterostructures over entire bias range under study, are suggested. The band-gap temperature coefficient and electron affinity for *a*-SiC:H are estimated. © *2005 Pleiades Publishing, Inc.*

1. INTRODUCTION

Currently, *a*-SiC:H alloy films are widely used to fabricate solar cells [1], thin-film field-effect transistors [2], etc. The characteristics of these devices are largely determined by the properties of heterostructures that consist of amorphous semiconductor and crystalline semiconductor materials. However, it is difficult to implement devices based on these heterostructures because of the lack of a clear understanding of the formation mechanisms and properties of heterostructures based on disordered semiconductors and the processes occurring in a heterostructure, including transport and recombination of charge carriers. The lack of deep insight into the physics of the processes taking place in the heterostructure complicates purposeful improvement of devices based on such heterostructures. Within this context, this report presents the results of examination of the transport mechanisms and properties of *a*-SiC:H/*c*-Si heterostructures, which were obtained in low-frequency glow-discharge plasma at a frequency of 55 kHz.

2. EXPERIMENTAL

The *a*-SiC:H/*c*-Si heterostructures were formed by deposition of *a*-SiC:H films in low-frequency glow-discharge plasma at a frequency of 55 kHz onto single-crystal Si substrates with a resistivity of 10 Ω cm. During the deposition, the CH_4 content in the gas mixture (R_C = [CH_4]/([SiH_4] + [CH_4]) 100%) was varied from 20 to 80%. The substrate temperature, discharge power, and pressure were kept constant at 320°C, 200 W, and 90 Pa, respectively. Then, Al contacts were deposited on the film and the rear surface of the substrate. The contacts to the *a*-SiC:H layer were formed via deposition through a mask.

The current–voltage (*I–V*) characteristics were measured both at forward biases (from 0 to 15 V) and at reverse biases (from 0 to –15 V) in the dark and under illumination. The temperature dependences of the *I–V* characteristics were measured in the temperature range 291–462 K. In the measurements of the *I–V* characteristics under illumination, the wavelength of incident radiation was varied from 500 to 1100 nm.

In order to determine the C content (X_C) in the *a*-SiC:H films, we used Rutherford backscattering spectroscopy. The location of the Fermi level in the amorphous alloys relative to the conduction-band bottom ($E_C - E_F$) was determined from measurements of the temperature dependence of the dark conductivity of the *a*-SiC:H films in the temperature range 300–500 K.

In this study, we used the method of capacitance–voltage (*C–V*) characteristics to determine the density of energy states in the mobility gap of the amorphous semiconductor and at the interface of heterostructures that consisted of amorphous and crystalline semiconductors.

3. RESULTS

Figures 1 and 2 show the forward and reverse portions of the *I–V* characteristics of the *a*-SiC:H/*c*-Si heterostructures, which were measured at various temperatures. It can be seen that the shape of the *I–V* characteristics is also affected by the methane content in the mixture of reaction gases in which the *a*-SiC:H layer formed, and not only by the magnitude and sign of the bias. The approximation of separate portions of the *I–V* characteristics using various relationships allowed us to determine the dominant mechanisms of carrier transport. It is found that the *I–V* characteristic of the heterostructure formed at R_C = 20% is described by the following relation in the range of small forward biases ($U < 1$ V):

$$J = J_0 \exp(AV). \quad (1)$$

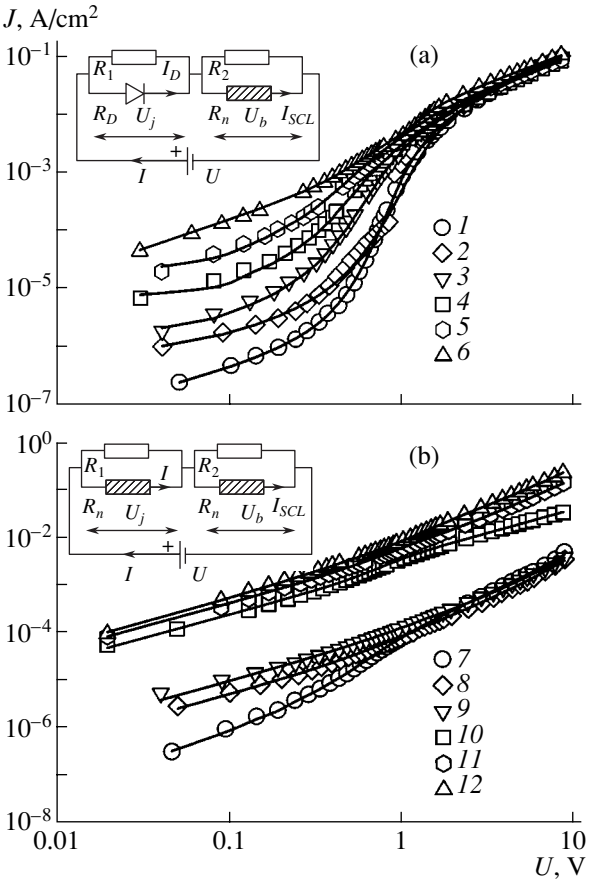

Fig. 1. Forward portions of the *I–V* characteristics of *a*-SiC:H/*c*-Si heterostructures. The solid lines correspond to calculated *I–V* characteristics. (a) Heterostructures formed at R_C = 20% and T = (*1*) 297, (*2*) 342, (*3*) 367, (*4*) 397, (*5*) 427, and (*6*) 462 K. (b) Heterostructures formed at R_C = 60% and T = (*7*) 291, (*8*) 336, (*9*) 361, (*10*) 391, (*11*) 421, and (*12*) 451 K. The equivalent electric circuits of the structures are shown in the insets.

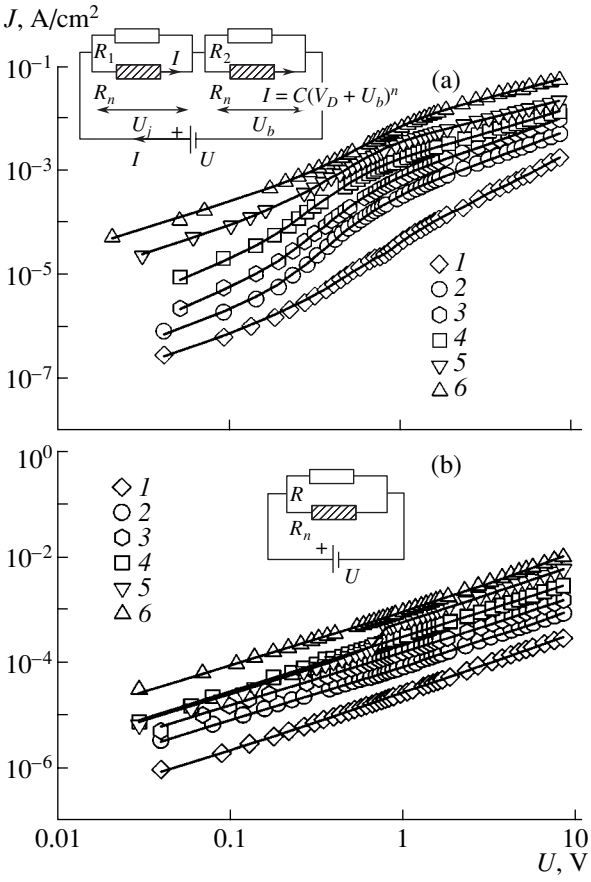

Fig. 2. Reverse *I–V* characteristics of *a*-SiC:H/*c*-Si heterostructures formed at (a) R_C = 20% and (b) R_C = 80%. The solid lines correspond to calculated *I–V* characteristics. T = (*1*) 297, (*2*) 342, (*3*) 367, (*4*) 397, (*5*) 427, and (*6*) 462 K. The equivalent electric circuits of the structures are shown in the insets.

Here, J_0 is the saturation current and A is a parameter.

In this case, the values of parameter A are almost independent of the temperature, while the saturation current decreases as $1/kT$ increases. Similar results have been obtained for the heterostructures *a*-Si:H/*c*-Si [3], *a*-SiGe:H/*c*-Si [4], and *a*-SiC:H/*c*-Si [5]. It was shown [6] that the dominant mechanism of carrier transport is multistep tunneling with the carrier capture at and emission from traps.

According to this mechanism, due to multistep tunneling, the holes from the valence band of *p*-type *c*-Si transfer into the amorphous semiconductor from one localized state to another with an energy difference of about kT. Such carrier transport continues until the tunneling rate becomes lower than the hole emission rate into the valence band or the recombination rate of holes with electrons from the conduction band of the amorphous semiconductor. In this case, the magnitude of J_0 in relation (1) equals

$$J_0 = B\left[\sigma_p v_{th} N_V \exp\left(-\frac{E_T - E_V}{kT}\right) + \sigma_n v_{th} N_C \exp\left(-\frac{E_C - E_F}{kT}\right)\right]. \quad (2)$$

Here, B is a constant that depends on the tunneling probability of carriers; σ_n and σ_p are the capture cross section for electrons and holes, respectively; v_{th} is the thermal velocity; N_V and N_C are the effective densities of states in the valence band and in the conduction band of the amorphous semiconductor, respectively; and E_F, E_T, E_V, and E_C are energies that correspond to the Fermi levels, traps, and edges of the valence and conduction bands.

If the emission rate of holes is higher than the rate of electron capture by the traps, the first term in Eq. (2) is dominant; otherwise, the second term is dominant.

In the region of high forward-bias voltages ($U > 1$ V), the *I–V* characteristic is governed by the bulk resistance of the amorphous film.

For heterostructures formed at $R_C = 60$ and 80%, the *I–V* characteristic in the region of low forward-bias voltages is governed by the bulk resistance of the *a*-SiC:H layer, while, in the region of high forward-bias voltages, the *I–V* characteristic is approximated by the relation

$$J = KV^m. \tag{3}$$

Here, K is a coefficient that depends on the film thickness, trap distribution, and conductivity of the material, and m is a constant. In this case, the current limited by the space charge is dominant [7].

At reverse biases for heterostructures formed at $R_C = 20$ and 60%, the current limited by the space charge is dominant in the region of low reverse-bias voltages. In contrast, in the region of high reverse-bias voltages, the current transport is governed by carrier generation and recombination in the depletion region, and the *I–V* characteristic is described by the relation

$$J = C(V_D + V)^n. \tag{4}$$

Here, V_D is the contact potential difference, C is a constant, and n is the exponent ($n < 1$).

For heterostructures formed at $R_C = 80\%$, the *I–V* characteristic over the entire studied range of reverse biases is governed by the bulk resistance of the *a*-SiC:H layer (Fig. 2).

Taking into account the above dominant transport mechanisms, we suggested equivalent electric circuits that describe the *I–V* characteristics of the heterostructures over the entire range of forward and reverse biases (see the insets in Figs. 1, 2). Using these equivalent electric circuits, we simulated the *I–V* characteristics of studied heterostructures over the entire range of forward and reverse biases.

In the suggested equivalent electric circuits, the diode describes the exponential voltage dependence of current (1). The bulk resistance of *a*-Si:H is described by two parallel resistors, one of which is a nonrectifying resistance (R_2) while the second one (R_n) has the nonlinear voltage dependence of resistance (3). The nonlinear resistance allows us to describe the portion of the *I–V* characteristic at high forward-bias voltages, which is governed by current limited by the space charge. The shunting resistance R_1, which is parallel to the diode, allows us to take into account the leakage of current through the heterojunction. Thus, the equivalent resistance of the circuit R_e, which is used for simulating the forward portions of the *I–V* characteristics of the *a*-SiC:H/*c*-Si heterostructures formed at $R_C = 20\%$, equals

$$R_e = \frac{R_D R_1}{R_D + R_1} + \frac{R_n R_2}{R_n + R_2}. \tag{5}$$

Here, R_D is the diode resistance. The resistances R_D and R_n are defined as

$$R_D = \frac{U_j}{J_0 \exp(AU_j)}, \tag{6}$$

$$R_n = \frac{U_b}{KU_b^m} = \frac{1}{KU_b^{m-1}}. \tag{7}$$

The voltage drop at separate parts of the electric circuit is calculated by the following formulas:

$$U_b = U - U_j = \left[J_0 \exp(AU_j) + \frac{U_j}{R_1} - K(U - U_j)^m\right] R_2, \tag{8}$$

$$U_j = U - U_b = \left[\frac{U_b}{R_2} + K(U_b)^m - J_0 \exp(A(U - U_b))\right] R_1. \tag{9}$$

Relations (5)–(9) were used to calculate the current flowing through the heterostructure according to the Ohm law $I = U/R_e$. In order to fit the calculated *I–V* characteristic to the experimental one, we used the adjustable parameters J_0, K, R_1, R_2, m, and A, which were determined from simulation. For *a*-SiC:H/*c*-Si heterostructures formed at $R_C = 60$ and 80%, the simulation parameters were K_1, K_2, R_1, R_2, m_1, and m_2, while R_e was determined from the following relation:

$$R_e = \frac{\left(\frac{U_1}{K_1 U_1^{m_1}}\right) R_1}{\frac{U_1}{K_1 U_1^{m_1}} + R_1} + \frac{\left(\frac{U_2}{K_2 U_2^{m_2}}\right) R_2}{\frac{U_2}{K_2 U_2^{m_2}} + R_2}. \tag{10}$$

In the case of reverse biases, R_e for the heterostructures formed at $R_C < 80\%$ equals

$$R_e = \frac{\left(\frac{1}{K_1 U_j^{m-1}}\right) R_1}{\frac{1}{K_1 U_j^{m-1}} + R_1} + \frac{\left(\frac{U_b}{C(V_D + U_b)^n}\right) R_2}{\frac{U_b}{C(V_D + U_b)} + R_2}, \tag{11}$$

while, for heterostructures formed at $R_C = 80\%$, R_e equals

$$R_e = \frac{\left(\frac{1}{KU^{m-1}}\right) R}{\frac{1}{KU^{m-1}} + R}. \tag{12}$$

The results of the simulation are shown by the solid lines in Figs. 1 and 2. It can be seen that the results of the calculations describe the experimental data adequately.

Table 1. Position of the Fermi level and the density of states N_{IE} for the *a*-SiC : H films, interface density of states N_{SS} for the *a*-SiC : H/*c*-Si heterostructures, and activation energies for the heterostructures at forward biases

R_C, %	X_C, %	$E_C - E_F$, eV	N_{IE}, cm^{-3}	N_{SS}, cm^{-2}	E_{jf}, eV	E_{Kf}, eV	E_{K1}, eV	E_{R1f}, eV	E_{K2}, eV	E_{R2f}, eV
20	6.5	0.78	3.5×10^{15}	4.2×10^{11}	0.46	0.06	–	0.37	–	0.02
60	25.4	0.91	2.2×10^{15}	5.5×10^{11}	–	–	0.36	0.28	0.34	0.36
80	42.5	0.94	9.1×10^{14}	5.2×10^{11}	–	–	0.22	0.31	0.21	0.28

Table 2. Interface density of states and activation energies for the *a*-SiC : H/*c*-Si heterostructures at reverse biases

R_C, %	X_C, %	N_{SS}, cm^{-2}	E_K, eV	E_{Rr}, eV	E_{K1}, eV	E_{R1r}, eV	E_C, eV	E_{R2r}, eV
20	6.5	4.2×10^{11}	–	–	0.35	0.64	0.36	0.31
60	25.4	5.5×10^{11}	–	–	0.22	0.27	0.24	0.42
80	42.5	5.2×10^{11}	0.21	0.37	–	–	–	–

From the results of simulating the forward portions, we constructed the temperature dependences of the parameters J_0, K, K_1, K_2, R_1, and R_2 and determined their activation energies, E_{Jf}, E_{Kf}, E_{Kf1}, E_{Kf2}, E_{R1f}, and E_{R2f}, respectively; these energies are listed in Table 1. The activation energies of the parameters K, R, K_1, R_1, C, and R_2 for reverse biases are given in Table 2.

4. DISCUSSION

Table 1 shows that the obtained value of E_{Jf} = 0.46 eV for the *a*-SiC:H/*c*-Si heterostructures, which were formed at R_C = 20%, differs considerably from the position of the Fermi level (E_F) for *a*-SiC:H formed under the same conditions. In this case, the holes from *p*-type *c*-Si tunnel to the defect level, which is spaced from the valence band top by 0.46 eV, where the holes are emitted into the valence band of the amorphous alloy.

An increase in the C content in the *a*-Si:H film leads to an increase in its resistivity and density of defect states [8]. These parameters exert a determining effect on the carrier transport in the amorphous semiconductor film and, in general, in the heterostructure based on it. In this case, the change in the mechanism of carrier transport in the *a*-SiC:H/*c*-Si heterostructures, which takes place as the C content in the *a*-SiC:H film increases, can be attributed to an increase in the resistivity of the amorphous film and density of defect states in the *a*-SiC:H band gap.

Application of forward bias gives rise to an injection of nonequilibrium carriers from the electrode in the neighboring layer of the amorphous semiconductor. These carriers occupy free energy states above the Fermi level. At a sufficiently high voltage, the excess space charge extends over the entire layer thickness and restricts the current that reaches the opposite electrode [9]. In this case, the traps capture virtually the entire excess charge. However, a small part enters the allowed band of the semiconductor as a result of thermal activation, which provides an increase in the current. The space-charge-limited current starts to be dominant when the concentration of nonequilibrium free carriers becomes comparable with that of thermally activated carriers [9]. In this case, the material conductivity is determined by the injected charge if the transit time of the electrons is short and their charge has no time to disperse in the dielectric-relaxation period (similarly to *a*-Si:H). In this situation, the activation energies E_{K1} and E_{K2} can be interpreted as the locations of the trap levels relative to the conduction band bottom, from which the captured electrons are thermally activated. This phenomenon results in an increase in the space-charge-limited current.

Figure 3 shows the dependence of E_{R1f} on the density of states at the interface N_{SS} of the *a*-SiC:H/*c*-Si heterostructures (the capacitance–voltage method [10] was used in the estimations). It can be seen from Fig. 3 that N_{SS} and E_{F1f} are directly interrelated. Since the resistance R_1 characterizes the leakage currents in the

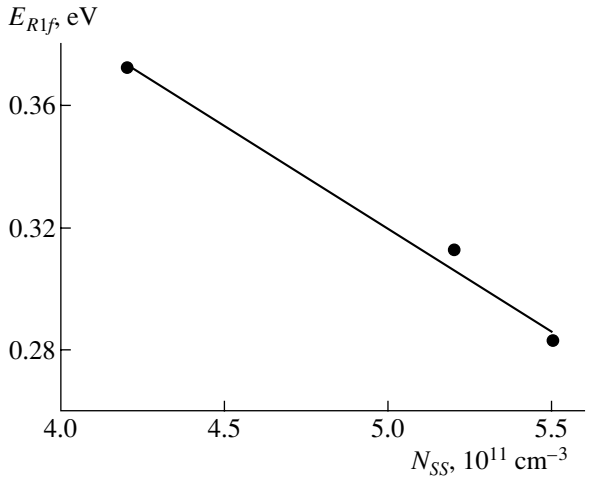

Fig. 3. Dependence of E_{R1f} on N_{SS} for forward biases. The solid line corresponds to the trend line.

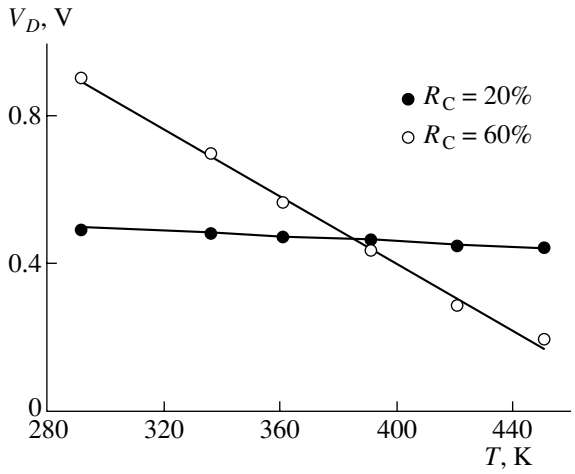

Fig. 4. Temperature dependence of V_D for the *a*-SiC:H/*c*-Si heterostructures. The solid lines correspond to calculated dependences.

a-SiC:H/*c*-Si heterostructures, the existence of such an interrelation indicates that these currents are governed by the states at the interface of the *a*-SiC:H/*c*-Si heterostructure.

Again using the capacitance–voltage method [10], we also observed correlation (see Table 1) between the values of N_{SS} and the density of states near the Fermi level of *a*-SiC:H (N_{IE}). Thus, we can suggest that the surface states in the *a*-SiC:H/*c*-Si heterostructures are caused by localized states in amorphous Si. Similar dependences were also observed for E_{R1r} obtained for reverse-biased heterostructures (see Table 2). The states near the Fermi level are governed by Si dangling bonds [11]. Therefore, we can suggest that the leakage currents in the *a*-SiC:H/*c*-Si heterostructures are governed by the interface states related to Si dangling bonds located near the Fermi level.

Table 2 shows that the obtained values of the activation energies E_C considerably differ from E_a = 0.56 eV, which corresponds to $E_g/2$ for single-crystal Si. This value holds for an ideal *p*–*n* junction based on single-crystal Si [12]. In this case, the carriers are generated in the depletion region of the amorphous alloy. Making allowance for the fact that the majority carriers are electrons, we can state that the energy levels from which the carriers are generated are located close to the conduction-band bottom.

Simulation of the reverse *I*–*V* characteristics of the *a*-SiC:H/*c*-Si heterostructures, which were measured at various temperatures, allowed us to estimate the values of V_D at these temperatures (Fig. 4). Analysis of the energy diagram of the *a*-SiC:H/*c*-Si heterostructure allowed us to obtain the following expression for the temperature dependence of V_D:

$$\begin{aligned} V_D &= \chi_1 + E_{g1}(0) - \alpha_1 T - kT\ln\left(\frac{N_{V1}}{N_{a1}}\right) \\ &- \chi_2 - \frac{E_{g2}(0) - \alpha_2 T}{2} + \frac{kT}{2}\ln\left(\frac{N_{V2}}{N_{C2}}\right) \\ &= \left[\chi_1 + E_{g1}(0) - \chi_2 - \frac{E_{g2}(0)}{2}\right] \\ &- T\left[\alpha_1 + k\ln\left(\frac{N_{V1}}{N_{a1}}\right) - \frac{\alpha_2}{2} - \frac{k}{2}\ln\left(\frac{N_{V2}}{N_{C2}}\right)\right]. \end{aligned} \quad (13)$$

Here, subscript 1 corresponds to *p*-type *c*-Si; subscript 2 corresponds to intrinsic *a*-SiC:H; χ is the electron affinity; $E_g(0)$ is the band gap at 0 K; α is the band-gap temperature coefficient; N_V and N_C are the effective densities of states in the valence band and in the conduction band, respectively; and N_A is the acceptor concentration in *c*-Si.

The results of simulation of the temperature dependence of V_D are shown in Fig. 4 in the form of solid lines. Using the results of the simulation, we estimated the electron affinity and band-gap temperature coefficient for *a*-SiC:H. In calculations of KDB-10-grade *c*-Si (B-doped Si with a resistivity of 10 Ω cm) and *a*-SiC:H, it was assumed that $N_{a1} = 1.50 \times 10^{15}$ cm^{-3} [13], $N_{V1} = 1.02 \times 10^{19}$ cm^{-3} [13], $\chi_1 = 4.05$ eV [12, 13], $E_{g1}(0) = 1.16$ eV [13], $\alpha_1 = 2.4 \times 10^{-4}$ eV/K [13], $N_{V2} = 1.00 \times 10^{21}$ cm^{-3} [11], and $N_{C2} = 1.00 \times 10^{22}$ cm^{-3} [11]. The obtained estimated values of electron affinity and the band-gap temperature coefficient for *a*-SiC:H are given in Table 3. Table 3 shows that the values of α_2 and χ_2 decrease as R_C increases.

Table 3. Electron affinity, α_2, and $E_{g2}(0)$ for *a*-SiC : H

R_C, %	X_C, %	χ_2, eV	α_2, eV/K	$E_{g2}(0)$, eV
20	6.5	3.51	1.5×10^{-3}	2.21
60	25.4	2.81	1.1×10^{-3}	2.30

5. CONCLUSIONS

In this study, we estimated the effect of the C content on the mechanism of charge transport in *a*-SiC:H/*c*-Si heterostructures. It was found that, for a heterostructure formed at R_C = 20%, multistep tunneling, with the carrier capture by and emission from traps, is dominant in the region of low forward-bias voltages ($U < 1$ V). In the region of high forward-bias voltages ($U > 1$ V), the *I*–*V* characteristic is governed by the bulk resistance of the amorphous film.

For heterostructures formed at R_C = 60 and 80%, the *I*–*V* characteristic in the region of low forward-bias voltages is governed by the bulk resistance of the *a*-SiC:H layer, while the space-charge-limited current is dominant in the region of high forward-bias voltages.

At reverse biases for heterostructures formed at R_C = 20 and 60%, the space-charge-limited current is dominant in the region of low reverse-bias voltages, while the charge transport in the region of high reverse-

bias voltages is governed by the processes of carrier generation and recombination in the depletion region of the amorphous semiconductor.

For heterostructures formed at R_C = 80%, charge transport over the entire range of reverse biases is governed by the bulk resistance of the *a*-SiC:H layer.

It was established that the leakage of current through the heterojunction is determined by interface states introduced by Si dangling bonds.

The electron affinity and the band-gap temperature coefficient for *a*-SiC:H are estimated.

ACKNOWLEDGMENTS

This study was supported by the Ministry of Education, grant nos. 517-GB-53TÉ, 501-GB-53Gr, and 392-GB-53-B.

REFERENCES

1. C.-K. Jung, D.-C. Lim, H.-G. Jee, *et al.*, Surf. Coat. Technol. **171**, 46 (2003).
2. H. Gleskova and S. Wagner, Appl. Surf. Sci. **175–176**, 12 (2001).
3. H. Matsuura, T. Okuno, H. Okushi, and K. Nanaka, J. Appl. Phys. **55**, 1012 (1984).
4. A. A. Sherchenkov, B. G. Budagyan, and A. V. Mazurov, Perspekt. Mater., No. 3, 24 (2003).
5. H. Mimura and Y. Hatanaka, Appl. Phys. Lett. **45**, 452 (1984).
6. H. Matsuura, Jpn. J. Appl. Phys. **27**, L513 (1988).
7. L. F. Marsal, J. Pallares, X. Correig, *et al.*, J. Appl. Phys. **79**, 8493 (1996).
8. A. Morimoto, T. Miura, M. Kumeda, and T. Shimizu, Jpn. J. Appl. Phys. **21**, L2 (1982).
9. M. A. Lampert and P. Mark, *Current Injection in Solids* (Academic, New York, 1970; Mir, Moscow, 1973).
10. B. G. Budagyan, A. A. Sherchenkov, A. E. Berdnikov, *et al.*, in *Proceedings of X International Symposium on Thin Films in Electronics* (Yaroslavl, 1999), Part 2, p. 238.
11. *Amorphous Silicon and Related Materials*, Ed. by H. Fritzsche (World Sci., Singapore, 1989; Mir, Moscow, 1991).
12. S. Sze, *Physics of Semiconductor Devices*, 2nd ed. (Wiley, New York, 1981; Mir, Moscow, 1984), Vol. 1.
13. K. V. Shalimova, *Physics of Semiconductors* (Énergoatomizdat, Moscow, 1985) [in Russian].

Translated by N. Korovin

Semiconductors, Vol. 39, No. 8, 2005, pp. 934–940. Translated from Fizika i Tekhnika Poluprovodnikov, Vol. 39, No. 8, 2005, pp. 970–975.

AMORPHOUS, VITREOUS, AND POROUS SEMICONDUCTORS

Raman Spectroscopy Study of the Carbon Structure of *a*-C:(H, Cu) and *a*-C:(H, Co) Composite Films

É. A. Smorgonskaya and V. I. Ivanov-Omskiĭ^

Ioffe Physicotechnical Institute, Russian Academy of Sciences, Politekhnicheskaya ul. 26, St. Petersburg, 194021 Russia

^ e-mail: Ivanov.Ivom@mail.ioffe.ru

Submitted December 27, 2004; accepted for publication January 12, 2005

Abstract—The main changes induced in the Raman spectrum of *a*-C:H films in the 1200- to 1700-cm^{-1} frequency region by modification with Cu and Co are ascertained. A comparison of the results obtained with the available data on various carbon structures reveals that the introduction of metals in concentrations comparable to the carbon content stimulates growth and ordering of graphite-like nanoclusters in the sp^2 carbon bonding system. It is found that, while similar structural rearrangements occur under thermal annealing of both *a*-C:H and composite *a*-C:(H, Cu) and *a*-C:(H, Co) films, the presence of metals interferes with thermally stimulated graphitization. The size of the graphite-like nanoclusters in annealed and unannealed films of all types is estimated, and Co is shown to produce a more efficient graphitizing effect than Cu. © *2005 Pleiades Publishing, Inc.*

1. INTRODUCTION

The objective when preparing *a*-C:(H, Me) composite films by incorporation of metals (Me = Co, Cu, Ag, Mo, Ni, and Fe) into amorphous hydrogenated carbon (*a*-C:H) is the development of new semiconductor structures containing nanosized metal clusters. Such systems have recently attracted considerable attention [1–4] as a step in the preparation of related materials with unusual optical or electrical properties, as well as of media with high data-recording densities. At the same time, the interaction of various metals with carbon in the disordered *a*-C:H matrix is also an intriguing problem. It is well known that, owing to the unique capacity of carbon atoms to form valence bonds with differently hybridized electrons and to the clustering of bonds of the same hybridization type, the *a*-C:H system primarily consists of sp^2- and sp^3-type nanoclusters. Note that the size, structure, and disorder of the clusters, as well as the percentage contents of clusters of different types, may differ depending on the actual conditions under which a film was fabricated, and this is what accounts for the rich variety of types and properties of *a*-C:H [5, 6] and the possibility of structural adaptation of *a*-C:H to foreign inclusions, which provides partial relief from internal stresses in the given conditions.

In this paper, we report the results of a comparative study of the local structural rearrangements in *a*-C:H resulting from incorporation of Cu and Co in concentrations comparable with the carbon content. The formulation of this problem is related, in particular, to optimization of the technology of *a*-C:H modification by introducing metals in an appreciable amount. Following the recent studies on *a*-C:(H, Me) films with a fixed Cu or Co content [7, 8], we chose, as the main experimental approach, Raman spectroscopy in the Raman shift range $\Delta\omega$ = 1200–1700 cm^{-1}, which corresponds to C–C sp^2 bond vibrations. These vibrations are known [6, 9, 10] to make a major contribution to Raman spectra of *a*-C:H when excited in the visible region of the spectrum. Thus, the method is very sensitive to possible structural rearrangements in *a*-C:H sp^2-coordinated clusters. We traced the cobalt- and copper-induced changes in the parameters of the *G* and *D* spectral bands typical of microcrystalline and disordered carbon structures [6, 9–13] under variation of the metal content. An analysis of these changes provided a basis for the conclusion that Cu and Co exert a graphitizing effect on the *a*-C:H structure under modification.

2. EXPERIMENTAL

The modified *a*-C:(H, Co) and *a*-C:(H, Cu) films, as well as the unmodified *a*-C:H, were prepared by dc magnetron cosputtering of graphite and metal (Co or Cu) or graphite only targets in argon–hydrogen plasma (80% Ar + 20% H_2). The films were deposited onto an Si (001) surface heated to 200°C. The other technological parameters can be found in [14]. The Co or Cu content was varied by changing the surface area ratio of the metal and graphite targets. The atomic ratio [Me]/[C] of the metal to carbon content in the films was monitored by Rutherford backscattering and instantaneous nuclear reactions, as was performed in [15]. Note that we observed correlation rather than exact equality of the value of [Me]/[C] ratio to the corresponding area

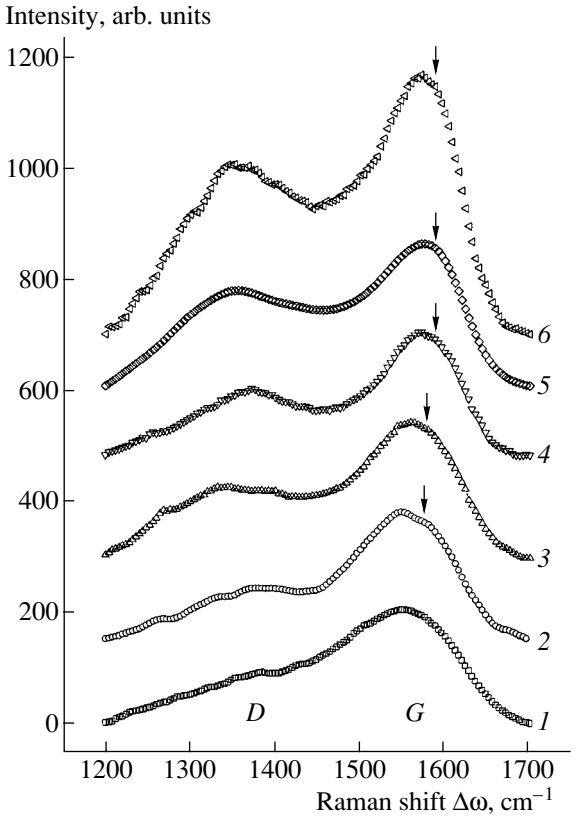

Fig. 1. Raman spectra of (*1*) *a*-C:H, (*2*, *3*) modified films *a*-C:(H, Cu), and (*4*–*6*) *a*-C:(H, Co) obtained with different metal contents. [Cu]/[C] = (*2*) 0.62 and (*3*) 1.0. [Co]/[C] = (*4*) 0.35, (*5*) 0.50, and (*6*) 0.73. Arrows indicate the feature that arises as a result of introduction of metals into *a*-C:H.

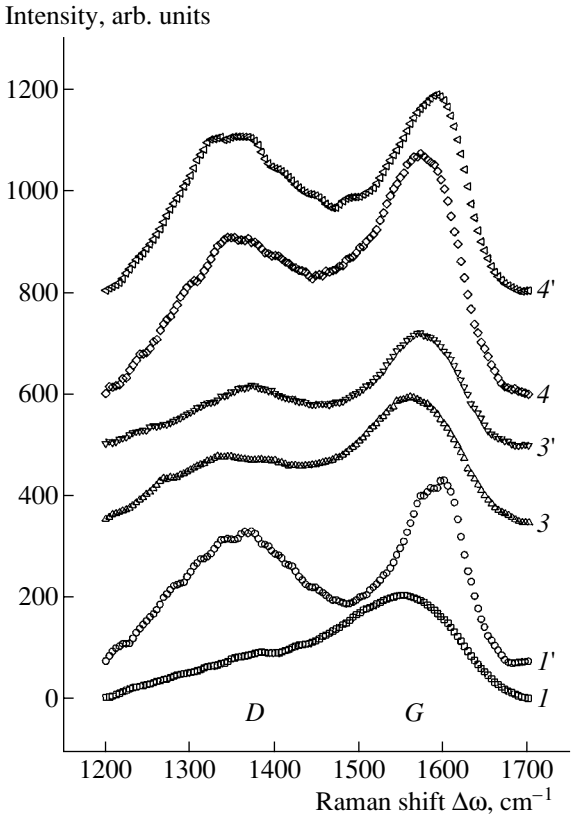

Fig. 2. Raman spectra of (*1*, *1'*) *a*-C:H, (*3*, *3*') *a*-C:(H, Cu), and (*4*, *4*') *a*-C:(H, Co) before (*1*, *3*, *4*) and after (*1'*, *3*', *4*') annealing at 380°C for 1 h. Metal content before annealing: (*3*, *3*') [Cu]/[C] = 1.0 and (*4*, *4*') [Co]/[C] = 0.73.

ratio. Some of the films were thermally annealed in vacuum for 1 h at 380°C.

The Raman scattering intensity was measured at room temperature with a SPEX Ramalog spectrometer under excitation with 488-nm unpolarized light.

3. THE RESULTS OF MEASUREMENTS AND ANALYSIS OF SPECTRA

Figure 1 presents the Raman spectra of *a*-C:(H, Cu) and *a*-C:(H, Co) composite films with different Cu and Co contents, as well as of an unmodified *a*-C:H film ([*Me*]/[C] = 0) obtained after subtraction of the background signal and smoothing. We can clearly see that, while the spectra measured after the modification of *a*-C:H with both metals retained the well-known broad *G* and *D* bands corresponding to carbon sp^2 bond vibrations, the shape and parameters of these bands have changed; indeed, the *D* band, which, in the absence of a metal, looks like a diffuse shoulder of band *G*, becomes well resolved. The *D* peak becomes more clearly pronounced as the metal content increases. Interestingly, in the films with Co, this effect becomes evident at lower metal contents than in the films with Cu. As for the *G* band, incorporation of a metal shifts its main peak, $\Delta\omega_{\max}^{G}$, toward higher frequencies, and the extent of this shift increases with the metal content, with the effect being more pronounced for Co. Indeed, in the case of *a*-C:(H, Co) with [Co]/[C] = 0.73, the shift relative to the *G* peak position in *a*-C:H ($\Delta\omega_{\max}^{G}$ = 1558 cm^{-1}) is 14 cm^{-1}, while, in *a*-C:(H, Cu) with [Cu]/[C] = 1, it is no larger than 4 cm^{-1}. In addition, at frequencies above that of the maximum of *G* ($\Delta\omega > \Delta\omega_{\max}^{G}$), a shoulder-shaped feature appears in the spectra of the composite films (Fig. 1), which makes the *G* band asymmetric.

The increase of the *D* band peak intensity and the shift of the *G* band to higher frequencies become enhanced after thermal annealing of the composite films. Figure 2 exemplifies the Raman spectra of annealed and (shown for comparison) unannealed samples of different composition. Annealing of an *a*-C:H film free of metal is seen to produce qualitatively similar, while larger, changes in the spectrum compared to the composite films. In particular, annealing of *a*-C:H shifted the peak of the *G* band to higher frequencies by

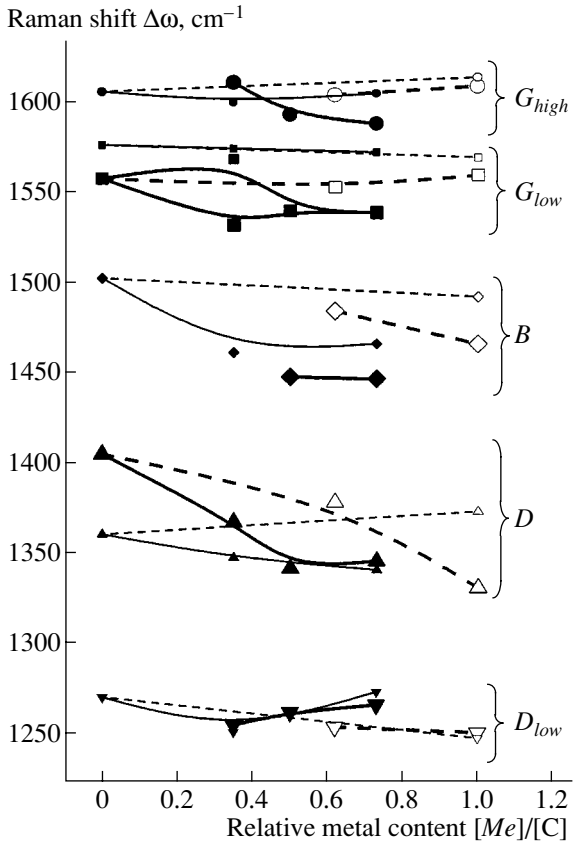

Fig. 3. Spectral position of the Raman components G_{high} (circles), G_{low} (squares), D (base-down triangles), B (diamonds), and D_{low} (base-up triangles) depending on the metal content in the a-C:(H, Co) films (filled symbols, solid lines) and a-C:(H, Cu) films (empty symbols, dashed lines) before (large symbols, bold lines) and after (small symbols, thin lines) annealing.

40 cm^{-1}; as a result, $\Delta\omega_{\max}^{G}$ reached 1600 cm^{-1}, which is substantially higher than in the case of the well-known G line of graphite (1581 cm^{-1}).

A detailed analysis of the experimental spectra according to their deconvolution [16] shows that the spectrum of the unannealed a-C:H film is fitted well by two Gaussian curves with maxima at $\Delta\omega_{\max}^{G}$ and $\Delta\omega_{\max}^{D}$ that correspond to the G and D bands, respectively. In contrast, the spectra of the composite films, both unannealed and annealed, as well as of annealed a-C:H, are, as a rule, superpositions of four to five components (see Fig. 3 in [16]); i.e., they are multicomponent spectra. Besides the main components of the D and G bands (the latter is referred to below as G_{low}), additional components can clearly be seen. The strongest of them are the high-frequency component G_{high} at $\Delta\omega_{\max}^{G_{high}}$ = 1590–1615 cm^{-1} and component B, with an intermediate frequency, peaking at $\Delta\omega_{\max}^{B}$ = 1450–1500 cm^{-1}. It is also possible to discern a very weak additional component D_{low} that manifests itself as a shoulder on the low-frequency side of the D band (Figs. 1, 2).

Estimates based on the relative integrated intensities of the components suggest that, in the case of a-C:(H, Co) with a high Co content, the G_{high} component can make a contribution to the spectrum ($\gtrsim$20%) comparable to that of the lower frequency component G_{low} [16]. It is this circumstance that accounts for the larger high-frequency shift of the G band as a whole with respect to its position in a-C:H in the case of a-C:(H, Co) compared to the a-C:(H, Cu) film (Fig. 1), for which the G_{high} contribution is substantially smaller (<10%). Component B is usually observed when a spectrum is decomposed into Gaussian components. When deconvolved into asymmetric Breit–Wigner–Fano profiles, as was done in [6] for various a-C:H samples, the B component was usually found in the region of the low-frequency tail of band G and was not considered separately.

The behavior of the maxima of all the components upon variation in the metal content in the films under study and annealing is shown in Fig. 3.

4. DISCUSSION

We use now the above results and the available data on specific features of Raman spectra of micro- and nanocrystalline graphite [11], various types of amorphous carbon [6, 17], and hydrocarbon compounds [18] as the basis for an analysis of the main changes in the carbon structure of a-C:H resulting from Co or Cu incorporation and heat treatment.

It is well known that, as single graphite crystals are crushed down to micro- and nanocrystallite sizes, the G line related to symmetric E_{2g} stretching vibrations of the C–C sp^2-coordinated bonds in six-membered aromatic rings of the graphene layers (the Γ point in the Brillouin zone of the crystal) shifts from 1581 cm^{-1} (graphite) to higher frequencies: up to 1590 or even 1600 cm^{-1} for crystallites ~2.5 nm in size or smaller [11]. Furthermore, in such nanosized graphite, the G line acquires an additional component near 1620 cm^{-1} that is associated with a peak in the phonon density of states (PDS) for $\mathbf{q} \neq 0$ in the vicinity of the Γ point, which arises from relaxation of the phonon wave-vector selection rule $\mathbf{q} \approx 0$ for Raman transitions in small crystallites. For the same reason, Raman transitions involving phonons in the vicinity of the K point in the Brillouin zone (A_{1g} symmetric breathing modes) become possible in nanocrystallites of graphite, thus giving rise to the well-known D band near 1355 cm^{-1}. As has been shown recently [19], the major contribution to the D band is made by vibrations that satisfy the condition $q \approx 2k$, where k is the wave vector of an electron involved in the transition (the quasi-selection rule). Significantly, it is the six-membered aromatic rings that are characterized by the A_{1g} modes, meaning that band D may serve as an indicator of the presence of graphite-

like nanoclusters in a carbon structure. In contrast to band *D*, the *G* band is observed for any arrangement of carbon sp^2 bonds in various rings and chains, including disordered ones. The smaller a ring cluster or the shorter a chain, the stronger their carbon bonds and, hence, the higher the corresponding frequency $\Delta\omega_{\max}^{G}$, and the higher this frequency is above the *G* band position in graphite. Indeed, the frequency of symmetric vibrations of the conjugated sp^2 bonds in the benzene molecule C_6H_6 is 1588 cm^{-1}, and the vibration frequency of the strong C=C double bond in the ethylene molecule C_2H_2 is 1630 cm^{-1}. At the same time, any disorder in a ring structure (distortions of bond lengths, valence angles, graphene layers, etc.) brings about a decrease in the $\Delta\omega_{\max}^{G}$ frequency relative to the *G* line in graphite, as is the case, for instance, in onion-like or amorphous structures [20], as well as a substantial broadening of both bands *G* and *D*.

In view of the above, the appearance of the high-frequency component G_{high} in the spectra of the composite films should be considered as an indication that incorporation of a metal into the *a*-C:H matrix gives rise to breaking of the sp^2-coordinated carbon bonds and formation of smaller nanoclusters in the form of rings and/or shorter carbon chains. Because, as was already mentioned, the contribution of G_{high} to the spectrum of *a*-C:(H, Co) is substantially larger than its contribution to *a*-C:(H, Cu), it may mean that incorporation of Co makes this destructive process more efficient than in the case of Cu. At the same time, as evident from Fig. 3, increasing the Co content in an unannealed *a*-C:(H, Co) film from [Co]/[C] = 0.5 to 0.73 shifts the G_{high} component to lower frequencies, from 1612 to ~1589 cm^{-1}, closer to the *G* line in nanographite. This effect implies that Co-induced bond breaking is accompanied by the inverse process of linking the dangling bonds to form longer chains and/or larger nanoclusters of rings (graphite-like nanoclusters). In addition, we cannot exclude the formation of single benzene rings. No such reconstruction of rings or chains is observed in *a*-C:(H, Cu) films at the Cu concentrations under study; indeed, as the Cu content increases, the G_{high} component shifts only to higher frequencies (Fig. 3).

The broad G_{low} component observed in the spectra of the composite films, just as in the case of the *G* band in the *a*-C:H samples, indicates pronounced disorder (amorphicity) of the carbon sp^2 bond structure. If, however, the Cu content in *a*-C:(H, Cu) is high enough, the maximum of G_{low} is shifted slightly to higher frequencies compared to *a*-C:H (Fig. 3), which indicates a certain Cu-induced ordering of the amorphous *a*-C:H subsystem. A small fraction of short chains with conjugated bonds (a small G_{high} contribution) is apparently incorporated into this amorphous structure. Unlike Cu, the strong destructive effect of Co, if present at a high enough concentration in *a*-C:(H, Co), gives rise to a still stronger disordering in the amorphous *a*-C:H subsystem, with the G_{low} component being shifted to lower frequencies (Fig. 3). However, since the contribution of G_{low} decreases as the Co content increases [16], it has to be concluded that the Co-induced disordering involves only a fraction of the sp^2 bonds. Regarding the growth in the G_{high} contribution, as was mentioned above, it is a consequence of ordering in combination with the formation of very small graphite-like nanoclusters. Note that the *G* band in the spectrum obtained for a relatively low Co content permits the isolation, in addition to G_{high}, of two more components, namely, G_{low1} and G_{low2}, one of which is the signature of amorphization and the other, of ordering (Fig. 3). We may assume, in this context, that the above processes are of a local nature and occur near metal atoms. On the whole, the behavior of the *G* band components indicates that Co and Cu induce graphitization of the carbon subsystem in the composite films.

An unambiguous conclusion in favor of graphitization follows from the increase in the relative intensity of band *D* observed to occur as the Co and Cu content in the composite films increases (Fig. 1). If we consider a less disordered system of sp^2 bonds (instead of a more disordered system), the enhancement of band *D* can occur only with an increasing number, ordering, and clusterization of six-membered aromatic rings. In this case, the typical size of the graphite-like clusters L_a may be roughly estimated from the ratio $I_D/I_G = \gamma L_a^2$ [17], where I_G and I_D are the intensities of bands *G* and

Relative intensity of Raman band *D* and characteristic dimensions of the graphite-like nanoclusters in *a*-C:H, *a*-C:(H, Cu), and *a*-C:(H, Co)

Film	[*Me*]/[C]*	Annealing	I_D/I_G	L_a, Å	*M*	$\Delta M^{ann}/M$, %
a-C:H	0	Before	0.39	8.4	12	
		After	0.71	11.4	21	75
a-C:(H, Cu)	0.62	Before	0.40	8.5	12	
	1.0	Before	0.52	9.7	16	
		After	0.54	9.9	16	0
a-C:(H, Co)	0.35	Before	0.54	9.9	16	
		After	0.62	10.6	19	
	0.50	Before	0.67	11.0	20	
	0.73	Before	0.65	10.9	20	
		After	0.78	11.9	23	15

* The value of [Me]/[C] was determined before film annealing.

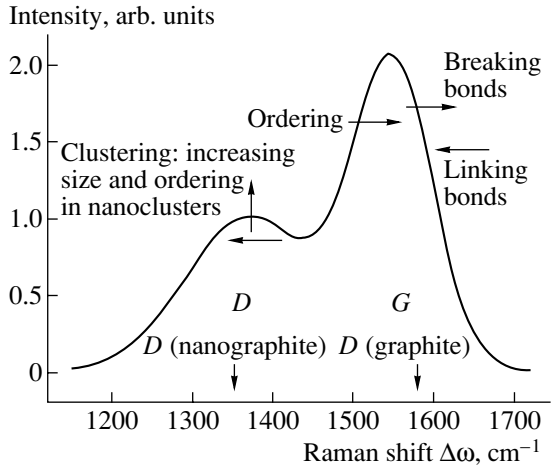

Fig. 4. Diagram illustrating the main changes in the Raman spectrum of *a*-C:H induced by modification with metals and/or thermal annealing (arrows) and the corresponding structural rearrangement in the carbon sp^2 subsystem.

D, respectively, and γ is a coefficient determined from the condition of joining this relation with the empirical expression $I_D/I_G = 44/L_a$ [12], which is valid at the transition from nanographites to a disordered system and yields $I_D/I_G \approx 2.2$ for $L_a \approx 2$ nm. The results of estimations of L_a, as well as of the characteristic number of six-membered rings *M* in graphene clusters, are listed in the table. For all the samples, L_a is on the order of 1 nm. Note that the maximum relative increase in L_a induced by incorporation of a metal (Co with [Co]/[C] = 0.73) is only slightly in excess of 30%. As should be expected from the pattern of the Raman spectra, Co stimulates growth of graphene clusters more efficiently than Cu. These estimates of the size of such nanoclusters are in reasonable agreement with electron microscope and optical studies of *a*-C:H [21, 22].

As for the spectral position of the peak of band *D*, it is governed by the relation between the size and number of graphite-like clusters with a given degree of disorder. The overall trend towards a low-frequency shift of the peak of band *D* that follows metal incorporation suggests the growth of graphite-like nanoclusters. The peak of *D* approaches the position of line *D* in the nanographites, which corresponds to Raman transitions at the *K* point of the Brillouin zone. Regarding the shape of the optical phonon branch near the *K* point, it is such that transitions in the larger nanoclusters involve, taking into account the size quantization, lower frequency vibrations [23]. The maximum of *D* may even lie at a lower frequency than that in the nanographites (Fig. 3). Such a circumstance should be attributed to disorder in the nanoclusters.

The *B* component is most likely a superposition of inhomogeneously broadened components of different origin. This component may receive contributions, in particular, from diffuse PDS peaks of graphite (near 1470 cm^{-1}) [24] or from a single graphene layer (in the vicinity of 1500 cm^{-1}) [23]. In addition, this region also contains one of the vibrational frequencies indicative of benzene rings (1486 cm^{-1}), whose formation in the films under study is possible, and the bending vibrations of sp^2 groups of CH or, possibly, sp^3-coordinated groups of CH_2 or CH_3, which manifest themselves in the IR spectra of *a*-C:H [25] and of *a*-C:(H, Co) at 1450 cm^{-1} [8].

The low-intensity component D_{low} can be assigned to the diffuse PDS peak near 1250 cm^{-1} [26]. The vibrations of a pair of coupled benzene rings at 1311 cm^{-1} may also possibly contribute to D_{low} [18]. In this case, the observed high-frequency shift of the D_{low} component induced by the metal incorporation may also be caused by an increasing concentration of benzene rings.

Figure 4 displays the overall changes in the *G* and *D* Raman bands induced by *a*-C:H modification with copper and cobalt and the corresponding rearrangement in the subsystem of carbon sp^2 bonds.

The spectral response of the Raman components to the metal content in the annealed films is also shown in Fig. 3. As in the case of the unannealed samples, the high-frequency component of band *G*, specifically, G_{high} (1601–1615 cm^{-1}), is the most clearly pronounced. The low frequency component G_{low} is shifted, due to annealing, to higher frequencies (1573–1577 cm^{-1}) and approaches, while not reaching it, the position of the *G* line in graphite. Annealing increases the ratio I_D/I_G (see table), and the maximum of the *D* band shifts, as a rule, with the exception of *a*-C:(H, Cu), to lower frequencies. All these observations provide evidence for thermally stimulated graphitization of the carbon structure in the films, which agrees with the earlier data available on *a*-C:H [27]. Graphitization induced by annealing, as well as by the incorporation of metals, includes the stage of sp^2 bond breaking. Some of these bonds, in fractions of chain structures, remain dangling (G_{high}), while others close to form more ordered graphene-like ring clusters (the high-frequency shift of G_{low} and an increase in I_D/I_G). The high-frequency shift of the *D* peak induced by annealing of *a*-C:(H, Cu) (Fig. 3) is probably due to the fact that structural ordering sets in primarily in the very small nanoclusters.

The table also lists estimates of the sizes of such clusters (L_a and *M* parameters) in the annealed films. The relative changes in I_D/I_G, L_a, and *M* induced by annealing in the composite films are smaller than those in unmodified *a*-C:H (see table); i.e., the presence of a metal suppresses graphitization. For instance, annealing *a*-C:(H, Cu) has almost no effect on the size of the graphite-like clusters; indeed, the relative change in the characteristic number of rings in a cluster, $\Delta M^{ann}/M$, is close to zero. In *a*-C:(H, Co), the effect of annealing is more pronounced. This circumstance may be attributed to the fact that, in an as-prepared *a*-C:(H, Co) film, Co is present primarily in the form of the carbide Co_2C,

which decomposes at a temperature T_{ann} = 380°C [28]. This situation gives rise to an enhanced concentration of dangling carbon bonds, which can subsequently link to form aromatic rings and eventually clusterize. Therefore, if, before annealing, *a*-C:(H, Co) contains a high enough amount of cobalt ([Co]/[C] = 0.73), the graphite-like clusters after annealing may be even larger than in annealed *a*-C:H. Since Cu does not chemically react with carbon, and there are no Cu–C valence bonds in *a*-C:(H, Cu), the Cu impurity inhibits the growth of graphite-like clusters more efficiently than Co.

Thus, thermal annealing produces the same kind of effects in the sp^2 structure of *a*-C:(H, Cu) and *a*-C:(H, Co) composite films as it does in unmodified *a*-C:H and *a*-C:H modified with metals, which means that the diagram in Fig. 4 remains valid in this case as well. While annealing intensifies graphitization, in the presence of a metal, particularly Cu, thermally stimulated graphitization is less efficient.

5. CONCLUSION

The main results of this study can be summarized as follows:

(1) An analysis of the experimental Raman spectra of *a*-C:(H, Cu) and *a*-C:(H, Co) composite films in the 1200- to 1700-cm^{-1} region, corresponding to vibrations of sp^2-coordinated carbon atoms, has revealed the main changes occurring in the carbon structure as a result of modification of *a*-C:H with copper and cobalt.

(2) It is shown that incorporation of Cu and Co into *a*-C:H in concentrations comparable to the carbon content brings about, on the one hand, breaking of the carbon bonds and fragmentation of chain and ring structures and, on the other hand, linking of a fraction of the dangling bonds and the formation of more ordered graphite-like nanoclusters.

(3) It is established that the destructive effect of Co in *a*-C:H is substantially stronger than that of Cu, which seems only natural for a metal capable of chemical interaction with carbon to produce the carbide Co_2C. This property of Co also accounts for the higher efficiency of graphitization of the sp^2 subsystem in *a*-C:(H, Co) than in *a*-C:(H, Cu).

(4) An analogy between the structural rearrangements in *a*-C:H induced by Cu and Co modification and those resulting from thermal annealing is revealed.

(5) It is shown that Cu and Co interfere with thermally stimulated graphitization of carbon in the course of composite film annealing. The role of Co as an inhibitor of graphitization during annealing is more weakly pronounced than that of Cu, which is accounted for by decomposition of Co_2C and formation of a high concentration of dangling bonds.

(6) Estimates show that the linear dimensions of the graphite-like nanoclusters are close to 1 nm (10–20 aromatic rings) and that the relative changes induced in them by an incorporation of metals in the concentration range under study or by annealing do not exceed 30%.

ACKNOWLEDGMENTS

This study was supported by the Russian Foundation for Basic Research, project no. 03-02-16289.

We also acknowledge the support of the Presidium of the Russian Academy of Sciences within the framework of the basic research program “The Effect of Atomic–Crystalline and Electronic Structure on the Properties of Condensed Media.”

REFERENCES

1. J. L. Flottard, J. Akinnifesi, E. Cambril, and B. Despax, J. Appl. Phys. **70**, 798 (1991).
2. V. I. Ivanov-Omskii, in *Diamond Based Composites and Related Materials*, Ed. by M. Prelas, A. Benedictus, L.-T. S. Lin, G. Popovici, and P. Gielisse (1997), NATO ASI Ser., Ser. 3, Vol. 38, p. 171.
3. Q. E. Huang, S. F. Yoon, Rusli, *et al.*, J. Appl. Phys. **90**, 4520 (2001).
4. A. V. Kolobov, J. Tominaga, T. K. Zvonareva, *et al.*, J. Appl. Phys. **92**, 6195 (2002).
5. J. Robertson, Prog. Solid State Chem. **21**, 199 (1991).
6. A. C. Ferrari and J. Robertson, Phys. Rev. B **64**, 075414 (2001).
7. V. I. Ivanov-Omskiĭ, T. K. Zvonareva, and G. S. Frolova, Fiz. Tekh. Poluprovodn. (St. Petersburg) **34**, 1450 (2000) [Semiconductors **34**, 1391 (2000)].
8. T. K. Zvonareva, E. I. Ivanova, G. S. Frolova, *et al.*, Fiz. Tekh. Poluprovodn. (St. Petersburg) **36**, 734 (2002) [Semiconductors **36**, 695 (2002)].
9. M. Tamor and W. Vassel, J. Appl. Phys. **76**, 3823 (1994).
10. J. Schwan, S. Ulrich, V. Batolly, *et al.*, J. Appl. Phys. **80**, 440 (1996).
11. R. J. Nemanich and S. A. Solin, Phys. Rev. B **20**, 392 (1979).
12. F. Tuinstra and J. L. Koenig, J. Chem. Phys. **53**, 1126 (1970).
13. A. M. Danishevskiĭ, É. A. Smorgonskaya, S. K. Gordeev, and A. V. Grechinskaya, Fiz. Tverd. Tela (St. Petersburg) **43**, 132 (2001) [Phys. Solid State **43**, 137 (2001)].
14. V. I. Ivanov-Omskiĭ and G. S. Frolova, Zh. Tekh. Fiz. **65** (9), 186 (1995) [Tech. Phys. **40**, 966 (1995)].
15. T. K. Zvonareva, V. M. Lebedev, T. A. Polyanskaya, *et al.*, Fiz. Tekh. Poluprovodn. (St. Petersburg) **34**, 1135 (2000) [Semiconductors **34**, 1094 (2000)].
16. É. A. Smorgonskaya, T. K. Zvonareva, E. I. Ivanova, *et al.*, Fiz. Tverd. Tela (St. Petersburg) **45**, 1579 (2003) [Phys. Solid State **45**, 1658 (2003)].
17. A. C. Ferrari and J. Robertson, Phys. Rev. B **61**, 14095 (2000).
18. D. Lin-Vien, N. B. Coltharp, W. G. Fateley, and J. G. Graselli, *The Handbook of Infrared and Raman Character-*

istic Frequencies of Organic Molecules (Academic, New York, 1991).

19. C. Thomsen and S. Reich, Phys. Rev. Lett. **85**, 5214 (2000).
20. E. D. Obraztsova, M. Fujii, S. Hayashi, *et al.*, Carbon **35**, 821 (1998).
21. V. I. Ivanov-Omskii, V. I. Siklitskii, A. A. Sitnikova, *et al.*, Philos. Mag. B **76**, 973 (1997).
22. S. G. Yastrebov, V. I. Ivanov-Omskii, V. I. Siklitskii, and A. A. Sitnikova, J. Non-Cryst. Solids **227–230**, 622 (1998).
23. C. Mapelli, C. Castiglioni, G. Zebri, and K. Mullen, Phys. Rev. B **60**, 12710 (1999).
24. R. Nicklow, N. Wakabayashi, and H. G. Smith, Phys. Rev. B **5**, 4951 (1972).
25. J. Ristein, R. T. Stief, L. Ley, and W. Bayer, J. Appl. Phys. **84**, 3836 (1998).
26. M. S. Dresselhaus, M. A. Pimenta, A. Marucci, *et al.*, in *Proceedings of International Symposium of Carbon* (Tokyo, 1998), p. 94.
27. V. I. Ivanov-Omskiĭ, A. V. Tolmachev, and S. G. Yastrebov, Fiz. Tekh. Poluprovodn. (St. Petersburg) **35**, 227 (2001) [Semiconductors **35**, 220 (2001)].
28. J. J. Delaunay, T. Hayashi, M. Tomita, and S. Hurono, J. Appl. Phys. **62**, 2200 (1997).

Translated by G. Skrebtsov

Semiconductors, Vol. 39, No. 8, 2005, pp. 941–943. Translated from Fizika i Tekhnika Poluprovodnikov, Vol. 39, No. 8, 2005, pp. 976–978.

CONFERENCE.
AMORPHOUS, VITREOUS, AND POROUS SEMICONDUCTORS

Transport of Protons in Amorphous Hydrogenated Carbon

V. I. Ivanov-Omskiĭ^ and S. G. Yastrebov

Ioffe Physicotechnical Institute, Russian Academy of Sciences, Politekhnicheskaya ul. 26, St. Petersburg, 194021 Russia
^ e-mail: ivanov.ivom@mail.ioffe.ru

Submitted December 27, 2004; accepted for publication January 12, 2005

Abstract—The effect of copper on broadening of the band of infrared-radiation absorption is observed in the region of extension of the OH…O stretching modes (~3100–3700 cm^{-1}) in amorphous carbon modified by copper. It is shown that this broadening of the absorption band, accompanied by its shift to lower frequencies, occurs due to transport of protons between neighboring hydroxyl groups in linear OH…O chains. The distribution function for the lengths of these chains is determined. *© 2005 Pleiades Publishing, Inc.*

1. INTRODUCTION

In the context of the search for a solution to the problem of designing compact fuel elements that can be integrated into silicon-based electronic circuits, we carried out studies aimed at identifying new materials based on amorphous carbon and exhibiting proton conductivity. In this paper, we report the results of studying proton transport in amorphous hydrogenated carbon modified by copper. To this end, we used infrared (IR) spectroscopy of carbon in the region of frequencies characteristic of stretching vibrations of O–H groups encompassed by hydrogen bonds (~3100–3700 cm^{-1}).

2. EXPERIMENTAL

Layers of amorphous hydrogenated carbon (*a*-C:H) were deposited onto substrates of single-crystal silicon using magnetron sputtering of a graphite target in plasma consisting of hydrogen and argon. In order to modify the hydrogenated carbon using metal nanoclusters, we applied cosputtering of targets composed of graphite and a corresponding metal [1]. We used copper as the activator of proton transport and as a potential catalyst for the hydrogen–proton transformation. The copper content amounted to ~30 at %. In order to study the optical absorption, we used a Specord 75IR double-beam spectrometer with a resolution of ~2 cm^{-1}. The absorption band related to the stretching vibrations of hydroxyl in the *a*-C:H and *a*-C:(H, Cu) films is shown in Fig. 1. It can be seen that the structure of the band is poorly pronounced; however, it is worth noting that there are an asymmetric broadening and appreciable shift of the band in comparison with the hydroxyl band of water vapors. This circumstance is indicative of the formation of hydrogen bonds between neighboring hydroxyl groups incorporated into the amorphous carbon matrix [2] or with other hydrogen-containing fragments of the structure.

3. RESULTS AND DISCUSSION

When analyzing the mechanism of broadening of vibrational bands for hydroxyl groups in amorphous carbon, we restrict ourselves to consideration of the interaction between hydroxyl groups involved in a hydrogen bond. It is well known that such interaction occurs due to proton transport, in other words, due to the proton delocalization resulting from proton hops from one hydroxyl group to a neighboring negatively charged oxygen atom in another closely spaced hydroxyl group.

The hydroxyl groups involved in this proton exchange can be considered as the fragments of branched networks. Let us consider a chain structure as an example of this network. A linear chain is the simplest of such structures. The frequency spectrum of eigenmodes of a linear chain that consists of hydroxyl

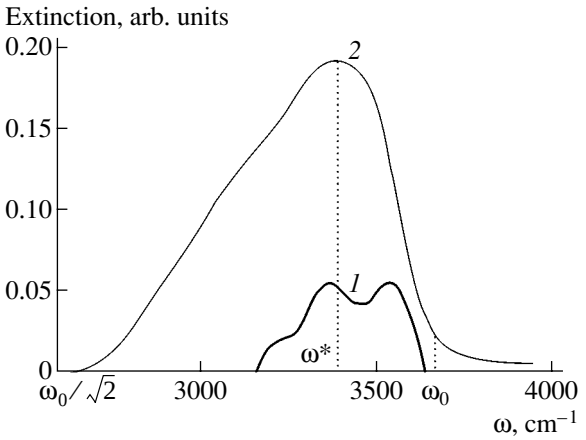

Fig. 1. Spectral band of extension vibrations for the O–H bonds in (*1*) *a*-C:H and (*2*) *a*-C:(H, Cu).

1063-7826/05/3908-0941$26.00 © 2005 Pleiades Publishing, Inc.

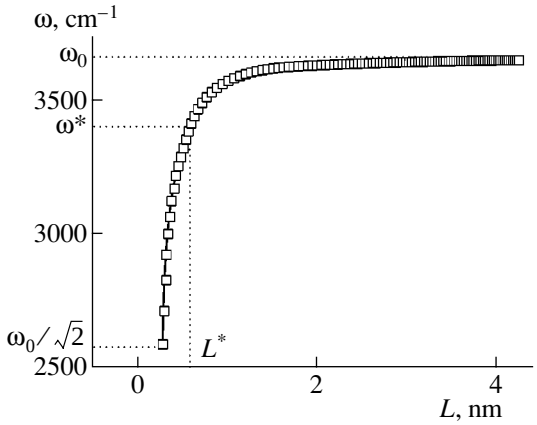

Fig. 2. Dependence of the vibration frequency on the size of chains of hydroxyl groups coupled by proton exchange.

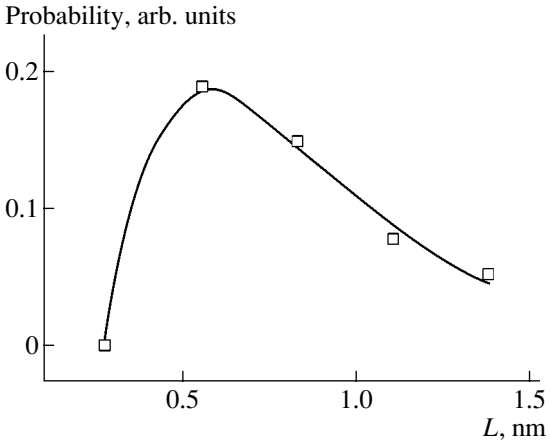

Fig. 3. The length distribution function for chains of hydroxyl groups coupled by proton exchange in *a*-C:(H, Cu).

groups is described by the following expression in the approximation of harmonic oscillators:

$$\omega = \omega_0 \left| \cos \frac{qa}{4} \right|. \quad (1)$$

Here, $\omega_0 = 3756$ cm^{-1} [3] corresponds to the frequency of vibrations of an isolated hydroxyl group, $\pi/L \le q \le \pi/a$ is the wave vector of vibrations of a chain of size L, and $a = 0.276$ nm [4] is the separation between oxygen ions in neighboring groups involved in the hydrogen bond (i.e., the hydrogen-bond length). The spectrum of frequencies ω is limited by the condition

$$\frac{\omega_0}{\sqrt{2}} \le \omega \le \omega_0. \quad (2)$$

The form of the function relating the eigenmode of chain vibrations to the chain size is illustrated in Fig. 2. Using the data shown in Fig. 2 and that obtained using formula (1) and Fig. 1, we can estimate the sizes of the chains. As can be seen from Fig. 2, the size of the hydroxyl-group chains involved in proton exchange, based on the frequency ω* corresponding to the peak in the absorption band for hydroxyl groups in the case of *a*-C:(H, Cu) (see Fig. 1), is found to be $L^* \sim 1$ nm. Assuming that the absorptance (Fig. 1) is proportional to the density of the chains, we can reconstruct the size distribution function for the chains. The corresponding result is shown in Fig. 3. The portion of the curve to the left of the peak is interpolatory and indicates that the probability of formation of OH…O chains with a length smaller than two covalent radii of oxygen is low. The function reproduced in Fig. 3 shows that proton transport can be effected at a distance of ~1.5 nm in *a*-C:(H, Cu), which means that it is possible to use this material for the fabrication of proton membranes.

In conclusion, we note that the concept of proton transport in hydroxyl chains has been adequately considered in a number of previous publications, for instance, in order to explain many phenomena in biological systems [5]. For example, encapsulation of water in single-wall carbon nanotubes, forming synthetic networks of hydroxyl groups, has recently been studied both experimentally and theoretically [6–10]. This line of research offers new ways forward with respect to the development of the physics of nanostructures.

4. CONCLUSION

We developed a model that makes it possible to determine the length of a chain of hydroxyl groups coupled by proton exchange from the shift of the OH⋯O vibrational frequencies in *a*-C:H in reference to the vibrational frequency of a hydroxyl group isolated in vacuum. We managed to determine the distribution function for the lengths of the hydrogen bonds in these chains in the case of bonds that are formed in hydroxyl chains involved in proton exchange in *a*-C:(H, Cu). Considering the proton exchange in the chains as a manifestation of proton transport, we can assume that amorphous hydrogenated carbon modified by copper is a promising material for the development of solid-state electrolytes with protonic conductivity.

ACKNOWLEDGMENTS

This study was supported in part by the Russian Foundation for Basic Research, project no. 03-02-16289-a. We also acknowledge the support of the Presidium of the Russian Academy of Sciences within the framework of the basic research program “The Effect of Atomic–Crystalline and Electronic Structure on the Properties of Condensed Media.”

REFERENCES

1. T. K. Zvonareva, V. I. Ivanov-Omskiĭ, A. V. Nashchekin, and L. V. Sharonova, Fiz. Tekh. Poluprovodn. (St. Petersburg) **34**, 96 (2000) [Semiconductors **34**, 98 (2000)].
2. V. I. Ivanov-Omskiĭ, Pis'ma Zh. Tekh. Fiz. **26** (12), 51 (2000) [Tech. Phys. Lett. **26**, 520 (2000)].
3. P. F. Bernath, Phys. Chem. Chem. Phys. **4**, 1501 (2002).
4. P. V. Hobbs, *Ice Physics* (Clarendon, Oxford, 1974).
5. V. M. Karpan, Y. Zolotaryuk, P. L. Christiansen, and A. V. Zolotaryuk, Phys. Rev. E **70**, 056602 (2004).
6. Y. Gogotsi, J. A. Libera, A. Güvenç-Yazicioglu, and C. M. Megaridis, Appl. Phys. Lett. **79**, 1021 (2001).
7. G. Hummer, J. C. Rasaiah, and J. P. Noworyta, Nature **414**, 188 (2001).
8. C. Dellago, M. M. Naor, and G. Hummer, Phys. Rev. Lett. **90**, 105902 (2003).
9. D. J. Mann and M. D. Halls, Phys. Rev. Lett. **90**, 195503 (2003).
10. F. Zhu and K. Schulten, Biophys. J. **85**, 236 (2003).

Translated by A. Spitsyn

Semiconductors, Vol. 39, No. 8, 2005, pp. 944–950. Translated from Fizika i Tekhnika Poluprovodnikov, Vol. 39, No. 8, 2005, pp. 979–985.

CONFERENCE.
AMORPHOUS, VITREOUS, AND POROUS SEMICONDUCTORS

The Effect of Erbium and Oxygen on the Photoluminescence Intensity of Erbium and the Composition of *a*-SiO_x:(H, Er, O) Films Deposited by DC Magnetron Sputtering

Yu. K. Undalov^, E. I. Terukov, O. B. Gusev, and V. Kh. Kudoyarova

Ioffe Physicotechnical Institute, Russian Academy of Sciences, Politekhnicheskaya ul. 26, St. Petersburg, 194021 Russia
^ e-mail: undalov@mail.ioffe.ru

Submitted December 27, 2004; accepted for publication January 12, 2005

Abstract—The effect of the oxygen content (C_{O_2}) in the gas mixture (20% of SiH_4 + 80% of Ar) + O_2 and the surface area of an erbium target (S_{Er}) on the composition and Er^{3+} photoluminescence of amorphous *a*-SiO_x:(H, Er, O) films prepared by dc magnetron sputtering has been investigated. Analysis of the experimental data shows that [Er–O] and [Er–O–Si–O] clusters are formed in the gas plasma due to the competing processes of oxidation and sputtering of Si and Er targets and to the interaction of [Si–O] and [Er–O] clusters with each other and with the oxygen in the gas phase. The discontinuities in the dependences of the contents of erbium-bound oxygen and erbium in a film, $N_O^{Er–O}$ and $N_{Er} = f(C_{O_2}, S_{Er})$, at $C_{O_2} \approx (5–6.5)$ mol % supports the hypothesis on the existence of different erbium clusters. The necessary conditions for preparing *a*-SiO_x:(H, Er, O) films with the highest photoluminescence intensity of erbium ions at a wavelength of 1.54 μm are determined.

1. INTRODUCTION

The use of erbium and oxygen ions as dopants in *a*-SiO_x:(H, Er, O) films makes it possible to obtain an Er^{3+} photoluminescence (PL) signal at a wavelength of 1.54 μm, which is weakly absorbed by a quartz light guide. As was shown in [1–6], the Er^{3+} PL intensity I_{PL}^{Er} in SiO_x:(H, Er, O) films depends on many parameters: the total oxygen content N_O^{tot}, the erbium content N_{Er}, the content of oxygen in erbium clusters $N_O^{Er–O}$, the concentration of erbium clusters, the concentration of photoactive erbium centers N_{Er}^{ph}, the content of oxygen $N_O^{Si–O}$ and hydrogen N_H in the SiO_x:H matrix, its structure, the defect concentration, and so on. When these films are prepared by dc magnetron sputtering, the above parameters are closely related (though ambiguously, as was shown in [4]) to the experimental conditions: the oxygen content C_{O_2} in the SiH_4–Ar gas mixture at the plasma input region and the area S_{Er} of the sputtered metallic erbium plate (Er target) (the other experimental parameters were kept invariable [4]). On the basis of the results of [4], it is easy to conclude that only the complete pattern of the dependence of I_{PL}^{Er} on all the above parameters, including the process parameters, can solve the problem of reproducible preparation of SiO_x:(H, Er, O) films with the highest possible I_{PL}^{Er}, making them applicable to practical use. However, it is fairly difficult to obtain a complete description of all these relations. The situation can be somewhat clarified by simplifying the problem as follows: one has to determine the dependence $I_{PL}^{Er} = f(N_O^{tot}, N_{Er})$ by relating it to the process parameters C_{O_2} and S_{Er}. In this case, the dependence $I_{PL}^{Er} = f(N_O^{tot}, N_{Er})$ should be represented as a hypothetical three-dimensional figure with a vertex corresponding to the maximum Er^{3+} PL intensity $(I_{PL}^{Er})_{max}$. The cross sections of this figure that do not pass through the point $(I_{PL}^{Er})_{max}$ will then have their own maxima at $I_{PL}^{Er} < (I_{PL}^{Er})_{max}$, as was shown in [1–6]. If we take into account the other above-mentioned factors affecting I_{PL}^{Er}, the shape of this figure becomes more complicated. However, the proposed simplified representation of the dependence of I_{PL}^{Er} on a large number of film parameters in the form $I_{PL}^{Er} = f(N_O^{tot}, N_{Er})$ will aid our understanding of the behavior of the *a*-Si:H–O–Er system as applied to the conditions of deposition of SiO_x:(H, Er, O) films by dc magnetron sputtering.

This study, which is a continuation of the investigations started in [4], is concerned with establishment of the conditions under which *a*-SiO_x:(H, Er, O) films pre-

pared by dc magnetron sputtering attain the largest values of I_{PL}^{Er}.

2. EXPERIMENTAL

The *a*-SiO_x:(H, Er, O) films were prepared according to the method described in [4]. The relationship between the film composition and I_{PL}^{Er}, with S_{Er} in the range 0–18 mm^2, at five fixed values of C_{O_2}: 0.15, 3.5, 6.5, 8, and 12 mol % (the partial oxygen pressure P_{O_2} ranged from 1.3×10^{-5} to 1.04×10^{-3} Torr) was studied. All the other parameters of the film deposition were kept constant, as in [4]. In particular, the measured total pressure (calibrated with respect to air) of the gas mixture, (20% of SiH_4 + 80% of Ar) + O_2, introduced into the gas phase of the plasma was always kept constant and equal to 7.5×10^{-3} Torr. The elemental composition of the films and their structure were determined, in the same way as in [4], using Rutherford backscattering (RBS) (N_O^{tot} and the Si content N_{Si}), nuclear resonance reaction (NRR) analysis (N_{Er}), and infrared (IR) spectroscopy (N_O^{Si-O} and N_H). The dependences N_H and $N_{Si} = f(S_{Er})$ are not considered here. The technique for measuring I_{PL}^{Er} and the optical band gap E_g^{opt} was also the same as in [4]. When measuring I_{PL}^{Er} for all the films, we used the same reference sample, which differed from that used in [4].

3. RESULTS AND DISCUSSION

On the basis of experimental data, a hypothesis was stated in [4] suggesting the existence of two types of erbium clusters ($[Er–O]^{n-}$ and $[Er–O–Si–O]^{m-}$) in *a*-SiO_x:(H, Er, O) films deposited by dc magnetron sputtering. The most likely scenario is that these clusters are formed in the plasma. The composition and content of Er clusters in the gas phase and films depend, all other factors being equal, on C_{O_2} and S_{Er} ($S_{Er} \approx 3$ mm^2 in [4]). The formation of Er clusters is characterized by a nonmonotonic change in N_O^{tot}, N_{Si}, N_O^{Si-O}, N_H, N_{Er}, and I_{PL}^{Er} as C_{O_2} is increased. The observed behavior of these dependences resembles a situation in which, for a certain relation between the contents of the components in the gas phase, favorable conditions are implemented for the formation of one of the above-mentioned types of Er clusters, $[Er–O–Si–O]^{m-}$ (and, possibly, their associates), in experimentally detectable amounts.

In this context, an evident question arises about the behavior of the system, in particular, the gas phase and the composition of the *a*-SiO_x:(H, Er, O) films with a change in S_{Er} at different fixed values of C_{O_2}. The results of experiments aimed at solving this problem are shown in Figs. 1–4.

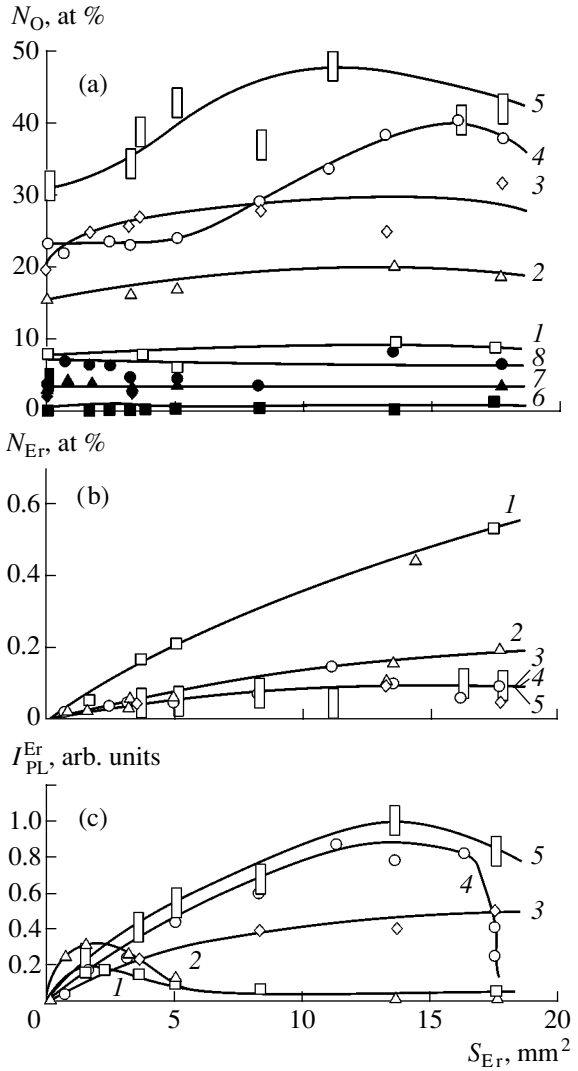

Fig. 1. Dependence of (a) the oxygen content N_O, (b) the erbium content N_{Er}, and (c) the photoluminescence Er^{3+} intensity I_{PL}^{Er} in *a*-SiO_x:(H, Er, O) films on S_{Er} at different fixed values of C_{O_2}: (*1*, *6*) 0.15, (*2*, *7*) 3.5, (*3*) 6.5, (*4*, *8*) 8, and (*5*) 12 mol %. (a) (*1–5*) N_O^{tot}, NRR data; (*6–8*) N_O^{Si-O}, IR data. (b) N_{Er}, RBS data.

Analysis of the experimental data allowed us to draw the following conclusions:

(1) The content of silicon-bound oxygen in the *a*-SiO_x:H matrix remains almost constant (or slightly varies) when there is a fixed value of C_{O_2} and S_{Er} is changed in the entire range under consideration (0–18 mm^2) (Fig. 1a, curves *6–8*). Taking into account the direct dependence of N_{Er} on S_{Er} (Fig. 1b), we can note, under certain assumptions, the absence of any sig-

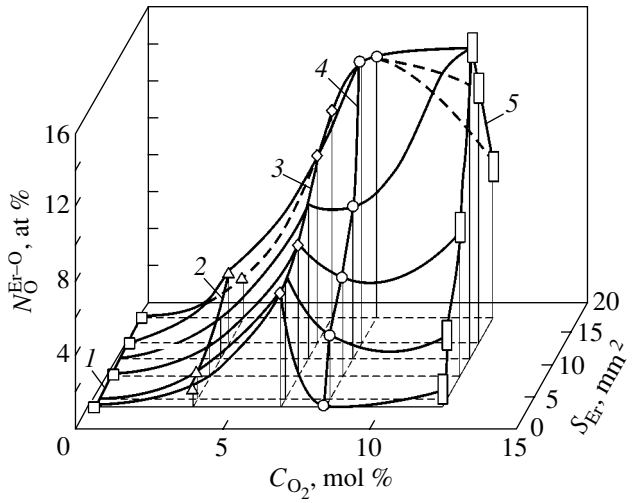

Fig. 2. Effect of C_{O_2} and S_{Er} on the content of erbium-bound oxygen in *a*-SiO_x:(H, Er, O) films. Curves *1–5* correspond to *1–5* in Fig. 1.

nificant effect produced by the erbium introduced into the system on the composition and structure of the amorphous matrix *a*-SiO_x:(H, Er, O). With an increase in C_{O_2}, the dependence $N_O^{Si-O} = f(S_{Er})$ shifts to larger values of N_O^{Si-O} (Fig. 1a, curves *6–8*). The matrix of a sample obtained at C_{O_2} = 8 mol% and $S_{Er} \approx 13.5$ mm^2 is characterized by the following parameters: a film with $N_O^{Si-O} \approx 9$ at% has $E_g^{opt} \approx 2.2$ eV and the refractive index $n = 2.44$. When C_{O_2} = const, the curves $N_O^{Si-O} = f(S_{Er})$ are always below the curves $N_O^{tot} = f(S_{Er})$ on the N_O axis (Fig. 1a). This fact indicates that the oxygen introduced into the gas phase is bound not only to the Si atoms of the amorphous matrix *a*-SiO_x:H but also to Er, H, and other atoms.

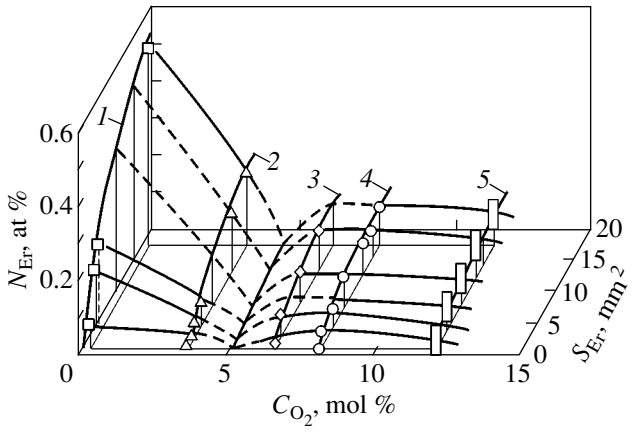

Fig. 3. The dependence $N_{Er} = f(C_{O_2}, S_{Er})$ for *a*-SiO_x:(H, Er, O) films. Curves *1–5* correspond to *1–5* in Fig. 1.

(2) By comparing the values of N_O^{tot} and N_O^{Si-O} for different fixed values of C_{O_2}, both at $S_{Er} = 0$ and at $S_{Er} > 0$ (Fig. 1a), we can estimate the content of oxygen bound to erbium in the films at $S_{Er} > 0$. Indeed, comparison of the dependences of the film composition and I_{PL}^{Er} on C_{O_2} and S_{Er} (Fig. 1) at C_{O_2} = const suggests that the total amount of oxygen bound to all the atoms apart from the Si atoms of the matrix and the Er atoms is such that it does not suppress Er^{3+} PL. To all appearances, unintentional impurity atoms, which insignificantly reduce I_{PL}^{Er}, only slightly affect the behavior of the curves $I_{PL}^{Er} = f(S_{Er})$. In addition, when the matrix composition does not change (N_O^{Si-O} = const) and C_{O_2} = const at $C_{O_2} \geq 6.5$ mol%, the value of I_{PL}^{Er} changes almost synchronously with N_O^{tot} (Figs. 1a, 1c). The difference $(N_O^{tot} - N_O^{Si-O})_{S_{Er}=0}$ includes the content of oxygen bound with unintentional minority impurities, in particular, hydrogen (O–H groups). When erbium is introduced into the system, the amount of this oxygen decreases by about N_O^{Er-O}. Therefore, at C_{O_2} = const, the following inequality is valid: $N_O^{Er-O} < [(N_O^{tot} - N_O^{Si-O})_{S_{Er}>0} - (N_O^{tot} - N_O^{Si-O})_{S_{Er}=0}] = (N_O^{tot})_{S_{Er}>0} - (N_O^{tot})_{S_{Er}=0} = f(C_{O_2}, S_{Er})$. Despite this circumstance, we can assume that both parts of this inequality change

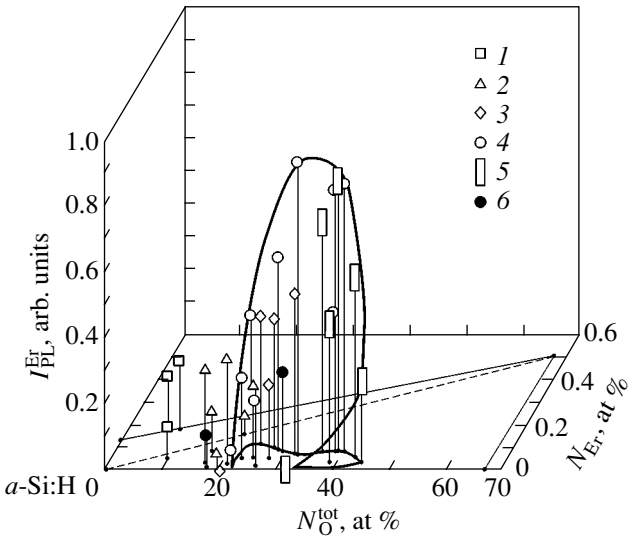

Fig. 4. Effect of the combinations of N_O^{tot} and N_{Er} on I_{PL}^{Er} for *a*-SiO_x:(H, Er, O) films depending on their position within the hypothetical region of homogeneity. Curves *1–5* correspond to *1–5* in Fig. 1. (*6*) The data [4] for films obtained at $S_{Er} \approx 3$ mm^2 and C_{O_2} = 6.5 and 9 mol %.

almost synchronously when C_{O_2} and S_{Er} are changed. In this case, the dependence $(N_O^{tot})_{S_{Er}>0} - (N_O^{tot})_{S_{Er}=0} = f(C_{O_2}, S_{Er})$ can be used to determine the surface relief $N_O^{Er-O} = f(C_{O_2}, S_{Er})$. By comparing the surfaces N_{Er}, N_O^{Er-O}, and $I_{PL}^{Er} = f(C_{O_2}, S_{Er})$, we can determine the conditions under which the composition of the Er clusters changes. Figure 2 shows the dependence $N_O^{Er-O} = (N_O^{tot})_{S_{Er}>0} - (N_O^{tot})_{S_{Er}=0} = f(C_{O_2}, S_{Er})$. As can be seen, the dependence has a kink in the vicinity of $C_{O_2} \approx$ 6.5 mol %, which has a pronounced ridge-like shape at $S_{Er} < 8$ mm^2. The position of this ridge is in good agreement with the discontinuity in the dependence $N_{Er} = f(C_{O_2}, S_{Er})$ at $C_{O_2} \approx 5$ mol % (Fig. 3) and with N_O^{tot}, N_O^{Si-O}, N_{Er}, N_{Si}, and $I_{PL}^{Er} = f(C_{O_2}, S_{Er})$ at $C_{O_2} \approx 6.5$ mol % [4]. We can attribute the presence of the ridge at $C_{O_2} \approx$ 6.5 mol % to the change in the composition of the Er clusters from [Er–O] to [Er–O–Si–O] [4]. At $S_{Er} \approx$ 8 mm^2, the ridge at $C_{O_2} \approx 6.5$ mol % begins to smooth out and even vanishes at $S_{Er} \approx 11$ mm^2. With an increase in C_{O_2} from ~11 to ~14 mol %, another peak arises, which is somewhat shifted along the S_{Er} axis (Figs. 1a, 2). The existence of the peak in the dependence $N_O^{Er-O} = f(C_{O_2}, S_{Er})$ at $C_{O_2} \geq 11$ mol % and $S_{Er} \geq 8$ mm^2 is due to an increase in the flux of [Er–O–Si–O] clusters, which contain the largest amount of erbium-bound oxygen N_O^{Er-O}. This circumstance is indicated by the increase in N_O^{tot} observed with an increase in S_{Er} at C_{O_2} = const, which is caused by the introduction of erbium into the system (Fig. 1a).

(3) It is well known that the local environment of erbium—the symmetry and chemical nature of the ligands, i.e., the first (oxygen in the case under consideration) coordination sphere—determines its luminescent activity [7]. It has been established that, at $C_{O_2} <$ 5 mol %, the nearest oxygen environment for erbium consists of about 3 atoms [2, 3, 8]. Hence, the increase in I_{PL}^{Er} may be due to not only the increase in N_{Er}^{ph} but also to a significant change in the oxygen environment nearest to erbium (an increase from ~3 to ~6 O atoms). In this case, the symmetry of the O atoms around an Er atom changes as well. The filling of the oxygen environment nearest to erbium with up to ~6 atoms, as in equilibrium systems, for example, in crystalline erbium silicates ($Er_2Si_2O_7$, Er_2SiO_5, and $Er_4Si_9O_{39}$), Er_2O_3, and *c*-Si⟨Er,O⟩ [9, 10], may occur when favorable conditions are implemented in the system; i.e., the gas phase contains a sufficient amount of oxygen and the [Er–O] and [Si–O] clusters interact with each other. Apparently, these conditions are implemented in our system at $C_{O_2} \geq 5$ mol % and $S_{Er} \geq 8$ mm^2, when $N_{Er} \approx 0.1$ at %, $(N_O^{tot})_{S_{Er}>0} - (N_O^{tot})_{S_{Er}=0} \geq 15$ at %, and $N_O^{tot} \geq 30$ at % in the film. Indeed, according to Fig. 1b [4] and Figs. 2 and 3, in the range $C_{O_2} \approx$ (5–6.5) mol %, the behavior of the dependences N_O^{Er-O} and $N_{Er} = f(C_{O_2}, S_{Er})$ changes. This change is accompanied by the replacement of [Er–O] with [Er–O–Si–O] clusters, which leads to an increase in I_{PL}^{Er} (Fig. 1c).

The atomic configuration Er–O, in which erbium has the largest coordination number (six oxygen atoms), i.e., the largest number of chemical bonds per atom, is assumed to be the most stable [11]. As a result, a possibility arises for the second (silicon) and third (oxygen) coordination shells of erbium (i.e., a [Er–O–Si–O] cluster) to be formed and exist in a nonequilibrium system. At the same time, due to the metastability of the system (the gas phase and the amorphous matrix), the third coordination shell in the [Er–O–Si–O] cluster cannot be completely occupied by oxygen atoms as it can in equilibrium systems, for example, erbium silicates [9]. However, an [Er–O–Si–O] cluster formed in the plasma seems to be more appropriate (under certain conditions) for the formation of an equilibrium-occupied first oxygen coordination sphere and the third oxygen coordination shell of erbium, as, for example, in Er_2SiO_5, i.e., spheres with 6 and 18 O atoms, respectively. As soon as nanoscale aggregation of the [Er–O–Si–O] clusters occurs in the gas phase (involving unbound oxygen ions), inclusions arise in the *a*-SiO_x:(H, Er, O) films, for example, Er_2SiO_5 [12]. It should be noted that the formation of such Er inclusions may result from the formation of corresponding clusters in the plasma rather than a supersaturation-induced deviation of the film composition from the homogeneity region of the *a*-SiO_x:(H, Er, O) system with respect to the Er clusters.

(4) The dependence $N_{Er} = f(S_{Er})$ at C_{O_2} = const (Fig. 1b), in contrast to the dependence $N_{Er} = f(C_{O_2})$ (Fig. 1b [4] and Fig. 3), monotonically increases at different fixed values of S_{Er}, demonstrating a direct relationship between N_{Er} and S_{Er}. The rate of increase in N_{Er} as S_{Er} is increased is inversely proportional to C_{O_2}. The steepest slope of the dependence $N_{Er} = f(S_{Er})$ is observed at C_{O_2} = 0.15 mol %, which indicates the increasing influence of S_{Er} on N_{Er} in comparison with the effect of the oxidation of the Er target. When the values of C_{O_2} are fixed in the range ~(6.5–12) mol %, the rate of change in N_{Er} varies only slightly with an increase in S_{Er}: the degree of oxidation of the Er target,

on reaching its maximum, tends to a constant value, thus strongly decreasing the effect of an increase in S_{Er} on N_{Er}. The weak dependence of N_{Er} on C_{O_2}, which, however, increases as S_{Er} is increased in the range $S_{Er} \geq 8$ mm^2 (Fig. 3), is due to mutual compensation of the processes of oxidation and sputtering of the Er target, interaction of the oxygen in the gas phase with the erbium-containing clusters, and some increase in the amount of sputtered erbium due to the increase in S_{Er}. The experiment showed that, despite attaining the allowable (according to [4]) increase in the homogeneous solubility of erbium in the amorphous matrix *a*-SiO$_x$:H by increasing the oxygen content in the gas phase and in the film, all attempts to significantly increase the value of N_{Er} (>0.1 at %, i.e., $>5 \times 10^{19}$ cm^{-3}) in order to increase N_{Er}^{ph} and I_{PL}^{Er} were unsuccessful due to oxidation of the Er target (in the case of dc magnetron sputtering). At the same time, the amount of oxygen in the gas phase seems to be sufficient to form the first coordination sphere and the third coordination shell around erbium, as indicated by the increase in N_O^{tot}, $N_O^{tot} - N_O^{Si-O}$, and $N_O^{Er-O} \approx (N_O^{tot})_{S_{Er}>0} - (N_O^{tot})_{S_{Er}=0}$, as well as I_{PL}^{Er}, at $N_{Er} \approx 0.1$ at % (for $S_{Er} \geq 8$ mm^2) (Figs. 1a–1c, 2).

The results reported in Fig. 1b are shown in Fig. 3 in the form of the dependence $N_{Er} = f(C_{O_2})$ for different fixed values of S_{Er}. Although experimental values of N_{Er} for $C_{O_2} \approx 5$ mol % and different values of S_{Er} are lacking in this study, we believe that the discontinuity in the dependence $N_{Er} = f(C_{O_2}, S_{Er})$ observed in Fig. 3 at $C_{O_2} \approx 5$ mol % undoubtedly exists. This statement is based on a comparison of Fig. 3 with Fig. 1b [4]. In the latter case, for the first time, the discontinuity at $C_{O_2} \approx 6.5$ mol % was shown for two different pressures of the gas mixture P_B^{tot}. The kink in the dependence $N_{Er} = f(C_{O_2})$ for all the values of $S_{Er} > 0$, as in [4], appears to correspond to the minimum Er content in the *a*-SiO$_x$:(H, Er, O) films: $N_{Er} \approx 0.01$ at % ($\sim 5 \times 10^{18}$ cm^{-3}). It can be seen from Fig. 3 that the dependence $N_{Er} = f(C_{O_2}, S_{Er})$ is represented by two different curvilinear surfaces at different sides of the kink point. The curves $N_{Er} = f(C_{O_2})$ for all the values of $S_{Er} > 0$ are steeper at $C_{O_2} < 5$ mol % than at $C_{O_2} > 5$ mol %, which is in good agreement with the similar dependence for $S_{Er} \approx 3$ mm^2 (Fig. 1b [4]). The difference in the coordinates of the kink point in Fig. 3 ($C_{O_2} \approx 5$ mol %) and Fig. 1b [4] ($C_{O_2} \approx 6.5$ mol %) does not exclude its existence and may be due to the low level of irreproducibility of the experimental results.

The above facts can be explained by the decrease in the sputtering yield of the Er target due to its oxidation, partial compensation of the decrease in the sputtered erbium due to an increase in S_{Er}, and the change of the kink point in the dependence $N_{Er} = f(C_{O_2})$ from one erbium cluster to another cluster of different composition ([Er–O] and [Er–O–Si–O]) in the plasma and in the film.

A greatly simplified scheme of the formation of [Er–O] and [Er–O–Si–O] clusters in the plasma can be described as follows: the presence of plasma-activated oxygen in the gas phase is responsible for oxidation of the surfaces of the Si and Er targets, resulting in SiO$_x$ and ErO$_y$ compositions, respectively, where $x < 2$ and $y < 1.5$. Argon ions knock out the [E–O] and [Si–O] clusters from the targets. When there is a relatively small content of oxygen in the gas phase ($0.15 \leq C_{O_2} < 0.5$ mol %), it is mainly expended on oxidation of the Si and Er targets and interaction with silane radicals. Under these conditions, [Er–O] and [Si–O] clusters are dominant in the gas phase. When a certain oxygen content is attained ($C_{O_2} > (5–6.5)$ mol %), the effect of the competing processes of oxidation and sputtering of the Er target on the value of N_{Er} leads to a decrease in N_{Er} to its minimum value, $N_{Er} \approx 0.01$ at % ($\sim 5 \times 10^{18}$ cm^{-3}) (Fig. 3), and, at a relatively large value of N_O^{Er-O} (Fig. 2), to an insignificant increase in I_{PL}^{Er} (Figs. 1d [4], 1c). It should be noted that the maximum value of I_{PL}^{Er} was also observed at the lowest Er content, $N_{Er} \approx 0.04$ at %, in [6], where the decrease in I_{PL}^{Er} was exclusively attributed to the formation of defects in the film as the Er content was increased. In our consideration, an increase in the oxygen content in the gas phase to $C_{O_2} > (5–6.5)$ mol % and an increase in the Er target area to $S_{Er} \geq 8$ mm^2 form conditions under which the combination of large values of N_O^{Er-O} (Fig. 2) and relatively small values of N_{Er} (~0.1 at %) (Figs. 1b, 3) leads to an increase in I_{PL}^{Er} (Fig. 1c). According to [4], when $C_{O_2} > 5$ mol %, other clusters ([Er–O–Si–O]) become dominant in the gas phase and in the films, as is indicated by the discontinuities in the dependences N_O^{Er-O} and $N_{Er} = f(C_{O_2}, S_{Er})$ in the vicinity of $C_{O_2} \approx 5$ mol % (Figs. 2, 3).

(5) From general considerations, it is possible suggest the existence of a direct relationship between N_{Er} and I_{PL}^{Er} for the *a*-SiO$_x$:(H, Er, O) films. However, despite the monotonic behavior of the curves $N_{Er} = f(S_{Er})$ (Fig. 1b), for all values of C_{O_2} under consideration, proceeding from Fig. 1c, two types of $I_{PL}^{Er} = f(S_{Er})$

dependence can be distinguished for all the values of C_{O_2} under study. The first type corresponds to $C_{O_2} \leq$ 3.5 mol % (curves *1*, *2*) and the second type corresponds to $C_{O_2} \geq 6.5$ mol % (curves *3*–*5*). The character of the surfaces N_O^{Er-O} and $N_{Er} = f(C_{O_2}, S_{Er})$ (Figs. 2, 3) suggests that the separation point between these two types of $I_{PL}^{Er} = f(S_{Er})$ dependence corresponds to $C_{O_2} \approx$ (5–6.5) mol %. Thus, the first type of $I_{PL}^{Er} = f(S_{Er})$ dependence, at $C_{O_2} \leq 3.5$ mol %, is characterized by a small increase in I_{PL}^{Er} in the initial portion ($0 < S_{Er} <$ 2 mm^2). Then, I_{PL}^{Er} decreases to very small values and is retained at this level even when S_{Er} significantly increases (to ~18 mm^2). The decrease in I_{PL}^{Er} (Fig. 1c, curves *1*, *2*) can be explained by the fact that, under the conditions of an oxygen deficit ($C_{O_2} < 5$ mol %), some part of the erbium added to the gas phase due to the increase in S_{Er} above 2 mm^2 is probably bound with silicon, forming nonradiative centers [Er–Si]. The additional decrease in the amount of Er (small though it was) in the plasma is more closely related to the oxidation of the Er target than the increase in the Er content resulting from an increase in S_{Er} from 0 to ~2 mm^2. In this case, the total concentration of erbium clusters ($N_c \approx N_{[Er-O]} + N_{[Er-O-Si-O]} + N_{[Er-Si]}$) is low, and, as can be seen from the portions of the curves $I_{PL}^{Er} = f(S_{Er})$ for $S_{Er} \leq 2$ mm^2, the relation $N_{[Er-O]} > N_{[Er-Si]} > N_{[Er-O-Si-O]}$ is valid, where $N_{[Er-O]}$, $N_{[Er-Si]}$, and $N_{[Er-O-Si-O]}$ are the concentrations of [Er–O], [Er–Si], and [Er–O–Si–O] clusters. Similar suppression of the sputtering of a small Er target ($S_{Er} \leq 2$ mm^2) occurs when C_{O_2} increases to ~12 mol % (curves *3*–*5*). Such a situation gives relatively low PL intensities ($I_{PL}^{Er} < 0.3$ arb. units), which only slightly differ from the corresponding values of I_{PL}^{Er} for $C_{O_2} = 0.15$ and 3.5 mol %.

The second type of $I_{PL}^{Er} = f(S_{Er})$ dependence, at $C_{O_2} > 6.5$ mol %, is characterized by a monotonic increase in I_{PL}^{Er} with an increase in S_{Er} from 0 to 14 mm^2 followed by a subsequent decrease from 14 to 18 mm^2 (Fig. 1c, curves *3*–*5*). The increase in C_{O_2} in the range above 5 mol % at $2 < S_{Er} \leq 14$ mm^2 leads to the interaction of [Er–O] and [Si–O] clusters with each other and with the oxygen in the plasma, as a result of which [Er–O–Si–O] clusters are formed; however, the ratio of different Er clusters radically changes, being determined now by the inequalities $N_{[Er-Si]} \ll N_{[Er-O]} <$ [Er–O–Si–O]. In this case, the flux of [Er–O–Si–O] clusters, containing a larger amount of oxygen in comparison with the [Er–O] clusters, increases. This effect can be seen from the increase in N_O^{tot} and N_O^{Er-O} (Figs. 1a, 2). The maximum value of I_{PL}^{Er} is attained at $S_{Er} \approx 14$ mm^2, when $N_{Er} \approx 0.1$ at % and the contents N_O^{Er-O} and $N_{[Er-O-Si-O]}$ are at their highest levels. The decrease in I_{PL}^{Er} at $S_{Er} > 14$ mm^2, $C_{O_2} > 6.5$ mol %, and $N_{Er} \approx 0.1$ at % is caused by the decrease in $N_{[Er-O-Si-O]}$ rather than changes in the composition (and structure) of the matrix if C_{O_2} = const (Fig. 1). The decrease in $N_{[Er-O-Si-O]}$, in accordance with curves *4* and *5* in Figs. 1a and 2 for $S_{Er} > 14$ mm^2, is due to the decrease in N_O^{tot} and N_O^{Er-O} under the effect of a weak change in N_{Er} as S_{Er} is increased (Fig. 1b, curve *3*). We believe that the decrease in the curves N_O^{tot} and $N_O^{Er-O} = f(S_{Er})$ in the regions corresponding to the decrease in I_{PL}^{Er} is due to a reduction in the flux of [Er–O–Si–O] clusters, which are the most enriched in oxygen. We should also add that, at C_{O_2} = 12 mol % and $S_{Er} \approx 25$ mm^2, when the film composition is characterized by the parameters $N_O^{tot} \approx 35.3$ at %, $N_{Er} \approx 0.17$ at %, and $N_O^{Er-O} \approx 4.3$ at %, $I_{PL}^{Er} \approx 0.4$ arb. units. At C_{O_2} = 16 mol % ($P_{O_2} \approx 1.3 \times 10^{-3}$ Torr) and $S_{Er} \approx 13$ mm^2, $I_{PL}^{Er} \approx 0.9$ arb. units. The parameters of these samples are not shown in Fig. 1. We report them to confirm the decrease in the curves N_O^{tot}, N_O^{Er-O}, and $I_{PL}^{Er} = f(S_{Er})$ (Figs. 1a, 1c, 2) and the weak increase in the curve $N_{Er} = f(S_{Er})$ (Fig. 1b) at $S_{Er} >$ 14 mm^2 and $C_{O_2} \geq 8$ mol %.

It can be seen from Fig. 4 that the films with compositions located in the hypothetical homogeneity region of the *a*-SiO$_x$:(H, Er, O) film [4] adjacent to the *a*-Si:H–O axis are characterized by relatively large values of I_{PL}^{Er}. For comparison, Fig. 4 also shows the compositions of two samples (points *6*) investigated in [4], for which I_{PL}^{Er} was determined using the same reference sample as in this study. As is known, the above-mentioned homogeneity region of the *a*-SiO$_x$:(H, Er, O) film contains Er clusters richer in oxygen than those in the rest region (adjacent to the *a*-Si:H–Er axis) [4]. It is suggested that the boundary of the homogeneity region in the *a*-SiO$_x$:(H, Er, O) film (shown by a thin line in the *a*-Si:H–Er–O plane in Fig. 4) formally determines the very strong decay of the Er^{3+} PL only because of the supersaturation of the amorphous matrix with respect to erbium, oxygen, or their chemical associates. For simplicity, the plot in Fig. 4 disregards the possibility (which we believe to be real) of initiation of the formation of nanocrystals of silicon and erbium silicates when the

amorphous matrix is supersaturated with erbium, as well as the possibility of deposition of some large particles (for example, [Er–O–Si–O] nanoclusters) formed in the gas phase on the film growth surface.

In summary, we should note that the relation between the ratio N_O^{tot}/N_{Er} with I_{PL}^{Er} used in [1], according to the data obtained here and in [4], is not evident and does not explain the effect of the composition of *a*-SiO_x:(H, Er, O) films on Er^{3+} PL. This conclusion is confirmed by considering the dependence $I_{PL}^{Er} = f(N_O^{tot}/N_{Er})$ for films deposited by dc magnetron sputtering under different conditions. First, the largest value of I_{PL}^{Er}, obtained by us at C_{O_2} = 12 mol % and $S_{Er} \approx 14$ mm^2, corresponds to N_O^{tot}/N_{Er} = 480, which significantly differs from the value of N_O^{tot}/N_{Er} = 10 reported in [1]. Apparently, different cross sections of the hypothetical figure $I_{PL}^{Er} = f(N_O^{tot}/N_{Er})$, not passing through the point $(I_{PL}^{Er})_{max}$ or corresponding to the optimal combination of the values of C_{O_2} and S_{Er}, were obtained here and in [1]. Second, our data indicate that analysis of the influence of the composition of *a*-SiO_x:(H, Er, O) films on Er^{3+} PL requires consideration of the effect of the experimental process conditions, in particular, the values of C_{O_2} and S_{Er}. In other words, we have to take into account the change in the composition of Er clusters that we observed at $C_{O_2} \approx$ (5–6.5) mol %. Significant deviation of the experimental conditions from those we used may change the position of the kink in the dependences N_O^{Er-O}, $N_{Er} = f(C_{O_2}, S_{Er})$, which would affect all the other parameters of the *a*-SiO_x:(H, Er, O) films.

4. CONCLUSIONS

Experiments concerned with the preparation of *a*-SiO_x:(H, Er, O) films by dc magnetron sputtering under an increase in S_{Er} from 0 to ~18 mm^2 and at fixed values of C_{O_2} in the range 0.15–12 mol % showed the following:

(i) The contents of erbium-bound oxygen and erbium in a film depend on the values of C_{O_2} and S_{Er}. The dependences N_O^{Er-O} and $N_{Er} = f(C_{O_2}, S_{Er})$ show a kink at $C_{O_2} \approx$ (5–6.5) mol % and $S_{Er} < 11$ mm^2, which confirms the presence of erbium clusters of different composition in the films ([Er–O] and [Er–O–Si–O]).

(ii) The behavior of the dependences N_O^{tot}, N_O^{Er-O}, and I_{PL}^{Er} on S_{Er} for $C_{O_2} > 5$ mol % in the entire range of S_{Er} under consideration indicates that there is a close relationship between these film parameters and the composition of the erbium clusters.

(iii) The monotonic increase in N_{Er} resulting from an increase in S_{Er} and the shift of the curves $N_{Er} = f(S_{Er})$ to smaller values of N_{Er} as C_{O_2} was increased indicate the existence of competing processes of oxidation and sputtering of the Er target.

(iv) The relatively large values of I_{PL}^{Er} obtained at $C_{O_2} > 8$ mol % and $S_{Er} \approx$ (8–14) mm^2 are due to the presence of [Er–O–Si–O] clusters.

(v) The largest values of I_{PL}^{Er} were obtained at C_{O_2} = 12 mol % and $S_{Er} \approx$ (8–14) mm^2. However, we believe that the value C_{O_2} = 8 mol % is preferable in practice, since it provides more stable plasma burning.

ACKNOWLEDGMENTS

This study was supported by INTAS (grant 03-51-6486), the Russian Foundation for Basic Research, and the program “New Materials” of the Russian Academy of Sciences.

REFERENCES

1. V. Kh. Kudoyarova, A. N. Kuznetsov, E. I. Terukov, *et al.*, Fiz. Tekh. Poluprovodn. (St. Petersburg) **32**, 1384 (1998) [Semiconductors **32**, 1234 (1998)].
2. C. Piamonteze, A. C. Iniguez, L. R. Tessler, *et al.*, Phys. Rev. Lett. **81**, 4652 (1998).
3. L. R. Tessler and A. C. Iniguez, J. Non-Cryst. Solids **266–269**, 603 (2000).
4. Yu. K. Undalov, E. I. Terukov, O. B. Gusev, and V. Kh. Kudoyarova, Fiz. Tekh. Poluprovodn. (St. Petersburg) **37**, 853 (2003) [Semiconductors **37**, 825 (2003)].
5. J. Michel, F. Y. G. Ren, B. Zheng, *et al.*, Mater. Sci. Forum **143–147**, 707 (1994).
6. Mun-Jun Kim, G. K. Mebratu, Joo-Yeon Sung, and Jung H. Shin, J. Non-Cryst. Solids **315**, 312 (2003).
7. D. L. Adler, D. C. Jacobson, D. J. Eagleshum, *et al.*, Appl. Phys. Lett. **61**, 2181 (1992).
8. L. R. Tessler, J. L. Coffer, J. Ji, and R. A. Senter, J. Non-Cryst. Solids **299–302**, 673 (2002).
9. J. Felsche, Struct. Bonding (Berlin) **13**, 99 (1973).
10. J. Michel, L. V. C. Assali, M. T. Morse, and L. C. Kimerling, in *Semiconductors and Semimetals*, Vol. 49: *Light Emission in Silicon: From Physics to Devices*, Ed. by D. J. Lockwood (Academic, San Diego, 1998), Part 4, p. 111.
11. P. L. Dubov, D. V. Korol’kov, and V. P. Petranovskiĭ, *Clusters and Matrix-Isolated Cluster Superstructures* (S.-Peterb. Gos. Univ., St. Petersburg, 1995) [in Russian].
12. E. I. Terukov, Yu. K. Undalov, V. Kh. Kudoyarova, *et al.*, J. Non-Cryst. Solids **299–302**, 699 (2002).

Translated by Yu. Sin’kov

Semiconductors, Vol. 39, No. 8, 2005, pp. 951–954. Translated from Fizika i Tekhnika Poluprovodnikov, Vol. 39, No. 8, 2005, pp. 986–989.

CONFERENCE.
AMORPHOUS, VITREOUS, AND POROUS SEMICONDUCTORS

Structural Transformations and Optical Properties of As_2S_3 Chalcogenide Glasses

I. V. Fekeshgazi*^, K. V. Mai*, N. I. Matelesko, V. M. Mitsa**, and E. I. Borkach****

** Lashkarev Institute of Semiconductor Physics, National Academy of Sciences of Ukraine, Kiev, 03028 Ukraine*
^ e-mail: fek_i@yahoo.com
*** Uzhgorod National University, Uzhgorod, 88000 Ukraine*
Submitted December 27, 2004; accepted for publication January 12, 2005

Abstract—The effects of melt temperature T_i and quenching rate V_i on the structure and optical properties of As_2S_3 glasses is studied. It is found that the glass band gap increases with T_i and V_i, whereas a decrease is observed in the glass density, refractive index (from 2.71 to 2.48), and two-photon absorption coefficient (from 0.37 to 0.15 cm/MW), which is accompanied by an increase in the optical-breakdown damage threshold.

1. INTRODUCTION

Chalcogenide arsenic trisulfide glasses are promising materials for fabricating various elements used in integrated optics, optoelectronics, and laser engineering [1–5]. At the same time, the rather low optical-breakdown damage of these glasses seriously restricts their wide application as power optics elements. It is known that the optical-breakdown damage of a material is controlled by its optical quality (the degree of homogeneity and the existence or absence of mechanical stresses and impurities), on which linear and nonlinear absorption and scattering losses depend. In turn, the optical quality of glasses depends on their synthesis conditions, under which various structural–topological groups are formed in the bulk. An analysis of results regarding the effect of structural-topological transformations on the refractive index (n), linear (α) and two-photon (β) absorption constants, and Raman scattering (RS) spectra, as well as on the dynamic and optical-breakdown damage of arsenic trisulfide (As_2S_3) glasses, is carried out.

2. SAMPLE PREPARATION AND METHODS OF STUDY

The most commonly used method for the fabrication of bulk glasses is rapid quenching of a material melt. The studies were carried out using samples synthesized from the elemental components As and S (ultra-pure grade, 99.99999%) at three melt temperatures (T) and three quenching rates (V). The temperature T_1 = 870 K is the lowest temperature at which an arsenic–sulfur interaction corresponds to a real time scale (~150 h), T_2 = 1120 K is the temperature at which arsenic sulfides are typically synthesized, and T_3 = 1370 K is the highest temperature at which As_2S_3 molecules retain their structure before being dissociated into elementary components.

The rate $V_1 = 10^{-2}$ K/s corresponds to cooling of the melt in a technological furnace, V_2 = 1.5 K/s is the cell cooling rate in air at room temperature and is the optimum rate for synthesizing arsenic sulfide, and the rate V_3 = 150 K/s corresponds to cell cooling in ice water (0°C). The glass microstructure was studied using an EMV-100B transmission electron microscope (TEM) at an accelerating voltage of 100 kV [6]. Samples 20–50 nm thick were prepared using a piezoelectric microtome with a tray for distilled water. Freshly cleaved fragments were caught on a copper grid and, immediately after drying, placed into the microscope column.

The bulk structure of the glasses was analyzed using the conventional criteria of microdispersity and microinhomogeneity degrees, which were determined as the ratio of the number of distinctly contoured boundaries to the number of pseudo-grains per 0.1-μm-long segment.

The linear-loss and two-photon absorption coefficients were determined using experimentally measured dependences of the intensity I of transmitted light on the intensity I_0 of light incident on the sample. These dependences were sublinear (Fig. 1, curve *1*) and adequately described by the formula (see [7, 8])

$$I = I_0 \frac{(1-R_0)^2 \exp(-\alpha d)}{1 + \beta I_0 \alpha^{-1}(1-R_0)[1-\exp(-\alpha d)]},$$

where R_0 is the light reflectance from the surface of a sample of thickness d and α and β are the linear-loss and two-photon absorption coefficients, respectively.

The inverse transmittance

$$I_0/I = \frac{1 + \beta I_0 \alpha^{-1}(1-R_0)[1-\exp(-\alpha d)]}{(1-R_0)^2 \exp(-\alpha d)}$$

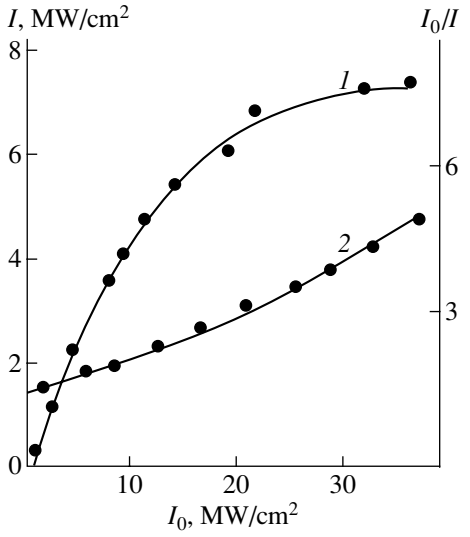

Fig. 1. Dependences of the transmitted light intensity I (*1*) and the ratio I_0/I (*2*) on the ruby laser light intensity I_0.

is directly proportional to I_0 (Fig. 1, curve *2*), which indicates the dominant contribution of two-photon transitions to the nonlinear light absorption.

The linear-loss α and two-photon absorption β coefficients calculated from the dependences shown in Fig. 1 are listed in the table.

The optical-breakdown threshold I_b was determined as the lowest density of laser radiation at which a bright flash was observed at the sample surface and, as a consequence, the intensity of the transmitted ruby laser 20-ns pulse abruptly decreased (at the half-maximum of the Gaussian time distribution).

3. RESULTS AND DISCUSSION

Various structural–topological elements were formed by varying the glass synthesis conditions (T_i and V_i). It was found that variation in T_i and V_i within the indicated ranges yielded a basic set of possible structural groups, which could be divided into two main types: a homogeneous *A* set mostly containing the bipyramidal structural units $AsS_{3/2}$, which are inherent in glasses with a microdisperse structure of various degrees of cohesion and a continuous structural network, and a *B* set containing the heteroatomic pseudomolecular units $As_2S_{4/2}$, As_3S_3, As_2S_5 and homogeneous sulfur aggregates S_8. These results are also confirmed by a comparative analysis of the Raman scattering (RS) spectra of arsenic trisulfide glasses in the stretching vibration range [9, 10]. Types *A* and *B* appear at the lowest and highest values of T_i and V_i, respectively. As T_i and V_i increased, the glass band gap (E_g) increased, the density ρ decreased, the refractive index and two-photon absorption coefficient decreased (from $n = 2.71$ to 2.58 cm/MW and from $\beta = 0.37$ to 0.15 cm/MW, respectively) (Fig. 2), and there was an accompanying corresponding increase in the optical-breakdown damage threshold I_b (see table).

Electron microscopy study of the glass bulk showed that operating conditions T_1 and V_1 yield a homogeneous matrix with uniformly distributed microcrystalline As_2S_3 inclusions 4–10 nm in size. At T_1 and V_2, as well as at T_1 and V_3, there existed cohered microdisperse pseudograins 1–2 nm in size and spherical microinclusions 5–10 nm in diameter, respectively. Under conditions T_2 and V_1, as well as T_2 and V_2, the glass structure was similar to that obtained at T_1 and V_2. Conditions T_3 and V_1 yielded a rather homogeneous microstructure consisting of cohered microdisperse drop-shaped pseudograins smaller than 50 nm in diameter. At T_3 and V_2, a rather homogeneous composition of heterogeneous pseudograins 5–10 nm in size was observed. At T_3 and V_3, there was a relatively uniform distribution of 30- to 50-nm spherical microinclusions in a microdisperse matrix.

The spectral dependences of the linear absorption coefficient near the intrinsic absorption edge are complicated. These dependences, in combination with nonlinear optical losses, control the glass optical-breakdown damage to laser beam fluxes.

A comparative analysis of the RS spectra of the arsenic trisulfide glasses in the stretching vibration

Physical parameters of vitreous As_2S_3

T, K	V, K/s	ρ, g/cm^3	E_g, eV	n (633 nm)	α, cm^{-1}	β, cm/MW	I_b, MW/cm^2
$T_1 = 870$	$V_1 = 10^{-2}$	3.201	2.12	2.712	2.16	0.37	30
	$V_2 = 1.5$	3.195	2.15	2.69	1.17	0.16	45
	$V_3 = 150$	3.192	2.21	2.664	2.22	0.15	55
$T_2 = 1120$	$V_1 = 10^{-2}$	3.193	2.18	2.705	1.96	0.4	30
	$V_2 = 1.5$	3.190	2.22	2.65	2.53	0.25	36–40
	$V_3 = 150$	3.186	2.26	2.602	1.305	0.18	30–40
$T_3 = 1370$	$V_1 = 10^{-2}$	3.192	2.22	2.602	1.90	0.24	30
	$V_2 = 1.5$	3.184	2.30	2.59	1.855	0.17	36–40
	$V_3 = 150$	3.176	2.38	2.580	1.73	0.15	50–60

range showed that the concentration of $As_2S_{4/2}$, $As_{3/3}$, S_8, and S_n structural units in the glass matrix structure increased with T_i and V_i [9]. In this case, the degree of structure rarefaction increased (the density decreased), and the ultrasound velocity in the As_2S_3 glass decreased; hence, the glass dynamic stability, expressed in terms of elastic moduli, decreased.

The results of this study confirm that low-frequency RS spectroscopy in the "boson peak" region, combined with ultrasonic studies, is an efficient method for determining the degree of structural correlation in glasses when various approximations of their structure are applied [10]. The resolution of low-frequency RS spectroscopy is better that of neutron diffraction in the same spectral region.

As the synthesis conditions of As_2S_3 glasses were varied, i.e., the melt temperature and quenching rate were increased (except in the case of conditions T_1 and V_2), a low-frequency shift of the "boson peak" from 26 cm^{-1} (T_1 and V_1) to 20 cm^{-1} (T_3 and V_3) was observed. This was accompanied by an increase in the structural correlation radius (R) and length (L), respectively, in the homogeneous and chain approximations of the glass structure. The relation $L/R \approx 2$ is valid in all cases.

Furthermore, it was found that the low-frequency peak shifts to higher frequencies, from 19 cm^{-1} ($z = 2.1$) to 26 cm^{-1} ($z = 2.4$), as the average coordination number $z = 3y + 2(1 - y)$ increased in the binary As_yS_{1-y} glasses. This increase was accompanied by a decrease in the peak intensity and a nonmonotonic decrease in the chain length L from 1.5 to 1.4 nm. The smallest value of L, $L = 1.42$ nm, at $z = 2.4$ corresponded to a dynamic stability maximum. The changes in the coordination number (from $z = 2.1$ to 2.4) and the corresponding increase in the elastic moduli of the As_yS_{1-y} glasses were consistent with the cluster topology (CT) concept on an increase in the dynamic stability of the glass matrix structure due to the strengthening of the interchain interaction and merging of one-dimensional clusters into layered-chain clusters near the composition $As_{40}S_{60}$ ($z = 2.4$) ($1D \longrightarrow 2D$ transition). A change from the $As_{40}S_{60}$ composition to arsenic-enriched compositions ($As_{42}S_{58}$) resulted in an increase in the low-frequency vibration intensity and growth of the chain clusters. As L increased, the glass dynamic stability decreased at $z > 2.4$, and the increase in the elastic moduli deviated from that predicted by the CT concept (according to the law $(z - 2.4)^{3/2}$). The detected rarefaction of the matrix structure of the As_yS_{1-y} glasses at $z > 2.4$ was accompanied by formation of the new structural units $As_2S_{4/2}$ and $As_{3/3}$.

A decrease in the two-photon absorption coefficient with T_i or V_i is caused by an increase in the band gap [11, 12]. The optical-breakdown damage estimated in the adiabatic approximation differed from the experimental data by almost three orders of magnitude. At the same time, according to the theory, the optical-breakdown damage threshold increases, since the linear and nonlinear loss coefficients decrease, whereas the band gap widens.

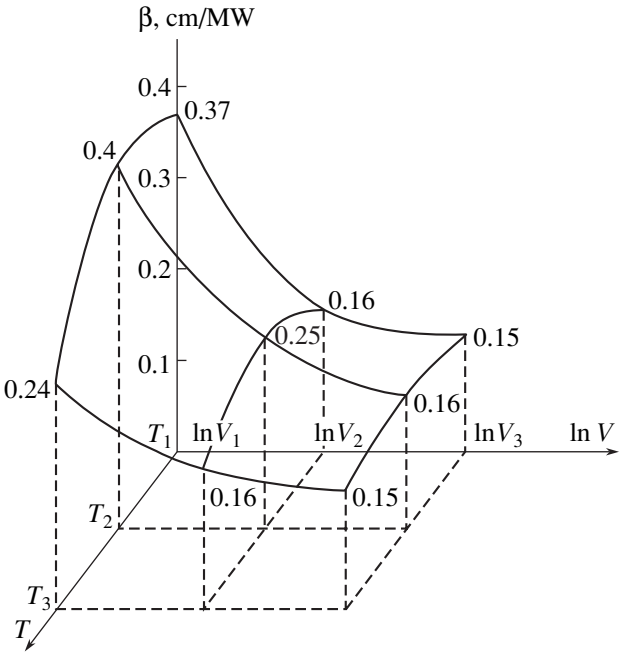

Fig. 2. Dependences of the two-photon absorption constant β on the melt temperature T_i and quenching rate V_i of the As_2S_3 glasses.

4. CONCLUSIONS

The systematic features of glass microstructure formation depending on melt temperature and quenching rate have been established using electron microscopy. It is shown that, optically, most homogeneous glasses are obtained under T_1 and V_2, T_2 and V_1, and T_2 and V_2 conditions.

The glass band gap increases with T_i and V_i, while a decrease is observed in the glass density, refractive index (from 2.71 to 2.48), and two-photon absorption coefficient (from 0.37 to 0.15 cm/MW), which is accompanied by an increase in the optical-breakdown damage threshold.

ACKNOWLEDGMENTS

This study was supported by the State Foundation for Basic Research of the Ministry of Education and Science of Ukraine, project no. F 7/273-2001.

REFERENCES

1. Z. U. Borisova, *Chalcogenide Semiconducting Glasses* (Leningr. Gos. Univ., Leningrad, 1983) [in Russian].
2. A. Feltz, *Amorphe und Glasartige Anorganische Festkörper* (Akademie, Berlin, 1983; Mir, Moscow, 1986).

3. S. V. Svechnikov, V. V. Khiminets, and N. I. Dovgosheĭ, *Complex Noncrystalline Chalcogenides and Chalcohalides and Their Application in Optoelectronics* (Naukova Dumka, Kiev, 1992) [in Russian].
4. G. Z. Vinogradova, *Glass-Formation and Phase Equilibria in Chalcogenide Systems* (Nauka, Moscow, 1984) [in Russian].
5. M. Bertolotti, V. Chumash, E. Fazio, *et al.*, J. Appl. Phys. **74**, 3024 (1993).
6. N. Mateleshko and E. Borkach, Semicond. Phys. Quantum Electron. Optoelectron. **7**, 171 (2004).
7. I. V. Fekeshgazi, K. V. May, V. M. Mitsa, and V. V. Roman, Proc. SPIE **2648**, 257 (1995).
8. V. V. Grabovskii, K. V. May, V. I. Prokhorenko, *et al.*, J. Appl. Spectrosc. **63**, 586 (1996).
9. R. Holomb and V. Mitsa, Solid State Commun. **129**, 655 (2004).
10. R. Golomb, N. Veresh, M. Koosh, and M. Gomesh, in *Proceedings of 4th International Conference on Amorphous and Microcrystalline Semiconductors* (St. Petersburg, 2004), p. 220.
11. I. Fekeshgazi, K. May, V. Mitsa, *et al.*, Proc. SPIE **2968**, 256 (1997).
12. I. V. Fekeshgazi, K. V. Maĭ, A. P. Klimenko, *et al.*, in *Proceedings of 4th International Conference on Amorphous and Microcrystalline Semiconductors* (St. Petersburg, 2004), p. 152.

Translated by A. Kazantsev

Semiconductors, Vol. 39, No. 8, 2005, pp. 955–959. Translated from Fizika i Tekhnika Poluprovodnikov, Vol. 39, No. 8, 2005, pp. 990–994.

CONFERENCE.
AMORPHOUS, VITREOUS, AND POROUS SEMICONDUCTORS

Electron Microscopy Study of a Chalcogenide-Based Polycrystalline Condensate Microstructure: The Effect of Composition and Thickness on Internal Lattice Bending

V. Yu. Kolosov^, L. M. Veretennikov, Yu. B. Startseva, and C. L. Schvamm

Ural State University of Economics, ul. 8 Marta 62, Yekaterinburg, 620219 Russia

^ e-mail: VladKol@usue.ru

Submitted December 27, 2004; accepted for publication January 12, 2005

Abstract—The grain microstructure of polycrystalline structures formed in thin amorphous Ge–Te, Tl–Se, and Cd–Te condensates has been studied using transmission electron microscopy. Pronounced internal lattice bending (up to 200 deg/μm) is detected in fine-grain structure crystallites using the bend extinction contour method. The effect of the initial film thickness and composition on the internal bending of the lattice grain is investigated. *© 2005 Pleiades Publishing, Inc.*

1. INTRODUCTION

The internal lattice bending in microcrystals that grow in an amorphous phase was detected in, and has been studied since, the 1980s [1, 2]. To date, many materials and compounds of various chemical types, whose thin films exhibit this effect, are known. Crystals with pronounced internal bending of their structure were identified and found to form in thin (up to 100 nm) amorphous chalcogenide (Se and Te) foils, metals and alloys (Re, Co–Pd, and Cu–Te), metal oxides (Fe_2O_3 and Cr_2O_3), and semiconductors (Ge–Te, Sb–S, Sb–Se, and Ge–Sb_2Se_3). Judging from the accumulated data (see [3] for more detail), the internal lattice bending mechanism is general and independent of the material; instead, the mechanism results from a material's initial state in the form of a thin film of an amorphous material.

Previously, a corresponding hypothesis was suggested that described the formation of strong transrotational (a term introduced in [3]) bending of the lattice as a consequence of compensation of the stresses that arise during surface nucleation in a thin amorphous film [4]. Figure 1 schematically shows the growth model of such a crystal.

Earlier [2, 3, 5], crystals with strongly bent lattice were mainly studied using rather large crystallites (~1 μm or larger) grown in thin amorphous films. The effect of the film thickness [6] and composition [7] on the internal bending was established in such films. In this paper, we consider the results of studying polycrystalline formations with grain sizes of up to 0.8 μm. The current interest in the internal bending of polycrystal grains is caused by the wide application of polycrystalline (including thin-film) materials. However, there are no data related to the effect of internal bending in fine grains on polycrystalline material properties. Such have not been undertaken because the patterns of bend extinction contours in small grains are much less informative (zone-axis patterns are often absent) and the indexing of individual contours is very complicated.

2. EXPERIMENTAL

Thin amorphous films were grown by thermal sputtering in vacuum at a residual pressure of 10^{-3} Pa using a VUP-4 setup. The films were deposited onto a freshly cleaved mica surface coated with a thin amorphous carbon layer (to prevent epitaxial growth). In order to study the effect of composition and thickness on the internal lattice bending in crystals growing in films, we obtained condensates of variable (along a single direction) composition and/or with a thickness gradient (along the perpendicular direction) (Fig. 2). The film component concentrations were varied by sputtering materials from two crucibles placed at opposite sub-

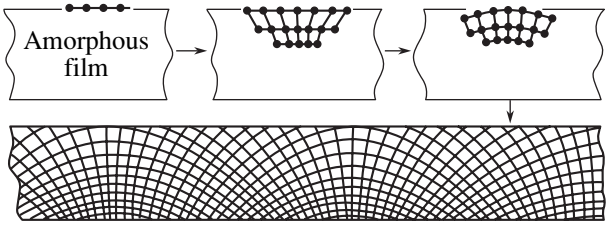

Fig. 1. Schematic diagram of the formation and growth of a crystal with strong internal lattice bending due to surface nucleation. The lines indicate lattice planes (about one line per ten planes); the bending is magnified about tenfold.

1063-7826/05/3908-0955$26.00 © 2005 Pleiades Publishing, Inc.

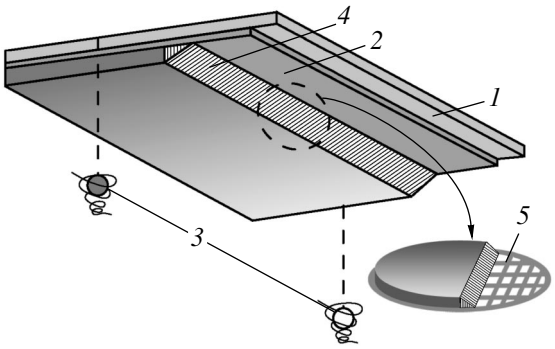

Fig. 2. Geometric layout of the growth of thin amorphous films: (*1*) substrate, (*2*) amorphous carbon layer, (*3*) crucibles with material, (*4*) thin amorphous film with thickness and composition gradients (shaded), and (*5*) a free film region, with thickness and composition gradients, placed on the electron microscopy grid.

strate edges. The thickness gradient was attained due to intentional substrate shielding, which was selected so that the entire thickness range (from 10 to 100 nm for various films) could be studied within a ~100-μm single cell of the electron microscopy grid (mesh 200). The deposition scheme is shown in Fig. 2.

After deposition, the amorphous films were separated from the substrate under surface tension forces in distilled water and placed onto a copper grid in preparation for electron microscopy studies (Fig. 2, *5*). Then, observations using a transmission electron microscope were carried out at accelerating voltages of 80–200 kV using bright- and dark-field imaging and selected-area diffraction.

The structural features of the growing crystals were studied by analyzing the patterns of bend extinction contours [8]. In particular, the internal lattice bending $\theta \approx 1/R$ [1] was determined according to the distance N between pair contours (hkl and $\bar{h}\bar{k}\bar{l}$) using the known formula $R = Nd/\lambda$ (corresponding to formulas from [9]), where R is the radius of the internal lattice bending, d is the interplane spacing of the set of planes corresponding to the contours, and λ is the electron beam wavelength. In fact, the local characteristic of the internal bending (lattice bending about the axis lying in the film plane) was determined in areas 0.1–0.01 μm in size. In most cases, the contours were indexed by comparison of bright- and the dark-field electron microscopy images of the same area of the sample under study [10].

In order to determine the distribution of sputtered materials over the film surface and, hence, the film composition, a calculation method formulated by Vekshinskiĭ [11] was used. By applying this technique, codes were developed on the basis of the MatLab 5.3 software that allowed estimation of the material distribution over a film surface of binary composition.

3. MAIN EXPERIMENTAL RESULTS AND THEIR ANALYSIS

3.1. Cd–Te Films

Films in the form of a Cd–Te binary system were prepared in a Te concentration range of 35–75%. The film thickness was varied from 15 to 60 nm. Due to spontaneous crystallization (at room temperature and immediately after deposition), the films were completely crystallized and represented polycrystalline tellurium (of hexagonal structure). The grain size varied from 0.1 to 0.5 μm.

The patterns of the bend extinction contours in images of tellurium crystal grains indicate preferential bending of the lattice planes about the axes lying in the film plane. The grains contained a rather large number of defects, especially in the thick film region, and their crystallographic orientations had appreciable differences (different diffraction contrasts, see Fig. 3). There were a small number of grains possessing the most appropriate contours for bending measurements (up to 10% from the total number of crystallites).

A numerical analysis of the crystallite lattice bending showed that its value varies from 20 to 200 deg/μm depending on the film thickness at the point of crystallite formation. Based on similar results from our previous studies (where this fact was unambiguously confirmed for larger crystals and grains), we can state that internal lattice bending in the grains is more probable than bending of the grain as a whole. This circumstance also holds in relation to the discussions in the next sections of the paper. A threefold decrease in the film thickness increased the internal bending of the grain lattice almost tenfold. In this case, the dependence was nonlinear; one of the possible approximations is shown in Fig. 3. Micrographs of crystallized film areas in the regions of corresponding thicknesses are also shown.

3.2. Ge–Te Films

Binary films of variable Ge–Te composition (50–80 at % of Ge) were grown in an amorphous state. The films were crystallized using the electron beam in the transmission electron microscope column. In the film region with a rather low germanium content (50–60 at %), single large (up to 5 μm) rhombohedral tellurium crystals grew under the beam. The crystals featured a high defect density and a complex system of bend contours.

The film regions with higher Ge contents were crystallized and segregated hexagonal tellurium grains from 0.03 to 0.4 μm in size appeared. As analysis of the negatives obtained using the electron microscope detected more than 50 grains with appropriate contours for measuring the internal lattice bending (crystals with pronounced pairs of bend contours, indicated by the circles in Fig. 4, were selected). It is noteworthy that the relative fraction of crystals that can be studied using the bend contour method is small. Apparently, this circum-

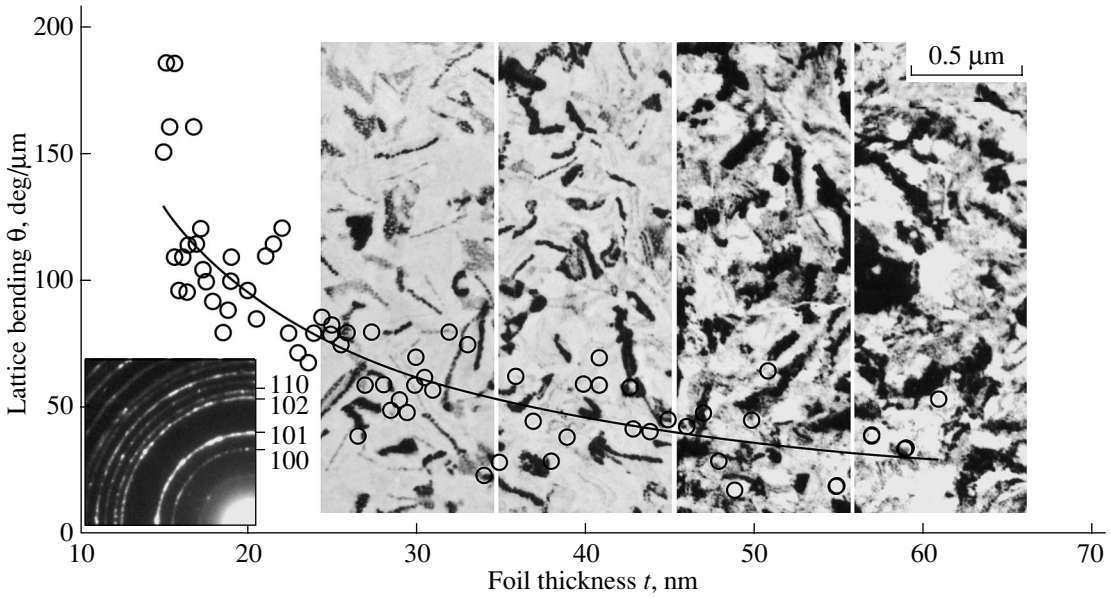

Fig. 3. Micrographs of Cd–Te film regions of various thicknesses and the dependence of the internal lattice bending on the film thickness. The inset shows the typical diffraction pattern and ring indices.

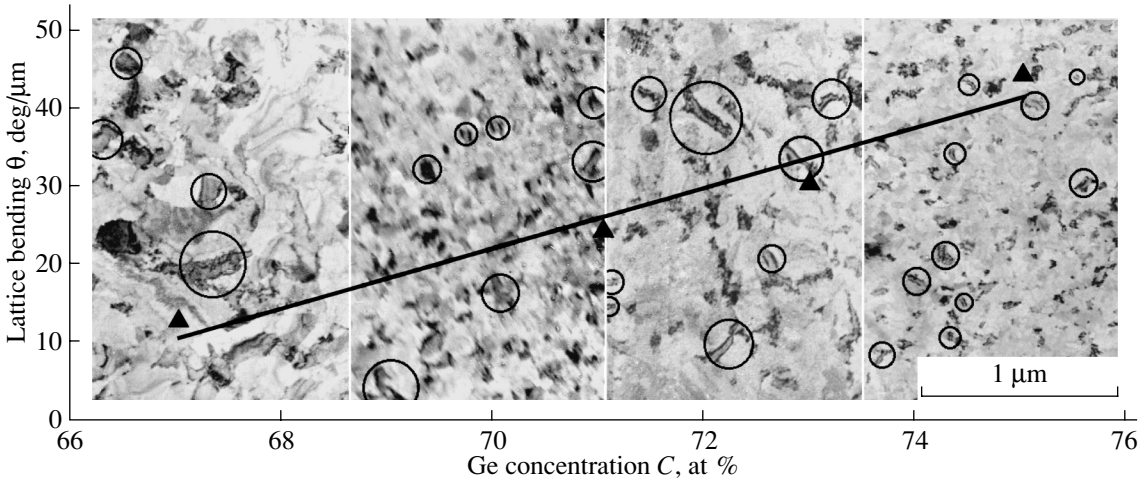

Fig. 4. Micrographs of the polycrystalline Te formations in a Ge–Te film with varying germanium content and the dependence of the internal bending of the grain lattice on the germanium content.

stance is due to the high total defect density in the grains, as well as their varied lattice orientation. In order to determine the internal bending, the distances between the most intense pair contours (corresponding to the {101} and {110} lattice planes) were measured in the negatives.

An analysis of the experimental data showed that the Ge content significantly affects the internal bending of lattice grains in the polycrystals used in the measurements. In particular, an 8% increase in the germanium content (from 67 to 75%) resulted in a fourfold increase in the internal bending (from 12 to 45 deg/μm, see Fig. 4). In this case, the dependence was close to being linear.

3.3. Tl–Se Films

Films of variable Tl–Se composition, with their Tl content ranging from 30 to 70 at %, were grown. The film regions with the highest Tl content experienced the most crystallization, which was initiated immediately after the film deposition and separation of the tetragonal tallium selenide phase. In regions with a lower Tl content, crystallization was slower, which allowed in situ studies of the crystals while they were being grown

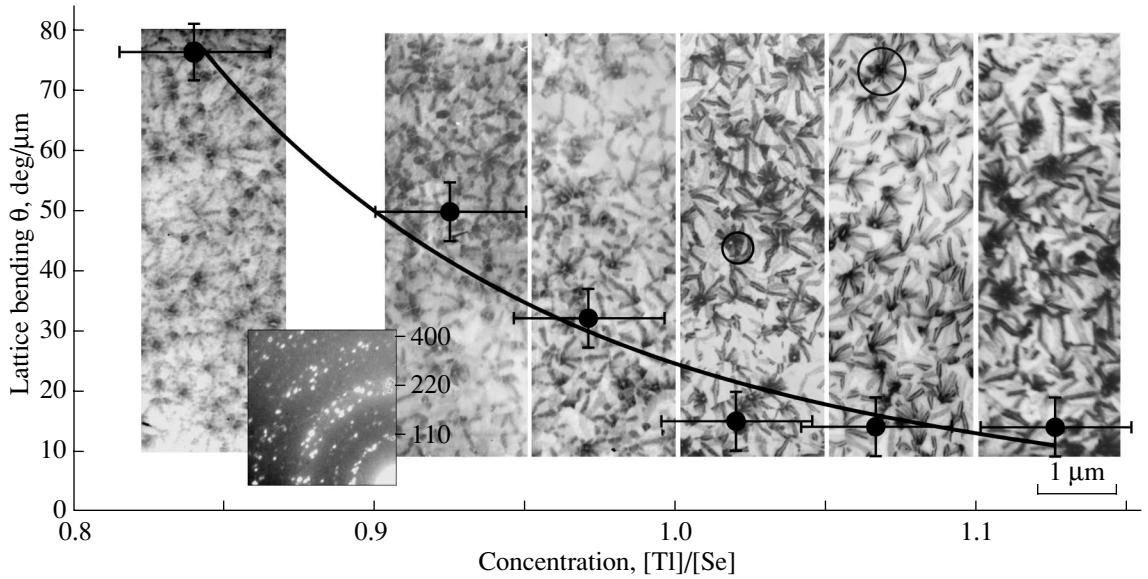

Fig. 5. Micrographs of polycrystalline TlSe film areas with varying composition and the dependence of the internal bending of the grain lattice on the film composition. Examples of grains with the [001] orientation normal to the film surface are indicated by the circles. The inset shows the typical diffraction pattern and ring indices.

(at a rate of ~1 μm/s) in the amorphous film (by varying the electron beam focusing directly in the electron microscope column).

Crystals with various morphologies were observed: fractal structures, a fine-grain polycrystalline structure (with a grain size of 0.3–0.8 μm), and spherulite-like structures. The dominant orientations were [001] (Fig. 5), [010], and [111]. Since this study is devoted to lattice bending in polycrystalline structures, hereafter, we consider only this type of structure. Polycrystalline formations in the Tl–Se condensates featured a much lower defect density in comparison with the Ge–Te and Cd–Te films. The patterns of bend extinction contours and the contours themselves were more distinct; zone-axis patterns of crossed bend contours were often observed. The number of grains with contour patterns appropriate for study was large; indeed, the measurements could be carried out for almost every grain, since they represented almost perfect single crystals. These measurements were facilitated by the rather close grain orientations as well as larger (than in the other films described above) crystallite sizes.

The internal bending in an aged polycrystalline film structure was as large as 80 deg/μm (measured, using the bend extinction contour method, by the brightest contours). A profound effect of the film composition on the internal bending of the grain lattice was detected, which is illustrated in Fig. 5 by the curve and micrographs. It is also worth noting that the shown approximation is not unique. For example, in the regions to the right and left of the composition [Tl]/[Se] = 1, the dependence can be approximated by straight lines. In this case, the bending rate varies by a factor of 4 as this composition changes. Generally, the results unambiguously suggest that an increase in the selenium content in the film in this composition range results in an increase in the internal bending of the TlSe grain lattice.

4. CONCLUSIONS

Electron microscopy of the polycrystalline formations in thin amorphous films based on certain chalcogenides allows to make the following conclusions.

(i) The bend contour technique allows determination of the internal lattice bending in a polycrystalline film even at grain sizes of fractions of a micrometer.

(ii) In the grains of Te and TlSe polycrystals growing in thin amorphous films consisting of binary Cd–Te, Ge–Te, and Tl–Se systems, internal lattice bending as great as 200 deg/μm (Cd–Te film) was detected using the bend extinction contour method.

(iii) As in the large grains and crystals studied previously, the film thickness and composition significantly affect the internal bending of the lattice planes in fine-crystalline condensates. In this case, the experimentally measured dependences are qualitatively close to similar dependences obtained for coarse-grained films [12] and isolated crystals in an amorphous environment.

(iv) The effect of the composition was detected in the Tl–Se and Ge–Te films. In the Ge–Te films, an increase in the Ge content by ~10% results in a fourfold increase in the internal bending of the tellurium grain lattice. In the Tl–Se condensates, a slightly smaller increase in the Se content causes a more than sevenfold increase in the internal bending of the TlSe crystal lattice. A similar pattern for the effect of the initial amorphous film composition on internal lattice bending was

earlier observed for separately growing crystallites, e.g., Se in thin condensates representing a Se–Te binary system [7].

(v) In the Cd–Te condensates, lattice bending in the polycrystalline grains increases almost tenfold as the film thickness decreases by a factor of 3. In this case, the dependence obtained is nonlinear: the lattice bending significantly increases in thinner film regions. This dependence is understandable, since larger degrees of elastic bending are attainable in thin films than in thick ones.

ACKNOWLEDGMENTS

This study was supported by the Russian Foundation for Basic Research (project no. Ural 04-02-96072) and INTAS (grant no. 00-100).

REFERENCES

1. V. Yu. Kolosov, Candidate's Dissertation (Inst. of Metal Physics, Ural Division, USSR Academy of Sciences, Sverdlovsk, 1982).
2. I. E. Bolotov, V. Yu. Kolosov, and A. V. Kozhin, Phys. Status Solidi A **72**, 645 (1982).
3. V. Yu. Kolosov and A. R. Tholen, Acta Mater. **48**, 1829 (2000).
4. V. Yu. Kolosov, *Abstracts of 7th All-Union Conference on Crystal Growth* (Inst. Kristallogr. Akad. Nauk SSSR, Moscow, 1988), Vol. 1, p. 13.
5. V. Yu. Kolosov, L. M. Veretennikov, A. A. Kuzmin, and V. A. Mamaev, in *Proceedings of ICEM-13* (Paris, 1994), Vol. 2A, p. 397.
6. V. Yu. Kolosov, L. M. Veretennikov, and N. V. Volhina, in *Proceedings of 14th International Congress on Electron Microscopy* (Cancun, Mexico, 1998), Vol. 2, p. 325.
7. V. Yu. Kolosov, A. R. Tholen, and L. M. Veretennikov, in *Final Programme and Proceedings, Scandem 2001* (Scandinavia Society for Electron Microscopy, Stockholm, 2001), p. 94.
8. *Electron Microscopy of Thin Crystals*, Ed. by P. B. Hirsch, A. Howie, R. B. Nicholson, D. W. Pashley, and M. J. Whelan (Plenum, New York, 1965; Mir, Moscow, 1968).
9. L. M. Utevskiĭ, *Diffraction Electron Microscopy in Physical Metallurgy* (Metallurgiya, Moscow, 1973) [in Russian].
10. D. B. Willams and C. B. Carter, *Transmission Electron Microscopy, III Imaging* (Plenum, New York, 1996).
11. S. A. Vekshinskiĭ, *New Method of Metallographic Studies of Alloys* (OGIZ, Moscow, 1944) [in Russian].
12. V. Yu. Kolosov, L. M. Veretennikov, and K. L. Shvamm, Poverkhnost, No. 1, 95 (2004).

Translated by A. Kazantsev

Semiconductors, Vol. 39, No. 8, 2005, pp. 960–962. Translated from Fizika i Tekhnika Poluprovodnikov, Vol. 39, No. 8, 2005, pp. 995–997.

CONFERENCE.
AMORPHOUS, VITREOUS, AND POROUS SEMICONDUCTORS

The Boson Peak in Raman Spectra of As_xS_{1-x} Glasses

D. Arsova*^, Y. C. Boulmetis, C. Raptis**, V. Pamukchieva*, and E. Skordeva***

** Institute of Solid-State Physics, Bulgarian Academy of Sciences, 1784 Sofia, Bulgaria*
^ e-mail: darsova@pronto.phys.bas.bg
*** Department of Physics, National Technical University of Athens, GR-15780 Athens, Greece*

Submitted January 24, 2005; accepted for publication February 1, 2005

Abstract—The Raman spectra of As_xS_{1-x} glasses with $x < 40$ at % ($Z < 2.4$) have been studied in a wide temperature range (20–300 K). A well resolved boson peak is observed in the low-frequency portion of the spectrum, not withstanding the appearance of floppy modes in the glasses under study. It is shown that the boson peak is characterized by two parameters: intensity and the peak position. A comparison of the intensity variation for the boson peaks indicates that the degree of disorder increases as x decreases. This effect is caused by floppy modes in the glass network and by sulfur phase separation. Studies of reduced boson peaks in the Raman spectra of As_xS_{1-x} glasses confirms the theoretical assumption that the shape of the peaks is independent of composition and temperature. © *2005 Pleiades Publishing, Inc.*

The low-frequency portion of the first-order Raman spectrum in glasses has been studied intensively using experimental and theoretical methods for more than 25 years. In this spectral region ($\omega < 100$ cm^{-1}), a well pronounced broad peak, referred to as the boson peak, is observed. As is well known, the boson peak is a universal special feature of the Raman spectra of unordered materials and is not observed in the Raman spectra of corresponding crystalline materials. The intensity of the measured boson peak $I_m(\omega, T)$ depends heavily on the temperature factor $n(\omega, T) = 1/[\exp(h\omega/kT) - 1]$, where $n(\omega, T)$ is the Bose–Einstein distribution at a temperature T for the vibrational energy $h\omega$ [1, 2]. Therefore, in order to determine the characteristic parameters of the boson peak, the reduced intensity $I_R(\omega, T)$ is often used and can be written as

$$I_R(\omega, T) = I_m(\omega, T)/\{\omega[n(\omega, T) + 1]\},$$

where $I_m(\omega, T)$ is the measured intensity of the boson peak. Shuker and Gammon [1] showed that the spectral dependence $I_R(\omega, T)$ should be identical to the shape of the curve for the density of vibrational states in unordered solids. The scattering mechanism responsible for boson-peak manifestation in the Raman spectra of glasses has not yet been completely clarified and is still debatable.

In this paper, we report the results of studying the Raman spectra of As_xS_{1-x} glasses with $x < 40$ at %. The average coordination number Z characterizing the degree of connectedness present in the glass network is smaller than 2.4 for the glasses under consideration. The critical value $Z = 2.4$ corresponds to the stoichiometric composition, As_2S_3 ($As_{0.4}S_{0.6}$). An excess of sulfur in the chosen compositions is conducive to the appearance of additional degrees of freedom (floppy modes) and brings about an increase in the degree of disorder in the glasses' structure. The network of such glasses becomes more flexible and the corresponding glasses are referred to as low-coordinated (low-constrained). The Raman spectra were measured in a wide temperature range in order to determine the effect of temperature on the boson-peak parameters. The objective of this study was to gain insight into the local structure and determine the degree of disorder of As–S glasses with $Z < 2.4$ using Raman spectroscopy. When analyzing the Raman spectra, we paid most attention to the low-frequency region with the aim of obtaining information about the manifestation and nature of the boson peak in these glasses.

Glasses belonging to the As_xS_{1-x} series were obtained by quenching the melt. The mixture of As and S elements (with a 99.999% purity) was put in a quartz cell; the cell was then evacuated, sealed, and heated for 24 h at 950°C in a swinging furnace. The melt was quenched by cooling the cells in air. The samples to be used in the Raman studies were fabricated in the form of thoroughly polished platelets. The Raman spectra were recorded in the wave number range 5–600 cm^{-1}. The pump radiation was emitted from a Kr^+ laser (the 647.1-nm line) with a power density of 40 W/cm^2. We used backscattering geometry. The signal was analyzed using a SPEX 1403 double monochromator and was detected by an RCA cooled photomultiplier. The spectral resolution was 1.5 cm^{-1}. *HH*- and *VH*-polarized components were measured independently. The boson-peak parameters were determined with higher confidence when the *VH* component was measured, since the level of quasi-elastic scattering is lower in the *VH* component than in the polarized *HH* component. The samples were mounted in a helium-filled cryostat during the measurements, which were performed in a wide temperature range (20–300 K).

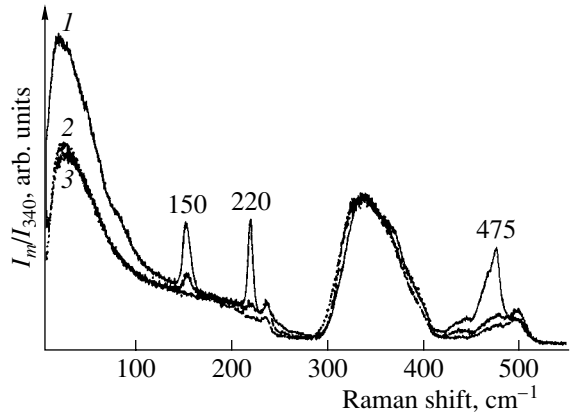

Fig. 1. Raman spectra of As_xS_{1-x} glasses with x = (*1*) 0.2, (*2*) 0.29, and (*3*) 0.31. The temperature of the measurements was 23 K.

The *VH* Raman spectra of three As_xS_{1-x} glasses with x = 0.2 (Z = 2.2), 0.29 (Z = 2.285), and 0.31 (Z = 2.309) were measured at a temperature of 23 K and are shown in Fig. 1. The spectra are normalized to the intensity of the band at 340 cm^{-1} in order to make it possible to compare the boson peaks for the three glasses. As is well known, the band at ~340 cm^{-1} is caused by As–S vibrations in $AsS_{3/2}$ pyramids. It is clearly seen from Fig. 1 that the boson-peak intensity increases as the sulfur content increases. The boson-peak intensity is at its highest for the $As_{0.2}S_{0.8}$ glass with Z = 2.2. For this composition, the degree of disorder is high due to the increased degree of freedom in the glass matrix. This inference is confirmed by the appearance of intense bands at 150, 220, and 475 cm^{-1}, which are typically attributed to phase-stratified S_8 rings, in the Raman spectrum of the $As_{0.2}S_{0.8}$ glass. The position of the boson peak ω_B shifts to higher frequencies as x (or Z) increases. These results are in good agreement with previously obtained composition dependences for the boson-peak parameters of As_xS_{1-x} glasses [3]. It is worth noting that, both in the reduced spectra and in the original Raman spectra, the composition dependences of the boson-peak parameters are similar. Since the intensity and the position of the boson peak vary as the glass composition is varied, we analyzed the reduced spectra.

The reduced Raman spectra are normalized in the low-frequency region by ω_B, (ω/ω_B), on the horizontal axis and by $I_{R\max}$, ($I_R/I_{R\max}$), on the vertical axis. The curves obtained in this way are often referred to as master curves and make it possible to compare the shape of the curves. After this procedure, we found that the boson-peak curves for the three glasses under study coincided completely; i.e., the shape of the curve $I_R(\omega, T = \text{const})$ is independent of the glass composition. The universality of the boson-peak spectral shape suggests that the nature of the low-energy vibrational states in As_xS_{1-x} glasses with $Z < 2.4$ should be identical. In contrast, we obtained a very complex composition dependence of the boson-peak spectral shape for Ge–As–S glasses [4]. This dependence is related to variation in the connectedness of the network in ternary glasses as the composition varies (the value of Z varied from 2.4 to 2.8 for the Ge–As–S glasses studied).

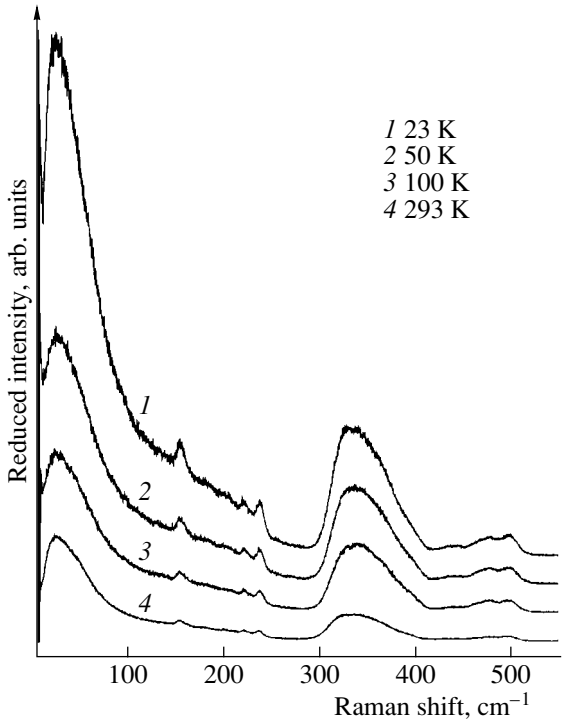

Fig. 2. Reduced Raman spectra of $As_{0.29}S_{0.71}$ glass (Z = 2.285) at four chosen temperatures. The scale on the intensity axis is the same for all temperatures.

Studies of the effect of temperature on the boson-peak parameters are hampered by the fact that the thermal factor $n(\omega, T)$ profoundly affects the low-frequency region of the spectrum as the temperature is lowered. Typically, the measured boson-peak intensity decreases drastically as the temperature decreases, and the Raman signal is also reduced if measured in the full-range spectrum. In Fig. 2, we show the reduced Raman spectra for the $As_{0.29}S_{0.71}$ glass (Z = 2.285) at four chosen sample temperatures. It can clearly be seen from Fig. 2 that the boson-peak intensity $I_{R\max}$ increases as the temperature decreases (in contrast to the above statement). However, the intensity of the band at about 340 cm^{-1} decreases; therefore, we do not suggest any quantitative correlations. It can be seen from Fig. 2 that ω_B is independent of temperature. We compared the shape of the reduced boson peak (using the method of master curves) for the three glasses under study at different temperatures. The comparison shows that the curves $I_R(\omega, T)$ coincide completely at temperatures ranging from 23 to 293 K. The universality (in particular, the temperature independence) of the boson-peak shape manifests itself to a greater extent in the binary As–S

glasses under study than in the ternary Ge–As–S glasses. An additional broad temperature-independent peak at ~140 cm^{-1} is found to be superimposed on the boson peak for ternary glasses [5].

As a result of our studies of the Raman scattering, we established that a well-resolved boson peak is observed in the As_xS_{1-x} glasses with $Z < 2.4$ in spite of the appearance of floppy modes. The boson peak is characterized by two parameters: intensity and position of the maximum. A comparison of the boson-peak intensities shows that the degree of disorder increases as the average coordination number Z decreases. This circumstance is due to flexibility of the glass network (the so-called low-constrained glasses) and the existence of phase separation of sulfur. Studies of the shape of the reduced boson-peak Raman spectra for the As_xS_{1-x} glasses confirmed theoretical predictions concerning the independence of the boson peak from the composition and temperature.

This study was supported by the Ministry of Education of Bulgaria (grant no. F-1309) and the basic research program "Thalis" administered by the National Technical University (Athens, Greece).

REFERENCES

1. R. Shuker and R. Gammon, Phys. Rev. Lett. **25**, 222 (1970).
2. A. J. Martin and W. Brening, Phys. Status Solidi B **64**, 163 (1974).
3. N. Mateleshko, M. Veres, V. Mitsa, *et al.*, Phys. Chem. Solid State **1**, 241 (2000).
4. E. Vateva and E. Skordeva, J. Optoelectron. Adv. Mater. **4**, 3 (2004).
5. Y. C. Boulmetis, A. Perakis, C. Raptis, *et al.*, J. Non-Cryst. Solids **347**, 187 (2004).

Translated by A. Spitsyn

Semiconductors, Vol. 39, No. 8, 2005, pp. 963–966. Translated from Fizika i Tekhnika Poluprovodnikov, Vol. 39, No. 8, 2005, pp. 998–1001.

CONFERENCE.
AMORPHOUS, VITREOUS, AND POROUS SEMICONDUCTORS

Reversible Photoinduced Changes in the Spectrum of Localized States in AsSe Films

L. P. Kazakova^, K. D. Tsendin, M. A. Tagirdzhanov, and N. S. Averkiev

Ioffe Physicotechnical Institute, Russian Academy of Sciences, St. Petersburg, 194021 Russia

^ e-mail: kazakova@mail.ioffe.ru

Submitted January 24, 2005; accepted for publication February 1, 2005

Abstract—Study of the temperature dependence of the carrier drift mobility in AsSe films undergoing photostructural transformations has revealed a reversible photoinduced change in the mobility and its activation energy. It has been established that the drift mobility and its activation energy depend on the conditions of sample annealing. The shape of the drift pulses indicates that the transport becomes more dispersive in irradiated films and those annealed after irradiation. The concentrations and energies of the localized states controlling the transport in AsSe films before and after irradiation have been determined. The data obtained indicate that the main parameters of traps for charge carriers can be controlled. © *2005 Pleiades Publishing, Inc.*

Owing to the lability of the structural network and charge carrier localization, both resulting from the disordered structure, chalcogenide glassy semiconductors (ChGSs) possess a number of properties inherent only in these materials. These properties include the ability of ChGSs to change their optical, physicochemical, and photoelectric properties under illumination [1–6]. An important feature of this effect is its reversibility; i.e., the initial properties of the material can be restored by annealing at a certain temperature.

At present, most researchers relate photoinduced changes in the properties of ChGSs to photostructural transformations, i.e., to changes in the structure of the substance under illumination [3, 7, 8]. However, the mechanism of photostructural transformations is still not quite clear. In particular, changes in the spectrum of localized states due to photostructural transformations have been left almost completely unstudied. Understanding the mechanism of photoinduced changes is extremely important for finding answers to fundamental questions related to the electronic processes in structurally disordered materials. In addition, this knowledge is necessary in the design of various micro- and optoelectronic devices based on ChGSs.

In order to elucidate the mechanism of photostructural transformations and the resulting changes in the spectrum of localized states, the carrier drift mobility in thin ChGS films of an AsSe composition was studied using the time-of-flight technique [9]. This method makes it possible to obtain the most direct information about the localized states controlling carrier transport.

AsSe was chosen as the material to be studied because AsSe films undergo strong photoinduced changes [7]. Irradiation of AsSe samples with light from a He–Ne laser (λ = 0.633 μm and power of 40 mW) for 20 min led to the strongest photodarkening at the given light intensity, which corresponds to a shift of the transmission spectrum by ~0.14 eV to longer wavelengths.

The samples studied had a sandwich structure. AsSe films with a thickness of ~3.5 μm were deposited by thermal evaporation in vacuum. Preliminarily, an aluminum layer, serving as the bottom electrode, was deposited onto the glass substrates. A semitransparent film of gold, deposited onto the AsSe layer by vacuum evaporation, served as the top electrode. The area of the top electrodes of the samples was ~4 mm^2. Prior to depositing the top electrode, both the irradiated and unirradiated samples were annealed at $T \approx 370$ K for 4 h. Some of the irradiated samples were annealed at $T \approx 350$ K for 4 h. Their initial transparency was almost completely restored after annealing of the irradiated samples at $T = 370$ K, and it increased from 10 to ~20% at $\lambda = 0.66$ μm, i.e., by approximately a factor of 2, after annealing at $T \approx 350$ K.

The drift mobility was studied by the time-of-flight technique but in the low-injection mode [9, 10], i.e., under the conditions of drift of a minor amount of charge, which has no effect on the electric field distribution. Nonequilibrium carriers were injected into a sample by the strongly absorbed light of an ILGI-503 nitrogen laser (λ = 0.337 nm and pulse width of ~8 ns). Photocurrent pulses corresponding to the drift of holes were recorded. Electron drift was not observed because of the low signal intensity. Temperature measurements were performed in heated air, which was pumped through the chamber containing a sample. The temperature was stabilized in such a way that temperature fluctuations during the period of measurement (~1 min) did not exceed 0.5°C.

The transient current observed during the drift of holes in the AsSe layers had the form of a prolonged continuous decay of current with time $I(t)$ (Fig. 1). The

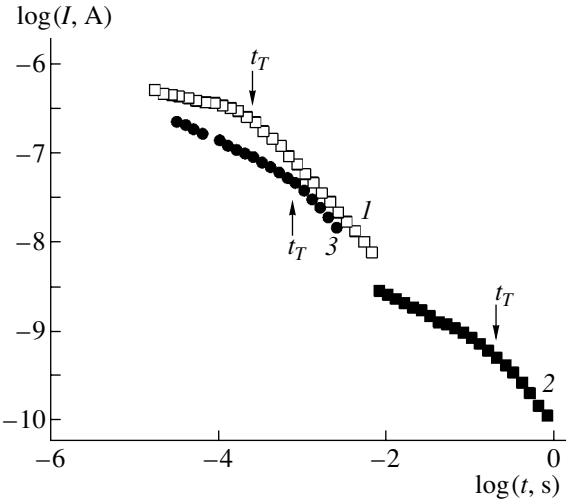

Fig. 1. Time dependence of the photocurrent in AsSe films: (*1*) initial, annealed after deposition; (*2*) irradiated; and (*3*) annealed after irradiation. L = 3.5 μm, V = 20 V, and T = 297 K.

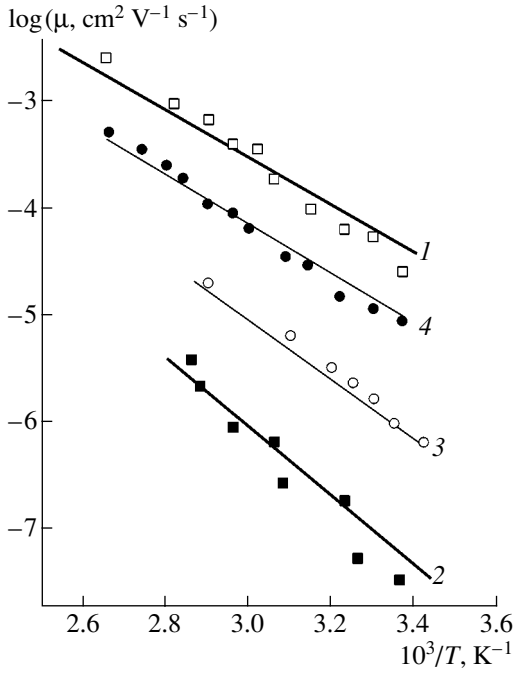

Fig. 2. Temperature dependence of the drift mobility of holes in AsSe films (*1*) before irradiation, (*2*) after irradiation, and (*3*, *4*) annealed after irradiation at (*3*) T = 350 K and (*4*) T = 370 K. L = 3.5 μm and V = 20 V.

transit time of carriers across a sample was found from the bend in the transient photocurrent curves, which were plotted on the log–log scale. The transit time (t_T) is indicated in the figure by arrows.

The carrier drift mobility μ was calculated with the formula [10, 11]

$$\mu = L^2/t_T V, \quad (1)$$

where L is the layer thickness and V is the voltage applied to the sample.

It can be seen from Fig. 1 that the photocurrent in the irradiated samples substantially decreased and the transit time increased by three orders of magnitude. The drift mobility changed accordingly: it decreased from $\mu \cong 2 \times 10^{-5}$ cm^2/(V s) at T = 300 K in the initial film to $\mu \cong 3 \times 10^{-8}$ cm^2/(V s) in the irradiated film. After annealing of the irradiated film at T = 370 K, μ became 8.5×10^{-6} cm^2/(V s); i.e., it returned to virtually its initial value. Such behavior of the drift mobility is in an agreement with the changes in drift mobility previously observed in thinner AsSe layers [12].

Temperature measurements in the range T = 290–380 K revealed that, in all of the samples studied, the drift mobility exponentially increases with temperature in accordance with a formula previously derived in terms of a model in which transport is controlled by multiple capture of carriers by a level of localized states with a density N_t [10, 13]:

$$\mu = \mu_0 (N_c/N_t) \exp(-E/kT). \quad (2)$$

Here, μ_0 is the carrier mobility in the allowed band and N_c is the effective density of states in the allowed band. Under the conditions of dispersive transport, the energy E corresponds to a level at which thermodynamic quasi-equilibrium between free and trapped carriers is established during the measurement period.

The activation energy of the drift mobility depended on the state of the film (Fig. 2). In the unirradiated and annealed films, the activation energy of the drift mobility was $E_1 = (0.5 \pm 0.05)$ eV. After irradiation, the activation energy increased to $E_2 = (0.75 \pm 0.05)$ eV. In the samples annealed at $T \approx 370$ K for 4 h after irradiation, the activation energy of the drift mobility was $E_3 = (0.51 \pm 0.05)$ eV, which is close to E_1. However, the activation energy in the films annealed at $T \approx 350$ K for 4 h after irradiation differed from E_1, $E_4 = (0.62 \pm 0.05)$ eV, with the drift mobility in these films equal being to $\mu \cong 6 \times 10^{-7}$ cm^2/(V s) at T = 300 K.

It can be seen from the data obtained that, if annealing of irradiated films restores the initial optical properties, the reversibility property also applies to the photoinduced changes in the drift mobility and its activation energy. If, however, the annealing fails to completely restore the initial optical properties, the drift mobility and its activation energy take intermediate values that correspond to a state lying between the initial and irradiated states of the film. This circumstance indicates that there are localized states distributed over energy in the band gap. This conclusion is also confirmed by experimental data obtained by studying the transient photocurrent $I(t)$ in the AsSe films (Fig. 1).

A study of the shape of the photocurrent pulses corresponding to carrier drift in the initial, irradiated, and irradiated and annealed AsSe films demonstrated that

the dependence $I(t)$ observed in all of the samples in a time interval at least an order of magnitude wide in the vicinity of the transit time can be described by the following power functions:

$$I(t) \propto \begin{cases} t^{-(1-\alpha_i)}, & t < t_T \\ t^{-(1+\alpha_f)}, & t > t_T, \end{cases} \quad (3)$$

where $0 < \alpha_i$ and $\alpha_f < 1$.

It is known that this type of $I(t)$ dependence is characteristic of dispersive transport [10, 11, 13], which takes place under the conditions of unattained thermodynamic equilibrium between free carriers and those captured by localized states distributed over energy. In this case, a strongly spatially spread carrier packet drifts across a sample at a velocity that decreases with time, and the center of gravity of the packet reaches the sample boundary at an instant of time $t = t_T$. The smaller the parameters α_i and α_f, the more dispersive the transport and the stronger the spreading of the carrier packet.

It was found that, on average, the values of the dispersion parameters α_i and α_f decreased in the irradiated films and those annealed after irradiation. For example, $\alpha_i \cong 0.8$ and $\alpha_f \cong 0.1$ in the initial films, $\alpha_i \cong 0.5$ and $\alpha_f \cong 0.2$ in the irradiated films, and $\alpha_i \cong 0.5$ and $\alpha_f \cong 0.05$ in those annealed after irradiation. The decrease in the dispersion parameters characterizing the $I(t)$ dependence in the irradiated films and those that were both irradiated and annealed indicates that the drifting carrier packet is more strongly spread and the energy range in which localized states controlling the drift mobility are distributed is wider in these films than a film in the initial state. The energy position of these localized states corresponds to the activation energies of the drift mobility in the initial, irradiated, and irradiated and annealed films. Formula (2) was used to evaluate the density of localized states at these levels. For $\mu_0 \cong 10$ cm^2/(V s) and $N_c = 10^{19}$ cm^{-3}, the following densities of localized states were obtained: $Nt_1 = 1 \times 10^{16}$ cm^{-3} at the level $E_1 = 0.5$ eV in the initial films; $Nt_2 = 3 \times 10^{14}$ cm^{-3} at $E_2 = 0.75$ eV in the irradiated films; and $Nt_3 = 1 \times 10^{16}$ cm^{-3} and $Nt_4 = 3 \times 10^{15}$ cm^{-3} at $E_3 = 0.51$ eV and $E_4 = 0.62$ eV, respectively, in the films annealed after irradiation.

The data obtained indicate that irradiation of the films and their subsequent annealing lead to considerable changes both in the energy position and in the density of localized states controlling the carrier drift mobility. The activation energy of the drift mobility in the unirradiated AsSe films virtually coincides with that in films of glassy As_2Se_3, for which the values of E are known [10, 13, 14–16] to be related to the position of levels corresponding to charged intrinsic defects C_1^-. This circumstance suggests that the nature of the localized states controlling the drift mobility in the initial AsSe films is the same, i.e., they are associated with selenium dangling bonds. The increase in the activation energy of the drift mobility in the AsSe films after irradiation correlates with the increase in E in As–Se films with a high content of arsenic (>50 at %) [17]. This fact gives grounds to believe that the localized states controlling the drift mobility in the irradiated films are associated with charged intrinsic defects P_2^-, formed by arsenic atoms with disrupted coordination. The possibility of the existence of charged P_2^- defects in arsenic-containing ChGSs was considered in [13]. As follows from the results of this study, the levels of the states related to P_2^- centers lie in the vicinity of the Fermi level, in an agreement with the experimentally determined value $E_2 = 0.75$ eV. The changes in the drift mobility and its activation energy after irradiation of the AsSe films can be understood if we assume that there is a considerable increase in the importance of the deep centers P_2^-, which may be the case if the concentration of P_2^- centers increases and that of the C_1^- centers decreases as a result of photostructural transformations. The subsequent annealing of the films presumably restores the C_1^- centers while simultaneously decreasing the concentration of P_2^--centers. Annealing at $T \approx 350$ K presumably fails to eliminate all the deep traps (P_2^- centers) and to completely restore the C_1^--centers. This effect gives rise to a broad spectrum of localized states in the interval 0.5–0.75 eV above the top of the valence band. The activation energy of 0.62 eV corresponds to the level for which a thermodynamic quasi-equilibrium between free and trapped carriers is attained during the measurement time. Annealing at $T \approx 370$ K virtually completely restores both the drift mobility and its activation energy. However, the small value of the dispersion parameter α_i in this case may be due to a stronger broadening of the level of C_1^- centers.

Thus, the analysis of the data obtained suggests that a reversible photoinduced change in the concentration and energy position of intrinsic charged defects controlling the carrier transport is possible in AsSe films.

It should also be noted that the annealing of the irradiated films at $T \approx 350$ K led to a 20-fold increase in the drift mobility, with their transparency increasing only by approximately a factor of 2. This circumstance indicates that the method of drift mobility is highly sensitive and makes it possible to notice changes in the spectrum of localized states even if the optical properties of the films have not yet changed significantly.

ACKNOWLEDGMENTS

The authors thank E.A. Lebedev for his support and A.S. Snytkina for help with the experiments.

The study was supported by programs of the Ministry of Science and Education of the Russian Federation.

REFERENCES

1. R. Chang, Mater. Res. Bull. **2**, 145 (1967).
2. S. A. Keneman, Appl. Phys. Lett. **19**, 205 (1971).
3. K. Tanaka, J. Non-Cryst. Solids **35–36**, 1023 (1980).
4. B. T. Kolomiets, V. M. Lyubin, and V. P. Shilo, Fiz. Khim. Stekla **4**, 351 (1978).
5. V. L. Averyanov, B. T. Kolomiets, V. M. Lyubin, and M. A. Taguyrdzhanov, in *Proceedings of 7th International Conference on Amorphous and Liquid Semiconductors*, Ed. by W. E. Spear (Edinburgh, 1977), p. 802.
6. K. Shimakawa, S. Inami, and S. R. Elliott, Phys. Rev. B **42**, 11857 (1990).
7. A. V. Kolobov and K. Shimakava, in *Electronic Phenomena in Chalcogenide Vitreous Semiconductors*, Ed. by K. D. Tséndin (Nauka, St. Petersburg, 1996), p. 365 [in Russian].
8. A. V. Kolobov and J. Tominaga, J. Optoelectron. Adv. Mater. **4**, 679 (2002).
9. W. E. Spear, J. Non-Cryst. Solids **1**, 197 (1969).
10. É. A. Lebedev and L. P. Kazakova, in *Electronic Phenomena in Chalcogenide Vitreous Semiconductors*, Ed. by K. D. Tséndin (Nauka, St. Petersburg, 1996), p. 141 [in Russian].
11. G. Pfister and H. Scher, Adv. Phys. **27**, 747 (1978).
12. L. P. Kazakova, L. Toth, and M. A. Taguyrdzhanov, Phys. Status Solidi A **71**, K107 (1982).
13. N. F. Mott and E. A. Davis, *Electronic Processes in Non-Crystalline Materials*, 2nd ed. (Clarendon, Oxford, 1979; Mir, Moscow, 1982).
14. R. A. Street and N. F. Mott, Phys. Rev. Lett. **35**, 1293 (1975).
15. M. Kastner, D. Adler, and H. Fritzsche, Phys. Rev. Lett. **37**, 1504 (1976).
16. V. I. Arkhipov, L. P. Kazakova, É. A. Lebedev, and A. I. Rudenko, Fiz. Tekh. Poluprovodn. (Leningrad) **21**, 724 (1987) [Sov. Phys. Semicond. **21**, 442 (1987)].
17. L. Toth, in *Proceedings of International Conference on Amorphous Semiconductors-84* (Gabrovo, 1984), Vol. 1, p. 236.

Translated by M. Tagirdzhanov

Semiconductors, Vol. 39, No. 8, 2005, pp. 967–977. Translated from Fizika i Tekhnika Poluprovodnikov, Vol. 39, No. 8, 2005, pp. 1002–1011.

ATOMIC STRUCTURE AND NONELECTRONIC PROPERTIES OF SEMICONDUCTORS

Causes of the Stability of Three-Bilayer Islands and Steps on a Si (111) Surface

A. V. Zverev, I. G. Neizvestny, I. A. Reĭzvikh, K. N. Romanyuk, S. A. Teys, N. L. Shwartz^, and Z. Sh. Yanovitskaya

Institute of Semiconductor Physics, Siberian Division, Russian Academy of Sciences, ul. Akademika Lavrent'eva 13, Novosibirsk, 630090 Russia

^ *e-mail: natasha@phys.spy.isp.nsc.ru*

Submitted October 11, 2004; accepted for publication October 26, 2004

Abstract—The initial stages of growth of Ge and Si layers on a singular Si (111) surface result in an unusual morphology of the growth surface if the layers are deposited at a low rate; i.e., triangular islands with a height of as much as three atomic layers are formed. A simulation based on the Monte Carlo method has been used to show that an additional barrier with a height of 0.5–0.6 eV, serving to incorporate atoms into dimerized bonds at the edges of the triangular islands, brings about enhanced growth of the islands in relation to their height and a change in the triangles' orientation. According to the suggested hypothesis, the increase in the islands' height and the limitation of their height to three bilayers are due to the effect of the edge dimers, whose orientation changes when the height of a step perpendicular to the $\langle \bar{1}\bar{1}2 \rangle$ direction becomes as large as three bilayers. Scanning tunneling microscopy has been used to detect new special features in the atomic structure of regular three-bilayer steps on a Si (557) surface. The results of an analysis of the images obtained using a scanning tunneling microscope confirm the hypothesis that a row of dimers is formed at the edge of a three-bilayer step.

1. INTRODUCTION

The method of self-organization is widely used to form low-dimensional structures in the course of epitaxial growth [1, 2]. It is found very beneficial to use stepped Si (111) surfaces as substrates for the growth of quantum wires, since one can obtain steps with a low density of kinks [3]. It has recently been shown that the Si (557) surface demonstrates potential as a substrate for the formation of nanostructures using the self-organization approach [4, 5]. This surface is represented by a system of parallel three-bilayer (3BL) steps that alternate with a period of 5.73 nm [6].

Self-organization of three-dimensional islands in heterosystems on the atomically clean surface of a semiconductor substrate has been studied intensively with the aim of obtaining ensembles of quantum dots [7, 8]. The available theories consider two-dimensional (2D) layer-by-layer growth as a process of formation of nuclei with monatomic height and their subsequent growth and coalescence, which leads to the filling of an atomic layer [9, 10]. For three-dimensional (3D) islands to appear, the nuclei of the next layer should be formed on the 2D islands well in advance of the islands' coalescence [11]. In Ge/Si and InAs/GaAs(001) heterosystems, the growth of 3D islands sets in after the formation of a wetting layer that consists of several atomic layers (the Stranski–Krastanov mechanism). The main cause of the transition to 3D growth is related to stresses that arise owing to mismatch between the lattice parameters of the adsorbate and substrate.

The initial stages of the growth of Ge and Si islands on an atomically clean Si (111) surface result in special features that contradict the classical concepts if the deposition rate is low (~10^{10} cm^{-2} s^{-1}). The islands first grow according to the 3D mechanism and attain a height that corresponds to three atomic layers [12–14]. In the course of further deposition, the islands increase in lateral size but cease to grow in height; eventually, they coalesce in a continuous wetting layer with a height of 3BLs. Subsequently, the growth proceeds according to the known concepts: 3D islands appear on the wetting layer if Ge is deposited on Si, whereas growth proceeds according to the 2D mechanism in the case of deposition of Si.

A number of peaks related to 3BL Ge islands on a Si (111) surface have been observed in Raman spectra [15]. These peaks are associated with dimensional quantization of the Ge phonon spectrum in the growth direction. Consequently, we can expect that the other physical parameters of these Ge islands on the Si (111) surface should also be quantized. Therefore, it is quite expedient to gain insight into the causes of formation and stability of the 3BL Ge islands. In this study, we use a simulation to consider the initial stages of the growth of Ge islands on an atomically clean Si (111) surface before the formation of the wetting layer; in addition, we study the effect of possible dimerization of the

bonds at the islands' edges on the morphology of the islands.

At the present time, it is established that there exist several types of dimers on Ge and Si surfaces. On a surface with the (001) orientation, two neighboring atoms unite into a dimer with a dimerized bond that is, on average, parallel to the substrate (a horizontal dimer G_s). The atoms that compose this dimer are the next nearest neighbors and both have two bonds with the substrate. Such dimers are referred to as symmetric [16] and are aligned in dimer rows to form (2×1)-type superstructures [17]. If an adatom diffuses along a dimer row, the activation energy for a diffusive jump is much lower than for a transverse jump [18]. Detailed experimental and theoretical studies show that the (001) surface is warped and dimerized [19, 20]. According to different publications, the difference in the Si atom height in a dimer ranges from 0.31 to 0.73 Å, while the lengths of the interatomic bonds lie in the range 2.25–2.32 Å. These values correspond to a dimer G_s tilt angle of ~8°–13° with respect to the (001) plane.

Chadi [16] described the structure of asymmetric G_a dimers formed at the edge of a monatomic step on an Si (001) surface. These dimers are perpendicular to the step edge and to the symmetric dimers at the upper terrace. In asymmetric dimers, one atom has three bonds with its nearest neighbors and one dimerized bond, whereas the second atom has bonds with its nearest neighbors and a single bond with the next nearest neighbor in the dimer. Fujikawa *et al.* [21] reported the existence of asymmetric dimers on a (105) Si surface.

Horizontal symmetric dimers with an arrangement of bonds differing from that considered in [15] are the elements of the Si (111)–(7×7) superstructure [22]. As was shown in [23], horizontal dimers are formed along the edge of the upper terrace at a height of one bilayer (BL) on the Si (111)–(7×7) superstructure and have a common bond parallel to the step. In contrast to the dimers in the substrate at the edges of the (7×7) cells, where each atom in a dimer has four saturated bonds, the $G_{(7 \times 7)\text{ed}}$ edge dimers formed along the 1-BL step have two bonds with the substrate and one bond that connects two neighboring atoms. In [23], the existence of horizontal dimers on a stepped Si (111)–(7×7) surface was confirmed by theoretical calculations in the tight-binding approximation and by experimental data obtained from scanning tunneling microscopy (STM).

In this study, we consider several variants of dimer formation perpendicular to the line of a 3BL step on a Si (111) surface. We made a detailed study of STM images of the edges of 3BL Ge nanoislands on a Si (111) surface and 3BL steps on Si (557) surfaces. We obtained new data on the atomic structure of regular 3BL steps on a Si (557) surface. We also advance a hypothesis that concerns the origination of a row of dimers perpendicular to the edge of a 3BL step; specifically, these dimers limit the height of the Ge and Si nanoislands to three bilayers and stabilize the height of 3BL steps on a clean Si (111) surface. The results of an analysis of the step profiles confirm the hypothesis that a row of perpendicular dimers is formed along the edge of a step.

2. INITIAL STAGES OF GE GROWTH ON SI (111) AT LOW DEPOSITION RATES

At low rates of Ge deposition onto a Si (111) surface, the formation of triangular Ge islands with a height of as much as three layers has been observed [12–14] before the onset of formation of the wetting layer. In [13], deposition was carried out at deposition rates (10^{-2}–10^{-3} BL/min) that were an order of magnitude lower than those in [12] (7×10^{-2} BL/min); in [12] and [13], the deposition temperatures were nearly the same (350–500°C). The triangular shape of the islands and the limitation of the islands' height to three bilayers are much more pronounced at lower deposition rates. The effect of origination of multilayered triangular Si islands in the initial stages of homoepitaxy was also described in [12].

Structural transformation into the (7×7) superstructure on a real Si (111) surface occurs at temperatures below 830°C [22]. The nuclei of epitaxial Ge and Si islands feature a clearly pronounced triangular shape with the sides aligned along the boundaries of the half-cells of the superstructure. The descending steps confining the islands are perpendicular to the $\langle \bar{1}\bar{1}2 \rangle$ directions [12]. Without structural transformation, the opposite orientation would be preferential. In that case, for each boundary atom, there would be a single dangling bond rather than the two present in the real orientation.

The smallest Ge or Si islands, with a height of one atomic layer, are formed when small clusters (containing 15–20 atoms according to estimations [24]) with an amorphous structure fill four neighboring half-cells of the (7×7) superstructure, with an F half-cell located in the center. A formed island acquires a (7×7) superstructure and then grows for some time as a 2D island, retaining its triangular shape [12–14].

Well in advance of the coalescence of one-layer Ge or Si islands, the nuclei of the next layer are formed on these islands near the edge or vertex of the triangle (rather than in the middle of an island). The second layer expands and fills the underlying island. Observations of Si deposition [12] have shown that the size of the lower layer of an island ceases to increase until this layer is completely covered by the next layer. This circumstance indicates that atoms are preferentially supplied to the top of an island from the substrate, rather than from the flux. In the case of Ge islands, the third layer is also formed on the second layer in the vicinity of the edge or top, whereas the fourth layer is practically not formed until the onset of coalescence of the islands. After deposition of a 0.5 BL of Ge, 80% out of

about the hundred islands found had a height of three bilayers [13].

The Si or Ge atoms were deposited onto identically prepared Si (111) surfaces, which were annealed at a temperature as high as 1250°C and then cooled to the required temperature immediately before deposition. The similar behavior of the Si and Ge islands in the initial stage of deposition suggests that the above special features of growth of both materials are determined by the properties of the Si (111) surface; apparently, the difference between the lattice parameters of Si and Ge is not very important at this stage.

There is another phenomenon that is indicative of the increased stability of the 3BL-high steps. If the Si (111) substrate plane is tilted in the $\langle \bar{1}\bar{1}2 \rangle$ direction, the orientation of the descending steps on vicinal Si (111) surfaces is the same as that at the boundaries of the triangular islands. As was shown in [25], only steps with a height of 1 BL or 3 BLs are present on such a surface. As the tilt angle increases, the fraction of 3BL steps increases until a structurally perfect (557) surface is formed; this surface consists only of 3BL steps separated by (111) terraces with a width of one (7×7) cell [6].

3. SIMULATION

In order to clarify the causes of formation of the 3BL-high islands, we simulated the initial stages of growth of Ge on a Si (111) surface. In the simulation, we developed and used a kinetic Monte Carlo model of epitaxial growth of 3D layers on a substrate composed of a crystal with a diamond-like lattice in a system with several components of different chemical nature [26]. The substrate plane corresponded to the (111) orientation. The main parameters of the model crystal were the energies at which the atoms bonded with their nearest neighbors and the energy barrier E_{dim} for incorporation of an atom into the lattice site, where this atom is thought to destroy the dimerized bonds. Since we simulated the deposition of Ge onto Si, the energies of the Si–Si (E_{11}), Ge–Ge (E_{22}), and Si–Ge ($E_{12} = E_{21}$) bonds were introduced.

According to the published data, $E_{11} = 1.3$ eV [27]. The values of E_{22} and $E_{12} = E_{21}$ were varied so that the density and sizes of the islands coincided with those of STM data [13] under identical growth conditions, i.e., the substrate temperature T, the deposition rate, and the amount of deposited material. The effect of structural transformation into the (7×7) superstructure on the diffusion of deposited atoms was taken into account by introducing an effective value of E_{12} that ensured that the calculated density of islands was in agreement with the experimental data.

Direct experimental data on the arrangement of atoms at the boundaries of multilayered Ge or Si islands on a Si (111) surface are lacking at present. In order to study the effect of dimerization of the atoms at the edges of the islands on their morphology, we varied the value of E_{dim}. A decrease in the probability of incorporating an atom into the lattice site ($P_{dim} = \exp(-E_{dim}/kT)$) occurred in all the cases where the neighboring atoms in the crystal lattice had dangling bonds directed to each other, meaning that these bonds could become dimerized. It is noteworthy that orientation of these dimers depends on the arrangement of the edge atoms in the crystal lattice. The dimers can be arranged both along and across the island edge.

By comparing the results of the simulation with the experimental data at $T = 380$°C and deposition rate $V = 3.9 \times 10^{-3}$ BL/min, we obtained $E_{12} = 1.0$–1.1 eV. It is this parameter that most profoundly affects the density of the islands. We can use the experimental data reported in [28, 29] indirectly to assume that the value of E_{22} should exceed that of E_{11}, though not to a great extent. We varied E_{22} from 1.3 to 1.5 eV. At $E_{dim} = 0.5$–0.6 eV and $P_{dim} = \exp(-E_{dim}/kT) = 10^{-4}$–$10^{-5}$, the growth in the height of the islands sets in well in advance of their coalescence at $E_{12} = 1.0$–1.1 eV and $E_{22} = 1.3$–1.5 eV.

A decrease in P_{dim} brings about an increase in the rate of origination of the upper atomic layers. This effect is illustrated in Fig. 1, where the dependences of the number of atoms in different atomic layers on the deposition time at two values of P_{dim} are shown.

In Fig. 2, we show images of real and simulated surfaces that have the same area and contain islands obtained under the same conditions and with an equal amount of deposited material. The density of the islands on the simulated and experimental surfaces is the same to within fluctuations. At lower heights of the energy barrier E_{dim}, the growth of two-dimensional (rather than three-dimensional) islands is observed. The islands on the simulated surface differed from those on the experimental surface in relation to their orientation at $P_{dim} \geq 10^{-4}$ (Figs. 2a, 2b). As a result of a decrease in the probability of incorporation of the atoms into dimers, the only rate at which the atoms attach to the $\langle \bar{1}\bar{1}2 \rangle$ steps decreases, whereas the rate of attachment to the $\langle 11\bar{2} \rangle$ steps, where dimers are not formed, is not affected. Therefore, beginning with certain values of $P_{dim} < 10^{-4}$, the $\langle \bar{1}\bar{1}2 \rangle$ steps start to be prevalent in the facets of the islands. The best agreement between the simulated and experimental systems of islands with respect to density, size, and orientation is attained at $E_{11} = 1.3$ eV, $E_{12} = 1.1$ eV, $E_{22} = 1.5$ eV, and $P_{dim} = 10^{-5}$.

4. HYPOTHESIS

We failed to simulate the experimentally observed limitation of the islands' height to three bilayers. Filling of the fourth and higher layers during deposition increased at a much higher rate at the simulated surface than in the experiment. Cessation of the growth in the height of the islands can occur if the conditions under

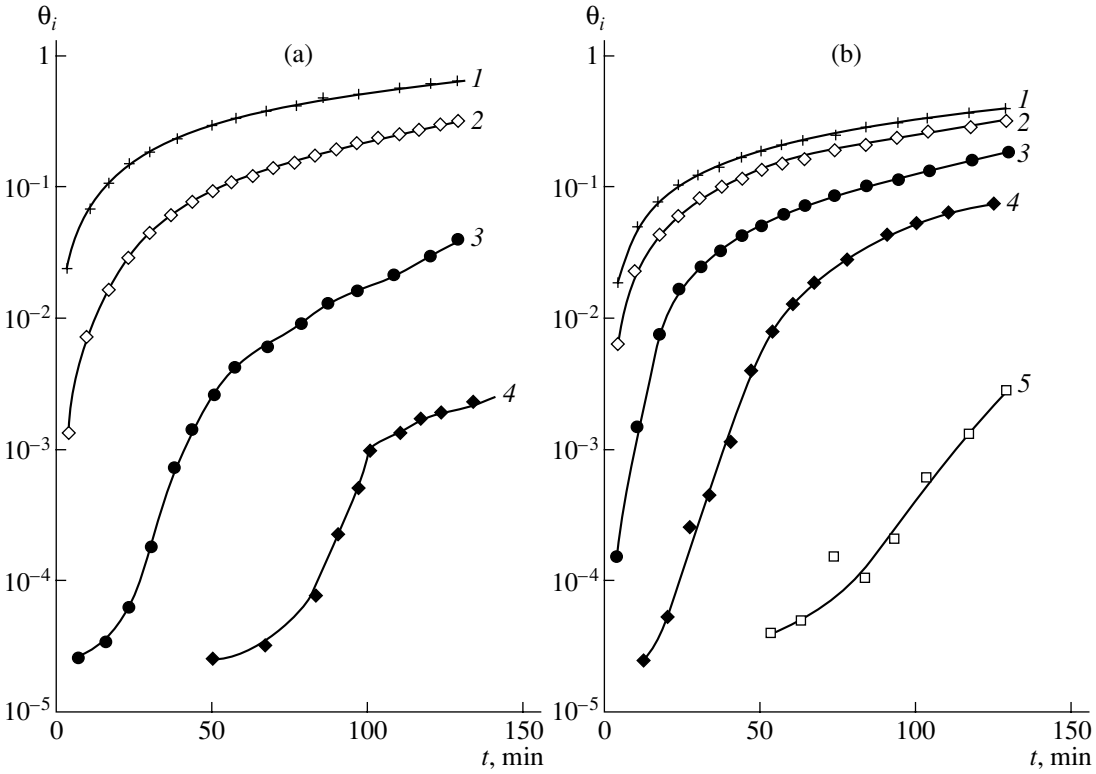

Fig. 1. Dependences of the coverage θ_i in various atomic layers on the deposition time at $E_{11} = E_{22} = 1.3$ eV, $E_{12} = 1.1$ eV, $T = 653$ K, and $V = 6.5 \times 10^{-5}$ BL/s. The numbers of the curves coincide with the numbers of layers $i = 1$–5, beginning with the substrate. The probability of incorporation of an atom into the lattice P_{dim} = (a) 10^{-3} and (b) 10^{-5}.

which the atoms diffuse through the islands' boundaries change when the 3BL height is attained. We formulated a hypothetical scheme that can account for the multilayer growth and subsequent limitation of the islands' height to three bilayers for both Ge and Si on the basis of the assumption that the arrangement of dimers at the boundaries may depend on the island height.

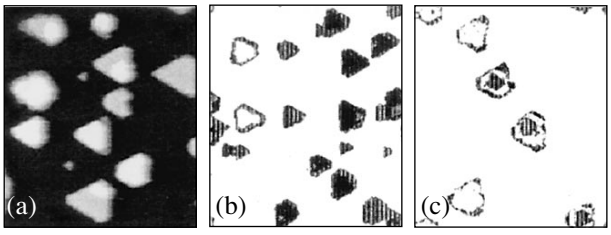

Fig. 2. Islands on (a) real and (b, c) simulated Si (111) surfaces with the same area (77×67 nm^2) at $T = 653$ K, $V = 6.5 \times 10^{-5}$ BL/s, and the coverage $\theta = 0.5$ BLs. (a) An STM image of the experimental surface possessing Ge islands with a height of 2 BLs and 3 BLs (the higher an island, the lighter its image). (b, c) Simulated surfaces with the diffusion parameters (b) $E_{11} = E_{22} = 1.3$ eV, $E_{12} = 1.1$ eV, and $P_{\text{dim}} = 10^{-4}$, and (c) $E_{22} = 1.5$ eV, $E_{12} = 1.0$ eV, and $P_{\text{dim}} = 10^{-5}$.

Following the formation of the second bilayer on an island, this bilayer acquires the (7×7) superstructure and the atoms in the first bilayer occupy the bulk lattice sites. In the case of the observed orientation of the boundaries, the edge atoms in the first bilayer can form only dimers that are parallel to the boundary. When the third bilayer is formed, the atoms in the two underlying bilayers are already at the bulk lattice sites, whereas only the third atomic layer is subjected to rearrangement. In this case, dimers that are perpendicular to the island boundary (transverse dimers) can be formed at the edge. In Fig. 3, we show a simulated image of a 3BL island on a (111) surface with the (7×7) superstructure rearrangement both on the substrate and at the island top. One can clearly see the horizontal $G_{(7\times7)\text{ed}}$ dimers at the sites where the (7×7) superstructure extends to the edge of the upper terrace. It is at this edge of the island that a row of transverse dimers perpendicular to the island edge can be formed from atoms of the first and second layers. Transverse dimers can form a row along the island boundary, similar to the row of dimers on a (001) surface. Such a row of dimers would retard the diffusion of atoms from the substrate to the top of an island. In this case, the (7×7) rearrangement prevents the forming of transverse dimers both between the first row and the substrate and between the second and third bilayers. A row of transverse dimers is not

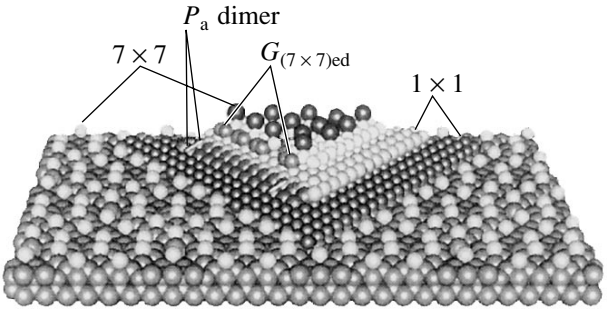

Fig. 3. Schematic representation of a 3BL island on the Si (111) surface rearranged into a (7×7) superstructure on the substrate and the island top. The $G_{(7 \times 7)ed}$ horizontal dimers in the third layer of the (7×7) structure are shown at the left-hand edge of the island; the P_a dimers formed by the atoms of the first and second bilayers are also shown. The rearrangement in the first and second bilayers and, also, the $G_{(7 \times 7)ed}$ and P_a dimers are not observed at the right-hand edge of the island.

formed at sites where the third BL does not extend to the island edge.

In Fig. 4, we illustrate different variants of the formation of transverse dimers that are perpendicular to an island edge and located at this edge. We will refer to these dimers as *P* dimers. In Fig. 4, we show different variants of the island-edge structure. The third bilayer and the substrate are not represented in the scheme of Fig. 4 because the atoms from this layer and the substrate are not involved in the formation of the *P* dimers. In Fig. 4a, we show an island edge with atoms that have dangling bonds and can be dimerized but have not yet undergone this process. In Figs. 4b and 4c, we show this edge with an asymmetric P_a dimer. The asymmetric P_a dimer consists of an atom from the upper layer of the second bilayer and an upper atom in the first bilayer. In this case, the lower atom has three saturated bonds and is displaced insignificantly from its initial site before dimerization, whereas the upper atom exhibits two saturated bonds and is displaced to a greater extent as a result of dimerization. In this case the tilt of the island edge is close to 30°. The variant of formation of a symmetric P_s dimer in a situation where both the edge atoms are symmetrically displaced from their sites and have an identical number of saturated bonds corresponds to an island-edge tilt of about 55° (the (001) plane), as is illustrated in Fig. 4d.

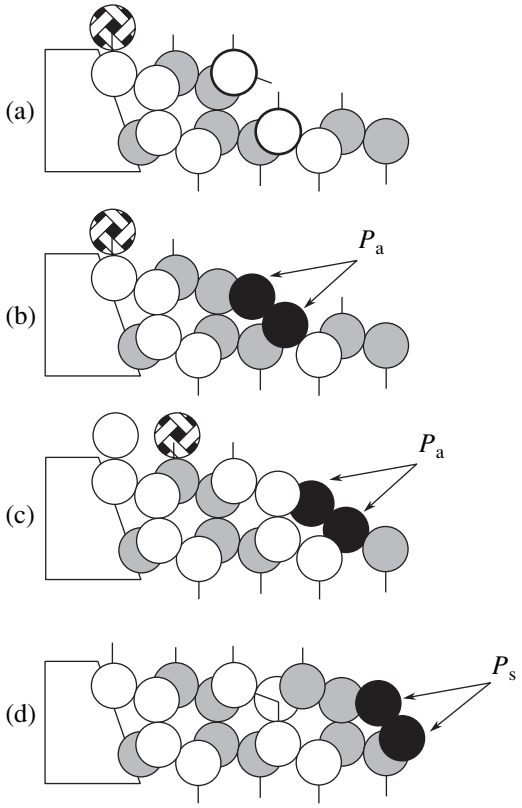

Fig. 4. Arrangement of atoms in the cross section perpendicular to an island edge and possible configurations of the edge *P* dimers. Substrate and third-bilayer atoms are not shown. The black circles correspond to dimerized atoms, the white circles correspond to atoms that are located in the drawing plane, and the gray circles correspond to atoms located beyond the drawing plane. (a) The island edge without a dimmer, (b) a P_a dimer tilted by an angle on the order of 30°, (c) a similar P_a dimer at the island edge, and (d) a P_s dimer tilted by an angle on the order of 55° to the substrate plane.

5. EXPERIMENTAL

The experiments were carried out using *n*- and *p*-Si samples with sizes of $12 \times 3 \times 0.4$ mm and resistivities of 10–10^3 Ω cm. Deviations from the (557) and (111) faces in the $[\bar{1}\bar{1}2]$ and $[11\bar{2}]$ directions were evaluated using an X-ray diffractometer. A clean Si surface was obtained and Ge epitaxy and STM studies were carried out in a vacuum chamber at a pressure no higher than 2×10^{-10} Torr; a RIBER-OMICRON system was used. In order to obtain the atomically clean Si surface, we heated a sample by applying a direct current for 20 s until a temperature of 1250°C was reached. The temperature was then lowered to 900°C in a time on the order of 1 min. After keeping the sample for 2 min at 900°C in the region of the surface phase transition, we lowered the temperature to 800°C at a rate of about 0.1–0.2 K/s. After formation of the (7×7) surface structure at about 800°C, the rate of the decrease in temperature was increased to 1 K/s and the final annealing was performed for 30 min at 400°C. The growth of the Ge layer was carried out in the temperature range 350–500°C at deposition rates of 10^{-2}–10^{-3} BL/min. The value of 1 BL, i.e., a double layer of Ge atoms in the [111] direction, was assumed to correspond to 1.44×10^{15} atom/cm^2. The STM images of the surface were recorded at room temperature. Tungsten needles, obtained by electrolytic etching in an alkali solution, were used as the STM tips.

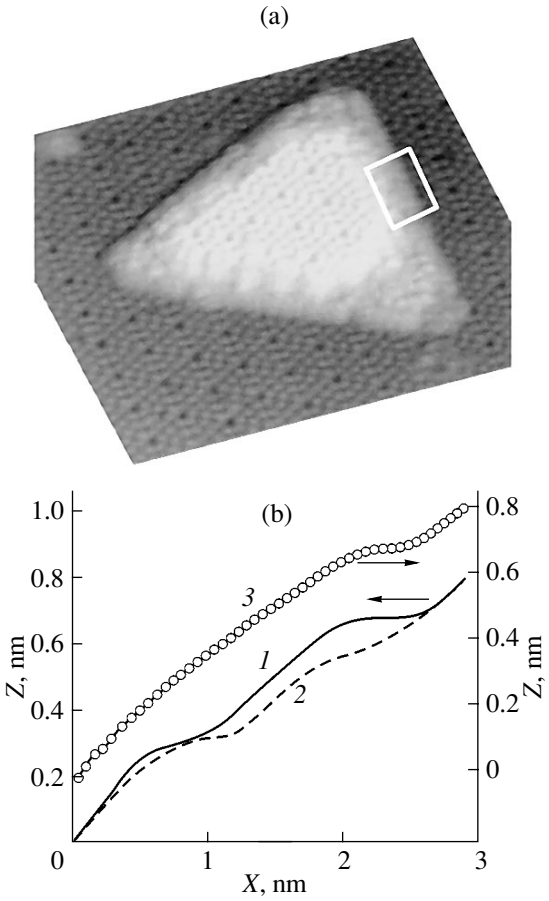

Fig. 5. A three-bilayer Ge island on a Si (111) surface: (a) an STM image (with an area of 27.1×27.1 nm^2) after deposition of 0.5 BLs of Ge at $T = 400$°C and $V = 0.004$ BL/min (the white rectangle outlines the portion of the island edge under study) and (b) three types of profiles (curves *1*–*3*) in the plane perpendicular to the island edge. The circles in curve *3* represent the resolution of the experimental setup.

Most of the STM images were recorded under the condition of a constant current in order to reveal the surface profile.

6. ANALYSIS OF THE PROFILES IN THE STM IMAGES OF A THREE-BILAYER GE ISLAND

In order to verify the hypothesis concerning the formation of *P* dimers at the edges of three-bilayer islands, we obtained STM images of the islands and analyzed the structure of their edges. In Fig. 5a, we show an STM image of an island at the Si (111) surface after depositing a 0.5 BLs of Ge. This 3BL island has a triangular shape with fairly smooth edges. The superstructural rearrangement is observed at the upper and lower terraces near the island edge. We analyzed the profiles perpendicular to the island edges. In Fig. 5b, we show the results of an analysis of the smoothest part of the edge of an island with a size of 6.2 nm. The profiles were measured along the scanning line in order to minimize the experimental noise. We analyzed more than twenty profiles and detected only three characteristic profile types, which are shown in Fig. 5b. It can clearly be seen in Fig. 5b that the initial portions of all three curves exhibit an identical slope on the order of 30°. In the profile of the first type (curve *1*), we can see two kinks, at heights of $h \approx 0.3$ nm and $h \approx 0.7$ nm, that correspond to the heights of the first and second bilayers. In the profile of the second type (curve *2*), the upper kink is located somewhat lower, at a height of $h \approx 0.6$ nm. In the profile of the third type (curve *3*), we can see a single slope for all the distances from the substrate to the end of third bilayer, where the kink sets in. Portions with profiles of the same type were observed at the extent of 2–5 nm and were located randomly along the island boundary.

Three types of experimental profiles for the island edge (Fig. 5b) correspond to the edge configurations shown in Fig. 4. Experimental profile *1* (Fig. 5b) corresponds to the scheme shown in Fig. 4a, illustrating a completely filled first bilayer and a second bilayer displaced by two atomic rows without dimers between the first and second layers. We relate the experimentally observed shift of the kink in the height in profile *2* (Fig. 5b) to the formation of an asymmetric P_a dimmer, which is shown in the scheme in Fig. 4b. Experimental profile *3* (Fig. 5b) corresponds to the case where an asymmetric P_a dimer is located at the island edge (Fig. 4c). It is quite probable that all three configurations have similar energies and can transform into one another during the growth process.

Using the suggested scheme, we can explain the fact that the height of the nanoislands is limited to three bilayers in the following way. The edge atoms of the second bilayer cannot be involved in the formation of a *P* dimer until these atoms are removed from the bulk lattice sites. As soon as the third layer is formed, this layer makes it possible for the atoms of the second bilayer to occupy the bulk lattice sites, and the P_a dimers are formed between the first and second layers. The appearance of a row of P_a dimers along an island edge reduces the atomic flux from the substrate to the island top and, correspondingly, reduces the rate of increase in the island height. At the points where the island height is smaller than three bilayers, a row of P_a dimers is not formed and the height of the other parts of the island increases to three bilayers.

The suggested model accounts for the growth of 3BL islands in transverse directions. Atoms can be incorporated into the island edge via migration from the substrate and from the island tops. The atoms coming from the substrate form the lower bilayers, while the atoms coming from the island top supply the material for the formation of the *P* dimers. Taking into account the fact that *P* dimers are not simultaneously formed along the entire island boundary, we can assume that the second and third bilayers continue to be filled, with a simultaneous increase in the lateral sizes of the island.

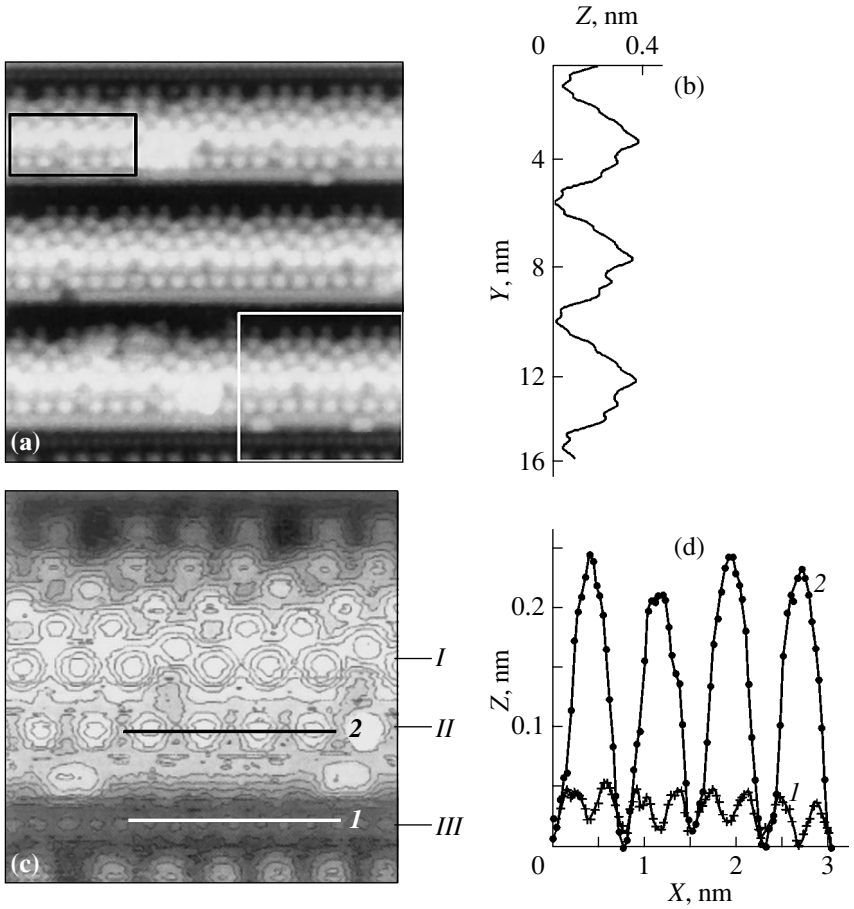

Fig. 6. The Si (557) surface. (a) An STM image obtained after a negative voltage is applied to the microscope tip. (b) The vertical-section profile averaged over the image area. (c) An enlarged fragment of the STM image (this fragment is outlined by the rectangle in the lower right-hand corner in Fig. 6a, the current isolines can be seen); here, *I* corresponds to the upper edge of the edge; *II* corresponds to a row of DAS atoms in the second bilayer; and *III* corresponds to a strip of unrearranged atoms at the lower terrace. (d) Profiles of horizontal sections *1* and *2* indicated in panel (c).

Thus, the thickness of the growing layer can exceed three bilayers only after coalescence of the 3BL islands.

The 3BL-high nanoislands cannot be formed in highly nonequilibrium conditions (at high deposition rates), as the rows of P_a dimers have no time to form.

It is possible that *P* dimers with not only a small but also a large tilt with respect to the substrate surface can be formed at the edge of a three-bilayer island. Evidently, asymmetric P_a dimers with a small tilt are formed in the course of epitaxy far in advance of the formation of P_s dimers that exhibit a large tilt. It is quite probable that the symmetric P_s dimers might be observed at the edges of the islands after annealing at certain temperatures.

7. ATOMIC STRUCTURE OF THREE-BILAYER STEPS ON AN SI (557) SURFACE

As was mentioned above, the majority of steps on the vicinal Si (111) surface, which tilt at various angles in the $\langle \bar{1}\bar{1}2\rangle$ direction, have a height of 3 BLs. This stability of the 3BL steps may also be related to the formation of *P* dimers. In order to verify this hypothesis, we obtained and carefully studied STM images of these steps. We analyzed the profiles of the 3BL steps that form a Si (557) surface.

Si (557) surfaces correspond to the tilt angle $\theta = 9.45°$ in the $\langle \bar{1}\bar{1}2\rangle$ direction and consist of alternating terraces with (111) planes and 3BL steps. The edges of the steps are parallel to the $\langle \bar{1}\bar{1}0\rangle$ direction. A single (7×7) cell is accommodated over the terrace width. We obtained these surfaces according to the method described in [6].

In Fig. 6a, we show an STM image of a fragment of the surface under consideration. In the course of scanning, the substrate was oriented so that the edges of all the steps were at the same height; i.e., the tilt of a terrace with a (7×7) cell was equal to 9.45° with respect to the horizontal. In Fig. 6a, one can clearly see the so-

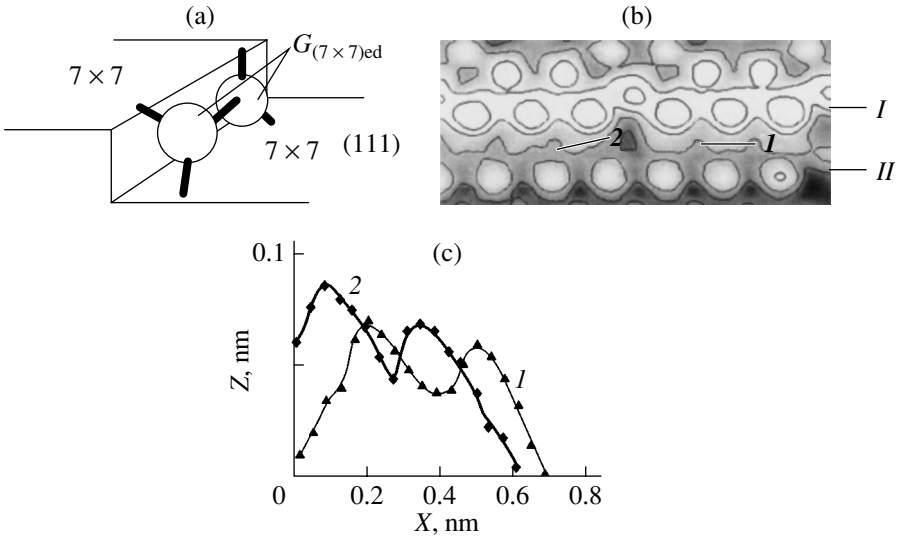

Fig. 7. $G_{(7\times7)ed}$ horizontal dimers at the edge of a step with a height of 1 BL on a Si (111) surface with the (7×7) structural rearrangement: (a) a schematic representation of a $G_{(7\times7)ed}$ horizontal dimer at the edge, (b) an enlarged STM-image fragment outlined by the dark rectangle in the upper left-hand corner of Fig. 6a (sections *I* and *II* correspond to Fig. 6b), and (c) profiles of sections *1* and *2* (see panel b) for two dimers along their major axis.

called DAS atoms of the (7×7) superstructure.[1] In our consideration, we use the term DAS atoms in reference to the atoms that occupy the same sites on the surface as adatoms in the DAS model of a (7×7) cell [22]. At the edge of the lower terrace, near the beginning of the step, we see a row of atoms occupying the bulk sites; at the same time, DAS atoms with the periodicity 2×1 can be seen in front of the upper terrace at the edge of the second bilayer. In Fig. 6b, we show the vertical profile of a Si (557) surface. In Fig. 6c, we use isolines to represent the enlarged right-hand lower fragment of the STM image; this fragment is outlined by the bright rectangle in Fig. 6a. In Fig. 6d, we show the profiles of horizontal sections over an unrearranged row of atoms (section *1* in Fig. 6c) and over a row of DAS atoms at the edge of the second bilayer (section *2*).

The vertical scale (along the *Z* direction) was determined by measuring the difference in the heights of the DAS atoms at the boundaries of the (7×7) cell and using the known angle of tilt of the terrace with respect to the horizontal. The presence of an unrearranged row of atoms indicates that there are no *P* dimers between the lower terrace and the first layer in the step. However, an analysis of the vertical profiles at the step edges on the Si (557) surface shows that the P_s dimers are quite likely to be present between the first and second layers in the step. We determined the angle of tilt of the lower step edge in reference to the terrace (the lower edge includes the first and second bilayers, counting from the lower terrace) and found it to be equal to 47°, which is close to 55°, the average tilt of a P_s dimer.

[1] DAS atoms are dimers, adatoms, and stacking faults.

A row of horizontal cell-edge $G_{(7\times7)ed}$ dimers can be seen at the step edge on the side of the upper terrace in the third bilayer of the step with the (7×7) rearrangement. In Fig. 7a, we show a schematic diagram a $G_{(7\times7)ed}$ dimer; in Fig. 7b, isolines are used to depict the fragment of an STM image of the upper step region that was outlined with the black rectangle in Fig. 6a. The undulating isolines at the terrace boundary, in the vicinity of which short straight lines are drawn to indicate the position of the $G_{(7\times7)ed}$ dimers. In Fig. 7c, we show two profiles along the above lines. The existence of two clearly pronounced peaks in the vicinity of all the edge DAS atoms indicates that $G_{(7\times7)ed}$ dimers are present. It is these dimers that prohibit the formation of *P* dimers at the edge of a step with a height smaller than 3 BLs.

In Fig. 8a, we show an STM image formed by applying a positive voltage to the STM tip; a fragment of this image (outlined by the rectangle in Fig. 8a) is represented in Fig. 8b using isolines. At this voltage polarity, the DAS atoms at the surface are not seen; at the same time, certain details of the structure of the step itself can be seen more clearly. The positions of unrearranged substrate atoms (along line *1*) are indicated in Fig. 8. The corrugated edge of the part of the step between the lower terrace and the second bilayer has a doubled period. In Fig. 8c, we show the profiles of horizontal sections along the unrearranged row (section *1*) and over the corrugated edge of the step (section *2*). In Fig. 8d, we show vertical sections of the step at the center of the hill (section *4*) and between the hills at the corrugated edge of the step (section *3*). These sections were imaged over many parts of the step and were then averaged. The largest slope of curve *3* corresponds to 56°, whereas this slope is equal to 39° for curve *4*. The

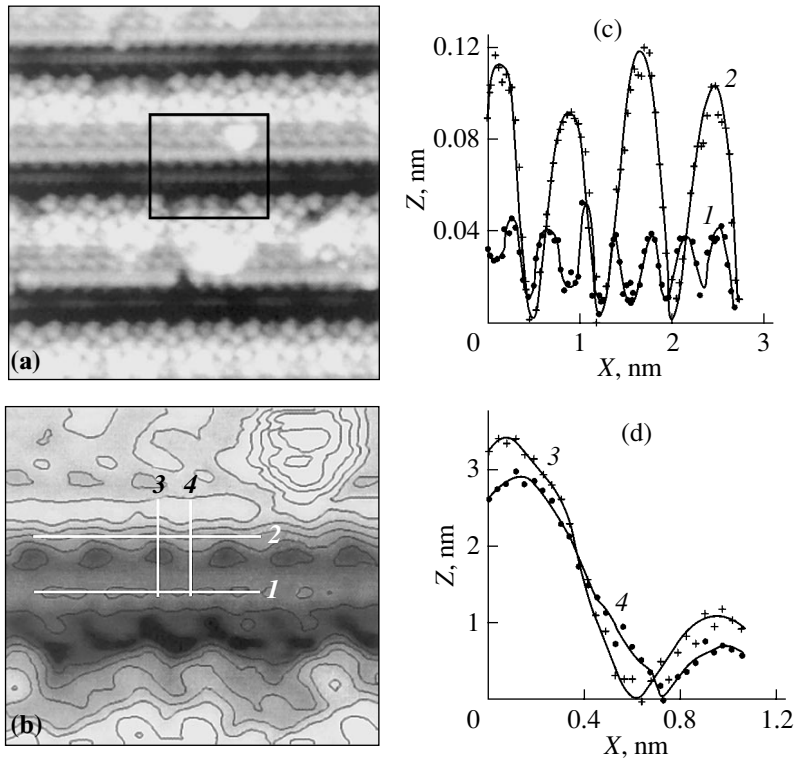

Fig. 8. (a) An STM image of a Si (557) surface after the application of a positive voltage to the microscope tip, (b) an enlarged fragment of the STM image with equicurrent isolines; (c) profiles of horizontal sections over the unrearranged row of atoms (section *1* in Fig. 6b) and the edge of a step with a height no larger than 2 BLs (section *2*); and (d) profiles of the vertical sections (*3* and *4* in Fig. 8b) at the edge of a step as high as 2 BLs: (*3*) between the hills and (*4*) in the center of the hill.

difference between the slopes of these curves (17°) is approximately equal to the difference in the tilt angle of dimers on a warped (100) surface (the doubled tilt angle for a G_s dimer with respect to a (001) surface). Therefore, we assume that a row of dimers is formed at the step edge; presumably, the tilt of these dimers alternates, which accounts for the doubled period within the entire portion of the edge, from the lower terrace to a height of 2 BLs. The step height along the assumed dimers (at the hill) was found to be equal to 0.30 ± 0.015 nm and to 0.355 ± 0.015 Å between the hills. These data are consistent with the fact that the upper atom in warped P_s dimers has a different height with respect to the STM tip.

8. DISCUSSION

Comparing the results of the analysis of the structure of steps on the Si (557) surface and those of the edges of islands, we should note the differences between the tilt angles and the arrangement of the edge atoms in these cases. These differences are observed despite the fact that the heights of the islands and steps are the same (3 BLs). The lower part of the step, with a height of 2 BLs at regular steps on the Si (557) surface, exhibits the largest tilt with respect to the lower terrace. The regions with tilt angles of 56° and 39° alternate with a period of (2 × 1). The difference between tilt angles corresponds, to within a high level of accuracy, to the difference between the tilt angles for dimers on a warped (001) surface. This observation suggests that a row of vertical dimers formed by atoms from the first and second bilayers exists.

The presence of an unrearranged strip of atoms belonging to the lower terrace in the immediate vicinity of the step was unexpected. This strip has not been reported in previous publications, although the structure of the Si (557) surface (the width of the upper terrace corresponds to the size of the 7 × 7 cell with the addition of two atomic rows [5]) suggests that this strip exists. The bulk arrangement of atoms we observed in the strip at the lower terrace indicates that the atoms in the first layer of the step are not dimerized with the atoms from the lower terrace. While the (7 × 7) cell adjoining the step from below prohibits the dimerization of the lower terrace, the absence of dimers between the strip and the first row in the step raises certain questions. We can suggest the following explanation for this fact. Symmetric dimers are formed in advance of the strip, and these dimers are more energetically favorable than the asymmetric dimers that can be formed even in the presence of the strip.

Evidence of the existence of $G_{(7\times7)ed}$ dimers at the upper terrace, as we observed in the STM images, is

consistent with the assumption that *P* dimers cannot form between the third and second bilayers. As can be seen from Fig. 6, there is a clearly pronounced difference between the terrace widths in the second and first layers. The second layer practically adjoins the first layer, and the terrace width in the second layer amounts to four–five atomic rows. The DAS atoms are located with a doubled periodicity within this width. The distance between the row of DAS atoms and the terrace edge is found to be larger than in the case of the 7×7 structure, as can be seen in Fig. 6b. As a result, the presence of DAS atoms in the second layer does not bring about the formation of horizontal dimers and does not inhibit the formation of vertical dimers between the first and second layers.

The tilt of even a quite smooth part of the edge in 3BL Ge islands on a Si (111) surface corresponds to $30° \pm 2°$, which indicates that the structure of a Ge island edge differs from that of a silicon 3BL step. As was shown above, P_a dimers with a tilt angle close to 30° can form between the first and second layers. Formation of a P_a dimer is possible when the step of the second layer is spaced from the step of the first layer, whereas the second layer should be immediately adjacent to edge of the first layer for a P_s dimer to be formed. The formation of P_a dimers should precede the formation of P_s dimers during epitaxial growth. The formation of such a region at an island edge results in diffusion along this region being facilitated owing to the formation of a row of dimers and the start of accelerated growth of the second and third layers at the other part of the island.

Thus, all the experimental data reported in this paper are consistent with the hypothesis concerning the formation of a row of perpendicular dimers both at the edge of a step with a height of 3 BLs on a Si (111) surface and at the edge of a Ge island, which can account for the increased stability of the 3BL steps and islands. The formation energy of symmetric and asymmetric edge *P* dimers could be estimated from calculations of the atomic structure of the three-bilayer steps using *ab initio* methods.

9. CONCLUSION

Thus, we obtained and studied STM images of three-bilayer Ge islands on a Si (111) surface and three-bilayer steps on a Si (557) surface. We simulated the kinetics of formation of the Ge islands on the Si (111) surface under the assumption that dimers are formed at the edges of the islands. We advanced a hypothesis that accounts for the initial multilayer growth and subsequent limitation of the height of the Ge and Si islands to three bilayers. The structure of the $\langle \bar{1}\bar{1}2 \rangle$-type steps that form the facets the islands allows for the formation of a row of transverse dimers if the height of the steps is exactly equal to three bilayers. These dimers impair the arrival of atoms from the substrate to the island top. Using the same assumption, we can explain the stability of three-bilayer steps on a vicinal Si (111) surface with deviation towards the $\langle \bar{1}\bar{1}2 \rangle$ direction. It is shown that the results of our analysis of the STM images confirm the presence of *P* dimers at the edges of the three-bilayer-high steps.

ACKNOWLEDGMENTS

This study was supported by the Russian Foundation for Basic Research (project nos. 02-02-17726 and 03-02-16506), a program organized by the Federal Center for Science and Technology, "Research and Development along Pioneering Lines in Science and Technology," in the civilian sector (project no. 2-MPN-02), and the program "Dimensionality" (grant no. 40.012.1.1.1153).

We thank A.N. Karpov for putting at our disposal the simulated images of the Si (111)–(7×7) surface.

REFERENCES

1. V. G. Dubrovskii, G. E. Cirlin, and V. M. Ustinov, Phys. Rev. B **68**, 075409 (2003).
2. G. Jin, Y. S. Tang, J. L. Liu, and K. L. Wang, Appl. Phys. Lett. **74**, 2471 (1999).
3. J. Viernow, J.-L. Lin, D. Y. Petrovykh, *et al.*, Appl. Phys. Lett. **72**, 948 (1998).
4. J. Viernow, D. Y. Petrovykh, F.-K. Men, *et al.*, Appl. Phys. Lett. **74**, 2125 (1999).
5. R. A. Zhachuk, S. A. Teys, A. E. Dolbak, and B. Z. Olshanetsky, Surf. Sci. **565**, 37 (2004).
6. A. Kirakosian, R. Bennewitz, J. N. Crain, *et al.*, Appl. Phys. Lett. **79**, 1608 (2001).
7. K. Brunner, Rep. Prog. Phys. **65**, 27 (2002).
8. Zh. I. Alferov, Fiz. Tekh. Poluprovodn. (St. Petersburg) **32**, 3 (1998) [Semiconductors **32**, 1 (1998)].
9. S. A. Kukushkin and A. V. Osipov, Usp. Fiz. Nauk **168**, 1083 (1998) [Phys. Usp. **41**, 983 (1998)].
10. V. I. Trofimov and V. A. Osadchenko, *Growth and Morphology of Thin Films* (Énergoatomizdat, Moscow, 1993) [in Russian].
11. V. I. Trofimov and V. G. Mokerov, Dokl. Akad. Nauk **375**, 465 (2000) [Dokl. Phys. **45**, 643 (2000)].
12. B. Voigtlaender, Surf. Sci. Rep. **43**, 127 (2001).
13. S. A. Teys and B. Z. Olshanetsky, Phys. Low-Dimens. Semicond. Struct., No. 1/2, 37 (2002).
14. U. Kohler, O. Jusko, G. Pietsch, *et al.*, Surf. Sci. **248**, 321 (1991).
15. A. B. Talochkin and S. A. Tiĭs, Pis'ma Zh. Éksp. Teor. Fiz. **75**, 314 (2002) [JETP Lett. **75**, 264 (2002)].
16. D. J. Chadi, Phys. Rev. Lett. **59**, 1691 (1987).
17. Y. W. Mo, R. Kariotis, B. S. Swartzentruber, *et al.*, J. Vac. Sci. Technol. A **8**, 201 (1990).
18. Zh. Zhang, F. Wu, H. J. Zandvliet, *et al.*, Phys. Rev. Lett. **74**, 3644 (1995).
19. H. Okada, Y. Fujimoto, K. Endo, *et al.*, Phys. Rev. B **63**, 195324 (2001).

20. J. Cai and J.-S. Wang, Phys. Rev. B **64**, 035402 (2001).
21. Y. Fujikawa, K. Akiyama, T. Nagao, *et al.*, Phys. Rev. Lett. **88**, 176101 (2002).
22. K. Takayanagi, Y. Tahishiro, S. Takahashi, and M. Takahashi, Surf. Sci. **164**, 367 (1985).
23. M. Hupalo, C. Z. Wang, B. J. Min, *et al.*, Phys. Rev. B **67**, 115333 (2003).
24. I.-S. Hwang, Mon-Su Ho, and T. T. Tsong, Phys. Rev. Lett. **83**, 120 (1999).
25. B. Z. Olshanetsky and A. A. Shklyaev, Surf. Sci. **82**, 445 (1979).
26. I. G. Neizvestny, N. L. Shwartz, Z. Sh. Yanovitskaya, and A. V. Zverev, Comput. Phys. Commun. **147**, 272 (2002).
27. H. Nakahara, M. Ichikawa, and S. Stoyanov, Surf. Sci. **329**, 115 (1995).
28. L. V. Sokolov, M. A. Lamin, V. A. Markov, *et al.*, Poverkhnost, No. 6, 53 (1991).
29. V. Cherepanov and B. Voigtlander, Appl. Phys. Lett. **81**, 4745 (2002).

Translated by A. Spitsyn

Semiconductors, Vol. 39, No. 8, 2005, pp. 978–982. Translated from Fizika i Tekhnika Poluprovodnikov, Vol. 39, No. 8, 2005, pp. 1012–1016.

AMORPHOUS, VITREOUS, AND POROUS SEMICONDUCTORS

The Properties of Amorphous Arsenic Chalcogenide Films Modified by Rare-Earth Complexes

S. A. Kozyukhin*^, A. R. Faĭrushin, and É. N. Voronkov****

**Kurnakov Institute of General and Inorganic Chemistry, Russian Academy of Sciences, Leninskiĭ pr. 31, Moscow, 119991 Russia*

^ e-mail: sergkoz@hotbox.ru

*** Moscow Power Engineering Institute, ul. Krasnokazarmennaya 17, Moscow, 111250 Russia*

Submitted October 21, 2004; accepted for publication October 28, 2004

Abstract—The optical and electrical properties of thin arsenic chalcogenide As–Se and As–S films modified by rare-earth complexes with various organic ligands (europium trisdipivaloylmethanate $Eu(thd)_3$ and lanthanide diethyldithiocarbamate $Ln(ddtc)_3$ (Ln = Pr, Eu)) have been studied. It is shown that the use of mixed rare-earth complexes possessing saturated vapor pressures close to chalcogenide vapor pressures allows thermal evaporation growth of films that are promising for producing planar optical waveguides. It is found that the introduction of $Eu(thd)_3$ complexes that incorporate oxygen into arsenic selenide decreases the absorptivity in the Urbach edge region and significantly decreases the conductivity activation energy, which is not characteristic of materials of this type. These results are attributed to the effect of oxygen on the medium-range order of the structure matrix. © *2005 Pleiades Publishing, Inc.*

1. INTRODUCTION

Currently, chalcogenide vitreous semiconductors (ChVSs) are widely used as a low-energy medium of reverse optical recording at an ultrahigh density. It is believed that the unique properties of these materials will allow their application in various telecommunication and integrated optical systems in the near future. This inference is based on the high transparency found in a wide wavelength range in the infrared region, the possibility of widely varying the refractive index, the low phonon energy, and the ease of manufacture of these materials. ChVS-containing rare-earth-element (REE) ions are primarily used to manufacture optical waveguides for telecommunication devices operating in the near-IR region, and, thus, the properties of such materials are actively being discussed [1–4]. In such applications, wide-gap multicomponent ChVSs, Ga–La–S, Ge–Ga–Se, Ge–As–S, As–Se–S, As–S, etc., are mainly used. As a modifying component, REE sulfides [5], chlorides, or oxides [6], are most frequently applied, whereas REEs themselves are used much less frequently [2]. Such glasses are synthesized in quartz cells at temperatures of ~1000°C in rotating furnaces and then quenched. The growth of thin-film amorphous structures from these glasses using thermal evaporation in vacuum is complicated, since they have high melting point and there is a difference in the saturated vapor pressures of the glass components. Amorphous films with good optical characteristics can be grown using laser deposition [7, 8]; however, this method is very laborious. Therefore, it is of interest to search for alternative methods of growing thin-film ChVS-based structures modified by REE ions.

The objective of this study was to grow amorphous thin films of arsenic chalcogenides As–X (X = Se, S) modified by complex REE compounds with organic ligands, as well as to analyze their electrical and optical properties. The novelty of this approach is the simultaneous use of two sources of thermal deposition: one with an inorganic component (ChVS) and the other with a volatile complex compound (CC). It should be noted that the use of organic components to synthesize amorphous hybrid materials with new properties is a recently developed approach and is of research interest [9, 10]. Such a method is used to synthesize low-melting oxide glasses, e.g., P_2O_5 and SiO_2-based nanocomposites [11]. Studies concerned with the use of chelate complexes for doping quartz optical waveguides with REE ions have also been carried out [12]. We do not know of any applications of such an approach to chalcogenide systems. The criteria for choosing an REE complex compound to act as a modifying component were described in detail in [13]. The basic parameters were the volatility and thermal stability of these complexes under conditions corresponding to chalcogenide deposition. Among the large number of compounds available, two CC types were chosen: REE trisdipivaloylmethanates with *o*-phenanthrolyne in the composition $Ln(thd)_3(Phen)$ [14] and REE diethyldithiocarbamates $Ln(ddtc)_3(Phen)$ [15]. The former compounds contain six oxygen atoms and nitrogen atoms in the central sphere surrounding an REE ion; the latter compounds contain no oxygen but incorporate a similar number of sulfur atoms and two nitrogen atoms.

1063-7826/05/3908-0978$26.00 © 2005 Pleiades Publishing, Inc.

2. EXPERIMENTAL

As_2S_3 and As_2Se_3 ChVSs were synthesized by alloying corresponding amounts of semiconductor-grade reagents in evacuated quartz cells at synthesis temperatures up to 750°C in a rotating furnace followed by cooling after switching off the furnace. An IR microscopy study of the glasses obtained using this technique did not detect opaque crystalline inclusions, and an analysis of the IR spectra showed that the glasses contained gas-forming impurities at about 10^{-4} wt %.

The complexes $Ln(ddtc)_3(Phen)$ (Ln = Pr, Sm, Eu) and $Eu(thd)_3(Phen)$ were synthesized using conventional techniques [16] and identified by data obtained from elemental and IR spectroscopic analyses. It should be noted that REE trisdipivaloylmethanates $Ln(thd)_3$ and REE diethyldithiocarbamates $Ln(ddtc)_3$ are more volatile than ChVSs. However, transformation of these compounds into mixed ligand complexes with *o*-phenanthrolyne (Phen) results in the transition of $Ln(thd)_3$ and $Ln(ddtc)_3$ to the gas phase under heating taking place after Phen splitting-off and at a higher temperature than for the initial complexes [16].

Thermal deposition was carried out using specially developed equipment [13]. The deposition conditions were experimentally selected in order to attain the maximum possible homogeneity and required thickness of the films. The composition reproducibility was monitored according to the ratio [ChVS]/[REE CC]. Room-temperature *I–V* characteristics were measured in sandwich-structure samples with aluminum and gold electrodes. The samples to be used for studying both the electrical and optical properties were grown in the same operating cycle. The film thickness varied from 0.2 to 5.4 μm and was measured interferometrically.

The chemical and phase compositions were studied using X-ray fluorescence analysis (a Spectro-scan V scanning spectrometer) and X-ray phase analysis (a DRON-2 diffractometer and a "Nonius" Guinier monochromator chamber). The film surface was analyzed using a BS 300 Tesla scanning electron microscope (the resolution was no lower than 100 nm/cm), a Soever Pro-NT-MDT atomic-force microscope (with the resolution no lower than 10 nm/cm), and a JEOL-840A scanning electron microscope with a PGT elemental analysis system. The infrared spectra of films deposited on KBr substrates were measured using a PE-FTIR 1600 spectrometer in the range 400–4000 cm^{-1}. The obtained set of results allowed determination of the phase and elemental composition of the grown films as well as assumptions to be made about a possible mechanism of REE CC incorporation into the amorphous matrix [13]. The results of the analysis showed that the highest REE content in the matrix was 2 at % for the used amorphous film growth method and CC type.

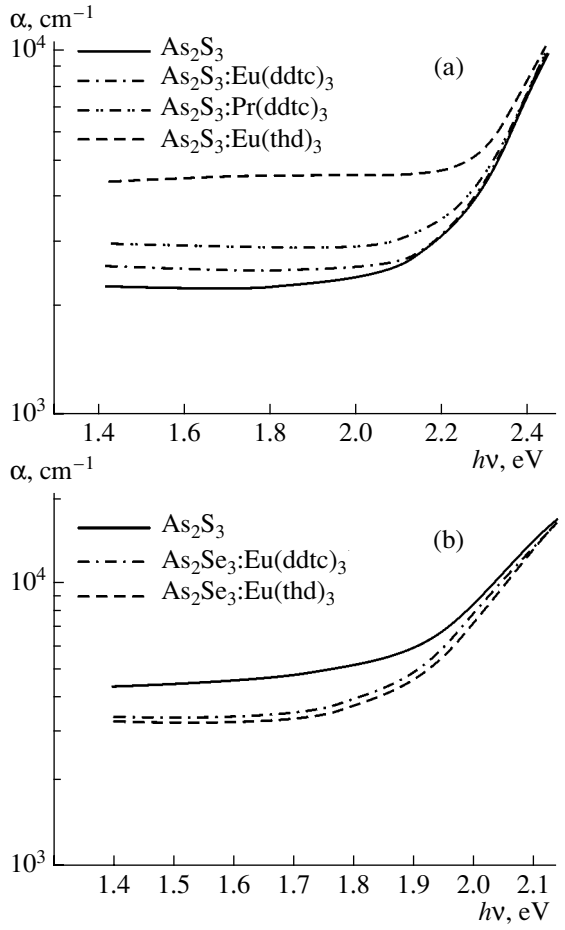

Fig. 1. Spectral dependences of the absorptivity of arsenic sulfide films that were either (a) unmodified or modified by introducing $Ln(ddtc)_3$ (Ln = Eu, Pr) and $Eu(thd)_3$ and (b) arsenic selenide either unmodified or modified by introducing $Eu(ddtc)_3$ and $Eu(thd)_3$.

3. RESULTS AND DISCUSSION

Figures 1a and 1b show the optical absorption-coefficient spectra $\alpha(h\nu)$ of amorphous As–S and As–Se films with various CCs. These dependences exhibit the following features.

(i) Modification of the arsenic sulfide films with $Eu(thd)_3$ and $Ln(ddtc)_3$ (Ln = Eu, Pr) increases absorptivity in the Urbach edge region, i.e., results in material "darkening" (Fig. 1a).

(ii) In contrast, modification of arsenic selenide films by introducing $Eu(thd)_3$ and $Eu(ddtc)_3$ CCs decreases absorptivity in a similar spectral region; i.e., the films are "bleached" during modification (Fig. 1b).

An elemental analysis of the films grown using this method showed that their composition differs from the initial ChVS in relation to enrichment with arsenic, which indicates incongruent evaporation of material during deposition. This effect explains the shift of the spectral dependences $\alpha(h\nu)$ of the nonmodified films with respect to similar dependences in [17].

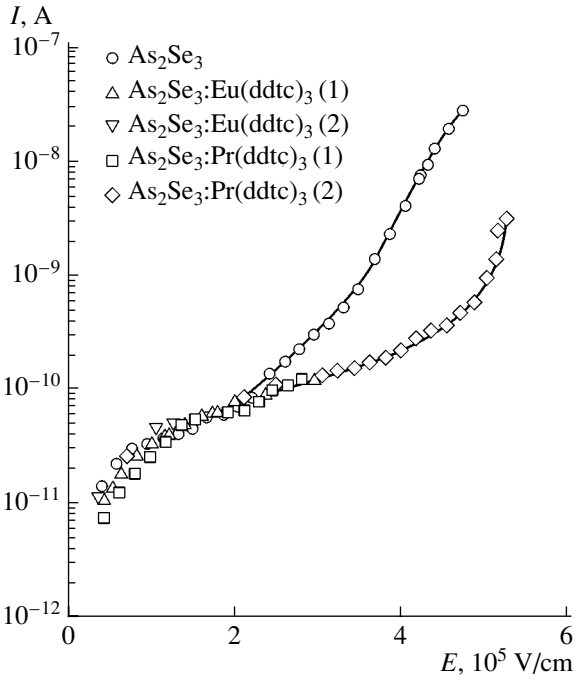

Fig. 2. Variation in *I–V* characteristics of amorphous As_2Se_3 films as a result of modification by introducing REE CC $Ln(ddtc)_3$ (Ln = Pr, Eu). The Ln content in samples (1) and (2) is 0.7 and 1.4 at %, respectively.

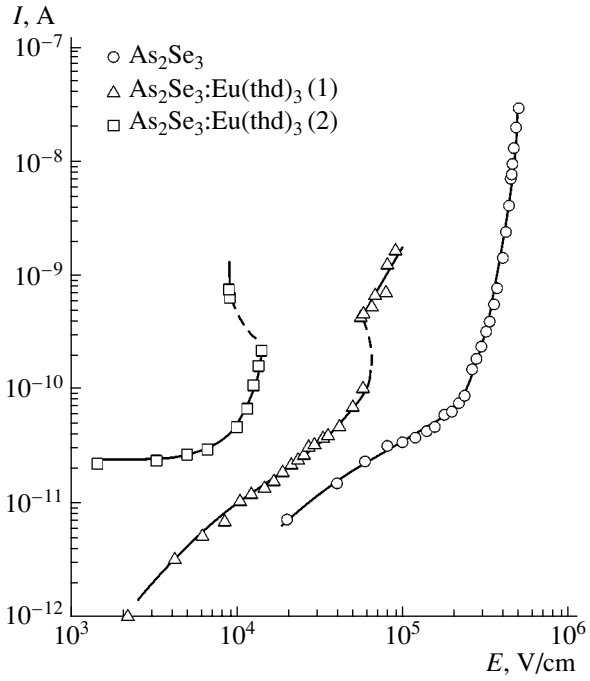

Fig. 3. Variation in *I–V* characteristics of amorphous As_2Se_3 films as a result of modification by introducing REE CC $Eu(thd)_3$. The Ln content in samples (1) and (2) is 0.7 and 1.4 at %, respectively.

The "darkening" effect, especially "photodarkening" in ChVSs, has been actively studied for more than 30 years; in contrast, "bleaching" has been observed much less frequently. Therefore, we studied the *I–V* characteristics $I(E)$ and temperature dependences of the conductivity $\sigma(T)$ in arsenic selenide films in which this effect has been observed. Figure 2 shows the room-temperature *I–V* characteristics of the As–Se films modified by introducing $Ln(ddtc)_3$ (Ln = Pr, Eu). Figure 3 shows similar dependences for the films modified by introducing $Eu(thd)_3$. We can see from the *I–V* characteristics that the type of organic ligands surrounding the REE ions is very important and controls the type of dependences.

In the case of oxygen-free CCs, $Ln(ddtc)_3$ (Ln = Pr, Eu) (Fig. 2), modification has almost no effect on the *I–V* characteristic in the ohmic conduction portion (at a field strength $E < 2 \times 10^5$ V/cm). At the same time, the point where the *I–V* characteristic becomes nonlinear shifts to higher electric-field strengths for the modified films. The *I–V* characteristics of the samples with Pr and Eu are almost identical, which can be attributed to strong screening of the central REE ion by ligand atoms.

In the case of modification by introduction of the oxygen-containing complex $Eu(thd)_3$ (Fig. 3), not only film bleaching occurred but also the *I–V* characteristic shape significantly changed. We can see in Fig. 3 that the film conductivity increases with the CC content and the portion of negative differential resistance (NDR) arises. A further increase in the electric-field strength is accompanied by instabilities. The exposure of the sample to currents above the NDR portion results in hysteresis phenomena and a change in the *I–V* characteristic shape. After the voltage was switched off, relaxation took place for several hours, and the initial *I–V* characteristic was restored. The *I–V* characteristic portion above the NDR can be approximated by the power-law dependence $I = AE^N$, where A and N are the constant approximation parameters (the coefficient N takes values from 1 to 1.7). As can be seen in Fig. 3, the threshold field decreases and the conductivity significantly increases with the CC content in the amorphous matrix.

The temperature dependences of the conductivity σ for the composition under consideration are shown in Fig. 4. The measurements were carried out under low electric-field strengths (before NDR onset). We can see that the conductivity activation energy decreases with the modifier content.

The local environment of an REE ion is an important parameter from the standpoint of luminescence yield. As has previously been shown, the presence of light elements such as C, F, N, and especially O, is an important condition for efficient luminescence of an Er^{3+} ion in crystalline and amorphous silicon [18]. We studied luminescence at $T = 300$ K for two types of amorphous films composed of arsenic sulfide with various CCs. The amorphous As_2S_3 film modified by introducing $Eu(thd)_3$ has a luminescence spectrum that involves transitions between energy levels typical of an

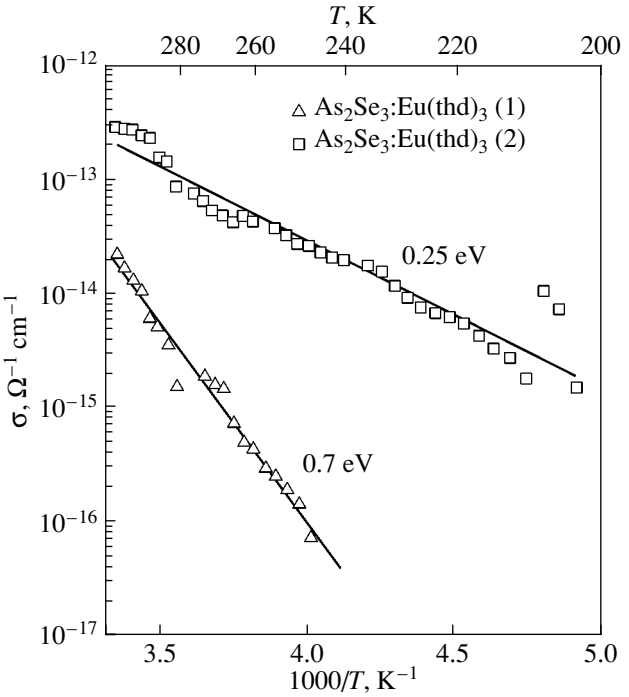

Fig. 4. Temperature dependences of the conductivity σ of amorphous As_2Se_3 films modified by introducing REE CC Eu(thd)$_3$. The Ln content in samples (1) and (2) is 0.7 and 1.4 at %, respectively. The conductivity activation energies are indicated.

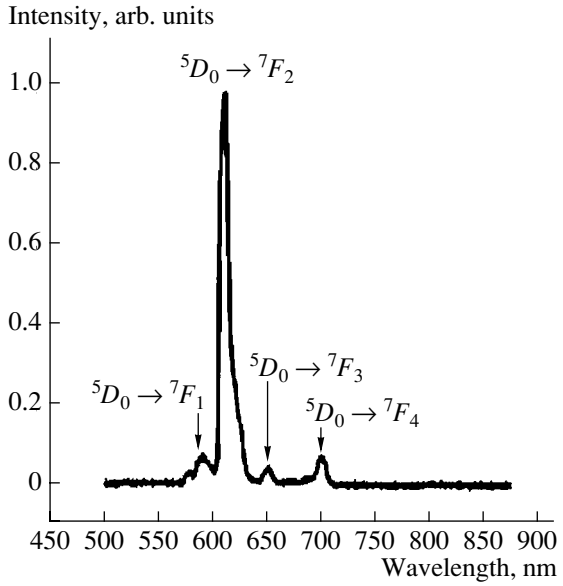

Fig. 5. Luminescence spectrum of the As_2S_3 film modified by Eu(thd)$_3$ (the excitation wavelength is 365 nm and T = 300 K).

Eu^{3+} ion: $^5D_0 \longrightarrow {}^7F_0$ (580 nm), $^5D_0 \longrightarrow {}^7F_1$ (593 nm), $^5D_0 \longrightarrow {}^7F_2$ (617 nm), $^5D_0 \longrightarrow {}^7F_3$ (652 nm), and $^5D_0 \longrightarrow {}^7F_4$ (697 nm) [19] (see Fig. 5). The "pure" arsenic sulfide film excited by light at the same wavelength of 365 nm does not luminesce in the range 500–800 nm at room temperature. No luminescence was detected at room temperature in the amorphous arsenic sulfide films modified by introducing CC Eu(ddtc)$_3$ either. These results indicate, first, the critical role of oxygen in an Eu^{3+} ion environment in relation to possible transitions and, hence, luminescence and, second, the CC structure retention when the ChVS is incorporated into the amorphous matrix, since the spectrum shown is almost identical to spectrum of the Eu(thd)$_3$ film.

In order to explain the results, we used the concept of various levels of structure modification in ChVSs [20]. According to this concept, two groups of vitreous semiconductors can be distinguished, between which the boundary is controlled by the rigidity threshold of the glass network. In one group, ordered regions are formed in a medium-range order without any network continuity violation, since the structural matrix of such materials contains bridge bonds and is more mobile. In the other group, the ordered regions have boundaries where the network continuity can be violated. The synthesis of such materials can be accompanied by the formation of macroscopic inhomogeneities and a certain morphology. The arsenic sulfide and selenide matrices belong to different groups. The former is more mobile, and it can exhibit transformations at the structural unit level without network continuity violation. This behavior is possible if the matrix has a sufficient content of hinge (bridge) bonds and their role is dominant in the processes occurring. Such bonds can be, e.g., arsenic–sulfur bonds. "Photodarkening" is also often associated with the switching of a large number of arsenic–chalcogen bonds, although this model is not always confirmed experimentally (see, e.g., [21]).

In the less labile and more rigid matrix of arsenic selenide, such structural transformations are less probable. The film instead corresponds to a glass structure; therefore, the introduction of complex and large CCs, such as Ln(ddtc)$_3$, into a matrix can violate the network continuity due to the formation of medium-range order regions. In this case, interfaces can arise between microscopic inhomogeneities, and the latter can grow. This growth decides the formation of a surface of a certain type. In this case, the bonds between these microregions become of crucial importance. They are actively formed by embedded coordination compounds and, hence, by the chemical bonds existing in them, e.g., heterobonds such as As–O and Se–O. In [8], it was shown that "bleaching" in ChVS films can be attributed to oxidation of the initial matrix during preparation. In the case under consideration, "bleaching" can also be associated with the incorporation of "light" elements, particularly oxygen, into the film composition, and the formation of new chemical bonds. The oxygen in the CC composition is also important for the electrical properties, as follows from Figs. 2 and 3. It is clear that a change in the defect spectrum in a material modified

by an oxygen complex is greater. The NDR portion is typical of ChVSs featuring the switching effect, and this effect itself is caused by local morphological changes in the amorphous matrix. These changes give rise to inhomogeneities, which can form conducting channels (see [22]). An experiment with modified arsenic selenide films showed that the switching effect occurs at higher voltages than in nonmodified films.

4. CONCLUSION

It is shown that the use of different-ligand complex compounds of rare-earth elements with saturated vapor pressures close to the chalcogenide vapor pressure allows vacuum thermal deposition of films that show potential for the development of planar optical waveguides. It is found that the introduction of $Eu(thd)_3$ complexes that incorporate oxygen into arsenic selenide decreases the absorptivity in the Urbach edge region. For these films, a significant decrease in the conductivity activation energy is observed, which is not typical of such materials. These results are explained by the effect of oxygen on the medium-range order of the structural matrix.

ACKNOWLEDGMENTS

We are grateful to N.P. Kuz'mina (Lomonosov State University) for preparation of the complex compounds, elemental analysis of the amorphous films, and participating in discussions of the results.

This study was supported by the Russian Foundation for Basic Research, project no. 05-03-33113.

REFERENCES

1. A. Zakery and S. R. Elliott, J. Non-Cryst. Solids **330**, 1 (2003).
2. S. G. Bishop, D. A. Turnbull, and B. G. Aitken, J. Non-Cryst. Solids **266–269**, 867 (2000).
3. H. Tamorin, M. T. de Araujo, E. A. Gouveia, *et al.*, J. Lumin. **78**, 271 (1998).
4. H. Harada and Keiji Tanaka, J. Non-Cryst. Solids **246**, 189 (1999).
5. A. M. Lozac'h, S. Barnier, and M. Guitard, in *Infrarouge Chim. Solids* (Paris, 1974), p. 127.
6. K. Wei, D. P. Machewirth, J. Wenzel, *et al.*, J. Non-Cryst. Solids **182**, 257 (1995).
7. S. G. Devinder, R. W. Eason, C. Zaldo, *et al.*, J. Non-Cryst. Solids **191**, 132 (1995).
8. E. N. Borisov, V. B. Smirnov, A. Tverjanovich, and Yu. S. Tveryanovich, J. Non-Cryst. Solids **326–327**, 316 (2003).
9. M. Takahashi, H. Niida, Y. Tokuda, and T. Yoko, J. Non-Cryst. Solids **326–327**, 524 (2003).
10. El. C. Zampronio, D. N. Greggio, and H. P. Oliveira, J. Non-Cryst. Solids **332**, 249 (2003).
11. E. L. Aleksandrova, E. I. Terukov, M. E. Kompan, and N. N. Khimich, in *Proceedings of IV International Conference on Amorphous and Microcrystalline Semiconductors* (St. Petersburg, 2004), p. 194.
12. R. P. Draper, B. C. McCollum, and E. Snitzer, J. Ligthwave Technol. **8**, 1680 (1990).
13. S. A. Kozyukhin, N. A. Markova, A. R. Faĭrushin, *et al.*, Neorg. Mater. **40**, 908 (2004).
14. N. G. Dzyubenko and L. I. Martynenko, in *Problems in Chemistry and Application of β-Diketonates of Metals* (Nauka, Moscow, 1982), p. 19 [in Russian].
15. N. P. Kuz'mina, R. A. Ivanov, A. B. Ilyukhin, and S. E. Paramonov, Koord. Khim. **25**, 635 (2000).
16. R. A. Ivanov, I. E. Korsakov, A. A. Formanovskiĭ, *et al.*, Koord. Khim. **28**, 713 (2002).
17. N. F. Mott and E. A. Davis, *Electronic Processes in Non-Crystalline Materials*, 2nd ed. (Clarendon, Oxford, 1979; Mir, Moscow, 1982).
18. L. R. Tesler and A. C. Iniguez, in *Amorphous and Microcrystalline Silicon Technology: Symposium, San Francisco, 1997*, Ed. by S. Wagner *et al.* (MRS, Pittsburgh, 1998), Mater. Res. Soc. Symp. Proc., Vol. 907.
19. M. I. Gaĭduk, V. M. Zolin, and L. S. Gaĭgerova, *Luminescence Spectra of Europium* (Nauka, Moscow, 1974) [in Russian].
20. A. I. Popov, in *Semiconductors and Semimetals* (Elsevier, Amsterdam, 2004), Vol. 78, p. 51.
21. P. Hari, S. Guzel, T. Su, *et al.*, J. Non-Cryst. Solids **326–327**, 199 (2003).
22. A. Madan and M. Shaw, *The Physics and Applications of Amorphous Semiconductors* (Academic, Boston, 1988; Mir, Moscow, 1991).

Translated by A. Kazantsev

Semiconductors, Vol. 39, No. 8, 2005, pp. 983–986. Translated from Fizika i Tekhnika Poluprovodnikov, Vol. 39, No. 8, 2005, pp. 1017–1020.

AMORPHOUS, VITREOUS, AND POROUS SEMICONDUCTORS

Interaction of Fullerene with Single-Crystal Silicon

O. M. Sreseli*^, I. B. Zakharova, S. P. Vul'*, T. L. Makarova*, L. V. Sharonova*, L. V. Belyakov*, and D. N. Goryachev***

** Ioffe Physicotechnical Institute, Russian Academy of Sciences, Politekhnicheskaya ul. 26, St. Petersburg, 194021 Russia*

^ e-mail: olga.sreseli@mail.ioffe.ru

*** St. Petersburg State Polytechnical University, Politekhnicheskaya ul. 29, St. Petersburg, 195256 Russia*

Submitted March 15, 2005; accepted for publication March 29, 2005

Abstract—The optical properties of layers of C_{60} fullerene on a silicon substrate are studied before and after a reducing annealing at 900–1050°C in a hydrogen atmosphere in order to detect the formation of silicon-carbide clusters. It is shown, on the basis of Raman scattering, infrared absorption, time-resolved photoluminescence spectra, and ellipsometric measurements, that the SiC clusters are not detected at the accuracy of the methods used. After annealing, the layer is in the form of a porous hydrogen-rich film of disordered graphite, possibly with a small amount of fullerene molecules. *© 2005 Pleiades Publishing, Inc.*

1. INTRODUCTION

Microminiaturization of modern devices has led not only to the accelerated development of nanotechnologies for semiconductors but also to extensive studies and a search for the corresponding nanomaterials. In this context, the interest of scientists has been particularly attracted to carbon in all its modifications, from nanodisperse diamond to carbon nanotubes [1, 2].

Numerous recently discovered carbon modifications (fullerenes with various compositions, single- and multiple-wall nanotubes, fullerites, and other carbon formations) have found application in nanotechnology and in the development of new devices.

Taking into account that there is a well-developed silicon-based industry, it is reasonable to design nanodevices on silicon substrates, which makes it important to study the interaction of carbon in general (and fullerenes in particular) with silicon substrates under various conditions.

In this paper, we report the results of studying the properties of the interface between fullerene and single-crystal polished silicon before and after annealing at temperatures of 900–1000°C in a hydrogen atmosphere. The objective of this study was to detect the possible formation of silicon carbide SiC clusters, which have been discussed for many years [3–5], at comparatively low temperatures.

2. EXPERIMENTAL

Fullerene C_{60} layers were deposited in vacuum onto the polished surface of KDB-10 silicon (*p*-Si:B with a resistivity of 10 Ω cm) with crystallographic orientation (100) using the hot-wall method at substrate temperatures of 500–600°C [6, 7]. The thickness of the layers was ~0.2–0.6 μm. The surface was specular and colored by interference to a green or red oxidation tint.

Some of the samples were annealed for 30–40 min at 900–1000°C in a hydrogen atmosphere (we used slow heating and natural cooling in the furnace in a hydrogen atmosphere). The samples were coated with silicon layers in order to reduce the possible sublimation of the fullerene film.

We studied the time-resolved photoluminescence (PL) spectra and the Raman spectra; in addition, we used ellipsometry to determine the refractive index and the fullerene-layer thickness. We applied Fourier spectroscopy to measure the transmission spectra in the far infrared (IR) region of the spectrum.

The time-resolved PL spectra of the initial and annealed fullerene layers on silicon were studied using a computer-controlled setup based on an ILGI-503 pulsed ultraviolet laser (the emission wavelength λ = 337 nm, the pulse width 10 ns, the repetition frequency 100 Hz, and the energy in a pulse 3 μJ). The setup also included an MDR-2 monochromator, an FÉU-79 photomultiplier, and a V9-5 converter.

The Raman (micro-Raman) spectra were measured using a Renishaw 1000 grating spectrometer equipped with a slot filter (in order to eliminate the Rayleigh lines) and a cooled CCD photodetector. The 514.5-nm line of a 163S argon laser was used. The resolution of the spectrometer was about 2 cm^{-1}. Filters were used to attenuate the laser-emission power density to a level no higher than 0.5 W/cm^2. The choice of a low power density was made due to the necessity of avoiding both photoinduced changes in the fullerene films and heating of the samples.

The optical constants of the films (the complex refractive index $N = n - ik$, where n is the real component of the refractive index and k is the extinction coef-

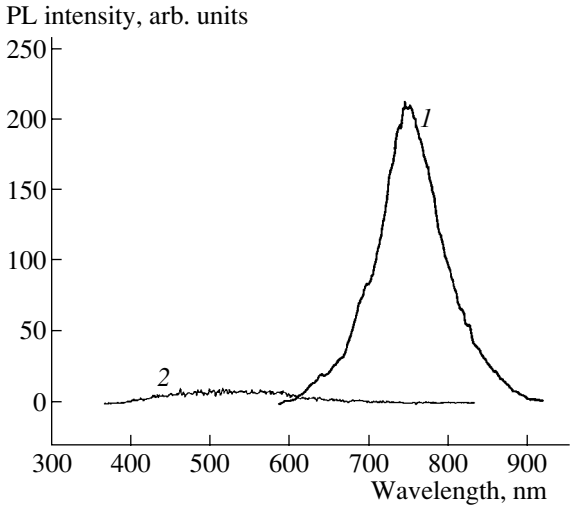

Fig. 1. Spectral curves representing photoluminescence of the C_{60} fullerene layers on silicon (*1*) before annealing and (*2*) after annealing in a reducing (hydrogen) atmosphere.

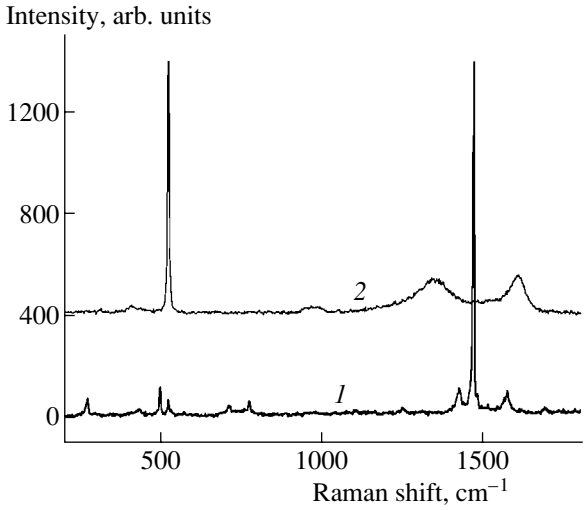

Fig. 2. Raman spectra of the C_{60} fullerene layers on silicon (*1*) before annealing and (*2*) after annealing in a reducing (hydrogen) atmosphere.

ficient (the absorption index)) and the film thicknesses were determined by the zero-ellipsometry method using an LÉF-3M laser ellipsometer. The radiation source was a He–Ne laser, and the radiation wavelength was 6328 Å. Measurements were carried out at various angles of incidence of the optical beam in the range φ = 50°–70°. The analysis was performed using a model of a homogeneous layer on a substrate with known optical parameters (for Si, n = 3.882 and k = 0.02). We solved the direct ellipsometry problem; i.e., we calculated the ellipsometry angles Ψ and Δ at the specified variable parameters of the layer (n, k, d) and determined the values at which the results of the calculation were in best agreement with experimental values of Ψ and Δ [8].

The transmission spectra in the spectral IR region were measured using an LAFS-01 FTIR (Fourier transform IR) spectrometer in the wave-number range 450–4000 cm^{-1} without pumping down the measurement chamber; the spectral resolution was equal to 4 cm^{-1}.

3. RESULTS

3.1. Fullerene Layers Before Annealing in a Hydrogen Atmosphere

The fullerene layers exhibited PL in the red and near-IR regions of the spectrum, and the recombination times were short (on the order of nanoseconds). A band that has a width of ~100 nm and corresponds to the emission from the fullerene film (see, for example, [9]) is clearly seen in the PL spectrum (Fig. 1, curve *1*).

The Raman spectra of the unannealed samples (Fig. 2, curve *1*) include an intense narrow line that is spaced by 1467 cm^{-1} from the pump line and is typical of C_{60} fullerene [10]; in addition, two satellites of the above line can be also seen (these satellites are located at 1423–1424 and 1571–1573 cm^{-1}).

According to the data of the ellipsometry measurements, the deposited fullerene layers not annealed in a hydrogen atmosphere exhibit a refractive index with n = 2.0–2.2 and $k \approx 0.04$, which are in agreement with the published data for C_{60} fullerene (n = 2.0–2.1) [11]. The somewhat larger value of n in our experiments suggests that there is a certain amount of destroyed fullerene molecules (for example, in the form of graphite).

The FTIR spectra measured before annealing (Fig. 3, curve *1*) include narrow absorption lines at wave numbers characteristic of C_{60}: ~530, 575, 1184, and 1430 cm^{-1} [12]. The other lines in the spectrum (at 668 and 1575 cm^{-1}) are more typical of graphite (or amorphous carbon). This observation may also indicate that the layers contain a certain number of damaged fullerene molecules, which apparently split off during evaporation in vacuum. The FTIR spectra of some of the samples include a line at 1700 cm^{-1} that is typically attributed to carboxyl groups. This observation can be related to adsorption of water during the period when the samples were kept in air.

Thus, the layers of C_{60} fullerene deposited on the surface of polished silicon exhibit optical properties that are characteristic of fullerene and are fairly uniform in their composition.

3.2. Fullerene Layers After Annealing in a Hydrogen Atmosphere

The optical properties of the samples changed radically as a result of annealing.

The band related to fullerene emission disappeared in the PL spectrum (Fig. 1, curve *2*).

The Raman spectra after annealing are represented by curve *2* in Fig. 2. In these spectra, the fullerene-

related line at 1467 cm^{-1} is not observed; however, the band related to the optical phonons in crystalline silicon is clearly seen at 521 cm^{-1}, and two wide bands peaked at 1345 and 1604 cm^{-1} are observed. The intense line related to the substrate (crystalline silicon) confirms the data on thinning of the layer, while the absence of the line at 1467 cm^{-1} suggests that most of the fullerene molecules were decomposed or evaporated during annealing. The lines peaked at 1345 and 1604 cm^{-1} are helpful in the determination of the composition of the remaining film. These lines belong to first-order *D* and *G* bands that are attributed to scattering by carbon in an sp^2-hybridized state. The *D* band is absent in the spectrum of single-crystal graphite and manifests itself in the presence of disorder (from the interfaces in polycrystalline graphite). In contrast, both bands are broadened in the carbon spectra and practically merge together. The results shown in Fig. 2 (curve *2*) indicate that, after annealing, the main mass of the remaining layer is composed of graphite exhibiting a medium degree of disorder (however, it has not reached the stage of amorphous graphite [13]).

The low-intensity band with a flat top extended from 945 to 985 cm^{-1} corresponds to a second-order band of Raman scattering from silicon.

The ellipsometry measurements indicate that the layer thickness decreases, in spite of the measures undertaken to prevent the evaporation of fullerenes during annealing. The parameters of the layers after annealing are consistent with a model of a homogeneous layer with the real refractive index $n = 1.3–1.5$ and a zero extinction coefficient. This extremely small refractive index can be attributed to the formation of voids and to loosening of the layers as a result of the annealing-related effect of partial evaporation of fullerene (an estimation according to the method of a two-component medium yields a porosity of 65–75%).

In addition, the destruction of an appreciable fraction of the fullerene molecules and their transformation, for example, into amorphous or polycrystalline carbon can be accompanied by hydrogenation of a layer in the course of annealing in a hydrogen atmosphere. It is well known that hydrogenation of carbon layers also brings about a decrease in the refractive index of these layers to values of 1.1–1.7 [14].

After annealing, the fullerene-related line at 526 cm^{-1} and the doublet at 1430–1436 cm^{-1}, as well as the graphite line at 668 cm^{-1}, were still observed in the FTIR spectra (Fig. 3, curves *2*, *3*). At the same time, the lines peaked at 575, 1184, and 1575 cm^{-1} disappeared. However, a new line at 1080 cm^{-1}, characteristic of asymmetric vibration of the Si–O–Si bonds, appeared in the spectrum. It is possible that this line arises and intensifies in the course of keeping the annealed samples in air, which results in oxygen adsorption (Fig. 2, curve *3*). New absorption lines also appeared, i.e., a doublet at 2340–2360 cm^{-1} and a low-intensity line at 2925 cm^{-1} (the latter line is possibly related the $C–H_x$ bonds).

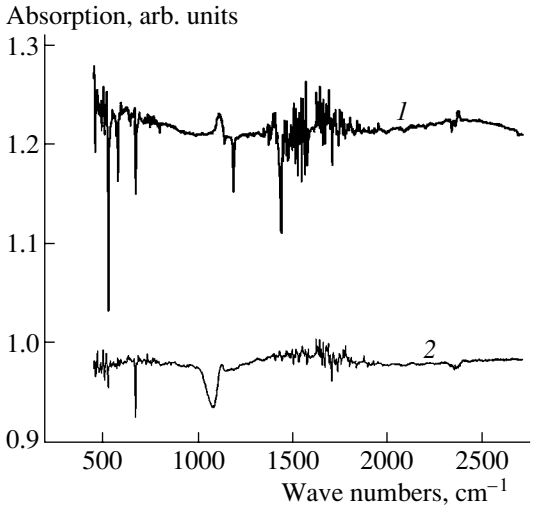

Fig. 3. FTIR spectra of the C_{60} fullerene layers on silicon (*1*) before annealing and (*2*) after annealing in a reducing (hydrogen) atmosphere.

These data indicate that the fullerene molecules are partially retained in the film. The results of optical studies of the fullerene layers after annealing in a hydrogen atmosphere suggest that the fullerene molecules possibly decompose and are partially evaporated. The remaining layer consists of porous hydrogenated disordered graphite with, possibly, a small number of fullerene molecules.

4. CONCLUSIONS

We studied the effect of reducing annealing of fullerene layers deposited onto silicon substrate on certain optical properties of these layers in order to reveal clusters of silicon carbide. The refractive index of the fullerene layers decreased appreciably as a result of the annealing. At the same time, the absorption lines that are located in the IR region of the spectrum and are characteristic of fullerenes were partially retained; in addition, new lines characteristic of hydrogen-like bonds in carbon and oxygen bonds in silicon appeared.

Lines characteristic of silicon carbide were not observed in the IR absorption spectra. The same is true for the photoluminescence spectra. We may assume that, in the best case, the fraction of the silicon carbide clusters obtained using the described technology is extremely small and cannot be observed using the measurement methods used.

At the same time, it is worth noting that, if the same procedures for deposition and annealing of a fullerene layer on the surface of nanoporous silicon are used [15], intense transient photoluminescence characteristic of cubic silicon carbide is observed in the wavelength range of 500–520 nm.

ACKNOWLEDGMENTS

This study was supported in part by the program "Physics of Solid-State Nanostructures" of the Ministry of Industry and Research Technologies of the Russian Federation; the program "Low-Dimensional Quantum Structures" of the Presidium of the Russian Academy of Sciences; and a grant from the President of the Russian Federation for the Leading Scientific Schools, no. NSh-2223-2003-02.

REFERENCES

1. V. F. Masterov, Soros. Obraz. Zh., No. 1, 92 (1997); I. V. Zolotukhin, Soros. Obraz. Zh., No. 3, 111 (1999).
2. *Optical and Electronic Properties of Fullerenes and Fullerene-based Materials*, Ed. by J. Shinar (Dekker, New York, 1999).
3. L. Moro, A. Paul, D. C. Lorents, *et al.*, J. Appl. Phys. **81**, 6141 (1997).
4. X. L. Wu, G. G. Siu, M. J. Stokes, *et al.*, Appl. Phys. Lett. **77**, 1292 (2000).
5. S. S. Deng, X. L. Wu, and S. H. Yang, Acta Mater. **52**, 1953 (2004).
6. T. L. Makarova, A. Ya. Vul', I. B. Zakharova, and T. I. Zubkova, Fiz. Tverd. Tela (St. Petersburg) **41**, 354 (1999) [Phys. Solid State **41**, 319 (1999)].
7. T. L. Makarova, N. V. Seleznev, I. B. Zakharova, and T. I. Zubkova, Mol. Mater. **10**, 105 (1998).
8. R. M. Azzam and N. M. Bashara, *Ellipsometry and Polarized Light* (North-Holland, Amsterdam, 1977; Mir, Moscow, 1981).
9. F. Yan, X.-M. Bao, and X.-W. Wu, Appl. Phys. Lett. **67**, 3471 (1995).
10. Y. Kuzmany, R. Pfeiffer, M. Hulman, and C. Kramberger, Philos. Trans. R. Soc. London, Ser. A **362**, 2375 (2004).
11. T. L. Makarova, Fiz. Tekh. Poluprovodn. (St. Petersburg) **35**, 257 (2001) [Semiconductors **35**, 243 (2001)].
12. M. R. Resmi, Shuguang Ma, R. Caprioli, and T. Pradeep, Chem. Phys. Lett. **333**, 515 (2001).
13. Y. Ward, R. J. Young, and R. A. Shatwell, J. Mater. Sci. **39**, 6781 (2004).
14. G. Compagnini, Appl. Opt. **33**, 7377 (1994).
15. O. M. Sreseli, D. N. Goryachev, V. Yu. Osipov, *et al.*, Fiz. Tekh. Poluprovodn. (St. Petersburg) **36**, 604 (2002) [Semiconductors **36**, 574 (2002)].

Translated by A. Spitsyn

Semiconductors, Vol. 39, No. 8, 2005, pp. 987–988. Translated from Fizika i Tekhnika Poluprovodnikov, Vol. 39, No. 8, 2005, pp. 1021–1022.

PERSONALIA

In Memory of Anatoliĭ Robertovich Regel' (1915–1989)

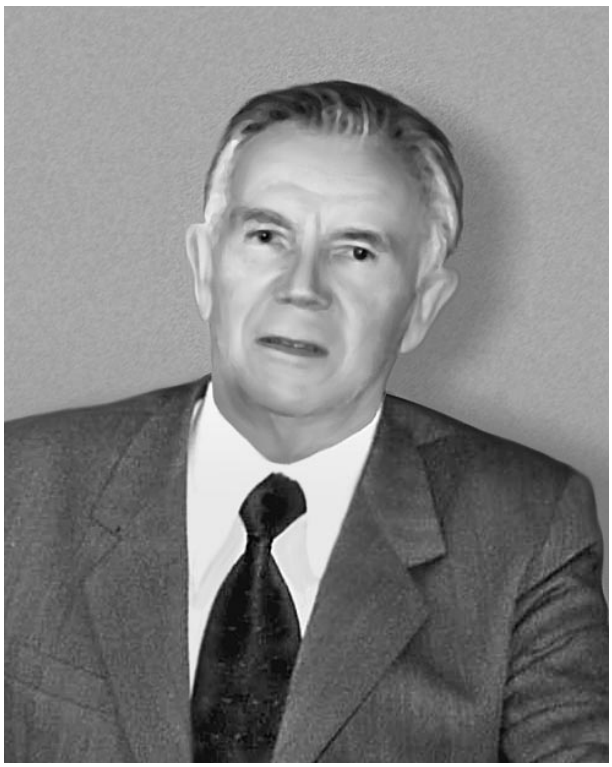

May 14, 2005, marked the passing of 90 years since the birth of Professor Anatoliĭ Robertovich Regel', Doctor of Physics and Mathematics, Honored Science Worker of the Russian Soviet Federal Socialist Republic, and an outstanding representative in the last galaxy of disciples of A.F. Ioffe. A.R. Regel' passed away in 1989, four-and-a-half months before his 75th birthday. Celebrating his 90th birthday, we pay homage to a person whose name is well known to the authors and readers of this journal thanks to his outstanding contribution to the development of semiconductor physics.

A.R. Regel' was born in St. Petersburg into the family of botanist R.É. Regel', whose predecessors were also botanists. In 1938, A.R. Regel' graduated from the Industrial Institute (at present, the St. Petersburg State Polytechnical University) and became a researcher at the Physicotechnical Institute of the USSR Academy of Sciences, where he was involved with studies of tank armor. At the very beginning of the Great Patriotic War, Regel' was sent, as a member of a special team of researchers from the Physicotechnical Institute, to Sevastopol, where, under the guidance of A.P. Aleksandrov and later I.V. Kurchatov, he was involved in work under field conditions concerned with the protection of the warships in the Black Sea fleet from German magnetic mines. In 1942, this work was continued in connection with ships in the Caspian and Amur flotillas and, later, the Pacific fleet. The developed method for demagnetizing ships was so efficient that none of the demagnetized ships were destroyed by magnetic mines during the entire period of the war. For his work, Regel' was awarded the Red Star Order and a medal "for the defense of Sevastopol."

In 1943, Regel' returned to the Physicotechnical Institute, where he continued his work in the area of tank armor; these studies were completed with the defense of his candidate thesis. Later on, the scientific interests of Regel' moved towards semiconductor physics. On the basis of a suggestion by Ioffe, Regel' undertook a detailed study of changes occurring in the electronic properties of semiconductors and metals as a result of melting; in addition, he also intended to study the electronic properties of these materials in a liquid state. The idea was to clarify the role of short- and long-range order (in the arrangement of atoms) in the formation of the energy-band structure. Regel' developed a new contactless method for measuring the electrical conductivity of solids and liquids in a rotating magnetic field. He exhaustively studied the electrical, thermal, and thermoelectric properties, as well as the density and viscosity, of a large number of semiconductors, metals, and alloys in the vicinity of melting, as a result of which the long-range order is destroyed. The results obtained played the determining role in the formation of contemporary concepts of liquid and amorphous semiconductors and brought Regel' worldwide recognition. Specialists in the field of semiconductor physics know well the Ioffe–Regel' criterion that defines the role of short-range order in determining the electronic properties of semiconductors. In his review of Regel's doctoral thesis, which was concerned with this problem, Ioffe wrote, in August 1956,

"*Regel's thesis is an outstanding event in semiconductor and solid-state physics…*

The studies carried out by Regel' have revealed the determining role of short-range order and, in particular, the coordination number in controlling the metallic and semiconductive properties of a material… The novelty and extensiveness of the results obtained and the ability of Regel' to adequately explain these results and incorporate them into a predictable general pattern

1063-7826/05/3908-0987$26.00

make the thesis under consideration a notable contribution to present-day knowledge about matter in its various states …"

In 1952, Ioffe had to leave the Physicotechnical Institute. He organized the independent Semiconductor Laboratory at the Presidium of the USSR Academy of Sciences; this laboratory, after two years, became the Institute of Semiconductors. Regel' was among a small team of Ioffe's closest colleagues who followed Ioffe and then formed the nucleus of the new institute. Ioffe highly valued the scientific competence, organizational aptitude, and personality of Regel' and appointed Regel' to be his successor as the director of the institute. After the death of Ioffe in October 1960, Regel' became the director of the Institute of Semiconductors. Regel' considered it his duty to preserve the structure, line of research, and staff of the institute. He took responsibility for general guidance of Ioffe's chosen line of research, i.e., thermoelectricity, where, in addition to a number of scientific problems, numerous practical applications appeared, especially in the field of thermoelectric cooling. Regel' was elected the chairman of the section on thermoelectric energy conversion in the council dealing with the problem of direct conversion of thermal energy to electric energy and the vice-chairman of the council on the physics and chemistry of semiconductors at the Presidium of the USSR Academy of Sciences. At that time, he became a permanent member of the editorial board of the journal *Fizika i tekhnika poluprovodnikov (Semiconductors)* and was involved in very time-consuming activity related to the erection of the new building for the institute (this new building had been planned by Ioffe himself). In spite of the fact that he was very busy, Regel' headed the laboratory and continued his extensive scientific activity.

In 1973, Regel' was awarded the Ioffe Prize by the Presidium of the USSR Academy of Sciences for a series of studies concerned with the electronic conductivity of liquid semiconductors. Studies carried out by Regel' and his coworkers on the chemical thermodynamics of semiconductors and published in three monographs were awarded the State Prize of the USSR in 1981. Regel' was awarded the Order of the Red Banner of Labor for his scientific achievements and was given the rank of Honored Science Worker of the Russian Soviet Federal Socialist Republic.

Regel' remained the director of the Institute of Semiconductors until 1972, when this institute was amalgamated with the Physicotechnical Institute. After the amalgamation and until his death, Regel' was the head of a large department that consisted of several laboratories.

Regel' gave much of his time to pedagogical activity. He supervised the work of his collaborators and numerous postgraduate students and often acted as an opponent for candidate and doctoral theses. It was amazingly easy to come and see Regel' on a matter of concern. It was sufficient to slightly open the door of his office, where he had installed a special writing-desk for himself (the large writing desk and armchair that belonged to Ioffe were kept in place as a memorial), and invitation to come in would immediately follow if he was not engaged in conversation with somebody else. Contact with Regel' was always extremely useful and instructive. During any discussion, Regel' was invariably benevolent and displayed an evident wish to help. If the help required not only advice from Regel' but also positive action, this action invariably followed.

It is not often that one can meet a person who enjoyed such wide popularity as Regel'. This popularity was due to both his scientific achievements and his amazing personality. Regel' loved skiing and kayak trips, loved and understood humor, loved nature and people, and was a convinced optimist. In his spare time, Regel' would drop in at the laboratory to compete with the younger members of staff in weight-lifting competitions using a two-pood weight without any consideration of status or position.

Regel was a man of principle; however, his adherence to principles was not inflexible. He could give up something of secondary importance in order to attain a more important success elsewhere. However, Regel' always had a moral barrier, which he could never be forced to step over. It is the presence of this barrier (in other words, probity) that was the most distinguishing feature of his personality. The people who knew Regel' will always remember him in their hearts.

S.G. Shul'man, R.V. Parfen'ev,
followers, colleagues, and friends.

The editorial staff endorses the kind words of praise contributed by followers and friends of Regel', who was our colleague and made a notable contribution to the progress of this journal.

Translated by A. Spitsyn